

ARISTOTLE UNIVERSITY OF THESSALONIKI



FACULTY OF EXACT SCIENCES

SCHOOL OF GEOLOGY

DEPARTMENT OF GEOPHYSICS

**Study of the influence of time
dependent stress changes on seismicity
rates with contribution in probabilistic
seismic hazard assessment in Greece**

Leptokaropoulos Konstantinos,
Environmental Engineer - MSc Geophysicist

Ph.D. Thesis

Submitted to the faculty of Exact Sciences, School of Geology of
Aristotle University of Thessaloniki

Thessaloniki, 2014

Λεπτοκαρόπουλος Κωνσταντίνος,
Μηχανικός Περιβάλλοντος, MSc Γεωφυσικός

**Μελέτη της επίδρασης των χρονικά εξαρτώμενων
μεταβολών του πεδίου των τάσεων στους ρυθμούς
σεισμικότητας με συμβολή στην πιθανοκρατική
εκτίμηση της σεισμικής επικινδυνότητας στην
Ελλάδα**

Διδακτορική Διατριβή

Υποβλήθηκε στο Τμήμα Γεωλογίας, Τομέα Γεωφυσικής,
Αριστοτέλειο Πανεπιστήμιο Θεσσαλονίκης
Ημερομηνία Προφορικής Εξέτασης: Νοέμβριος 2014

Εξεταστική Επιτροπή

Καθηγήτρια, Παπαδημητρίου Ελευθερία, Επιβλέπων

Αν. Καθηγήτρια, Orlecka-Sikora Beata, Μέλος τριμελούς Συμβουλευτικής
Επιτροπής

Καθηγητής, Καρακώστας Βασίλειος, Μέλος τριμελούς Συμβουλευτικής
Επιτροπής

Καθηγητής, Παναγιωτόπουλος Δημήτριος, Εξεταστής

Καθηγητής, Lasocki Stanisław Εξεταστής

Καθηγητής, Βαλλιανάτος Φίλιππος, Εξεταστής

Καθηγητής, Τσακλίδης Γεώργιος, Εξεταστής

© Λεπτοκαρόπουλος Μ. Κωνσταντίνος

© Α.Π.Θ

Μελέτη της επίδρασης των χρονικά εξαρτώμενων μεταβολών του πεδίου των τάσεων στους ρυθμούς σεισμικότητας με συμβολή στην πιθανοκρατική εκτίμηση της σεισμικής επικινδυνότητας στην Ελλάδα

ISBN

Η έγκριση της παρούσης Διδακτορικής Διατριβής από το Τμήμα Γεωλογίας του Αριστοτελείου Πανεπιστημίου Θεσσαλονίκης δεν υποδηλώνει αποδοχή των γνώμων του συγγραφέως» (Ν. 5343/1932, άρθρο 202, παρ. 2)

THESSALONIKI

2014

KONSTANTINOS M. LEPTOKAROPOULOS

Environmental Engineer, MSc Geophysicist

STUDY OF THE INFLUENCE OF TIME DEPENDENT STRESS
CHANGES ON SEISMICITY RATES WITH CONTRIBUTION IN
PROBABILISTIC SEISMIC HAZARD ASSESSMENT IN GREECE

Submitted to the School of Geology

Department of Geophysics

Defense Date

Three members of Advisory Committee

Professor of Seismology, Papadimitriou Eleftheria, Supervisor

Assoc. Professor of Geophysics, Orlecka-Sikora Beata, Member

Professor of Seismology, Karakostas Vasileios, Member

Seven members of Examining Committee

Professor Papadimitriou Eleftheria (supervisor)

Assoc. Professor Orlecka-Sikora Beatra (advisor)

Professor Karakostas Vasileios (advisor)

Professor Panagiotopoulos Dimitrios (examiner)

Professor Lasocki Stanisław (examiner)

Professor Vallianatos Fillipos (examiner)

Professor Tsaklidis Georgios (examiner)

© Konstantinos Michail Leptokaropoulos, 2014

© A.U.Th

All Rights Reserved

STUDY OF THE INFLUENCE OF TIME DEPENDENT STRESS
CHANGES ON SEISMICITY RATES WITH CONTRIBUTION IN
PROBABILISTIC SEISMIC HAZARD ASSESSMENT IN GREECE

ISBN:

«The approval of this Ph.D. Thesis by the school of Geology of the Aristotle
University of Thessaloniki does not imply acceptance of the opinions of the author»
(L. 5343/1932, Article 202, par. 2)

This thesis was partially supported by the THALES Program of the Ministry of Education of Greece and the European Union in the framework of the project entitled "Integrated understanding of Seismicity, using innovative Methodologies of Fracture mechanics along with Earthquake and non extensive statistical physics – Application to the geodynamic system of the Hellenic Arc. SEISMO FEAR HELLARC".

This thesis was partially funded by the research project titled as "Seismotectonic properties of the eastern Aegean: Implications on the stress field evolution and seismic hazard assessment in a tectonically complex area", GSRT 10 TUR/ 1-3-9, Joint Research and Technology Programmes 2010 – 2011, financed by the Ministry of Education of Greece.



This work was partially supported by the research project No. N N307234937, financed by the Ministry of Education and Science of Poland during 2009 to 2011. Support from the bilateral agreement between Aristotle University of Thessaloniki and Institute of Geophysics of Polish Academy of Sciences during 2013 is acknowledged.

To past and future

To my father Michael and my niece Michaela

The scientist does not study nature because it is useful;
he/she studies it because he/she delights in it,
and he/she delights in it because it is beautiful.

If nature were not beautiful,
it would not be worth knowing,
and if nature were not worth knowing,
life would not be worth living.

Herny Poincare (1854-1912)

Table of Contents

Table of Contents	11
Preface.....	15
Acknowledgements	17
Abstract	19
Περίληψη.....	21
Publications	29
Chapter 1. Introduction	35
1.1 Seismicity Rate Changes – Aim of the Study	35
1.2 Seismotectonic Features of the Broader Aegean Region	38
1.3 State of the Art	42
1.3.1 Review studies.....	42
1.3.2 Seismicity Rate changes during the earthquake cycle: The early studies.....	43
1.3.3 Seismicity rate changes and static Coulomb stress changes.....	45
1.3.4 Seismicity rate changes and dynamic triggering	55
1.3.5 Other phenomena associated with seismicity rate changes	59
1.4 Relevant research performed in the study area	62
Chapter 2. Rate/State Modeling	67
2.1 Introduction	67
2.2 Method - Rate/State Model Principles & Description	68
2.2.1 Rupture Models Determination	72
2.2.2 Δ CFF Calculation	74
2.2.3 Determination of Long Term Slip Rates (Stressing Rate).....	75
2.2.4 Characteristic Relaxation Time and Product $A\sigma$	76
2.2.5 Reference Seismicity Rate Evaluation	78
2.2.5.1 Selection of bandwidth, h	82
2.2.6 Model Evaluation quantification of the Results	84
2.2.7 Contribution to Probabilistic Seismic Hazard Assessment	85
2.3 Applications	89
2.3.1 Area 1 – Corinth Gulf.....	91
2.3.1.1 Introduction	91
2.3.1.2 Data	93
2.3.1.3 Parameters values	94
2.3.1.4 Results – Discussion.....	96
2.3.1.5 Contribution to Seismic Hazard Assessment.....	100

2.3.2 Area 2 – Central Ionian Sea.....	101
2.3.2.1 Introduction	101
2.3.2.2 Data	103
2.3.2.3 Parameters values	104
2.3.2.4 Results – Discussion.....	107
2.3.2.5 Contribution to Seismic Hazard Assessment.....	110
2.3.3 Area 3 – South Aegean (4 sub-areas).....	111
2.3.3.1 Introduction	111
2.3.3.2 Data	113
2.3.3.3 Parameters values	114
2.3.3.4 Results – Discussion.....	115
2.3.3.5 Contribution to Seismic Hazard Assessment.....	128
2.3.4 Area 4 – Western Turkey (4 sub-areas).....	132
2.3.4.1 Introduction	132
2.3.4.2 Data	133
2.3.4.3 Parameters values	136
2.3.4.4 Results – Discussion.....	136
2.3.4.5 Contribution to Seismic Hazard Assessment.....	144
2.3.5 Area 5 – North Aegean (4 sub-areas).....	149
2.3.5.1 Introduction	149
2.3.5.2 Data	151
2.3.5.3 Parameters values	153
2.3.5.4 Results – Discussion.....	156
2.3.5.5 Contribution to Seismic Hazard Assessment.....	165
2.3.6 Area 6 – Thessalia (Central Greece).....	169
2.3.6.1 Introduction	169
2.3.6.2 Data	171
2.3.6.3 Parameters values	172
2.3.6.4 Results – Discussion.....	172
2.3.6.5 Contribution to Seismic Hazard Assessment.....	174
2.4 Integration of Results – Contribution of the Study to Probabilistic Seismic Hazard Assessment.....	175
2.5 Discussion and Summary.....	188
Chapter 3. Stress Changes Inverted from Seismicity Rates	195
3.1 Introduction – State of the Art.....	195
3.2 Stress Inversion Methodology	198

3.3 Applications and Results	200
3.3.1 Area 1 – Efpalio 2008-2012 (Corinth Gulf)	202
3.3.1.1 Introduction-Overview	202
3.3.1.2 Data	204
3.3.1.3 Parameterization	206
3.3.1.3.1 Reference and Background Seismicity Rates	206
3.3.1.3.2 Characteristic Relaxation Time (t_a)	207
3.3.1.3.3 $A\sigma$ and Stressing Rate (\dot{S}_r).....	209
3.3.1.4 Results – Discussion.....	210
3.3.1.4.1 Temporal evolution of stress field derived from seismicity rate changes	210
3.3.1.4.2 Comparison with ΔCFF derived from elastic dislocation model	212
3.3.1.4.3 Spatial distribution of stress changes.....	217
3.3.1.4.4 ΔCFF changes close to the fault segments associated with the 2010 doublet....	219
3.3.1.4.5 Stress changes associated with spatio-temporal earthquake clustering	221
3.3.2 Area 2 – Samos-Kusadasi/ Karaburun Peninsula 2007-2012.....	225
3.3.2.1 Introduction	225
3.3.2.2 Data	226
3.3.2.3 Parameterization	228
3.3.2.4 Results – Discussion.....	230
3.3.2.4.1. Samos-Kusadasi	236
3.3.2.4.2. Karaburun Peninsula	243
3.3.3 Corinth Gulf (1975-2013).....	247
3.3.4 Lefkada (1999-2013).....	249
3.3.5 Western Crete (2009-2014).....	250
3.4 Discussion	252
Chapter 4. Concluding Remarks	259
Appendix A - Earthquake Catalogue for Western Turkey	261
Appendix B - General Orthogonal Regression.....	267
Appendix C - Identification of Completeness Magnitude.....	269
Appendix D – Kernel Estimator of Magnitude Distribution and Exceedance Probability Estimation.....	273
Appendix E – Forward Rate/State Modelling for the Efpalio 2010 Doublet	275
References	277

Preface

The aim of the thesis is to investigate the changes on earthquake occurrence rates at specific areas of the broader Aegean region and their relation with the evolution of the stress field in order to contribute to a probabilistic, time dependent seismic hazard assessment. Stress changes origin is due to seismic slip caused by large earthquakes in addition with the constant tectonic loading on the major regional faults. The study region is one of the most active tectonically areas in Mediterranean with plenty of recorded earthquakes especially during the last 25 years, when seismicity network became more efficient. This thesis was compiled under the Postgraduate Program Studies of School of Geology, Aristotle University of Thessaloniki.

In the **first chapter** the aim of the study is introduced. After a brief illustration of the most prominent seismotectonic features of the study area, the importance of seismicity rate changes in hazard analysis research is presented through a historical recursion on previous work. Studies concerning changes in earthquake production rates and their association with stress changes and other natural processes (afterslip, viscoelastic relaxation) are explicitly discussed. The main focus is on studies concerning seismicity rate changes with Rate/State dependent friction approach and how this concept was developed during the last two decades. An overview on the methodology and results from seismicity rates related studies accomplished for the Aegean and the adjacent areas is finally summarized.

In the **second chapter** the Rate/State model principles and formulation is described in detail. The model parameters, the techniques applied to handle earthquake catalog data, the process of stress changes calculations and the tools utilized for qualitative and quantitative evaluation of the results are demonstrated. Uncertainties in parameter values determination and constraints employed together with the selected range of parameter values is

also provided. Rate/State model application are presented for different regions of the study area, i.e. Corinth Gulf, Central Ionian Islands, Hellenic Arc, Western Turkey, Northern Aegean Sea and Central Greece. Comparison between observed and expected seismicity rates is quantified and earthquake probabilities for exceedance of $M=6.0$ and $M=6.5$ during the next decade are illustrated. All of the obtained results are finally integrated in respect with time dependent seismic hazard. An attempt to verify the model performance in connection with the mostly recent strong earthquakes ($M \geq 5.8$) that took place in the broader Aegean region since June 2012.

In the **third chapter** the development and application of a stress inversion algorithm, based upon Rate/State dependent friction concept is introduced. This method is used to derive stress changes from real earthquake occurrence rate changes, in areas exhibiting high recording seismicity rates. After explicitly determining the physical quantities incorporating in the modeling (characteristic relaxation time, reference seismicity rates) stress changes were sought in both space and time and their possible connection with earthquake clustering and fault interactions. Stress changes inverted from seismicity rate changes were also compared with the results derived from independent methods and their correlation was quantified.

In the **forth chapter** the results are summarized, concluding remarks are retrieved and perspectives for future research and improvement of the method efficiency are suggested.

Acknowledgements

The stress tensors were calculated using the DIS3D code of S. Dunbar, which was later improved by Erikson (1986) and the expressions of G. Converse.

Some plots were made using the Generic Mapping Tools version 4.5.3 (www.soest.hawaii.edu/gmt, Wessel and Smith 1998).

I would like to express my sincere gratitude to all those who supported me and my scientific research:

First of all I am most grateful to my supervisor, Professor Eleftheria Papadimitriou for her continuous concern and support since the first day I... invaded the Geophysics Department of Aristotle University of Thessaloniki. The scientific assistance and financial support she offered me, together with her encouragement for “searching” and “daring”, significantly helped me to build my scientific profile. I deeply appreciate her attitude of almost “forcing” me participating to International Scientific Conferences and Workshops.

I wish to express my sincere gratitude to Professor Beata Orlecka-Sikora, from the Institute of Geophysics, Polish Academy of Sciences, for the stream of knowledge she offered me and for teaching me exploring issues from different points of view. Moreover I'd like to thank her for the employment position she offered me in IGF-PAN.

I'm also very grateful to Professor Vassilios Karakostas, of the Geophysics Department of Aristotle University of Thessaloniki for teaching me being methodical and effective in my work and also for giving me the opportunity to earn important knowledge concerning field experiments, catalog elaboration and data acquisition process.

I owe many thanks to the staff of Geophysics Department of the Aristotle University of Thessaloniki, for providing me valuable scientific

knowledge and the pleasure to share this knowledge with the undergraduate students attending lectures in the School of Geology. I wish to thank all of the colleagues I met during these years for the scientific companionship and also for the moments of fun we shared inside and outside the University. I especially acknowledge my main inspiration sources Aggela Adamaki, Chara Gkarlaouni, Popi Paradisopoulou and Nikos Svigkas, for being excellent colleagues, precious scientific partners and sincere friends.

Further, I warmly thank AGH University of Science and Technology, Krakow, and Polish Academy of Sciences, Warsaw, Poland, for scientific and financial support during my post graduate studies. Especially, I would like to acknowledge Dr. Janusz Mirek for his software assistance in the initial stages of my research and Professor Stanisław Lasocki for his precious comments and suggestions concerning statistical issues.

To all of my friends who were standing by my side all of these years, I would like to express my love and respect. I'd like to make some special dedications: To Thodoris Vassiliadis for awarding me with the Master Degree of Laughing Science. To Yiannis Tsironis I owe as many thanks as the bottles of beer we used to consume after endless hours of hard working. To Chara Mantara for understanding and appreciating the results and the importance of my efforts.

Last but not least, I am indebted to my family, for all the love that gave me and for respecting and substantially supporting my decision to follow the hard life of a scientist! Mum, Dad, Nektarie, thank you so much!

Abstract

Seismicity rate changes in selected regions of the broader Aegean area were studied by application of the Dieterich (1994) Rate/State formulation. The coseismic slip of the strongest events ($M_w \geq 5.8$) that occurred during selected “study” periods was considered to contribute to the stress field evolution along with the continuous tectonic loading. Stress changes were calculated just before and after each strong event and their influence was then examined in connection with the occurrence rate of the smaller magnitude events above the individually determined magnitude of completeness in each sub-area and for the respective time intervals, named as “study” or “forecasting” periods. After defining the probability density function (PDF) of seismicity distribution, a Rate/State model was used to combine static Coulomb stress changes (ΔCFF) with seismicity rates and to compare the observed with the expected rates of earthquake production for each time period and sub-area. Different parameter values combinations were tested in order to evaluate the model sensitivity. Qualitative and quantitative correlation between the observed and the expected seismicity rates provide a test for the validity and sufficiency of the model. Earthquake probabilities for exceedance of magnitudes $M=6.0$ and $M=6.5$ during the next decade were finally illustrated. After deriving seismicity evolution from stress changes, the inverse method was attempted. Spatial and temporal evolution of the stress field in well monitored areas of Aegean were carried out. The highest accuracy and large sized regional catalogues were utilized in order to invert seismicity rate changes into stress variation through a Rate/State dependent friction model. After explicitly determining the physical quantities incorporating in the modeling (characteristic relaxation time, fault constitutive parameters, reference seismicity rates) stress changes in both space and time were derived and their possible connections with earthquake

clustering and fault interactions were evaluated. The forward modeling approach resulted to satisfactory correlation between real and synthetic seismicity rates and is expected to constitute a useful mean for the time dependent seismic hazard assessment. The inverse method yielded promising results in the cases where the available data were sufficient and should provide a powerful tool for future research as the earthquake data becomes enriched and more precise.

Εκτεταμμένη Περίληψη

Οι μεταβολές των ρυθμών σεισμικότητας σε επιλεγμένες περιοχές του ευρύτερου χώρου του Αιγαίου, μελετήθηκαν με την εφαρμογή ενός μοντέλου Ρυθμού/Κατάστασης (Dieterich, 1994). Οι μεταβολές του πεδίου των τάσεων συνυπολογίστηκαν από τις μεταβολές που οφείλονται στην σεισμική ολίσθηση που προκαλείται από τη γένεση κάθε ισχυρού σεισμού και από τις μακράς διάρκειας μεταβολές που οφείλονται στη συνεχή τεκτονική φόρτιση. Η επίδραση των μεταβολών των τάσεων στους ρυθμούς σεισμικότητας μελετήθηκαν πριν και μετά από κάθε ισχυρό σεισμό σε κάθε περιοχή. Το μέγεθος πληρότητας των καταλόγων υπολογίστηκε ξεχωριστά για κάθε περιοχή και περίοδο μελέτης. Οι ρυθμοί σεισμικότητας των μικρότερου μεγέθους σεισμών εξομαλύνθηκαν με την εφαρμογή μιας συνάρτησης πυκνότητας πιθανότητας και η επίδραση των τάσεων στις μεταβολές των ρυθμών αυτών ενσωματώθηκε στο μοντέλο Ρυθμού/Κατάστασης προκειμένου να υπολογιστούν οι αναμενόμενοι ρυθμοί σεισμικότητας. Σημαντικό εύρος των τιμών των παραμέτρων χρησιμοποιήθηκαν ώστε να ελεγχθεί η ευαισθησία και η αποτελεσματικότητα του μοντέλου. Έγινε ποιοτική και ποσοτική εκτίμηση της συσχέτισης μεταξύ παρατηρούμενων-αναμενόμενων ρυθμών σεισμικότητας ούτως ώστε να γίνει έλεγχος της αποτελεσματικότητας και της απόδοσης του μοντέλου. Υπολογίστηκαν επίσης οι πιθανότητες γένεσης σεισμού του οποίου το μέγεθος να υπερβαίνει το 6.0 και το 6.5 εντός της επόμενης δεκαετίας. Στη συνέχεια πραγματοποιήθηκε αντιστροφή της διαδικασίας Ρυθμού/Κατάστασης, ώστε να χρησιμοποιηθούν οι παρατηρούμενοι ρυθμοί σεισμικότητας για να υπολογιστούν οι μεταβολές του πεδίου των τάσεων. Για το σκοπό αυτό μελετήθηκαν οι μεταβολές των ρυθμών σεισμικότητας σε περιοχές όπου το σεισμολογικό δίκτυο εξασφαλίζει επαρκή ποσότητα και ακρίβεια των

δεδομένων. Αρχικά γίνεται εκτενής μελέτη του καθορισμού των φυσικών παραμέτρων που υπεισέρχονται στη μοντελοποίηση (καταστατικές παράμετροι ρηγμάτων, ρυθμοί σεισμικότητας αναφοράς) και στη συνέχεια υπολογίζονται οι μεταβολές των τάσεων στο χώρο και στο χρόνο. Μελετάται επίσης η πιθανή συσχέτιση των υπολογιζόμενων μεταβολών των τάσεων με την παρουσία συστάδων σεισμών (clusters) και την αλληλεπίδραση μεταξύ των ρηγμάτων. Και οι δύο προσεγγίσεις του μοντέλου Ρυθμού/Κατάστασης που εφαρμόστηκαν οδήγησαν σε ικανοποιητική συσχέτιση μεταξύ πραγματικών και αναμενόμενων τιμών των υπό μελέτη μεταβλητών (ρυθμοί σεισμικότητας – τάσεις). Η μεθοδολογία αυτή αναμένεται να αποτελέσει ένα χρήσιμο εργαλείο για την μελλοντική σεισμολογική έρευνα που αφορά στην χρονικά εξαρτώμενη μελέτη σεισμικής επικινδυνότητας ειδικά μετά τον συνεχή εμπλουτισμό των διαθέσιμων καταλόγων με περισσότερα και ακριβέστερα δεδομένα.

Ο σκοπός της παρούσας διατριβής είναι η μελέτη της αλληλεπίδρασης μεταξύ των μεταβολών των ρυθμών σεισμικότητας και των μεταβολών του πεδίου των τάσεων στην ευρύτερη περιοχή του Αιγαίου, με συμβολή στην πιθανοκρατική, χρονικά μεταβαλλόμενη σεισμική επικινδυνότητα. Ο χώρος του Αιγαίου χαρακτηρίζεται ως μια από τις περισσότερο ενεργές σεισμικά περιοχές στην Μεσόγειο, με υψηλούς ρυθμούς σεισμικότητας και σημαντική συχνότητα γένεσης ισχυρών σεισμών ($M \geq 6.0$). Η περιοχή αυτή παρουσιάζει επίσης σημαντικό βαθμό ετερογένειας όσον αφορά τις σεισμοτεκτονικές ιδιότητες και την ποιότητα καταγραφής των σεισμών από το Σεισμολογικό Δίκτυο. Για το λόγο αυτό ήταν απαραίτητος ο διαχωρισμός της περιοχής σε 15 υπο-περιοχές, με βάση κοινά σεισμοτεκτονικά κριτήρια (μηχανισμοί γένεσης) και κριτήρια σεισμικότητας (ρυθμοί σεισμικότητας, μέγεθος πληρότητας).

Οι περιοχές αυτές είναι: Κορινθιακός κόλπος, κεντρικό Ιόνιο, Ελληνικό τόξο (4 υπό-περιοχές), Δυτική Τουρκία (4 υπό-περιοχές), Βόρειο Αιγαίο (4 υπό-περιοχές) και Θεσσαλία. Η ανάλυση της μεταβολής των ρυθμών σεισμικότητας έγινε ξεχωριστά για κάθε μια από τις 15 αυτές υπό-περιοχές και τα αποτελέσματα ενοποιήθηκαν και αξιολογήθηκαν, ώστε να εξαχθούν τα τελικά συμπεράσματα.

Τα δεδομένα που χρησιμοποιήθηκαν στην παρούσα διατριβή προέρχονται από το Εθνικό Ενοποιημένο Δίκτυο Σεισμογράφων (Hellenic Unified Seismological Network). Επιπλέον χρησιμοποιήθηκαν ένας τοπικός κατάλογος για την περιοχή Karaburun-Kusadasi, καθώς και ένας κατάλογος με ισοδύναμα μεγέθη σεισμικής ροπής, M^*_w , για την Δυτική Τουρκία που συντάχθηκαν στα πλαίσια της διατριβής αυτής. Προκειμένου να δημιουργηθεί ο κατάλογος αυτός χρησιμοποιήθηκαν δεδομένα από το Διεθνές Κέντρο Σεισμολογίας (International Seismological Center) και προτάθηκαν νέες εμπειρικές σχέσεις που συνδέουν μεγέθη διαφορετικών κλιμάκων και ινστιτούτων με το μέγεθος σεισμικής ροπής. Τα μεγέθη πληρότητας για κάθε περιοχή και χρονική περίοδο υπολογίστηκαν με τη μέθοδο ελέγχου καλής προσαρμογής, η οποία τροποποιήθηκε και εφαρμόστηκε επίσης στα πλαίσια της παρούσας διατριβής.

Στο **πρώτο κεφάλαιο** γίνεται η εισαγωγή του σκοπού της διατριβής και περιγράφονται συνοπτικά οι κυριότερες σεισμοτεκτονικές ιδιότητες της ευρύτερης περιοχής του Αιγαίου. Εν συνεχεία, επισημαίνεται η σημασία της ανάλυσης των ρυθμών σεισμικότητας στη μελέτη σεισμικής επικινδυνότητας. Για το σκοπό αυτό παρουσιάζεται μια εκτενής αναδρομή σε παλαιότερες αλλά και πλέον πρόσφατες επιστημονικές εργασίες που είχαν ως αντικείμενο τις μεταβολές των ρυθμών σεισμικότητας. Γίνεται εκτενής αναφορά σε εργασίες που

σχετίζονται με τη μελέτη των μεταβολών της σεισμικότητας και τη σύνδεση τους με τη μεταβολή των στατικών και δυναμικών τάσεων καθώς και άλλων φυσικών διεργασιών (ποροελαστικά, ιξωδοελαστικά φαινόμενα). Ιδιαίτερη αναφορά γίνεται σε εργασίες που βασίζονται στην ανάπτυξη και εφαρμογή τεχνικών που βασίζονται στη μέθοδο Ρυθμού/ Κατάστασης κατά τις τελευταίες δυο δεκαετίες. Τέλος, παρουσιάζονται οι μέθοδοι και τα αποτελέσματα των εργασιών που είχαν ως αντικείμενο τη μελέτη των ρυθμών σεισμικότητας στον Ελλαδικό χώρο και τις γειτονικές περιοχές.

Στο **δεύτερο κεφάλαιο** της διατριβής περιγράφονται οι αρχές και οι μαθηματικές εξισώσεις που διέπουν τη μέθοδο Ρυθμού/ Κατάστασης και το πως αυτές εφαρμόζονται στην παρούσα εργασία. Σύμφωνα με την μέθοδο αυτή, οι αναμενόμενοι ρυθμοί σεισμικότητας μπορούν να μοντελοποιηθούν με βάση τους ρυθμούς σεισμικότητας αναφοράς, τις φυσικές καταστατικές παραμέτρους των ζωνών διάρρηξης και το ιστορικό του πεδίου της τάσης. Η εξέλιξη του πεδίου της τάσης οφείλεται τόσο στην απότομη σεισμική ολίσθηση κατά τη γένεση ισχυρών σεισμών, όσο και στη συνεχή τεκτονική φόρτιση εξαιτίας της διαρκούς σχετικής κίνησης των λιθοσφαιρικών πλακών. Κατά την παρουσίαση των μαθηματικών εξισώσεων γίνεται περιγραφή των παραμέτρων που υπεισέρχονται στις σχέσεις αυτές καθώς και η φυσική τους σημασία. Ακολουθεί εκτενής περιγραφή του τρόπου υπολογισμού/ καθορισμού του εύρους των τιμών των παραμέτρων αυτών και γίνεται σύγκρισή τους με τις αντίστοιχες τιμές που έχουν χρησιμοποιηθεί σε παλαιότερες εργασίες ή έχουν υπολογιστεί από εργαστηριακά πειράματα. Επιπλέον, μεγάλο εύρος των τιμών των παραμέτρων χρησιμοποιήθηκε ούτως ώστε να μελετηθεί η απόδοση του μοντέλου ως συνάρτηση καθεμιάς εκ των παραμέτρων αυτών.

Οι ρυθμοί τεκτονικής φόρτισης στις κυριότερες ζώνες διάρρηξης υπολογίστηκαν από τους αντίστοιχους ρυθμούς ολίσθησης, όπως αυτοί υπολογίστηκαν από εργασίες ανάλυσης γεωδαιτικών δεδομένων, λαμβάνοντας υπόψη και τον συντελεστή σεισμικής σύζευξης. Ο χαρακτηριστικός χρόνος εκτόνωσης υπολογίστηκε λαμβάνοντας υπόψη τη μέση περίοδο επανάληψης καθώς και βιβλιογραφικές αναφορές. Το γινόμενο $A\sigma$ υπολογίστηκε από τη σχέση που το συνδέει με τον χαρακτηριστικό χρόνο εκτόνωσης και τον ρυθμό τεκτονικής φόρτισης και έγινε έλεγχος των αποτελεσμάτων σε σχέση με τις τιμές που προτείνει η διεθνής βιβλιογραφία. Οι ρυθμοί σεισμικότητας αναφοράς και οι παρατηρούμενοι ρυθμοί, υπολογίστηκαν αφού έγινε εξομάλυνση της σεισμικότητας με τη χρήση μιας Γκαουσιανής συνάρτησης πυκνότητας πιθανότητας πυρήνα (Kernel), δύο μεταβλητών. Μεγάλο εύρος τιμών του παράγοντα ομαλοποίησης, h , που καθορίζει τον βαθμό εξομάλυνσης της σεισμικότητας χρησιμοποιήθηκαν σε όλες τις εφαρμογές. Οι διαστάσεις των ζωνών διάρρηξης υπολογίστηκαν από την χωρική κατανομή των ισχυρότερων μετασεισμών και την γεωμετρία των ρηγμάτων, λαμβάνοντας επιπλέον υπόψη περιορισμούς και εμπειρικές σχέσεις. Η μέση σεισμική ολίσθηση σε κάθε περίπτωση υπολογίστηκε από τις προαναφερθείσες τιμές σε συνδυασμό με τη σεισμική ροπή. Οι τιμές του λόγου του Poisson, του μέτρου δυσκαμψίας και του φαινόμενου συντελεστή τριβής (που ενσωματώνει την επίδραση της πίεσης των πόρων) που υιοθετήθηκαν στην παρούσα διατριβή επιλέχθηκαν από εργασίες που αφορούν τα ίδια σεισμοτεκτονικά περιβάλλοντα.

Στη συνέχεια έγινε εκτίμηση των αποτελεσμάτων των αναμενόμενων ρυθμών σεισμικότητας όπως αυτοί υπολογίστηκαν από την εφαρμογή του μοντέλου Ρυθμού/ Κατάστασης. Για το σκοπό αυτό έγινε χαρτογράφηση του λόγου αναμενόμενων/ παρατηρούμενων

ρυθμών σεισμικότητας για διαφορετικές τιμές παραμέτρων και για όλες τις περιόδους μελέτης. Επιπλέον έγινε εκτίμηση του Συντελεστή Γραμμικής Συσχέτισης (Pearson) και του διαστήματος εμπιστοσύνης του (95%). Τέλος, ως συμβολή στην πιθανοκρατική εκτίμηση της σεισμικής επικινδυνότητας, έγινε ο υπολογισμός της πιθανότητας υπέρβασης μεγέθους 6.0 και 6.5 σε κάθε μια από τις περιοχές μελέτης εντός ενός χρονικού ορίζοντα διάρκειας μίας δεκαετίας. Η εκτίμηση της πιθανότητας αυτής έγινε λαμβάνοντας υπόψη τον μέσο ρυθμό σεισμικότητας σε κάθε περιοχή, με τη χρήση ενός μη-παραμετρικού εκτιμητή πυρήνα της κατανομής των μεγεθών.

Εν συνεχεία παρουσιάζονται τα αποτελέσματα της εφαρμογής του μοντέλου ρυθμού-κατάστασης για όλες τις περιοχές μελέτης, καθώς και πίνακες με τις τιμές των παραμέτρων και τις χρονικές περιόδους που μελετήθηκαν σε κάθε περιοχή. Αναλυτικότερα για κάθε περιοχή παρουσιάζονται: Οι αναμενόμενοι ρυθμοί σεισμικότητας, οι χάρτες με τους λόγους αναμενόμενων/ παρατηρούμενων ρυθμών σεισμικότητας, οι συντελεστές γραμμικής συσχέτισης για επιλεγμένο εύρος παραμέτρων και για όλες τις περιόδους μελέτης και οι πιθανότητες γένεσης ισχυρών σεισμών με μέγεθος μεγαλύτερο του 6.0 και του 6.5 για ορίζοντα 10 ετών. Τέλος γίνεται συγκέντρωση και ενοποίηση των αποτελεσμάτων και παρουσιάζεται η μεταβολή του συντελεστή συσχέτισης σε σχέση με το πλήθος των δεδομένων και το χρονικό διάστημα που αυτά καλύπτουν. Η δυνατότητα πρόγνωσης του μοντέλου ελέγχεται σε σχέση με τα επίκεντρα των πρόσφατων (μετά τον Ιούνιο του 2012) ισχυρών ($M > 5.8$) σεισμών που συνέβησαν στην περιοχή μελέτης. Έγινε ποιοτική και ποσοτική εκτίμηση του κατά πόσο τα επίκεντρα αυτά εντοπίζονται σε περιοχές όπου το μοντέλο προβλέπει αυξημένους ρυθμούς σεισμικότητας και τα αποτελέσματα παρουσιάζονται σε ένα χάρτη, μαζί με τις

αντίστοιχες πιθανότητες γένεσης. Διαπιστώθηκε ότι 7 από τους 8 σεισμούς αυτούς συνέβησαν εντός ή πολύ κοντά σε περιοχές αυξημένης αναμενόμενης σεισμικής δραστηριότητας.

Στο **τρίτο κεφάλαιο** παρουσιάζεται αρχικά η ιδέα και οι προσπάθειες που έχουν γίνει διεθνώς για την ανάπτυξη και την εφαρμογή του αντίστροφου μοντέλου Ρυθμού/ Κατάστασης. Σύμφωνα με το μοντέλο αυτό, οι μεταβολές του ρυθμού σεισμικότητας όπως αυτός καταγράφεται από πυκνά σεισμολογικά δίκτυα μπορεί να δώσει σημαντικές πληροφορίες σχετικά με την χωρική και χρονική μεταβολή του πεδίου των τάσεων. Γίνεται η περιγραφή των εξισώσεων που διέπουν την μέθοδο αντιστροφής και των δεδομένων στα οποία έγινε η εφαρμογή του μοντέλου αυτού (Ευπάλιο 2008-2012, Σάμος-Κουσάντασι 2007-2012, Καραμπουρούν 2007-2012, Κορινθιακός Κόλπος 1975-2013, Λευκάδα 1999-2013, Δυτική Κρήτη 2009-2014). Σε κάθε περίπτωση γίνεται περιγραφή του τρόπου υπολογισμού των τιμών των παραμέτρων (ρυθμοί σεισμικότητας αναφοράς, χαρακτηριστικός χρόνος εκτόνωσης, ρυθμός τεκτονικής φόρτισης, γινόμενο $A\sigma$). Εν συνεχεία περιγράφονται τα αποτελέσματα τα οποία αφορούν την χρονική μεταβολή του πεδίου των τάσεων όπως αυτή προκύπτει από τις μεταβολές στους ρυθμούς σεισμικότητας. Για τα τρία πρώτα σετ δεδομένων τα οποία περιέχουν περισσότερους σεισμούς και καλύτερα προσδιορισμένα επίκεντρα γίνεται επιπλέον ανάλυση: Υπολογισμός των χωρικών μεταβολών του πεδίου των τάσεων και σύγκριση/ συσχέτιση με τα αντίστοιχα αποτελέσματα που προκύπτουν από την εφαρμογή του μοντέλου ελαστικής εξάρμωσης. Ιδιαίτερη έμφαση δόθηκε στην εκτίμηση των αποτελεσμάτων σε κοντινές και μακρινές αποστάσεις από τα επίκεντρα των ισχυρότερων σεισμών, ενώ έγινε αναγνώριση συστάδων σεισμικότητας και συσχέτιση τους με τις μεταβολές του πεδίου των τάσεων. Το κεφάλαιο κλείνει με συζήτηση

σχετικά με την προσέγγιση αντιστροφής, τις αβεβαιότητες και τα προβλήματα που συνοδεύουν τη μέθοδο, καθώς και τη συνολική εκτίμηση των αποτελεσμάτων.

Στο **τέταρτο κεφάλαιο** γίνεται οι σύνοψη των αποτελεσμάτων της διατριβής και αναφέρονται οι προοπτικές για μελλοντική έρευνα προκειμένου να βελτιωθεί η απόδοση της μεθοδολογίας.

Publications

Most of the results obtained in this thesis have been published in a series of conferences announcements and research papers in International Journals:

Peer Reviewed Papers in International Scientific Journals

1. **Leptokaropoulos, K. M.**, Papadimitriou, E. E., Orlecka-Sikora, B., Karakostas, V. G., Seismicity rate changes in association with time dependent stress transfer in the region of northern Aegean Sea, Greece, *Bull. Geol. Soc. Greece*, XLIII, 2093–2103, 12th International Congress, Patras, Greece, 2010.
2. **Leptokaropoulos, K. M.**, Papadimitriou, E. E., Orlecka-Sikora, B., Karakostas, V. G. (2012), Seismicity rate changes in association with the evolution of the stress field in northern Aegean Sea, Greece, *Geophys. J. Int.*, 188, 1322 – 1338.
3. **Leptokaropoulos K. M.**, Karakostas V. G., Papadimitriou E. E., Adamaki A. K., Tan O., and İnan S., (2013), A Homogeneous Earthquake Catalogue for Western Turkey and Magnitude of Completeness Determination, *Bull. Seismol. Soc. Am.*, 103, 5, 2739-2751.
4. **Leptokaropoulos, K. M.**, Papadimitriou E. E., Orlecka-Sikora, B. Karakostas V. G. and Vallianatos, F., Modeling Seismicity Rate Changes Along The Hellenic Subduction Zone (Greece), *Bull. Geol. Soc. Greece*, 13th congress of the Geological Society of Greece, 5-8 September 2013, Chania, Greece.
5. Tan, O., Papadimitriou, E., Pabuçcu, Z., Karakostas, V., Yoruk, A. and **Leptokaropoulos, K. M.**, A detailed analysis of microseismicity in Samos and Kusadasi (eastern Aegean) areas, *Acta Geophys.*, DOI: 10.2478/s11600-013-0194-1.

6. **Leptokaropoulos K. M.**, Papadimitriou E., Orlecka-Sikora B., Karakostas V., Forecasting seismicity rates in western Turkey as inferred from reference seismicity and stressing history, *Nat. Hazards*, 73, 1817-1842, DOI 10.1007/s11069-014-1181-9.
7. **Leptokaropoulos K. M.**, Papadimitriou E. E. Orlecka-Sikora B. Karakostas V. G. and Vallianatos F., Time dependent earthquake occurrence rates along the Hellenic Arc, (Scheduled to be published in *Bull. Seismol. Soc. Am.*, Vol. 104, 6, December, 2014, available on-line, doi:10.1785/0120130298).
8. **Leptokaropoulos K. M.**, Papadimitriou E., Orlecka-Sikora B., Karakostas V., Evaluation of Coulomb Stress Changes from Earthquake Productivity Variations in Western Corinth Gulf, Greece, (Submitted in *Pure Appl. Geophys., Special Issue* – under revision)

Oral Presentations in International Conferences

9. **Leptokaropoulos, K. M.**, Papadimitriou, E. E., Orlecka-Sikora, B., Karakostas, V. G., Seismicity rate changes in association with time dependent stress transfer in the region of northern Aegean Sea, Greece, *Bull. Geol. Soc. Greece*, XLIII, 2093–2103, 12th International Congress, Patras, Greece, 2010, (oral presentation).
10. **Leptokaropoulos, K. M.**, Papadimitriou, E. E., Orlecka-Sikora, B., Karakostas, V. G., Study of time dependent earthquake occurrence in Greece: Relationship between seismicity rate changes and stress transfer and implications for time dependent seismic hazard assessment, XIX Congress of the Carpathian-Balkan Geological Association, September 2010, Thessaloniki, Greece (oral presentation).
11. **Leptokaropoulos, K. M.**, Papadimitriou E. E., Orlecka-Sikora, B. Karakostas V. G. and Vallianatos, F., Expected seismicity rates in

association with stress field changes in southern Aegean, Greece, European Seismological Commission, ESC, 33rd General Assembly, 19 – 24 August 2012, Moscow, Russia, (oral presentation by E. E. Papadimitriou).

12. **Leptokaropoulos, K. M.**, Karakostas, V. G., Adamaki, A. K., Papadimitriou E. E., Tan, O. and Inan, S., Minimum Magnitude of Completeness in a revised Earthquake Catalog of western Turkey, International Earth Science Colloquium on the Aegean Region, IESCA, 1 – 5 October, 2012, Izmir, Turkey (oral presentation).
13. **Leptokaropoulos, K. M.**, Papadimitriou E. E., Orlecka-Sikora, B. Karakostas V. G., Evaluation of Coulomb Stress Changes from Earthquake Productivity Variations after the 2010 Earthquake Sequence in Corinth Gulf, Greece, IAHS IAPSO IASPEI Joint Assembly, Gothenburg, Sweden, 22-26 July 2013 (oral presentation by E. E. Papadimitriou).
14. **Leptokaropoulos, K. M.**, Papadimitriou E. E., Orlecka-Sikora, B. Karakostas V. G. and Vallianatos, F., Modeling Seismicity Rate Changes Along The Hellenic Subduction Zone (Greece), *Bull. Geol. Soc. Greece*, 13th congress of the Geological Society of Greece, 5-8 September 2013, in Chania, Greece (oral presentation).

Poster Presentations in International Conferences

15. **Leptokaropoulos, K. M.**, Papadimitriou, E. E., Orlecka-Sikora, B., Karakostas, V. G., Stress interactions among active fault zones of the Corinth Gulf and their impact on seismicity rate changes and time-dependent seismic hazard, 7th International Workshop on Statistical Seismology, May 2011, Thera (Santorini), Greece, (poster presentation).

16. **Leptokaropoulos, K. M.**, Papadimitriou, E. E., Orlecka-Sikora, B., Karakostas, V. G., Probabilistic seismic hazard assessment by detection of seismicity rate changes and their connection with the stress regime variation in Greece, ESF-LFUI Research Conference: Continuing Challenges In Earthquake Dynamics: New Methods for Observing and Modelling a Multi-Scale System, September 2011, Obergurgl, Austria, (poster presentation).
17. **Leptokaropoulos, K. M.**, Papadimitriou, E. E., Orlecka-Sikora, B., Karakostas, V. G., Stress Field Variation after the 2001 Skyros Earthquake, Greece, Derived from Seismicity Rate Changes, EGU General Assembly 2012, 22 – 27 April 2012, Vienna, Austria, (poster presentation).
18. **Leptokaropoulos, K. M.**, Karakostas, V. G., Papadimitriou E. E., Adamaki, A. K., Tan, O. and Pabuçcu Z., An Equivalent Moment Magnitude Earthquake Catalogue for Western Turkey and its Quantitative Properties, EGU General Assembly 2013, 7 - 12 April 2013 in Vienna, Austria (poster presentation).
19. **Leptokaropoulos K. M.**, Papadimitriou E., Orlecka–Sikora B, Karakostas V., Static Stress Changes Inverted from Microseismicity in Eastern Aegean Sea, EGU General Assembly 2014, 27 April – 2 May 2014, Vienna, Austria, (poster presentation).

Other publications

20. Tan O., Papadimitriou, E., Karakostas, V., Pabuçcu, Z., **Leptokaropoulos, K. M.**, Inan, S., Ergintav, S., Yoruk A., Acikgoz, C., Sevim, F. and Karaaslan, A., Seismicity and seismotectonic properties of the central east Aegean Sea & western Turkey: a complex deformation zone, International Earth Science Colloquium on the Aegean Region,

- IESCA, 1 – 5 October, 2012, Izmir, Turkey (oral presentation by E. E. Papadimitriou).
21. Tan O., Pabuçcu Z., Yörük A., Sevim F., Açıköz C., Ergintav S., **Leptokarpoulos K. M.**, Papadimitriou E., Karakostas V., 1 May 2012 Foça (İzmir Bay) earthquake and its aftershocks: Normal faulting in İzmir Bay, International Earth Science Colloquium on the Aegean Region, IESCA, 1 – 5 October, 2012, Izmir, Turkey (Poster presentation).
 22. Pabuçcu Z., Tan O., Yörük A., Papadimitriou E., Karakostas V., **Leptokarpoulos K. M.**, Ergintav S., İnan S., Karaaslan, A., Açıköz C., Sevim F., Analysis of the micro-earthquake activity at the Samos Island, Aegean Sea based on data from 2007 to 2012, EGU General Assembly 2013, 7 - 12 April 2013 in Vienna, Austria (abstract submitted).
 23. Orlecka-Sikora, B, Lasocki S., and **Leptokarpoulos K.**, IS-EPOS - a prototype of EPOS Thematic Core Service for seismic processes induced by human operations, EGU General Assembly 2014, 27 April – 02 May **2014**, Vienna, Austria, (poster presentation).

Chapter 1. Introduction

1.1 Seismicity Rate Changes – Aim of the Study

Although small earthquakes are not taken into consideration for seismic hazard assessment they play an important role in monitoring and understanding the physical processes that take place in earth's lithosphere. Since seismicity is directly associated with physical quantities and mechanical properties of the crust such as strain accumulation, stressing rate and frictional response of the rupture zones, earthquakes provide a major source of information that cannot be obtained by direct measurements. Spatial and temporal seismicity rate anomalies are usually reported as the most frequent intermediate-term precursory phenomenon. These changes can be observed for periods lasting for some days to few years prior to a strong earthquake and extend over areas larger than the rupture zone of the impending earthquake (Fedotov, 1965; Mogi, 1977, 1985). It is therefore commonly accepted that anomalies in the seismicity rate of the small magnitude events may be precursors of a potential strong earthquake in many cases, since they alter the stronger earthquake probabilities introducing time-dependency to seismic hazard assessment. Changes in seismicity patterns are consequently likely to be correlated with changes in stress, as evidenced by aftershock sequences, or by more subtle seismicity dynamics caused by the nucleation processes of large earthquakes (Marsan and Wyss, 2010). Other phenomena that may induce changes in earthquake production rates are post seismic deformation (afterslip), pore fluid diffusion, magma intrusion in volcanic areas, viscoelastic relaxation, aseismic slip (creeping), tidal triggering and anthropogenic activities. Quantitative measures of a change in seismicity rates are also required, especially when trying to detect specific patterns (e.g. relative quiescence) prior to large shocks, as an attempt to identify precursory

phenomena that could be used for earthquake prediction strategies (Marsan and Wyss, 2010).

The causative connection between the evolution of stress and seismicity rates was studied and quantified by Dieterich (1994) who proposed a formulation that associated shear stress changes with seismicity rate variation following the Rate/State dependent friction concept. Later this perspective was modified by introducing the more complex static Coulomb failure stress concept (ΔCFF or ΔCFS), incorporated into the Rate/State model (Reasenberg and Simpson, 1992; Scholz, 2002). Following this concept, the evolution of seismicity depends on the initial, unperturbed seismicity rate (named as reference rate), stress changes, friction coefficient, secular tectonic stressing rate and constitutive properties of the rocks in the fault zones. Positive Coulomb stress changes amplify the reference seismicity, and therefore small stress changes are capable to produce large changes in seismicity rate in areas of high reference seismicity (Toda et al., 2005). Similarly, seismicity rate depressions in the stress shadows are evident only in areas with high recorded seismicity rates immediately beforehand.

The first goal of the present study is to investigate how the stress changes caused by successive strong main shocks perturb the seismicity rates through a Rate/State dependent friction model. The approach applied incorporates the physical properties of the fault zones (characteristic relaxation time, fault constitutive parameters, effective friction coefficient) with a probabilistic estimation of the spatial distribution of smoothed seismicity rates, derived from the application of a Probability Density Function (PDF). In doing so, the expected rates were calculated and compared with the observed ones after each main shock and before the following one. The qualitative and quantitative correlations were also investigated between the observed seismicity rates at the inter-seismic

periods and the expected ones, as they were predicted by the Rate/State model. The calculations aim to identify areas of increased expected seismicity rates as candidates to accommodate a major earthquake in the future (Toda and Stein, 2003). Results strongly depend on the model parameters and their influence in the model performance was tested by the evaluation of a parametric (Pearson) correlation coefficient and its confidence intervals, resulting from different input parameter values applying into the testing regions and periods. Seismicity rate results were filtered by certain criteria and constraints in an attempt to overcome model uncertainties and to provide more reliable results for specific areas of major interest, i.e. in areas with increased ΔCFF values. By this procedure the model sensitivity was tested, and parameter values that appear to simulate more realistically the tectonic procedures taking place in the crust were evaluated. Thus, despite the ambiguities and the difficulties involved in the experimental parameter value determination, the simulated results will provide evidence for their potential fluctuation through a detailed data analysis. This time-dependent approach is expected to contribute to the evaluation of the future seismic activity and the seismic hazard assessment. As an implication of time-dependent seismic hazard, exceedance probabilities of earthquakes with $M \geq 6.0$ or $M \geq 6.5$ are provided for the next decade and the spatial distribution of the expected rates is illustrated as well.

The second goal of the study is to investigate seismicity rate changes in both space and time domain and to utilize these changes in order to obtain information concerning the stress field variations. Up to the present only a few studies that calculate stress changes from earthquake occurrence rates obtained from catalogs have been accomplished. Few studies have achieved successful results because of the nonlinearity of earthquake rate changes with respect to both stress changes and time (Dieterich et al, 2000). The analysis is

carried out by considering the changes of earthquake production rates. The selected data correspond to certain areas and come from recent catalogues with adequate level of completeness before and after a main shock occurrence. After explicitly determining the physical quantities incorporating in the modeling stress changes were sought for both space and time along with their possible connection with spatio-temporal earthquake clustering and fault interactions. The spatial distribution of aftershock productivity rates is compared with the static stress changes due to the coseismic slip at different depths inside the seismogenic layer, defined from the vertical distribution of the aftershocks. Seismicity rates of the smaller magnitude events with $M \geq M_c$ for different time increments before and after the main shock are then derived from the application of a Probability Density Function (PDF). The differences between the earthquake occurrence rates before and after the main shock are compared and used as input data in a stress inversion algorithm based upon the Rate/State dependent friction concept in order to provide an independent estimation of stress changes (previously calculated by elastic dislocation model). The stress patterns derived from these two (forward and inverse) approaches are compared with each other and their correlation is quantified along with its confidence intervals. Different assumptions and combinations of physical and statistical parameters are tested for the model performance and robustness to be evaluated. Simulations provide a measure of how accurate and practical is the use of seismicity rate changes as a stress meter for both positive and negative stress steps.

1.2 Seismotectonic Features of the Broader Aegean Region

The Aegean region and the surrounding areas are considered as one of the most active tectonic regions of the Alpine - Himalayan belt, containing active volcanoes, exhibiting the highest deformation and seismicity rates in

the Mediterranean domain and consisting of several major rupture zones with diverse seismotectonic properties (Fig. 1.1). The most prominent tectonic feature of the broader Aegean area is the subduction of the eastern Mediterranean lithosphere under the Aegean microplate along the Hellenic Arc (Papazachos and Comninakis, 1969), which has been recognized as a subduction zone with a Wadati – Benioff seismic plane. This zone is gently dipping at an angle of 30° at its shallow part until 100km depth and then is descending with a steeper angle of 45° (Papazachos and Comninakis, 1971; Papazachos et al., 2000). Seismic tomography studies also illustrated the deeper branches of the subducted lithosphere up to a depth of 600 km (Spakman et al., 1988, Papazachos and Nolet, 1997). As a consequence of this subduction, an extended zone of reverse faulting is evident along the Hellenic arc. Papadimitriou and Karakostas, (2008) described that the Hellenic Arc is laterally bounded by Subduction - Transform Edge Propagators (STEPs) in the plate boundaries that are ongoing tearing of oceanic lithosphere near the horizontal terminations of subduction trenches (Govers and Wortel, 2005), the dextral Cephalonia Transform Fault (CTF) in the west (Scordilis et al., 1985) and the sinistral Rhodos Transform Fault (RTF) in the east (Papazachos and Papazachou, 2003). The subduction of the African plate's northern oceanic edge along the Hellenic Arc is occurring at a faster rate than the northward motion of this plate (Bellier et. al, 1997) and because of this, the Hellenic Arc is moving in southward direction relative to Eurasia (McKenzie, 1970; McClusky et. al, 2000) resulting to an extensional regime within the Aegean and western Turkey.

The North Anatolia Fault (NAF) is one of the longest active right lateral fault systems, which extends for approximately 1,500 km, from eastern Turkey through the Marmara Sea where it bifurcates into at least two sub-parallel branches. The westward propagation of the NAF is the second dominant effect in the region which sustains the existence of strike slip faults,

most of them dextral, along the North Aegean Trough (NAT) and the surrounding area. McKenzie (1978) showed that the northward motion of the Arabian platform pushes the smaller Anatolian plate westwards along the NAF, continuing along the NAT which is the boundary between the Eurasian and Aegean plates. A wide extensional regime governs the Aegean Sea due to the combined effect of Anatolia westward motion and subduction rollback, leaving almost no significant contraction and reverse faulting in the aforementioned regions. These rapidly extending areas, with a N-S rate of extension of around 40-60mm/yr, across the whole province, lie between Crete and Bulgaria, including the Greek mainland and western Turkey, as well as the southern Bulgaria, the former Yugoslavian republics and Albania (McKenzie, 1978; Le Pichon and Angelier, 1979; Jackson and McKenzie, 1988, Ambrasseys and Jackson, 1990).

The third major tectonic effect is due to the convergence between Apulian plate and the Hellenides, Albanides and Dinarides (McKenzie, 1972; Ritsema, 1974). This convergence is a continental-type collision on an orogen that is characterized by significant neotectonic activity (Cloetingh et al., 2007). During the Tertiary, the Apulian continental margin was affected by compressional tectonics due to the continuing collision. Subduction of Apulia beneath the Hellenic margin of the upper European Plate took place in the Miocene (Le Pichon and Angelier, 1979). A belt of thrust faulting runs along the southwestern coasts of Croatia and Montenegro and continues south along the coastal regions of Albania and northwestern Greece, resulted from continental collision between Outer Hellenides and the Adriatic microplate (Papadimitriou et al., 2005). The direction of the maximum compression axis is almost normal to the direction of the Adriatico - Ionian geological zone.



Fig. 1.1. The study area with its main seismotectonic properties. CTF, Cephalonia Transform Fault; NAT, North Aegean Trough; NAF, North Anatolian Fault; RTF, Rhodes Transform Fault. The dark arrows indicate the orientation of the back arc extension.

All of these complex, dynamic plate interactions induce a large scale crustal deformation causing very intense seismic activity in the entire site. Because of the large expanse and the strong seismotectonic heterogeneity of the study area, it is necessary to divide it into smaller ones characterized by common seismotectonic properties and accommodating data of similar quality and density. Since many devastating earthquakes have been repeatedly reported during historical times and recorded during the instrumental era, causing extensive damage and loss of lives, the seismic hazard assessment is of primary importance priority for the broader Aegean region.

1.3 State of the Art

1.3.1 Review studies

Many recent studies have been carried out providing information on the importance of seismicity rate changes and their association with the seismotectonic processes, describing specific mathematical tools for evaluation procedures and statistical analyses. Marsan and Wyss (2010) review and describe the existing methods developed for measuring seismicity rate changes and for testing the significance of these changes (Habermann, 1981, 1983; Mathews and Reasenber, 1988; Marsan, 2003; Marsan and Nalbant, 2005). They also illustrate these methods with several examples (see references therein). Statistical and mathematical approaches of theory and data analysis concerning the power law distribution of earthquake rate changes have also been carried out (Correig et al., 1997; Parsons, 2002; Coral, 2003; Console et al., 2003, 2006a; Molchan and Kronrod, 2005; Saichev and Sornette, 2006; Marsan and Langline, 2008; Adamaki et al., 2011). Harris (2000), Steacy et al. (2005) and Hainzl et al. (2010) summarize the previous studies and methods regarding stress transfer, earthquake triggering and time-dependent seismic hazard. They review all the methods that incorporate seismicity rate changes with static and dynamic stress changes, Rate/State friction, fluid flow, viscoelastic phenomena and volcanism. They conclude that although such approaches have often proved useful and successful, we still need to improve our knowledge about the physics underlying these complex natural processes. Felzer (2008) described in detail a procedure to calculate the average seismicity rate from an earthquake catalog. Her analysis implied correction in magnitudes for rounding and magnitude errors, b-values determination along with their standard error, completeness thresholds estimations for selected periods and calculation of seismicity rates via different methods. Moreover, the author estimated the potential bias and

error produced by earthquake clustering and finally she applied her method to the California earthquake catalog from 1850-2006. Discussion regarding the spatial seismicity rates and maximum credible magnitudes for background earthquakes is given by [Petersen et al. \(2008\)](#) as well.

1.3.2 Seismicity Rate changes during the earthquake cycle: The early studies

The occurrence rate of small magnitude events is often extrapolated to estimate the earthquakes rate of larger size shocks, or to calculate the probability of a strong event occurrence. In doing so, the use of G-R law has been routinely incorporated into many regional seismic hazard assessment studies ([Cornell, 1968](#); [Frankel et al., 1996](#)). Seismicity rate of smaller magnitude events is proportional to the rate of the regional stress increase (tuning parameter) and this is in turn proportional to the rate of occurrence of the larger earthquakes. Observations favor the hypothesis that seismicity rate of smaller earthquakes in a region is only weakly dependent on time if the area is sufficiently large. If the smaller earthquakes were correlated with the earthquake cycle, then they could be used for the temporal prediction of earthquakes ([Kossobokov et al., 2000](#)). This technique is though questionable: the same authors still notice that the large “characteristic” earthquakes do not fall on an extrapolated Gutenberg–Richter curve. Moreover it is often observed that the frequency magnitude distribution demonstrates different slope for stronger events than for the smaller ones. In the Aegean region the change of the slope takes place around $M \sim 7$ which is attributed to the maximum magnitude saturation for individual seismic sources ([Papazachos et al., 1999](#)). Extreme events exceeding the extrapolation have been characterized as "Dragon Kings", a phenomenon also observed in many dynamic systems exhibiting power law distributions ([Sornette, 2009](#); [Sachs et al., 2012](#))

Wyss and Habermann (1979) performed a systematic search for seismicity rate changes in the fault segment of the Kurile island arc. They defined seismic clusters, background seismicity rates and seismic quiescence. They found that in most of the segments and for most of the time the seismicity rates were fairly constant except for one seismic enhancement and a seismic quiescence period within two sections of the arc. They also quantified these anomalies, calculated the statistical significance and combined their duration with the main shock dimensions. Habermann and Wyss (1984) attempted to discrete the background seismicity rates from anomalies in seismic activity by studying earthquake production rate changes as potential precursors in the Imperial Valley, California. They mostly focused their work on the determination and identification of background seismicity but also on the detection of its changes with respect to the magnitude.

Jones and Hauksson (1997) examined seismicity rates for events of $M \geq 3.0$ in southern California from 1945 to 1996 in terms of the seismic cycle concept (Imamura, 1937; Fedotov, 1965; Mogi 1969, 1981; Shimazaki, 1978; Reasenberg and Simpson, 1992; Sykes, 1996). They found that high seismicity level preceded both the 1952 Kern County ($M=7.5$) and 1992 Landers ($M=7.3$) earthquakes, and low activity occurred right after them. They also noted that the seismicity rate ($M \geq 3.0$) was almost constant from 1969 to 1992. As they pointed out, neither the Kern County nor the Landers shock could be considered as a plate boundary events. Ellsworth et al. (1981) found that the only statistically significant variation in the seismic cycle around the 1906 earthquake was the rate decrease that was observed right after that earthquake. Maeda and Wiemer (1999) investigated the precursory seismic quiescence of about 1.5 year prior to the 1987 $M=6.7$ Chiba-Toho-Oki earthquake, in central Japan. Significance tests for seismicity rate changes

were also performed. They used data from two independent catalogs and the quantitative analysis they carried out showed that the precursory quiescence and rate increase is not unique, since changes in occurrence rates of this duration and significance often occur in both datasets. Such variations in rates of earthquake production could probably not be detected in a real time forecast. They concluded that quiescence is present but it is very difficult to be distinguished from background seismicity fluctuations at a considerably high confidence level.

1.3.3 Seismicity rate changes and static Coulomb stress changes

The most popular strategy followed in seismicity rate studies is their connection with the Coulomb stress changes, commonly based upon [Dieterich \(1994\)](#) Rate/State formulation. [Toda et al. \(1998\)](#) investigated how the 1995 Kobe earthquake transferred stress to nearby faults, altering their proximity to failure and consequently changing earthquake probabilities. They quantified the spatial correlation between the seismicity rate change and Coulomb stress variation. The correlation was found to be significant for stress changes greater than 0.2-1.0 bars and the non-linear dependence of seismicity rate changes on stress variations was compatible with a Rate/State dependent formulation of earthquake occurrence. They used their analysis in order to derive probabilities of strong earthquake occurrence as an implication for time dependent seismic hazard.

[Stein \(1999\)](#) associated the static Coulomb stress changes with seismicity rate changes in the broader region of California and translated the results into earthquake probabilities in order to assess time dependent seismic hazard. Interpretation of data analysis results showed that the variance of the stress field after a strong earthquake can influence not only the evolution of seismic activity but also the time to failure for an impending earthquake. The study showed that in the case of the 1994, Northridge

earthquake, 65% of the observed seismicity rate changes were correlated with the calculated Coulomb stress changes. There was also discussion on earthquake triggering caused by dynamic (Belardinelli et al., 1999; Kilb et al., 1998) and tidal (Vidale et al., 1998a, 1998b; Lockner and Beeler, 1999) stress changes.

Wyss and Wiemer (2000) investigated the interaction between the Landers earthquake and the two largest earthquakes followed (Big Bear and Hector Mine), as well as the sustained fluctuations of seismicity rates in neighboring areas of southern California. They found out that decreases in earthquake production rates were not noticed as clearly as the increases but the pattern of both increases and decreases approximately matches the one predicted by the Coulomb stress changes. They interpreted the observed changes in earthquake occurrence rates by proposing a qualitative model of the crust. Seismicity rates changes and stress transfer before the occurrence of large earthquakes was the subject of discussion of Bowman and King (2001). They described a simple physical based model connecting static stress changes with the accelerated moment release prior to a large main shock (also see Mignan et al., 2006). They applied their model in California for all the earthquakes with $M \geq 6.5$ that took place since 1950 and assumed that this model can be applied without significant modification in any active tectonic region. Nevertheless, they pointed out that it is not easy to perform such analysis in an earthquake-predictive sense, since the properties of the fault segments to be ruptured are not well constrained before the main shock occurrence.

Wang and Chen (2001), applied a 3 dimension model to investigate stress transfer caused by the $M=7.3$ Chi-Chi earthquake in 1999. A wide range of effective friction coefficient was applied in their approach. They also carried out statistical tests to find out if the stress distribution of the pre-

shock sequence significantly differed from that of the post-shock sequence and showed that the distributions of ΔCFF before and after the main shock varied significantly. In general, enhancement of seismic activity was observed in regions which experience positive ΔCFF but in some stress shadows the observed rates were not as low as predicted for depths shallower than 10km. This was attributed in different processes such as dynamic stress triggering or cumulative influence of static stress changes caused by the smaller magnitude aftershocks. The same earthquake sequence was the subject of [Wang et al. \(2003\)](#) study. The authors searched for seismicity rate changes in connection with both static and dynamic stress variation due of the main shock. Static stress changes were found to influence significantly (but not purely) seismicity rate changes and therefore they sustained the primary triggering mechanism. Although these changes were small, their influence was significant especially for depths between 0km and 10km and for a period up to 2 weeks after the main shock. The authors believe that they did not obtain sufficient information to draw conclusions about the role of dynamic stress changes as an important physical triggering factor.

The changes of moderate-size earthquake production rates before and after the 1992 Landers earthquake were investigated by [Du and Sykes \(2001\)](#). Their analysis regarded the Coulomb failure stress evolution since 1812 in Southern California, by considering circular regions and equal-area annuli centered on the epicenter of the Landers main shock. The changes in the frequency of moderate-size events were most prominent within a circular region with a radius of about 160km from the Landers epicenter. The most pronounced changes before 1992 do not indicate a relation to stress buildup to the Landers sequence itself. Finally it was not clear which ones of these fluctuations in seismicity rates may be precursory to large events, and which ones sustained random variations or were related to other physical processes.

Using the accumulative stress changes in California, **Toda and Stein (2002)** calculated the probability of an impending earthquake in Parkfield. Their analysis included spatial and temporal investigation of seismicity rate changes after strong earthquake occurrence in the region. Strong correlation was found between the variation of the stress field and seismicity rate changes and the estimated probability of a Parkfield earthquake was reduced by 22% according to the given stress history. The obtained results can explain why this earthquake did not occur during the 1980' but fail to explain its absence in the next decade. Finally a high probability for an $M \geq 6.0$ in Parkfield until 2011 was derived. **Marzocchi et al. (2003)** simulated the long term interaction among remote earthquakes. After the generation of synthetic catalogues and the calculation of the stressing rate variation induced by remote earthquakes, they estimated the changes in seismicity rates on simple seismogenic fault model. They found that the post-seismic stress changes induced by remote earthquakes were not negligible compared to the tectonic loading rates. Studying southern California seismicity it resulted that the rate of seismicity experienced a major change at about the time of occurrence of the remote Chile (1960) and Alaska (1964) earthquakes. A significant change in stressing rate was also produced due to these two events.

Toda and Stein (2003), used a large data sample of small events following the 1997 Kagoshima doublet, Japan in order to test the spatio-temporal distribution of seismicity as it is predicted by a Rate/State dependent friction model. They focused their analysis on off-fault regions as the sample in these areas is considered to be more sufficient and reliable and pointed out the weaknesses and uncertainties regarding the model performance and the parameter value determination. According to their results dynamic stress changes play secondary role in seismic activity variation and seismicity rate enhancement in positive ΔCFF areas is more

profound than seismicity rate decreases in stress shadows. Finally they calculated earthquake probabilities for $M \geq 5.0$ and $M \geq 6.0$ in positive ΔCFF regions for a 10 year horizon.

Helmstetter and Sornette (2003b) used the southern California seismicity and assumed that any earthquake may trigger other earthquakes and that foreshocks, main shocks and aftershocks are physically indistinguishable. An interesting result they obtained was that the precursory modification of seismic activity before a main shock is independent of its magnitude and therefore large earthquakes are not more predictable than the smaller ones. They also demonstrated that the rate of foreshocks before large events is increased at large distances and up to decades before the main shock. **Woessner et al., 2004** applied an objective spatio-temporal mapping approach and formulated a measure of the statistical significance of rate changes within the decaying aftershock sequence of Kagoshima, Japan, 1997. They compare their method with the ones of **Toda and Stein (2003)** and **Stein (2003)**. In particular, their mapping showed that a statistically significant rate decrease followed the Kagoshima main shock in different areas from those **Toda and Stein (2003)** estimated. Their quantitative analysis showed that both off-fault and onto-fault aftershock activity was increased but also decreased locally by the nearby second mainshock. The coseismic rate changes for off-fault aftershocks could be adequately explained by static stress changes.

Toda et al. (2005) attempted to forecast the evolution of seismic activity in southern California by the application of a Rate/State model. The evolution of seismicity was found to be strongly depended on the background seismicity rates. Even small changes in static stress yielded significant seismicity rate increase in regions with high reference seismicity rates. Similarly, seismicity rate depression in stress shadows was only obvious in areas exhibiting intense background activity. For this reason background

seismicity rate has to be determined as accurately as possible. In some cases enhancement in the rates of earthquake occurrence could not be explained by the static stress changes. In these cases other physical processes such as dynamic stress changes and pore fluid effects had to be taken into account. Finally the authors presented the probabilities that an earthquake with $M \geq 5.0$ will occur in the study area between 2005 and 2011.

The relation between aftershock rates following the Chi-Chi earthquake in Taiwan (1999) and coseismic ΔCFF was the subject of [Ma et al. \(2005\)](#) study. Once more, seismicity rate increases in areas which experience positive Coulomb stress changes was confirmed. The spatial distribution of seismicity prior and following the main shock appears to be identical but the number of shocks differs significantly. Contrarily to [Felzer and Brodsky \(2005\)](#), they found 4 zones with negative ΔCFF where seismicity was also depressed, supporting the presence of stress shadows. These results were derived due to the rich data (low M_c) available for a long period before the main shock. [Felzer and Brodsky \(2005\)](#) studied the rates of aftershock decrease after strong earthquakes in California in order to test the stress shadow hypothesis. For this purpose they applied a time ratio metric i.e. they calculated the ratio of the time between the main shock and the first event to follow it and the time between the last earthquake to precede the main shock and the first event to following. Large values of this ratio indicate a long wait for the first earthquake to follow the main shock and thus a potential stress shadow. On the other hand small values of the time ratio indicate the presence of aftershocks. They found that stress shadows were absent after the occurrence of the 4 main shocks they considered. Moreover, they noticed significant seismicity rate decreases in large areas and periods when no stress shadow was predicted. According to their suggestion the aftershocks were either triggered by a mix of dynamic and static stress changes or they were

entirely triggered by dynamic stress changes. Relatively to this issue, the Coulomb failure stress concept argues that seismicity rate decrease is observed in faults with specific focal mechanism and not to the whole seismicity. Therefore a stress shadow should be followed by a variation of the average focal mechanism in a specific area. **Mallman and Parsons (2008)**, studied 119 earthquakes with $M_s \geq 7.0$ worldwide and found that significant variations of the average focal mechanism was observed in only two cases. After performing statistical analysis they found out that there was indeed a decrease of the population of certain types of focal mechanisms after a main shock. Concluding, they noted that stress shadows presence is quite rare and difficult to detect, but their existence is confirmed.

Parsons (2005c) investigated if a sudden stress perturbation is able to revise earthquake probability as well as the earthquake occurrence rates. He also attempted to calculate the stress change threshold for this probability to become significant. Parsons applied different models and performed tests for many values of parameters such as the dip and the rake of the fault and the coefficient of friction. Disparity resulting from interaction probability methodology was also examined. For a fault with a well-understood earthquake history, a minimum stress change to stressing rate ratio of 10:1 to 20:1 is required to significantly skew probabilities with greater than 80–85% confidence level. That ratio must be closer to 50:1 to exceed 90–95% confidence levels. In practical terms, this would be a large earthquake or other stress perturbation happening closer than a few tens of kilometers from a fault zone of well-documented earthquake history that is loaded at a moderate rate.

Seismicity rate study in order to investigate the Parkfield-Coalinga interaction over the years preceding the 1983 Coalinga earthquake was carried out by **Tiampo et al. (2006)**. To achieve this goal they applied the

Pattern Informatics (P.I.) method. P.I. index quantifies changes in the number of small events in local regions in relation to the seismicity rate over the entire region, or, in other words, as it relates to larger spatial scales. They found that significant anomalous seismicity changes occurred during the mid-1970s in this region prior to the Coalinga earthquake that illustrate a reduction in the probability of an event at Parkfield, while the probability of an event at Coalinga is seen to increase. This suggests that the one event did not trigger or hinder the other, rather that the dynamics of the earthquake system are a function of stress field changes on a larger spatial and temporal scale. Strong evidence was also provided that a temporal change in the regional stress field can be detected by using algorithms that quantify the anomalous activity in seismicity in terms of seismic moment release and stress rate.

Peng et al., (2007) analyzed and compared seismicity rates immediately before and after 82 main shocks in Japan with magnitudes between 3 and 5, by using waveform recorded by a borehole array. The method they carried out allowed them to obtain almost 5 times as many aftershocks in the first 200 sec as listed in the JMA catalogue. They discovered that the early aftershocks decay on lower rates in comparison with the later ones. The seismicity rate in the last 200 sec prior to the main shock appeared steady instead of increasing with time. They noted that this behavior was compatible with the ETAS and the Rate/State models if heterogeneous stress change along the fault was assumed.

Catalli et al. (2008), developed a Rate/State model to simulate the seismicity rate changes during the 1997 Umbria- Marche earthquake sequence in Italy. They considered ΔCFF caused by the coseismic slip of 6 earthquakes with $(5.0 \leq M \leq 6.0)$ and 39 smaller ones. Their main goal was to study the sensitivity of simulated results in the selection of model parameters, especially $A\sigma$, the values of which cannot be measured in the

earth's crust. They applied a likelihood-based method in order to find out the best fit of $A\sigma$ and the results they obtained showed that the main features of the temporal evolution of seismicity were in good agreement with the real data, although the observed temporal fluctuations displayed a more complex pattern. Before them, [Nostro et al. \(2005\)](#) studied the stress interactions during the sequence and found that 7 out of the 8 larger events took place in areas where static stress changes were positive. Moreover 82% of the epicenters of all shocks were found to be in the aforementioned locations (considering resolution of stress field in optimal oriented planes – OOPs). Nevertheless less than half of the available focal mechanisms were in agreement with these OOPs. They therefore inferred that stress transfer itself is not capable to illustrate the spatial distribution of seismicity rate changes and the focal mechanisms of the aftershocks.

The $M=7.9$, Wenchuan earthquake that occurred in China in 2008, was studied by [Toda et al. \(2008\)](#). The results of their analysis indicated seismicity rate increases as well as increases in ΔCFF in a wide area. They showed that 3 of the major neighboring fault segments were about 0.2-0.5 bars closer to failure after the main shock. Nearby areas were found to be in high seismic risk region, since many of these segments haven't ruptured for a long period and therefore an impending earthquake is expected to be devastating. The expected seismicity rate of smaller events was estimated along with the probabilities of occurrence of an $M \geq 6.0$ and $M \geq 7.0$ in the regional fault systems for a ten years horizon. These probabilities were found to be much higher in comparison with previous estimates, a fact that indicates the importance of time-dependency in seismic hazard assessment.

[Aron and Hardebeck \(2009\)](#) studied the relationship between seismicity rate changes and modeled ΔCFF from the 2003 $M=6.5$ San Simeon and the 2004 $M=6.0$ Parkfield earthquakes in Central California. They found

that both static and dynamic stress changes can adequately explain the observed aftershock deficiency, but a short burst of seismicity at specific areas where the modeled ΔCFF were negative can only be due to dynamic triggering. [Chan et al. \(2010\)](#) attempted to forecast the Italian seismicity through a spatio-temporal physical model. They considered the Rate/State stress transfer imparted by all of the $M \geq 4.0$ earthquakes that occurred during 2007-2008. Their approach consisted of two parts. The evaluation of the reference seismicity rate through a time independent forecast and a Rate/State model application to evaluate the seismicity rate changes. The combination of the results of these two steps provided a time-dependent seismicity rate estimation. They concluded that the time dependent part of the model showed only marginal improvement to the forecasting accuracy in comparison with the time-independent one. The forecasting performance was also better when a non-declustered catalog was used.

[Cocco et al. \(2010\)](#) focused in the impact of physical model parameters imparted in the Rate/State model and the correlations between them. They studied the spatio-temporal evolution of seismicity for the 1992 Landers earthquake sequence and they proposed an optimal strategy to constrain model parameters for near-real-time forecasts. This required a robust validation through retrospective modeling and statistical tests. They demonstrated that different sets of model parameters could yield the same rates of aftershock decay. They also defined and applied 'background' and 'reference' seismicity rates and resolved stress changes by two alternative strategies (OOP's and prescribed receiver faults).

After applying 5 different source models to calculate ΔCFF , [Xie et al. \(2010\)](#) focused on seismicity rate changes as a function of time on every fault under the influence of ΔCFF . They used as case study the $M=7.9$ Wenchuan, China earthquake in 2008. Their results indicated that the spatial distributions

of aftershocks correlated well with the regions where stress was calculated to increase using the related models. The spatial distributions of stress changes were correlated well with the spatial patterns of the aftershocks. They finally compared their results with other studies (i.e. [Toda et al., 2008](#); [Shan et al., 2009](#)).

Console and his colleagues published during the last decade a series of studies for investigating seismicity rate changes by pure stochastic, or combined stochastic-physical based models ([Console et al., 2003](#); [2006a](#); [2006b](#); [2007](#); [2010a](#); [2010b](#); [2010c](#); [Murru et al., 2009](#)). After implementing these approaches for earthquake clustering, stress transfer and forecasting in different areas (Greece, Italy, New Zealand) they finally proposed 3 grid-based models which they submitted to the CSEP ETH Testing Center ([Falcone et al., 2010](#)): The first model for short-term forecasts is a purely stochastic epidemic type earthquake sequence (ETAS) model. The second short-term model is an epidemic rate-state (ERS) forecast based on a model that is physically constrained by the application to the earthquake clustering of the Dieterich Rate/State constitutive law. The third forecast is based on a long-term stress transfer (LTST) model that considers the perturbations of earthquake probability for interacting faults by static Coulomb stress changes. While the first two models only use the information contained in a seismic catalog (time, latitude, longitude, depth, magnitude), the LTST model also uses geological and geodetic information. Since then these models are being tested for their efficiency.

1.3.4 Seismicity rate changes and dynamic triggering

Seismicity rate changes have also been studied in terms of fault mechanics and dynamic triggering ([Kilb et al., 2000](#); [Voisin et al., 2000](#); [Gomberg, 2001](#); [Poliakov et al., 2002](#); [Kilb et al., 2002](#); [Gomberg et al., 2003](#); [Perfettini et al., 2003b](#)). [Parsons et al. \(1999\)](#) introduced a three dimensional

inventory of the southern San Francisco Bay area faults and used it to calculate stress applied by the 1989 M=7.1 Loma Prieta earthquake. They also compared seismicity rates preceding and following the 1989 earthquake in respect to the focal mechanism and the type of slip in each fault segment. **Gomberg et al. (2000)** examined theoretically the predictions of the timing of earthquake failure by introducing formulas for seismicity rate changes caused by stress perturbations based upon the Rate/State friction concept and the Coulomb failure stress. They found that clock advances predicted by Rate/State models asymptotically become equivalent to Coulomb predictions under a variety of conditions. They showed that the faults which demonstrate increased aftershock rates are those that are on the brink of failure at the time of the main shock.

Felzer et al. (2002) investigated the potential triggering of 1999 Hector Mine earthquake in California from the aftershocks following the 1992 Landers earthquake and not the main shock itself. Based upon the assumption that each aftershock can trigger aftershocks with the same rate as the previous ones, they showed that most of the aftershocks following an M>7.0 main shock are a result of secondary triggering. They also provide statistical evidence to support the hypothesis that the magnitude of any single aftershock is statistically independent on the magnitude of the main shock.

By using the Epidemic Type of Aftershock Sequence (ETAS) model, **Helmstetter and Sornette (2003a)**, showed that the proportion of aftershocks that are directly triggered is equal to the proportion of the events that are indirectly triggered by the main shock. The importance of those indirectly triggered aftershocks casts therefore doubts on the relevance of prediction of aftershock rates based upon the Coulomb stress changes due to the main shock only. **Helmstetter and Sornette (2003c)** also applied the ETAS model in

a predictive way, in order to forecast the future rates of triggered seismicity decay. The importance of small earthquakes for stress transfer and earthquake triggering was also studied by Helmstetter et al. (2006). Felzer and Brodsky (2006) investigated the decay of aftershock linear density with distance and under some assumptions they concluded that the probability of aftershock triggering is directly proportional to the amplitude of seismic waves. On the contrary Richard-Dinger et al. (2010) criticized their work suggesting that dynamic triggering does occur but the aftershock decrease with distance does not provide evidence of such triggering.

Ziv (2003) and Ziv and Rubin (2003) studied triggering processes and aftershock sequences in quasi-static fault models, governed by Rate/State depended friction. They showed that the increase of seismicity rates far from the rupture zone is a consequence of multiple stress transfer and that very distant aftershocks are not directly triggered by the main shock. Instead they are secondary aftershocks induced by the main shock aftershocks (Felzer et al., 2002). They also explained why in some cases at the early stages of an aftershock sequence the simulated seismicity rates exceeded the predicted rate and in the later stages simulated seismicity rates fall below the predicted rate.

Hardebeck (2004) introduced a general method for translating stress changes into earthquake probability changes which can potentially be used with any fault model. For this purpose she applied two physical based models in the case study of 1992 Landers earthquake sequence where the data is reliable, to minimize the uncertainties. Tests for whether the computed earthquake probability changes following a stress change is significant with respect to the uncertainties were also carried out. Nevertheless she concluded that the results were significant for time intervals of about half to ten years after the main shock, period relatively short in

comparison with the mean recurrence time and therefore it can be applied only for low slip-rate faults.

Gomberg et al. (2005a, 2005b), studied models of seismicity rate changes caused by the application of static stress perturbation to a population of faults and compared the results with those derived from Dieterich (1994) model. The model they applied is related with the ones proposed by Stein et al. (1997) and Hardebeck (2004). They suggested that the probability of failure for a specified fault segment depends on the stress variations but also on the maturity of the fault, i.e. how close to their failure times they are. A probabilistic approach of this problem is much more convenient than a deterministic one and the changes in earthquake production rates strongly depend on the state of the faults and the constitutive laws that describe their behavior.

Pollitz and Johnston (2006) investigated the influence of static and dynamic stress changes on the aftershock rates. For this purpose they compared the rates of aftershock productivity after strong earthquakes with those after aseismic and impulsive events. They found that in the first case the rates were significantly higher and persisted for weeks after the main shock. This suggests that at least in the near field, dynamic stress changes associated with the passage of seismic waves is the dominant cause of aftershocks which can lead to immediate or delayed triggering.

Using two different fault models, Kaneko and Lapusta (2008) simulated several plausible scenarios of spontaneous earthquake nucleation. They investigated their response to static shear stress steps and inferred the corresponding aftershock rates. They found that nucleation processes at weaker patches are characterized by aftershock rates similar to spring-slider models although there are notable deviations. On the other hand the nucleation processes at rheological transitions and the corresponding

aftershock rates are significantly different. A two-node stochastic model for aftershocks was established by [Bebbington \(2008\)](#) and was applied in order to estimate the parameter values of the Rate/State dependent friction model of [Dieterich \(1979\)](#). The author estimated parameter $A\sigma$ and the stressing rate from three earthquake sequences in Japan, assuming different aftershock volumes, magnitude cutoff and time windows. The comparison of the values he obtained with the ones published by other authors were found to be in good agreement.

1.3.5 Other phenomena associated with seismicity rate changes

Seismicity rate changes caused by transient aseismic processes such as fluid flow and fault creep and magma intrusion were studied by [LLENOS et al. \(2009\)](#). For this purpose they tried to combine the two most common approaches for seismicity rate studies, the ETAS model ([Ogata, 1988](#)) and the frictional Rate/State model ([Dieterich, 1994](#)). They identified the parameters that relate to one another in the two models and examine their dependence on stressing rate. Stressing rate transients were found to increase the background seismicity rates without affecting aftershock productivity. Fluid diffusion and its relation with earthquake triggering were also discussed by [Hainzl and Ogata \(2005\)](#) and [Hainzl and Kraft \(2006\)](#).

[Helmstetter and Shaw \(2009\)](#) used the [Dieterich \(1994\)](#) formulation in order to model seismicity rate triggered by after-slip. They derived relationships and compare the results with aftershock data from California. The postseismic behavior of faults was found to be more complex than previously predicted on the basis of steady state approximation of the friction law. Depending on model parameters and the initial friction the fault exhibits either decaying afterslip, slow earthquakes or aftershocks. Finally they noted that the whole process is very complex and not only many assumptions were

made in modeling performance, but also important processes such as fluid flow, viscous deformation and dynamic stress changes were neglected.

Perfettini and Avouac (2007) studied the aftershock sequence followed the 1992 Landers earthquake and showed that the postseismic deformation resulted mainly from frictional afterslip, probably deeper than the seismogenic zone. They interpreted this fact due to the transition with depth from a rate-weakening to a rate-strengthening rheology. Recent investigations of **Wang et al. (2009, 2010, 2012)** also suggest a strong influence of the after-slip, (besides the aftershocks considered) and viscoelastic deformation on the development of the stress distribution. They performed their analysis in the 1999 Izmit aftershock sequence (North Anatolian Fault) and in the sequence followed the 2004 Parkfield earthquake in Southern California. Their results showed that early post-seismic displacements following the main shocks can be in principal explained by stress-driven creep in response to coseismic stress perturbations, and the large aftershocks located in the zone loaded by the main shock. According to their analysis, post-seismic activities (including aseismic relaxation and large aftershocks) can be reasonably explained by stress relaxation processes. The data for constraining coseismic slip could thus be enriched post-seismically, especially based on geodetic measurements in the first month following the main shock. The contribution from aftershock-induced elastic relaxation was generally less than 10% of the observed post-seismic displacements, but it could be influential at some individual sites.

The temporal evolution of background seismicity rate during the 1997-1998 Umbria-Marche earthquake sequence in Italy, was investigated by **Lombardi et al. (2010)**. The ETAS model was applied to distinguish the background seismicity rate from the coseismic triggered rate of aftershocks. The stationary ETAS model, which assumed stable background seismicity

rate, failed to reproduce the observed pattern of earthquake production rates. The most likely explanation was the underestimation of background seismicity rate in the beginning of the sequence which lasted for a few months. This happened because the main shock occurrence activated transient driving processes causing the variation in background seismicity rates. According to the authors these processes deal with fluid flow and pore-pressure relaxation which were promoted by the coseismic stress changes generated by the repeated main shocks.

[Belardinelli et al. \(2011\)](#) investigated the correlation between seismicity rates and ground uplift rates, based upon stress transfer from an inflating deformation source in Campi Flegrei caldera during the 1982-1984 unrest. The model they proposed was able to simulate adequately the maximum amplitudes and the duration of the observed seismicity rates during this period but it failed to reproduce the seismicity rates after the end of 1984, possibly because of the different deformation source that acted after the 1982-1984 uplift. They also concluded that seismicity rate changes can be affected by either decreasing or increasing the stressing rate in a volcanic region. Seismicity rate analysis in volcanic region was also performed by [Toda et al. \(2002\)](#) who found that the seismicity rate is proportional to the calculated stressing rate, and that the duration of aftershock sequences is inversely proportional to the stressing rate.

The evolution and relationship between the stress field and the rates of earthquake production via cellular automaton models was attempted by [Weatherley et al. \(2000\)](#). During the approach of their crack model to criticality, the rate of events of all sizes increased and the stress deficit of small adjacent regions correlated. This provided the necessary conditions for a large event generation in the crack model. Large events occurred almost randomly in the partial stress drop model. Fluctuations of stress deficit in the

model were found to be consistent with small fluctuations about a mean-state of high stress with the event sizes following a power-law distribution. These features identify the partial stress drop model as a self-organized critical system, a system which remains perpetually close-to-failure in large events. Similar approaches were performed by [Jaumé et al. \(2000\)](#) as well. Following the concept of self organized criticality, the precursory scale (Ψ) approach has also been applied for seismicity rate research ([Evison and Rhoades, 2002, 2004; Papadimitriou et al., 2006](#)).

1.4 Relevant research performed in the study area

The first who investigated seismicity patterns with the purpose to identify earthquake prone regions was [Papazachos \(1980\)](#) who divided the Aegean and the surrounding area into 19 seismic zones on the basis of seismotectonic criteria such as seismicity rates and focal mechanisms. Later this map was modified ([Hatzidimitriou et al., 1985](#)) although only small differences in comparison with the original one were introduced. This division was performed by the author in order to determine constant background rates in each area so he can identify deviations of the observed seismicity rates from this background rate. Two quiescence periods were identified before the occurrence of 2 strong events ($M \geq 7.0$) in south Peloponnese, (1947), and the Ionian islands, (1953), respectively. Within the west part of Hellenic arc he observed a decrease of seismicity rate since 1961, suggesting that a strong earthquake ($M > 7.0$) may occur during the next ten years or so. [Papazachos and Comninakis \(1982\)](#) also spotted two seismic quiescence periods 1932-1947 and 1967-1981 and interpreted this seismicity rate anomaly as a potential precursor of a $M \geq 7.0$ earthquake expected in southwest Peloponnese. Their results also partially agreed with the ones obtained by [Wyss and Baer \(1981\)](#) for the same region and the adjacent eastern regions of the Hellenic arc, who observed an 80% drop of seismicity

rates during 1962-1977 with respect to the rate of the former period 1950-1962.

Cominakis and Papazachos (1980) studied the space-time distribution of the intermediate depth earthquakes in the Hellenic subduction zone and investigated regularity patterns of seismicity rates. They detected subsequent periods of high (1926-1948) and low rate (1901-1925 and 1949-1980) seismic activity for earthquakes with $M \geq 6.2$. They also detected a similar period of enhanced seismic activity ($M \geq 7$) during the eighteenth century which demonstrated similar clustering characteristics with the one occurred during 1926-1948. According to these observations they stated that an intermediate depth increased seismic activity will possibly initiate in 2005 and last for about 2 decades.

Papadimitriou and Papazachos (1985) investigated seismicity rate evolution in the Aegean and surrounding area through the “seismic gap” concept. After introducing a modified definition of seismic gap more appropriate for the available data and the regional conditions, they determined the average return period and the background seismicity rates. Afterwards they identified 11 such gaps where seismicity rates were reduced by more than 15% in respect to the background seismicity rate, suggesting the potential for the generation of strong earthquakes ($M \geq 6.0$ or $M \geq 6.5$) within the following decade.

Latousakis and Drakatos studied the temporal evolution of seismicity rates during several aftershock sequences that took place in the broader Aegean region (e.g. Corinth Gulf, North Aegean, Cephalonia Transform Zone, Central Aegean) from 1971 to 1998. They published the results of their work in a series of papers during the 1990's (**Latoussakis et al., 1991; Latoussakis and Drakatos, 1994; Drakatos et al., 1994; Drakatos and Latoussakis, 1996; Drakatos, 2000**). Based upon Omori law (**Omori, 1894**), the Akaike Information Criterion (AIC - **Akaike, 1974**) and the method firstly

applied by [Matsu'ura \(1986\)](#), they found that the occurrence rate of aftershocks is significantly reduced prior to a relatively strong event. After these time increments characterized as 'relative quiescence', seismicity rates increase again following the strong event occurrence, as it is predicted by the Omori law.

[Evison and Rhoades \(2000\)](#) used the earthquake catalogue of the Aristotle University of Thessaloniki and identified 10 sequences of precursory swarms related to major main-shock events along the Hellenic subduction zone. They found significant correlation among these cases and relevant activity recorded in New Zealand and Japan. They concluded that in many cases, precursory swarms are closely related to main-shock occurrence. The interpretation they provided for this observation was that the swarms are part of a long term seismogenic process which culminates in a major earthquake ([Evison and Rhoades, 1998](#)). [Console et al., 2006b](#) applied a series of time-invariant, long-range, and short-range forecasting models utilizing the non declustered instrumental catalogue of Greece from 1981 to 2002 and they showed that time-dependent models fits better to data in comparison with time-invariant ones. They thus concluded that in order to perform a robust and reliable forecast, both spatial and temporal variation of seismicity rate changes should be considered.

[Papadimitriou et al. \(2005\)](#) studied the seismicity rate variations of moderate-size earthquakes ($M > 5$) that occurred before and after the 1956, $M=7.7$ Amorgos earthquake, in Aegean Sea. They investigated seismicity rate changes in association with static stress variation by constructing an evolutionary model, combining coseismic slip and tectonic loading on the major fault segments of the study area. They found that the rates of the moderate-size events just before the main shock appear to be considerably increased when they are compared to those of either prior to subsequent periods. The changes in the occurrence rates were found to be more striking

for distances of 100-150 km from the main shock. The stress shadow resulted from the accumulated stress interaction may explain the remarkable quiescence in strong earthquakes after 1957.

Karakostas (2008, 2009) distinguished the two main directions usually followed in seeking for characteristic patterns before a strong event occurrence: the accelerated moment release (Bufe and Varnes 1993, Bowman et al., 1998) and stress transfer between faults in a fault network. The accelerating moment release model has been proved to hold in areas almost ten times the fault length. In areas of smaller dimensions (three to four times the fault length) precursory decelerated moment release has been detected either from the temporal variation of the Benioff strain release (Papazachos et al. 2005), or from the seismicity rates (Papadimitriou et al. 2005). Karakostas (2009) studied seismicity rate changes in association with the pre-stress field before the occurrence of 5 strong ($M \geq 6.2$) earthquakes in Greece during 1995-2006. The spatio-temporal distribution of smaller magnitude events was examined in comparison with the stress pattern necessary for the generation of the strong earthquakes. Increased seismicity rates were found in most of the cases in areas of positive stress changes. Seismicity rates appear to return to the background levels after a short period of about 2-3 years. Some years prior to the main shock occurrence a significant decrease of the rates of intermediate size events ($M \geq 4.5$) was observed. These results support the use of the seismicity rate as an expression of seismicity increase, as it comes from complete samples, like the ones used in the present study, that follow the Gutenberg–Richter relation.

Chapter 2. Rate/State Modeling

2.1 Introduction

In this chapter the basic principles of Rate/State modeling are presented along with the description and determination process of the involved parameters. The Dieterich (1994) Rate/State dependent friction model combined with static Coulomb stress changes (ΔCFF) was applied for investigating the spatio-temporal evolution of seismicity rate changes in specified areas of the broader Aegean region. The coseismic slip of the stronger earthquakes ($M_w \geq 5.8$) was considered to contribute to the stress field evolution along with the continuous tectonic loading on major faults. These stress field variations alter the unperturbed (reference) seismicity rates as they were calculated for selected time intervals, named as 'learning periods'. Stress changes are calculated just after each strong event occurrence and their influence is then examined in connection with the smaller magnitude earthquake occurrence rates. Qualitative and quantitative comparison between the smoothed observed seismicity rates and the expected ones, as they were forecasted by the Rate/State model were investigated for the interseismic periods (named as 'study' or 'forecasting' periods) between subsequent strong earthquakes. The influence of the Rate/State parameters in the model efficiency is explored by evaluating the Pearson linear correlation coefficient between simulated and observed earthquake occurrence rates along with its 95% confidence limits. The calculations aim to identify areas of expected increased seismicity rates as candidates to accommodate enhanced seismic activity. Seismicity rate results are filtered by certain criteria and constraints, in an attempt to overcome model uncertainties and to provide more reliable results for specific areas of major interest, that is, in areas with increased positive Coulomb stress

changes values. The obtained results are demonstrated along with the evaluation of the forecasting model ability. This latter issue is also investigated in connection with the latest strong earthquakes occurred in the Aegean region after the ending point of the model forecasting period, i.e. January 2013.

2.2 Method - Rate/State Model Principles & Description

It is usually evident that deviations of seismicity rates that are considered as normal in a regional scale, may be connected with seismicity bursts or even an impending strong earthquake, since these changes alter the earthquake occurrence probabilities introducing time-dependency to seismic hazard assessment. According to Rate/State dependent friction concept, the constitutive properties and system interactions that result to the onset of the unstable slip must be defined in order to specify the time t , at which a particular source nucleates. This time is defined as

$$t = F[C, \tau(t)] , \quad (2.1)$$

where C represents the initial conditions and $\tau(t)$ stands for some given stressing history. In general, the initial conditions, $C=C(n, r, \dot{\tau}_r)$, are a function of the nucleation sources, n , the background seismicity rate, r , and the stressing rate, $\dot{\tau}_r$. The evaluation of seismicity rate changes in terms of Coulomb static stress changes is performed on the basis of a Rate/State model, proposed by Dieterich (1994). The model anticipates that a sudden positive stress step, results to an immediate increase of the seismicity rate, which is temporary and attenuates as a function of time following Omori's decay law. Similarly, a sudden stress drop brings on a seismicity rate depression, which also tends to recover with time to the initial (unperturbed) rate, due to the effect of the constant tectonic loading. These rate changes can be observed either along the fault which caused the main shock (onto-fault

aftershocks), or in nearby faults (off-fault aftershocks) up to a distance, proportional to the final slip distribution regardless the dynamics of the rupture (Gomberg et al., 2003). There is one important distinction to be made between onto-fault and off-fault aftershocks. Whereas onto-fault aftershocks are second order phenomena compared to the mainshock in terms of the seismic moment release, off fault triggered events may have similar or even larger magnitude than the triggering event. This is because they are occurring on fresh unruptured fault segments rather than on the residual patches within or near the mainshock rupture where the stresses have, overall, been relaxed (Scholz, 2002). The target is focused on these off-fault aftershocks also because they occur far enough from the source fault, where the stress changes are not influenced from slip details (Toda and Stein, 2003). Contrarily, along fault aftershocks occurrence is strongly influenced by short scale slip discontinuities, often not being simulated by the assumed slip model with uniform slip across the fault.

The proposed formulation and its applications (e.g. Toda et al., 1998; Toda et al., 2005; Catalli et al., 2008; Leptokaropoulos et al., 2012) manifested that seismicity rate changes strongly depend upon clock-advanced failure, stress evolution and reference seismicity rate. Eventually, the changes of the earthquake production rates, R , are estimated as a function of ΔCFF , fault stressing rate, $\dot{\tau}_r$, reference seismicity rates, r , and the physical constitutive fault properties, expressed by a fault constitutive parameter, A (Dieterich and Kilgore, 1996). Seismicity rate, R , is connected with the aforementioned parameters as

$$R = \frac{r}{\gamma \dot{\tau}_r} , \quad (2.2)$$

where γ , is the state variable for seismicity formulation that evolves with time and stressing history. Its value alters because of the stress

perturbations, causing seismicity rate changes. This evolution of the state variable is demonstrated by equation (B16) of Dieterich (1994) as follows

$$d\gamma = \frac{1}{A\sigma} [1 - \gamma\dot{\tau}_r] dt \quad , \quad (2.3)$$

where σ is the total normal stress. Product $A\sigma$, controls the direct effect of friction in Rate/State model (Cocco et al., 2010). Under constant stressing rate the state variable is equal to

$$\gamma_0 = \frac{1}{\dot{\tau}_r} \quad . \quad (2.4)$$

By substitution of (2.4) into (2.2), it is shown that when stress perturbation is absent, seismicity rate, R , remains constant and equal to the reference rate, r . If a strong earthquake occurs in the region, it alters the stress field and the state variable changes into a new value

$$\gamma_n = \gamma_{n-1} e^{-\frac{\Delta CFF}{A\sigma}} \quad , \quad (2.5)$$

where γ_{n-1} is equal to γ_0 for the first perturbation. ΔCFF is the coseismic Coulomb stress changes, given by

$$\Delta CFF = \Delta\tau + \mu' \cdot \Delta\sigma_n \quad , \quad (2.6)$$

where $\Delta\tau$, is the shear stress change, $\Delta\sigma_n$, is the normal stress change and μ' , the apparent coefficient of friction, including pore pressure effects and temporal changes of effective normal stress (Linker and Dieterich, 1992; Simpson and Reasenber, 1994; Harris and Simpson, 1998). It is profound from (2.5) that a positive stress step causes a decrease of γ value. This means that if the fault slips at a higher rate, then it yields a higher earthquake production rate (Toda et al., 2005). Equation (2.5) is applied to estimate the new value of the state variable γ , after a large earthquake occurring in the region. This change in the state variable derived from (2.5), is transient and recovers with time inversely to the fault tectonic stressing rate $\dot{\tau}$. For the next inter-event time step, the new value of state variable is given by

$$\gamma_{n+1} = \left(\gamma_n - \frac{1}{\dot{\tau}_r} \right) e^{-\frac{\Delta t \dot{\tau}_r}{A\sigma}} + \frac{1}{\dot{\tau}_r} , \quad (2.7)$$

where Δt is a time increment used to recalculate the state variable value at each time step and γ_{n+1} and γ_n are the values of the state variable at the beginning and the end respectively, of the time increment when every strong event occurs. In the absence of a new stress perturbation, the state variable tends to reach its initial value, γ_0 , with time, due to the influence of the tectonic loading. Note that the indicators, n , and $n+1$, correspond to the value of the state variable just after the first major event and just before the next one, respectively. Therefore the effect of the subsequent stress change on seismicity strongly depends on the seismicity rate (a manifestation of the state variable – or equivalently the fault stressing rate) immediately beforehand (Toda and Stein, 2003).

Following Dieterich (1994) the characteristic relaxation time for the perturbation of earthquake rate, t_a (or aftershock duration), defined as the time required by the perturbed seismicity rate to recover to the reference seismicity level, is related to the other parameters as

$$t_a = \frac{A\sigma}{\dot{\tau}_r} . \quad (2.8)$$

The forecasted seismicity rates R are calculated from (2.2), by substitution of the value of state variable γ which corresponds to each case. This value may yield either because of a sudden stress perturbation caused by a strong earthquake (γ from (2.5)), or because of the tectonic loading at an inter-event period between two major shocks (γ from (2.7)). Finally the seismicity rate equation, as a function of time, t , has the form (Dieterich and Kilgore, 1996)

$$R(t) = \frac{r}{\left[\exp\left(\frac{-\Delta CFF}{A\sigma}\right) - 1 \right] \exp\left(\frac{-t}{t_a}\right) + 1} . \quad (2.9)$$

In the following sections we explicitly describe the evaluation procedure of the aforementioned physical quantities and the parameters that are incorporated in the Rate/State formulation.

2.2.1 Rupture Models Determination

Earthquakes nucleated on active fault surfaces that are often approximated with rectangles dipping within the brittle layer of the earth's crust. Fault planes are adequately described by the use of geometric parameters such as the length, L , and the width, w , as well as the fault plane solution. The dimensions of the aforementioned parameters can be evaluated from the spatial distribution of the aftershocks following the main event, but such information is either unavailable or insufficient in most of our case studies because of the limited density and efficiency of the National Seismological Network in certain areas. Therefore, in order to calculate the rupture parameters that are necessary for the model application, empirical relationships were employed when field observations or relevant information from previous investigations were not available. These relationships were taken from [Papazachos et al. \(2004\)](#) who collected worldwide data and proposed scaling laws for different seismotectonic environments, according to which fault length (in km) can be calculated as a function of the earthquake magnitude. Different relationships were obtained for strike slip faults (2.10a), for continental dip-slip (either normal or reverse) faults (2.10b) and for thrust faults in subduction zones (2.10c)

$$\log L = 0.59M - 2.30, \quad (2.10a)$$

$$\log L = 0.50M - 1.86, \quad (2.10b)$$

$$\log L = 0.55M - 2.19. \quad (2.10c)$$

Estimates from equations (2.10) and the respective relations proposed by [Wells and Coppersmith \(1994\)](#) were found to be in good agreement in several cases. Fault widths were estimated from the dip angle of the fault and

the distance measured down-dip from the surface to the upper and lower edges of the rectangular dislocation plane, respectively, as $w = \frac{h}{\sin(dip)}$, where h , is the width of the seismogenic layer. The seismogenic layer typically lies between approximately 2 and 20 km, in the back arc region, as it comes from the focal depth determinations of the larger events (Papazachos et al., 2009, Fig. 2.1), and from studies of aftershock sequences with accurate depth determinations (e.g. Papazachos et al., 2000; Karakostas et al., 2003, 2010, 2012; Tan et al., 2014). The value of h adopted in this study was 12km (3-15 km). The estimation of the rupture widths associated with low angle thrust faulting along the subduction zone was accomplished after the constraint $L \geq W$ was fulfilled (Lin and Stein 2004; Messini et al., 2007).

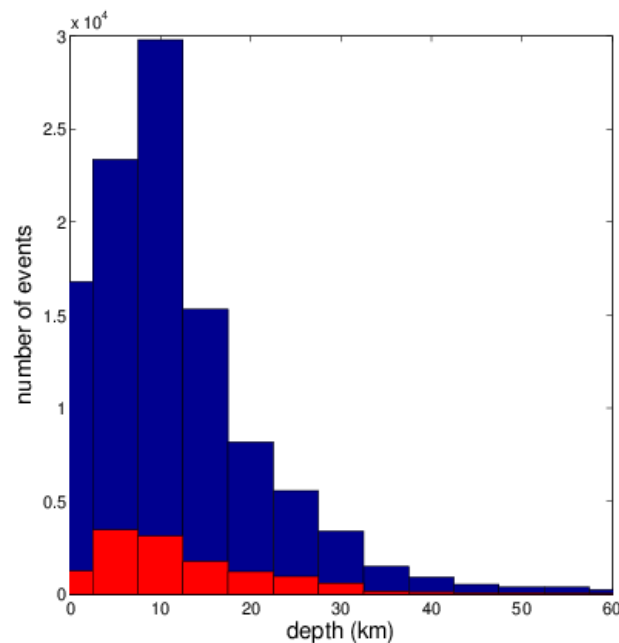


Fig. 2.1. Depth distribution of earthquake foci in the back arc area of the Aegean. 83% of the better located $M \geq 2.5$ events after August 2008 have depths ≤ 20 km (red bars), whereas 85.5% of all recorded events after 1981 are located at depths ≤ 20 km (blue bars).

The average coseismic slip, \bar{u} , was calculated from the seismic moment, M_0 , of an earthquake as

$$M_0 = G \cdot \bar{u} \cdot S = G \cdot \bar{u} \cdot L \cdot w, \quad (2.11)$$

where G is the shear modulus and S is the fault surface ($S=L \cdot w$). The along strike and down dip components of the slip vector were computed in

terms of the geometry of each segment. The shear modulus G was set here equal to $3.3 \cdot 10^5$ bars for the back arc area (Stein et al., 1997; Papadimitriou and Sykes, 2001; Toda et al., 2005) and $5.0 \cdot 10^5$ bars for the subduction zone: According to Bird and Kagan (2004) this later value encompasses both crustal and mantle values and therefore it is more appropriate for oceanic convergent boundaries and subduction zones. The Poisson ratio was fixed at $\nu=1/4$ (Stein et al., 1997; Parsons et al., 1999; Papadimitriou and Sykes, 2001; Pollitz and Sacks, 2002; Ganas et al., 2005).

2.2.2 ΔCFF Calculation

Coulomb stress changes were calculated by application of the constant apparent friction model (2.6) from the coseismic displacements of the stronger ($M \geq 5.8$) events that occurred in the study area since the beginning of a given learning period. Nostro et al. (2005) showed that this approach provides similar results with the isotropic poroelastic model (Beeler et al., 2000; Cocco and Rice, 2002). According to this latter model the pore pressure changes depend on the volumetric stress changes such that $\Delta P = -B \Delta \sigma_{kk} / 3$. Following this formulation it yields

$$\Delta CFF = \Delta \tau + \mu \left(\Delta \sigma_n - B \frac{\Delta \sigma_{kk}}{3} \right) \quad , \quad (2.12)$$

where $\Delta \sigma_{kk}$, is the alteration of the trace of the stress tensor and B is the Skempton's coefficient which theoretically ranges from 0, for dry soil, to 1, for fully saturated soil. Robinson and McGinty (2000) estimated the values of the stress tensor components from geodetic results, earthquake focal mechanisms and P-wave polarity data. In such way they determined the orientation of σ_{11} , σ_{22} and σ_{33} and also the magnitude of the deviatoric stress and combined these results with dislocation theory to study the aftershock distribution of 1994 Arthur's Pass earthquake (New Zealand). The apparent friction coefficient, μ' , is related to the above parameters as: $\mu' = (\mu - \alpha)(1 - B)$, where, α , is the Linker and Dieterich (1992) parameter to account for the temporal

changes of the effective normal stress. If in the fault zone $\Delta\sigma_{11}=\Delta\sigma_{22}=\Delta\sigma_{33}$, so that $\Delta\sigma_{kk}/3= \Delta\sigma$, then the apparent coefficient of friction is defined as $\mu'=\mu(1 - B)$. [Catalli et al. \(2008\)](#) derived values of $\mu'=0.45$ when they applied the isotropic poroelastic model and $\mu'=0.27$ when they applied the constant apparent friction model. [Cocco et al. \(2010\)](#) used the value of 0.4 for the apparent coefficient of friction, yielding from $\alpha=0.25$, $\mu=0.75$ and $B=0.47$. [Stein et al. \(1997\)](#), [Nalbant et al. \(1998\)](#) and [Paradisopoulou et al. \(2010\)](#) applied a value of apparent friction coefficient, $\mu'=0.4$ whereas [Papadimitriou and Sykes \(2001\)](#) set $\mu'= 0.6$ for NAF, Western Turkey and North Aegean. Calculations performed with different values of μ' (0.2–0.9) in the study of 2001 Skyros sequence, confirm that the resulted ΔCFF values are generally insensitive in μ' fluctuation ([Karakostas et al., 2003](#)). The value adopted in this study was $\mu'=0.4$, whereas additional calculations carried out with $\mu'=0.6$ yielded identical results.

2.2.3 Determination of Long Term Slip Rates (Stressing Rate)

The determination of the stressing rate on the major faults of the study area is necessary for the expected seismicity rate estimation. It is assumed that the stressing rate is time independent and its spatial distribution is uniform. The values of stressing rate are used to determine the state variable γ , applied in the Rate/State model, for each time step. In the present study, the slip rates on the major faults as they were defined from geodetic data ([McClusky et al., 2000](#); [Reilinger et al., 2006](#)) were used in order to determine the stressing rates onto them. For the calculations, only 60% of the geodetic slip rate value was considered for accounting the seismic part of the secular tectonic motion. Different values for seismic coupling along the NAF and its surroundings have been proposed and they vary between 20-75% ([Ward, 1998](#); [Ayhan et al., 2001](#); [Bird and Kagan, 2004](#)), but most of them suggest a value close to 60%. Here a constant stressing rate, averaged from the one

upon each fault segment is considered for each sub-area, uniform throughout the seismogenic layer (both along strike and dip direction). Nevertheless, not a unique value of the uniform stressing rate was employed in the calculations, but a trial with a broad range of values was attempted in each case study in order to cope with the uncertainties yielding from the evaluation process and also to take into account different level of seismic coupling.

2.2.4 Characteristic Relaxation Time and Product $A\sigma$

Characteristic relaxation time expresses the amount of time necessary to be elapsed until the rates of earthquake production restore to the values that prevailed before the main event occurrence. It becomes then clear that tectonic stressing rate governs the duration of the stress perturbation effects on the seismicity rate. This effect is stronger on faults with low stressing rates because they require more time to recover to their initial conditions (Toda et al., 2002; Parsons, 2002; Llenos et al., 2009). The estimate of characteristic relaxation time in the shallow crust under hydrostatic effective normal stress leads to values from months to decades (Beeler et al., 2014 and references therein). Dieterich (1994) pointed out that t_a values range from 0.2 to 12 yrs for different regions worldwide, suggesting a value of 10.2 years for shallow earthquakes ($h < 70$ km) and for magnitudes greater than 6.0. Perfettini and Avouac (2004) obtained a $t_a = 8.5$ when studying the 1999 Chi-Chi aftershock sequence, consistent with an average value of ~7 yrs (ranging from 5 to more than 10 years) as derived by Rousset et al. (2012) for the same aftershock sequence. Toda et al. (2005) estimated characteristic relaxation time varying from 7-66 years for various fault segments in Southern California, whereas Toda and Enescu (2011) arbitrarily assigned a spatially variable of t_a for the Japanese Arc, being < 20 yrs offshore, in a close distance from the trough and getting much higher values (up to 100 yrs) in the mainland. According to an

alternative approach, the ratio of the mean recurrence time to the characteristic time, t_r/t_a , is found ranging between 10-50 (Tajima and Kanamori, 1985; Wesson, 1987; Dieterich, 1994). Given that the average recurrence time of the strongest events in the broader Aegean site is assumed to be approximately 250 years, it results to a characteristic relaxation time between 5–25 years. However, following Dieterich (1994) the tested values of t_a in the present study were extended in some cases covering a broader range from 2.5 to 30 years.

The former values of stressing rate and characteristic time were set in equation (2.8) to obtain a wide range of $A\sigma$ values for each case studied. The attempt to estimate from direct measurements separately the A and σ values is very difficult, especially in the earth's interior. From laboratory observations, parameter A was found taking values in a range between 0.005 to 0.015 for various rock types, temperatures and pressure conditions (Dieterich, 1994; Scholz, 1998). Harris and Simpson (1998) suggested that acceptable values of A should be between $10^{-4} - 10^3$, whereas the effective normal stress, σ , depends on depth, regional stress, fault orientation and pore pressure (Hainzl et al., 2010). Most commonly the combined parameter $A\sigma$ is considered as a product instead, which describes the frictional resistance of the fault segments, i. e. the instantaneous response of friction to a sudden change of slip speed (Toda and Stein, 2003). Regarding the results of previous studies, the range of $A\sigma$ is found between 0.01bars to 6–9bars (Harris and Simpson, 1998; Catalli et al., 2008), with values between 0.4bars – 1bars being more popular in many investigations (Stein et al., 1997; Stein, 1999; Belardinelli et al., 1999; Guatteri et al., 2001; Toda and Stein, 2003; Toda et al., 2005; Ghimire et al., 2008; Hainzl et al., 2010). Several recent studies though, suggest lower values of $A\sigma$. For example Hainzl et al. (2013) applied values varying from 0.0016 bars to 0.16bars) whereas Maccaferi et al. (2013) accepted a value of 0.05 bars for their analysis in the extensional regime of Iceland. The

role of $A\sigma$ was analyzed by [Catalli et al. \(2008\)](#) who showed that the total number of triggered events in a given time interval after a main shock increases, when $A\sigma$ decreases, also in agreement with [Belardinelli et al. \(2003\)](#).

To summarize, characteristic relaxation time and stressing rate was determined and product $A\sigma$ was derived by their values. This means that in addition to the reference seismicity rate (see the following section), only two out of these three parameters needed to be defined. Therefore, the Rate/State model is constituted of 3 free parameters and the influence of their variance on the results has to be evaluated. [Hainzl et al. \(2009\)](#) introduced the coefficient of variation (CV), as a fourth free parameter. They fixed the value of t_a and fitted the remaining parameters using the maximum likelihood method. There is also a connection between stressing rate, $\dot{\tau}$, and the reference seismicity rate, r , since the seismic moment released by the reference seismic activity should be equal to the seismic moment induced by tectonic loading over long periods ([Hainzl et al., 2010](#)). According to [Kostrov \(1974\)](#), there is a linear relationship between these two parameters as $\dot{\tau}_r = \langle M_0 \rangle \frac{r}{V}$, where $\langle M_0 \rangle$ is the scalar value of summed seismic moment tensor divided by the number of earthquakes and V , stands for the volume of the seismogenic layer.

2.2.5 Reference Seismicity Rate Evaluation

From now on the definition based on [Cocco et al. \(2010\)](#) for reference and background rates will be adopted throughout the manuscript: "Reference" seismicity rate refers to a time-independent spatially smoothed seismicity rate calculated by using a non-declustered catalogue. On the other hand, we refer to "background" seismicity rate, as a time-independent average seismicity rate computed in a predefined time window from a declustered catalogue.

A common issue of debate is whether reference or background seismicity rates are the most appropriate input data for seismicity rate studies. The main argument of those who use declustered datasets (or equivalently background seismicity rates) is that two kinds of seismicity can be distinguished in general: the first one is the time independent seismicity, which is supposed to be constant in time, given a constant fault stressing rate and can be considered as normal for a certain region (Habermann and Wyss, 1984). The second is the triggered one, such as aftershock sequences which decay with time according to the Omori's law. The later type of seismicity is not characteristic of one region and quite often it is removed from the datasets for specific kind of analyses. The methods that have been developed to discriminate the dependent from independent fraction of seismic activity are divided into conventional and stochastic approaches. The methods forming the first group can be classified into two classes: window based and link based methods. The window-based methods remove the smaller earthquakes in a space-time window around a larger event, usually named as main shock (Utsu, 1969; Gardner and Knopoff, 1974; Keilis-Borok and Kossobokov, 1986; Molchan and Dmitrieva, 1992). Most commonly, the larger the magnitude of the main shock the bigger the window size. The link-based methods remove events which are within a compromised space-time distance to an earlier event (Reasenber, 1985; Frohlich and Davis, 1990; Davis and Frohlich, 1991).

In these conventional declustering methods, it is difficult to find optimal parameters for the sizes of space-time windows or the link distance and therefore the declustering output may be quite sensitive to such subjective choices. Moreover shortcoming of conventional declustering is that removing earthquakes in the catalogue may cause losses of potentially useful information. For these reasons stochastic declustering methods were

developed. Most of these models for the space-time-magnitude occurrences of earthquake clusters are in the form of branching point process (Adamopoulos, 1976; Kagan, 1991; Musmeci and Vere-Jones, 1992; Rathbun, 1993; Ogata, 1998; Ogata et al., 2003; Ogata, 2004; Zhuang et al., 2002, 2004; Console and Murru, 2001; Console et al., 2003, Marzocchi and Lombardi, 2008). These models generally classify seismicity into two components, the background and the clustered, where each earthquake, whether it be from the background component (or generated by another event), produces (triggers) its own offspring (aftershocks) according to some branching rules (Zhuang et al., 2004).

It is shown in many recent studies however, that the independent fraction of seismicity, as it is assumed, actually exhibits temporal fluctuations which can be noticeable even during short time scales (Hainzl and Ogata, 2005; Tsukakoshi and Shimazaki, 2006; Lombardi et al., 2010). Regardless the cause of these anomalies (coseismic stress perturbations, fluid flow, pore pressure relaxation), the fact is that even the most recent and sophisticated declustering algorithms (Zhuang et al., 2002; 2005; 2011; Marzocchi and Lombardi, 2008, Tibi et al., 2011; Jacobs et al., 2013) cannot ensure that the remaining seismicity will correspond to a time independent, stationary physical process, in many of the cases. On the contrary it is preferred to use reference seismicity rates coming from non-declustered catalog (Catalli et al., 2008; Cocco et al., 2010; Leptokaropoulos et al., 2012), from the recorded seismicity and a certain stressing history, to predict the evolution of the occurrence rates in any space-time window.

It must be pointed out that in this sense, the reference seismicity rate cannot be considered as the rate of earthquake occurrence in the absence of any stress perturbation (Cocco et al., 2010). In order to observe the actual reference seismicity rate one should wait for a long time (about the double of

the characteristic relaxation time, t_a) after any stress perturbation in the study area (Console and Catali, 2006). Ideally, to obtain the reference seismicity rate, one should average seismicity rates over centuries or at least over a period much longer than the characteristic relaxation time (Toda et al., 2005). Since strong earthquakes are sufficiently frequent and the instrumental records cover a period of approximately one century, it is unrealistic for any available data set to contain only unperturbed events reflecting the actual reference seismicity earthquake occurrence rate.

In the present study, reference and also observed seismicity rates for any inter-event time interval are computed by spatially smoothing the seismicity. The selected smoothing technique is more properly applied in areas as small as data adequacy permits. This happens because the spatial smoothing intrinsically present, delineates realistically the real seismicity rates in datasets with similar statistical properties i.e. data density and variance. For this purpose a probability density function (PDF) of epicenters distribution was considered. This function determines the seismicity rates at the center of each cell of a normal grid superimposed on each study area and these values are considered constant in time as the same is considered for the secular tectonic stressing rate. The PDF is estimated by a bivariate kernel density estimator of the form (Silverman, 1986; Efron, 1993)

$$f(x, y) = \frac{1}{nh^2} \sum_{i=1}^n K\left(\frac{x - X_i}{h}, \frac{y - Y_i}{h}\right) \quad , \quad (2.13)$$

where K stands for the Gaussian Kernel of the form:

$$K(x, y) = \frac{1}{2\pi} e^{-\frac{(x^2+y^2)}{2}} \quad , \quad (2.14)$$

with X_i , Y_i , being the epicentral coordinates (longitude, λ and latitude, ϕ , respectively), x and y , representing the boundaries (geographical coordinates) of each cell center (on which the PDF value is estimated), n , is

the number of events, inside each cell and h , is the bandwidth (or window width, or smoothing parameter) having the same units as X_i , Y_i , x , y . The kernel determines the regularity and the shape of the estimator, whereas the window width controls the degree of smoothing. From equations (2.13) and (2.14) the probability is derived

$$P = \frac{1}{4n} \sum_{i=1}^n \left[\operatorname{erf}\left(\frac{y_2 - Y_i}{h\sqrt{2}}\right) \cdot \left(\operatorname{erf}\left(\frac{-x_1 + X_i}{h\sqrt{2}}\right) - \operatorname{erf}\left(\frac{-x_2 + X_i}{h\sqrt{2}}\right) \right) + \operatorname{erf}\left(\frac{y_1 - Y_i}{h\sqrt{2}}\right) \cdot \left(\operatorname{erf}\left(\frac{-x_2 + X_i}{h\sqrt{2}}\right) - \operatorname{erf}\left(\frac{-x_1 - X_i}{h\sqrt{2}}\right) \right) \right], \quad (2.15)$$

$$\text{with } \operatorname{erf}(x) = \frac{2}{\sqrt{\pi}} \int_0^x e^{-t^2} dt, \quad (2.16)$$

which is twice the integral of the Gaussian distribution with mean zero and variance of 1/2. Finally the seismicity rate is estimated for the given time period, Δt , as $R=n/\Delta t$. This corresponds to the real seismicity rate of the given time period and is compared with the value of expected seismicity rate for the respective period resulted from (2.9).

2.2.5.1 Selection of bandwidth, h

As shown in equations 2.13 and 2.15, the value of probability density, P , is a function of the bandwidth, h , which represents the expanse of the area which is being influenced by each value P and therefore it determines the degree of smoothing. In general, high values of the window width represent better systematic variations, whereas lower values are usually set for revealing random local fluctuations. The bandwidth may have a single value, h , two values depending on the x and y coordinates variance, h_x and h_y , respectively, or being adaptive when the smoothing is performed around each epicenter (rather than around each cell), and increases when the data become sparse (e.g. Helmstetter et al., 2006a; Werner et al., 2010, Botev et al., 2010). In the present study the division into the subareas was done by taking into account a relatively homogenous seismicity rate level and therefore we applied the first approach. Calculation of h_x and h_y provided identical values

with the single one in the sub-areas and therefore the constant smoothing factor assumption could be applied with sufficiency.

Several methods were proposed for a proper h value estimate such as the second derivative of the probability density function (Silverman, 1978), the optimal data-based selection of the smoothing parameter (Hall et al., 1991), several variations of the cross validation method (Sain et al., 1994) and the rule of thumb (Silverman, 1986). In general, high values of the window width represent better the systematic variation, while smaller values make random fluctuations clearer. In the present study the Silverman's (1986) formulation was applied

$$h \approx \sigma \cdot K^{\frac{1}{6}}, \quad (2.17)$$

where $\sigma^2=0.5(s_{xx} + s_{yy})$ and s_{xx} and s_{yy} are sample variances of X_i and Y_i , respectively, and K the number of events included in the period of interest. An example of different smoothing level (bandwidth) applied in seismicity from 1965 to 1981 in North Aegean and Corinth Gulf is demonstrated in Fig. 2.2.

Lower values are preferable because in such way each earthquake has a limited area of influence and consequently low seismicity areas should be better distinguished. The applying values of bandwidth though, fluctuate between 0.04° to 0.30° (or alternatively radius of 4.5km to 33.3km). Silverman's (1986) formula for appropriate h estimation in respect to the data number and variance provides values between 0.07° - 0.14° depended upon the selected sub-areas and the respective data sets used for the analysis.

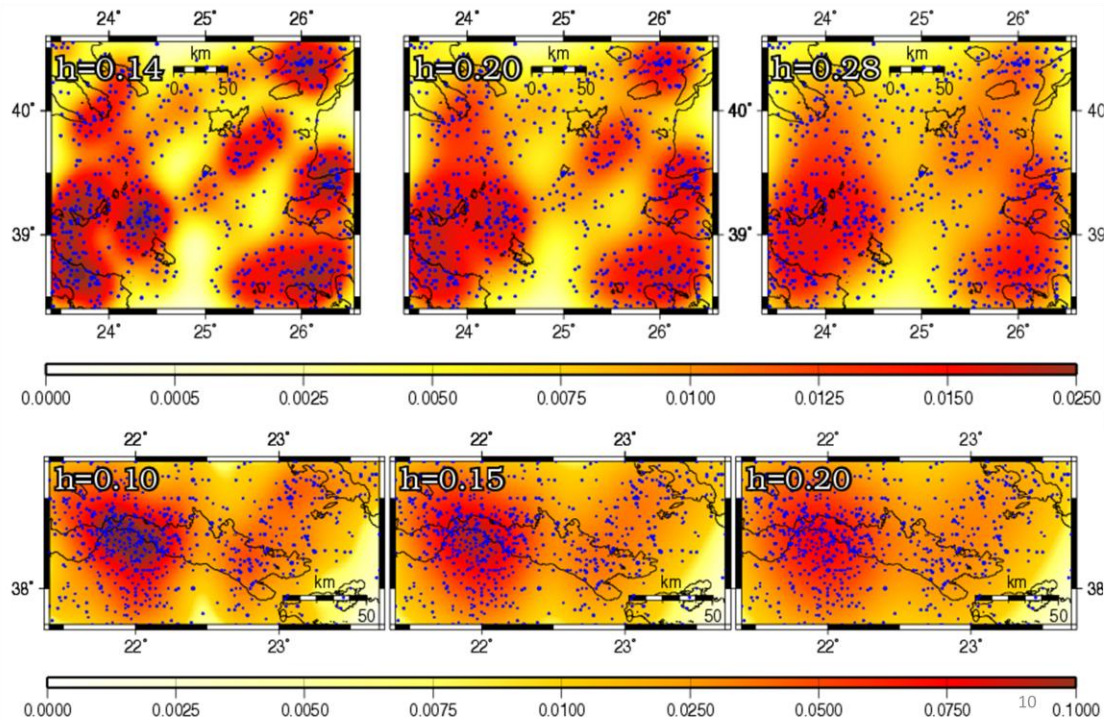


Fig. 2.2. Smoothed seismicity rates in North Aegean (upper frames) and Corinth Gulf (lower frames). Blue dots correspond to earthquakes with $M \geq M_c$ that occurred in the two sites from 1964 to 1981. Lower bandwidth values reveal local seismicity rate peaks whereas higher values over-smooth the seismicity rate all over the study area.

2.2.6 Model Evaluation quantification of the Results

Once the modeled seismicity rates were calculated (2.9), they were compared with the observed ones (2.15) for the respective inter-event time windows constituting the study periods. A comprehensive qualitative representation was accomplished by mapping the ratio of expected/observed seismicity rates in the study areas. The closer this ratio to unity the better the forecasting ability that the model provides. The comparisons were performed for all calculated pairs except those with extremely low values of seismicity rates ($< 0.0001 \text{ events} \cdot \text{cell}^{-1} \cdot \text{yr}^{-1}$) which correspond to areas with very low seismic activity, associated with minor faults or even large epicentral errors. This constraint provides statistically more robust results because the comparison of seismicity rates in relatively less active areas with different properties is avoided.

Quantitative comparison was accomplished by calculating the Pearson's linear correlation coefficient (PCC) and its 95% confidence intervals for a variety of combinations of parameter values. Although PCC is a parametric coefficient, assuming the normality of the data set, in all examined cases the sample size is adequately large, exceeding 400 observations, such that the central limit theorem can be recalled to approximate normality. Significance testing for PCC was also performed by estimating the corresponding p-value that is the highest level of significance at which the null hypothesis, stating that $PCC=0$, can still be rejected. In all cases where $PCC>35\%$ the p-value was found less than 10^{-5} indicating that there is a linear relationship between observed and expected seismicity rates. The linear correlation was estimated in all cases (i.e. the study areas and the respective time windows), once for the entire data set and once more, only for the data accommodated in areas experiencing positive ΔCFF . This approach was selected for two reasons: First, as already shown in previous studies, most of the subsequent large earthquakes occur in such areas (Toda and Stein, 2003). Moreover, onto-fault aftershocks inevitably occur in areas of apparent stress shadow because of the weakness of the applying rupture model to simulate stress changes in the near field. This apparent misfit is avoided by targeting on remote (off-fault), positive ΔCFF areas, as already mentioned in previous sections.

2.2.7 Contribution to Probabilistic Seismic Hazard Assessment

The corner stone of the analysis carried out is to provide a more comprehensive and accepted in the common consensus measure of the estimated seismicity rate changes, which can be also incorporated for probabilistic seismic hazard assessment implications. Strictly settled, the goal of probabilistic seismic hazard analysis (PSHA) is to quantify the rate (or probability) of exceeding various ground-motion levels (traditionally Peak

Ground Acceleration, PGA) at a site (or a map of sites) given all possible earthquakes (first formulized by [Cornell, 1968](#)). According to Senior Seismic Hazard Analysis Committee (SSHAC), “PSHA is a methodology that estimates the likelihood that various levels of earthquake-caused ground motions will be exceeded at a given location in a given future time period. The results of such an analysis are expressed as estimated probabilities per year or estimated annual frequencies”. PSHA therefore, comprises two main components: an earthquake rupture forecast, which provides the probabilities for a complete set of fault rupture scenarios, and a ground-motion model, which predicts the intensity of seismic shaking at a site, conditional on the earthquake scenario ([McGuire, 2004](#); [Wang and Jordan, 2014](#)). The contribution of this thesis to PSHA is to provide the exceedance probabilities of a predefined magnitude during a specified time period in particular sites (seismic sources) of the broader Aegean region.

Previous studies assessing seismic hazard by probabilistic means have been accomplished in the study area. [Stein et al. \(1997\)](#) translated the calculated coseismic stress changes due to $M \geq 6.7$ earthquakes along NAF (1939-1992), into earthquake probability gains. In doing so they used an earthquake nucleation constitutive relation, which includes both permanent and transient effects of the sudden stress changes, and managed to assess and update seismic hazard for their study area. [Parsons et al. \(2000\)](#) calculated the probability of strong shaking in the vicinity of Istanbul for a time horizon of 10 and 30 years. They considered the time-dependent effect of the coseismic Coulomb stress change variations caused by the 1999 Izmit earthquake and calculated $62 \pm 15\%$ and $32 \pm 12\%$ probabilities of $PGA > 0.35g$ for the next 30 and 10 years, respectively. In a similar but far more detailed study, [Parsons \(2004\)](#) estimated time-dependent probabilities by applying different approaches incorporating stress transfer. He derived probability values for a $M \geq 7.0$ earthquake ranging from 21%-53% to take place in the Marmara Sea

region during 2004-2034. [Papaioannou and Papazachos \(2000\)](#) introduced and applied a procedure for assessing stationary and time-dependent seismic hazard for 144 broad sites (seismogenic sources) in the Aegean area. They estimated stationary seismic hazard in terms of macroseismic intensity, peak horizontal ground acceleration and velocity at each one of these 144 sites. Time dependent seismic hazard was assessed in terms of the occurrence probability of strong ground motion with macroscopic intensity greater than VII at each one of the aforementioned sites for the period 1996-2010.

[Tsapanos et al. \(2004\)](#), applied the methodology developed by [Kijko and Graham \(1998, 1999\)](#) and the PGA attenuation relation proposed by [Margaris et al. \(2001\)](#), to produce hazard maps for Greece and the surrounding areas, including 7 major cities. The levels of seismic hazard at the sites of the seven Greek cities were assessed in terms of probabilities that a given PGA value will be exceeded at least once in 1, 50 and 100 years at the sites of the cities. The new map showed that spatial distribution of seismic hazard corresponds well with the features of shallow seismicity within the examined region.

Probabilistic seismic hazard assessment in Greece was also carried out by [Tselentis and Danciu \(2010\)](#) and [Tselentis et al. \(2010\)](#), from engineering ground motion parameters and acceleration response/ elastic input energy spectra, respectively. In the first study the authors concluded with probabilistic hazard maps for the ground motion parameters estimated for a fixed return period of 475 years. From these maps the estimated values were reported for 52 Greek municipalities and additionally probabilistic macroseismic intensity maps were obtained as well. In the second paper, probabilistic hazard maps were reproduced by determining the seismic hazard at grid points covering their study region.

[Paradisopoulou \(2009\)](#) provided a new insight on seismic hazard evaluation by translating the calculated stress changes into earthquake

probabilities applying an earthquake nucleation constitutive relation, combining both permanent and transient effects. More specifically, following the methodology and formulation published by [Stein et al., 1997](#), she evaluated the probability of a strong ($M \geq 6.5$) earthquake occurrence in some of the active fault segments of the broader Aegean area, for a time horizon equal to 30 years. For the probability calculations 4 different approaches were followed. A Poisson model given the average return periods of $M \geq 6.5$ earthquakes; a conditional probability estimate ([Hagiwara, 1974](#)) assuming a lognormal distribution and given the average return periods of $M \geq 6.5$ earthquakes. The expected seismicity rates were estimated given the conditional probability incorporating the permanent stress change effect. In addition to conditional probability the permanent effect of stress changes was introduced to provoke or the inhibit time-to-failure. Then expected seismicity rates were used to estimate the conditional probability including the transient influence of stress changes and finally 3 values were obtained in each case corresponding to the minimum, average and maximum probability for a 30-year period. She concluded that in several cases there was a significant difference among the probabilities with respect to the consideration of stress effects and therefore these stress changes should not be excluded from probability calculations.

In this thesis the exceedance probability of an $M \geq 6.0$ and $M \geq 6.5$ event is estimated in the selected study areas for a 10-year time period. As stated in [Toda et al. \(2003\)](#), one can easily transform maps of the expected number (or probability) of $M \geq M_i$ events into the number (or probability) of earthquakes of any magnitude for any time period, given a magnitude-frequency relation. Here, the magnitude distribution is estimated for each sub-area (seismic source) according to a non-parametric approach rather than determining the parameters of a specified theoretical distribution (i.e. Gutenberg-Richter law). This decision was made after [Lasocki and Papadimitriou \(2006\)](#) found that

there are significant deviations from a simple power law in 3 seismic active areas of Greece (Cephalonia Transform Zone, North Aegean and Thessalia) and this fact has impact on evaluation of return periods and consequently, hazard estimation. The model free, unbounded estimation (Kijko et al., 2001; Lasocki and Orlecka-Sikora, 2008) applied in this study ensures a satisfactory agreement between the average return period estimates and actual observations (description of the method and formulation is given in Appendix D). The exceedance probabilities for $M \geq 6.0$ and $M \geq 6.5$ were estimated in each sub-area of the broader Aegean region for a time horizon of a decade, given the expected seismicity rates as they were estimated in Chapter 2. The 95% confidence intervals of probabilities were established by estimating the 95% confidence bounds for the non-parametric kernel estimator of cumulative distribution function of magnitude by the means of bootstrap resampling.

2.3 Applications

After explicitly describing the procedure of forecasting seismicity followed in this study, the results of its application in selected areas of the broader Aegean region are demonstrated. A total of 6 different sites (namely Corinth Gulf, Central Ionian Sea, South Aegean, Western Turkey, North Aegean and Thessalia) differing in seismotectonic properties were studied (Table 2.1). However, three of these sites (North Aegean, South Aegean and Western Turkey) were large enough to exhibit considerable internal inhomogeneity. The probabilistic seismicity rate evaluation that was selected for the purpose of this study is more properly applied in smaller areas as described in section 2.2.5. In order to compromise both constraints (data sufficiency and homogeneity) each one of the previously mentioned areas were further divided into 4 smaller sub-areas in which these preconditions regarding the data were fulfilled.

Table 2.1. Information on datasets and parameter values that applied in the 6 study sites and their sub-areas (given in the first column) that are studied in the present thesis. The second column shows the duration of the study periods selected, the third column the Completeness magnitude, M_c , as calculated for each application and the fourth column provides the forecasting (study) periods tested. The fifth, six and seventh columns show the Rate/State model parameter range that was estimated i.e. the stressing rate, the characteristic relaxation time and product $A\sigma$ respectively. The range of the bandwidth value selected to smooth reference and observed seismicity rates is given in eighth column.

Region	Learning Periods	M_c	Study Periods	$\dot{\tau}$ (bar/yr)	t_a (years)	$A\sigma$ (bar)	h (°)
Corinth Gulf	1970-1981	3.7	1981-1992 1992-1995 1995-1999 1999-2008 2008-2013	0.01-0.10	2.5-25	0.025-2.5	0.04-0.24
	1985-1995	3.5	1995-2008 2008-2013				
Central Ionian Sea	1973-1983	4.3	1983-1997 1997-2003 2003-2012	0.025-0.15	2-30	0.05-4.5	0.04-0.24
	1989-1997	3.6	1997-2003 2003-2012				
South Aegean 1	1971-1997	4.0	1997-2008 2008-2012	0.005-0.06	2.5-25	0.0125-1.5	0.04-0.24
	1981-1997	3.7					
South Aegean 2	1971-2004	4.3	2004-2007 2007-2012				
	1991-2004	3.9					
South Aegean 3	1991-2009	4.1	2009-2012				
	2001-2009	3.7					
South Aegean 4	1971-1996	4.4	1996-2008 2008-2012				
	1991-1996	4.1					
Western Turkey 1	1991-1999	3.7	1999a-1999b 1999b-2010	0.04-0.25	2.5-25	0.10-6.25	0.04-0.30
Western Turkey 2	1979-1992	3.8	1992-2003 2003-2005a 2005a-2005b 2005b-2010	0.01-0.08	5-30	0.05-2.4	0.04-0.24
Western Turkey 3	1987-1996	4.1	1996-2008 2008-2010	0.01-0.10	5-30	0.05-3.0	0.04-0.26
Western Turkey 4	1991-1995	3.7	1995-1999 1999-2000 2000-2002 2002-2010	0.01-0.06	5-30	0.05-1.8	0.04-0.28
North Aegean 1	1970-1981	3.5	1981-1982 1982-1983 1983-2001 2001-2012	0.005-0.08	2.5-25	0.0125-2.0	0.04-0.24
North Aegean 2		4.1	1981-1983 1983-2001 2001-2012	0.01-0.15	2.5-25	0.025-3.75	0.04-0.24
North Aegean 3		4.1	1981-1982 1982-1983 1983-2001 2001-2012	0.01-0.08	2.5-25	0.025-2.0	0.04-0.24
North Aegean 4		3.8	1981-1997 1997-2012	0.01-0.08	2.5-25	0.025-2.0	0.04-0.24
Thessalia	1970-1980	3.6	1980-1995 1995-2012	0.01-0.08	2.5-30	0.025-2.4	0.04-0.24

2.3.1 Area 1 – Corinth Gulf

2.3.1.1 Introduction

Corinth Gulf region (Fig. 2.3) is dominated by intense extensional deformation and exhibits high seismic activity, since it consists one of the most rapidly deforming continental extension areas in the Mediterranean domain. This rift has been generalized as an East-West trending, asymmetric half-graben with North-South oriented extension controlled by a series of en-echelon north dipping normal faults along the southern coast together with minor south dipping antithetic faults along its northern boundary (Roberts and Jackson, 1991; Armijo et al., 1996; Bell et al., 2008).

During the Quaternary, the Aegean extension was accelerated by the southwestward propagation of the North Anatolian fault (NAF), which has reactivated the structure of the Corinth rift approximately 1 Ma ago (Armijo et al., 1996). Presently, the rift extension is accommodated in a narrow band off-shore, presenting an extension rate that is greater in the western part (15 mm/yr) compared with the central (10 mm/yr) and the eastern part (<5 mm/yr) (e.g., Davies et al., 1997; Clarke et al., 1998; Briole et al., 2000). The total extensional deformation is related to some combination of the three following processes: back arc extension due to subduction at the Hellenic Trench (McKenzie, 1972; Doutsos et al., 1988); westward propagation of the North Anatolian fault (Taymaz et al., 1991; Armijo et al., 1996); gravitational collapse of lithosphere thickened in the Hellenides orogeny (Jolivet, 2001). Detailed descriptions of these motions can be found in Briole et al. (2000), Avallone et al. (2004) and Bernard et al. (2006).

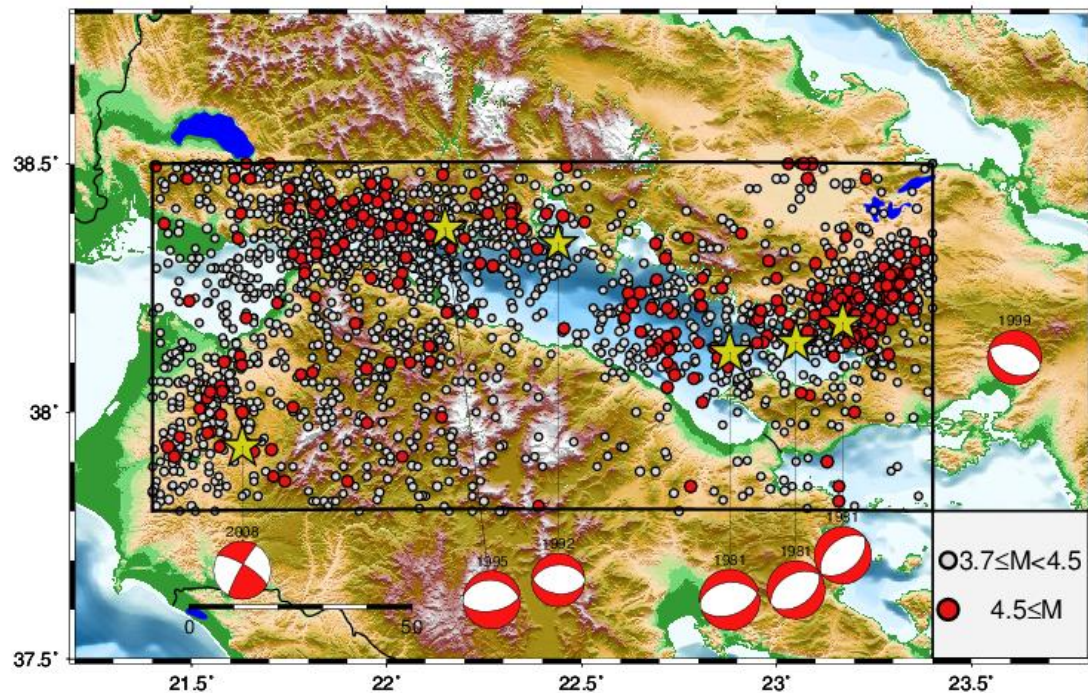


Fig. 2.3. Morphological map of the study area (indicated by the rectangle). Seismicity with $M \geq 3.7$ that occurred in the study area since 1970 is shown along with the fault plane solutions of the strongest shocks (their epicenters are depicted by yellow stars) that were taken into account for the ΔCFF calculations incorporated in the Rate/ State model.

The Corinth Gulf is not only the one of the most active sites but also the most accessible one to observations because only its central part is below the sea level (Briole et al., 2000). The highest seismic activity recently is concentrated mostly in the western part of the gulf, with considerably lower seismicity in the central part. The deployment of either temporal or permanent local dense seismological networks in the western part of the Corinth gulf has revealed a continuous high seismic activity in this area in the last two decades (Rigo et al., 1996, Hatzfeld et al., 2000; Lyon-Caen et al., 2004; Bernard et al., 2006; Pacchiani and Lyon-Caen, 2010). Information on the strong earthquakes in the Corinth Gulf, both historical and instrumental, is provided by Ambraseys and Jackson (1990, 1997), Papazachos and Papazachou (2003) and Ambraseys (2009) whereas implementations in co-seismic stress transfer was recently accomplished by Console et al. (2013).

2.3.1.2 Data

For the seismicity rate variation analysis in Corinth Gulf the data from the Hellenic Unified Seismological Network (HUSN) was elaborated. Corinth Gulf sustains one of the best monitored areas of the Aegean region, since the adequately dense National seismological network and the local morphology conduce to satisfactory azimuthal coverage, and thus low completeness magnitude threshold and considerable hypocentral accuracy. M_c was estimated for overlapping 10-year windows by the Modified Goodness-of-Fit Test (MGFT – [Leptokaropoulos et al., 2013](#)). This approach led to an almost uniform spatially M_c equal to 3.7 since 1970 (2438 events during 43 years period) and 3.5 since 1985 (2860 events for 28 years time interval). For this reason two different reference rate periods were considered: One that corresponds to the period 1970-1981 and another one which includes the data occurred from 1985 to 1995. The origin time, epicentral location, seismic moment and focal mechanism of the strongest events ($M \geq 5.9$) that were taken into account for Coulomb stress changes calculations are shown in Table 2.2. The 4 out of the 5 forecasting periods correspond to the inter-event time periods between successive strong main-shocks (1981-1992, 1992-1995, 1995-1999, 1999-2008), except for the last one that begins on 8th of June 2008 and ends on 31st of December 2012.

Table 2.2. Source parameters of the 11 earthquakes with $M \geq 5.9$ modeled for coseismic static Coulomb stress changes calculations.

Event	Date	Epicentral Coordinates	M_w	M_0 ($\cdot 10^{25}$ dyn·cm)	Focal Mechanism			Reference
					Strike($^\circ$)	Dip($^\circ$)	Rake($^\circ$)	
1981	24FEB	38.070°N 23.040°E	6.7	8.75	262	42	-80	1
1981	25FEB	38.141°N 23.089°E	6.4	3.97	241	44	-85	1
1981	04MAR	38.203°N 23.249°E	6.3	2.70	230	45	-90	1
1992	18NOV	38.340°N 22.440°E	5.9	0.85	265	43	-99	2
1995	15JUN	38.370°N 22.150°E	6.5	6.10	277	33	-76	3
1999	07SEP	38.062°N 23.537°E	6.0	0.92	115	57	-80	4
2008	08JUN	37.945°N 21.544°E	6.5	4.60	301	74	7	2

1. Taymaz et al., 1991; 2. Global CMT; 3. Bernard et al. (1997); 4. Kiratzi and Louvari (2003);

2.3.1.3 Parameters values

In this application a constant stressing rate was considered on each fault segment, uniformly distributed throughout the seismogenic layer (both along strike and dip direction), as shown in Table 2.3. The values of stressing rate at the center of each fault segment were estimated from the slip rates of these segments, as they were defined from geodetic data analysis (Reilinger et al., 2006) assuming 60% of the geodetic slip value to account for the seismic part of the secular tectonic motion (Table 2.3). The average values of $\dot{\tau}$ were found to be 0.02 – 0.085 bar/yr, nevertheless a more widespread range from 0.01 to 0.10 bar/yr was examined in this study. The characteristic relaxation time was selected to be between 2.5–25 years (see section 2.2.4). The previously mentioned values of stressing rate and characteristic time yield to a wide range of $A\sigma$ values, between 0.025 and 2.5 bars. The bandwidth was given values between 0.04° to 0.24° (or alternatively radii of 4.5km to 26.7km), whereas according to equation (2.17) an $h \sim 0.07^\circ$ was suggested. All ΔCFF calculations were done at the depth of 9 km, which represents approximately the nucleation depth in this area (Karakostas et al., 2012). The effective friction coefficient was set $\mu' = 0.4$ whereas the shear modulus, G , and Poisson's ratio, ν , were fixed at $3.3 \cdot 10^5$ bar and 0.25, respectively.

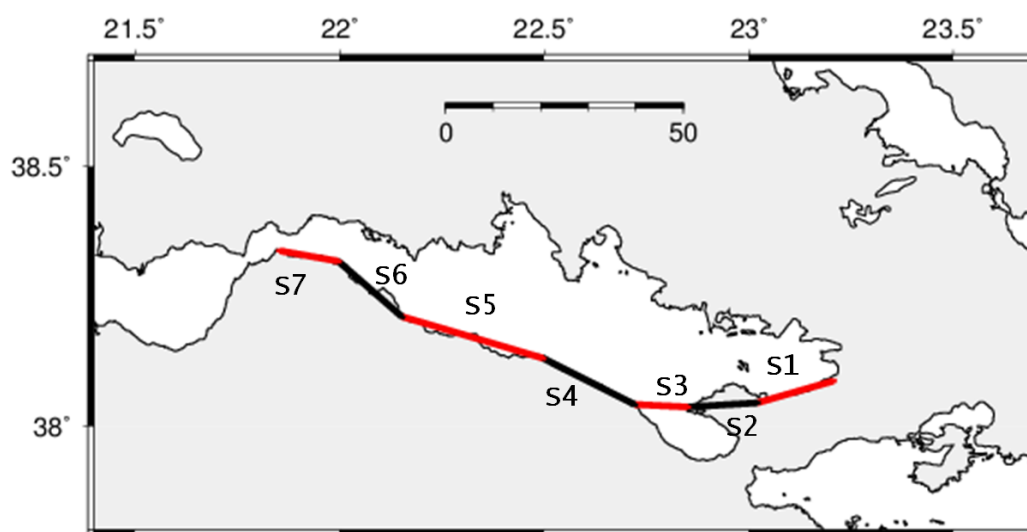


Fig. 2.4. Major fault segments in Corinth Gulf and their code names (Table 2.3).

Table 2.3. Information on the major regional fault segments (Fig. 2.4) on which tectonic loading is considered for the Rate/State model calculations. Columns represent in turn: the code name of segment, its boundaries, strike, dip, rake, length, width, sense of slip (N: for normal, Ob: for oblique), slip components along strike (positive for sinistral slip) and vertical to it (positive for normal slip) and the stressing rate.

SN	Fault Boundaries				Strike (°)	Dip (°)	Rake (°)	Length (km)	Width (km)	Type of slip	SS (mm/y)	DS (mm/yr)	Stressing Rate (bar/yr)
	°N	°E	°N	°E									
S1	38.087	23.207	38.045	23.021	244	44	-85	16.8	21.6	N	1.2	-5.2	0.0400 – 0.0850
S2	38.045	23.021	38.037	22.851	268	45	-80	14.4	21.2	N	1.2	-5.2	0.0400 – 0.0850
S3	38.037	22.851	38.131	22.721	271	45	-80	11.5	21.2	N	1.0	-5	0.0400 – 0.0675
S4	38.131	22.721	38.211	22.497	295	30	-80	21	30	N	0.8	-4.4	0.0300 – 0.0600
S5	38.211	22.497	38.317	22.152	293	30	-95	31.2	30	N	0.4	-4.4	0.0231 – 0.0463
S6	38.317	22.152	38.337	21.854	308	34	-76	17.5	27	N	0.6	-4.2	0.0307 – 0.0512
S7	38.337	21.854	38.305	21.748	275	34	-70	12.7	27	Ob	1.8	-2.4	0.0181 – 0.0295

2.3.1.4 Results – Discussion

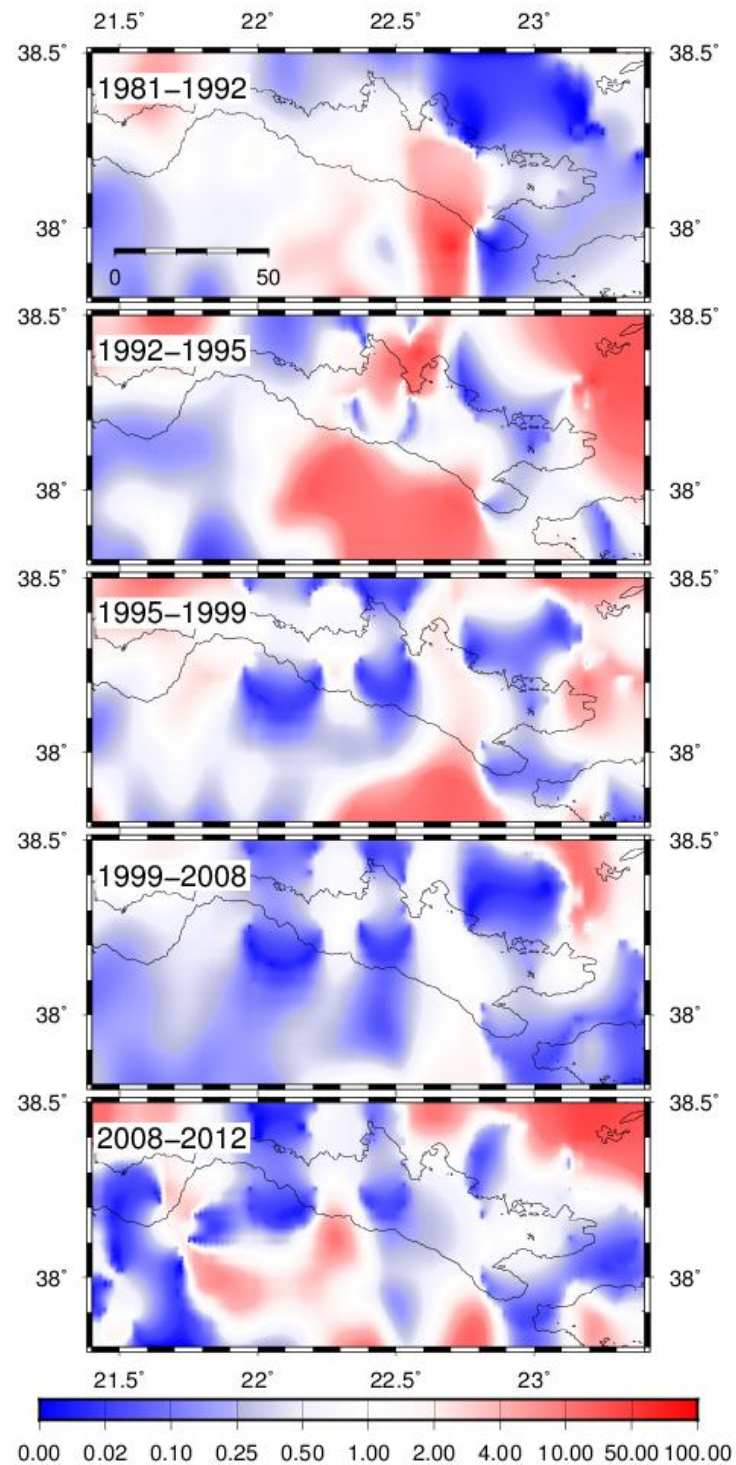


Fig. 2.4. Ratio of expected/observed seismicity rates for Corinth Gulf area, with reference seismicity rate obtained from 1970-1981 ($M>3.7$). Red colors show that the expected values are overestimated in comparison with the observed ones whereas blue colors show higher observed seismicity rates than the simulated ones. White areas correspond to ratio value between 0.5-2, suggesting sufficient model performance. Parameter values applied are: $h=0.07^\circ$, $\dot{\tau}_r = 0.03\text{bar}\cdot\text{yr}^{-1}$ and $t_a=5\text{yrs}$ $A\sigma=0.15\text{bar}$).

Fig 2.4 shows the comparison of the Rate/State modeling results with the observed seismicity rates during the inter-event time periods between the successive strong events shown in Table 2.2. Reference seismicity rate is calculated from the period 1970-1981. For the first 2 study periods (1981-1992 and 1992-1995) sites where the forecasted seismicity rates are either underestimated or overestimated are both evident. The ratio of expect/observed seismicity rates is generally closer to 1 in the central and western part of the study area. The next two periods (1995-1999 and 1999-2008) demonstrate extended areas where the model forecasts seismicity rates similarly with or slightly lower than the observed ones. In the last study period (2008-2012) the pattern quality is identical with the one of the first two periods, although there are fewer cells where expected seismicity rates are higher than the observed ones. The qualification of the model performance is given in Fig. 2.5. It is shown that the two first periods (1981-1992 and 1992-1995) the correlation coefficient is lower than 0.5 with an exception in the case of high bandwidth values ($h > 0.12^\circ$) which are in general inappropriate for the given dataset. On the other hand, for the subsequent periods 1995-1999 and 1999-2008 there is much stronger correlation between real and synthetic seismicity rates reaching up to 80%. The last study period (2008-2013) demonstrates a PCC value of approximately 0.5 and it is the most sensitive together with 1992-1995 in bandwidth fluctuation. Assuming only positive ΔCFF areas doesn't lead to a considerable influence in none of the cases and the correlation is only changed by less than 10%. Stressing rate between 0.02 and 0.03 bars/yr and characteristic relaxation time of 5yrs seems to provide the best fitting of the model to the observed data, especially for the periods where the PCC is sufficiently high (1995-1999, 1999-2008).

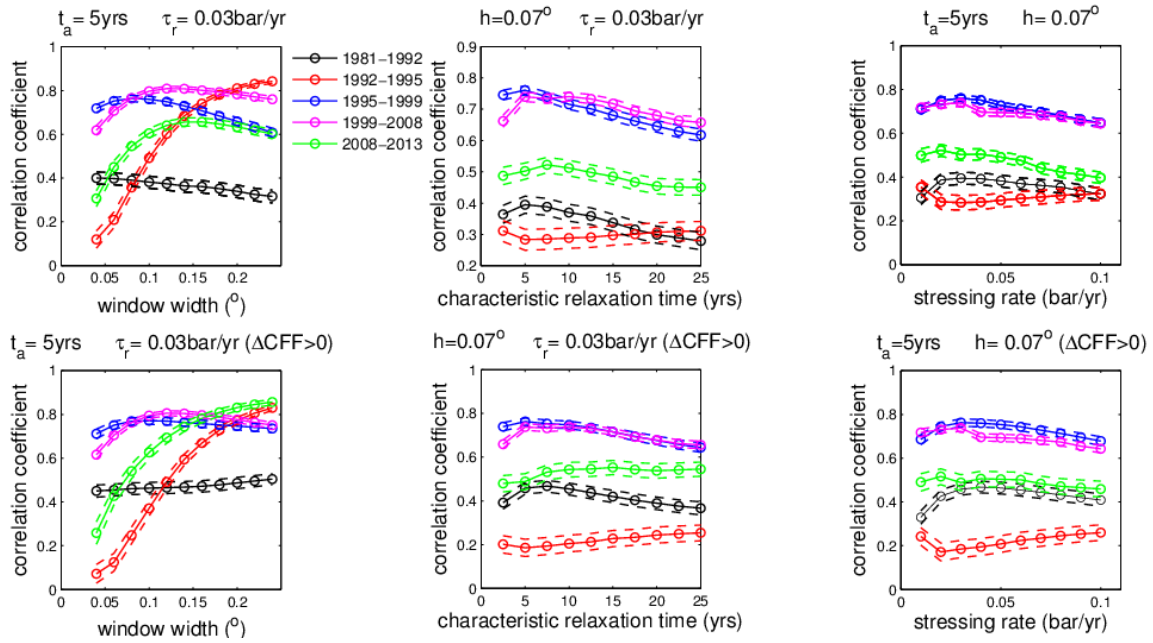


Fig. 2.5. Quantitative evaluation of the difference between observed-synthetic seismicity rates during the inter-event time periods for Corinth Gulf area (colored lines). Solid lines indicate the value of Pearson linear Correlation Coefficient (PCC) whereas its 95% confidence intervals for each coefficient are also depicted by fainter lines. The upper frame figures yielded from the entire data set, whereas the figure below by taking into account only those cells experiencing positive ΔCFF . Reference seismicity rate corresponds to the period 1970-1981.

The second approach regards seismicity rates forecasted after the Aigion, 15th June 1995 earthquake, and assuming reference seismicity rate estimated from 1985 to 1995 (Fig. 2.6). Now the ratio of expected/observed rate is close to unity in larger number of cells in comparison with the previous approach (Fig. 2.4). There are still some areas where the forecasted rates are underestimated in all the testing periods. Moreover, the expected rates are overestimated in a considerable fraction of the study area for the period 2008-2012. The correlation coefficient is also improved in all cases when the reference seismicity rate is estimated from a more recent period (fig. 2.7): PCC is almost constant above 75% for the first two forecasting periods (1995-1999 and 1999-2008) and reaches up to 90%, whereas for 2008-2013 it is close to 60%. These values of PCC are also slightly improved when only positive ΔCFF are considered for 1992-1995 and 2008-2013 while they are almost

identical for the second period (1999-2008). It is also evident here that the highest PCC is generally achieved for lower values of t_a and $\dot{\tau}_r$.

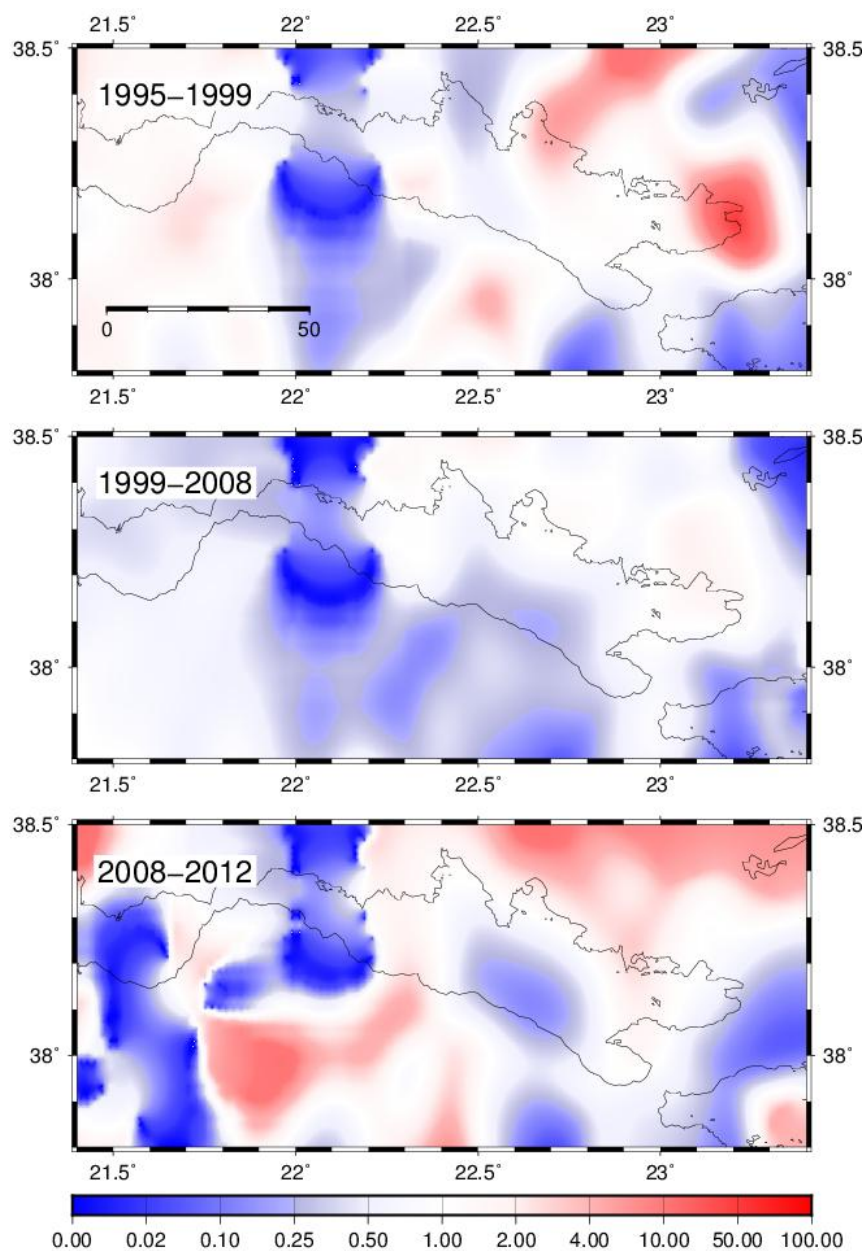


Fig. 2.6. Ratio of expected/observed seismicity rates for Corinth Gulf area, with reference seismicity rate obtained from 1985-1995 ($M>3.5$). Red colors show that the expected values are overestimated in comparison with the observed ones whereas blue colors show higher observed seismicity rates than the simulated ones. White areas correspond to ratio value between 0.5-2.0, suggesting sufficient model performance. Parameter values applied are: $h=0.07^\circ$, $\dot{\tau}_r=0.03\text{bar}\cdot\text{yr}^{-1}$ and $t_a=5\text{yrs}$ ($A\sigma=0.15\text{bar}$).

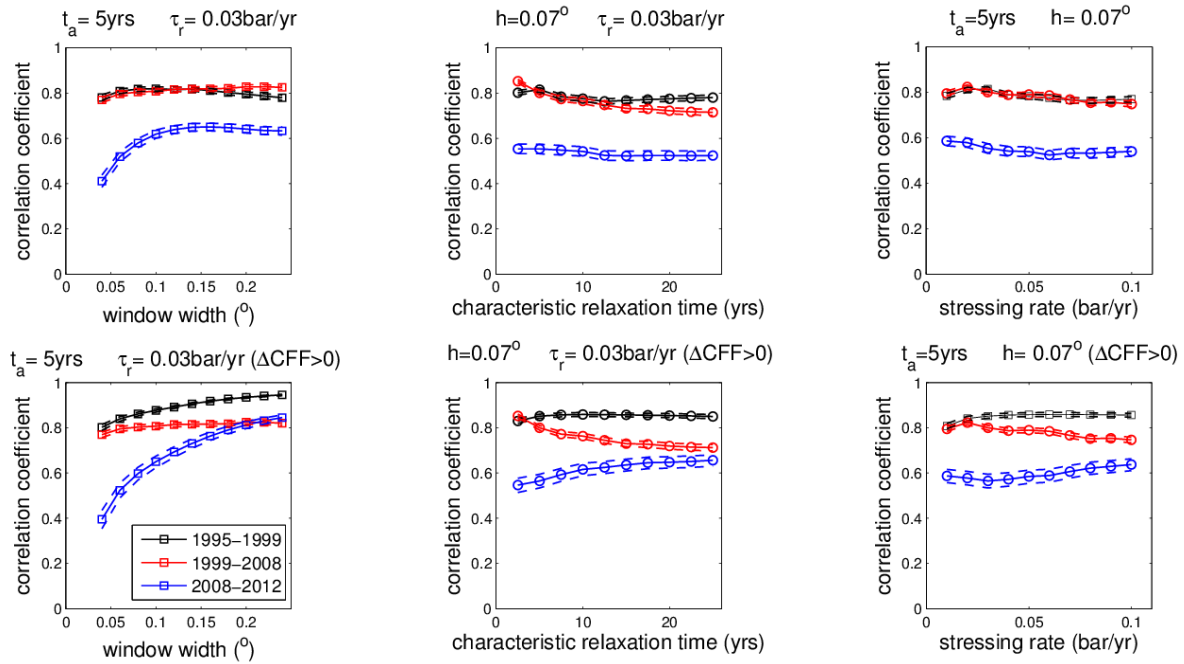


Fig. 2.7. Quantitative evaluation of the difference between observed-synthetic seismicity rates during the inter-event time periods for Corinth Gulf area (colored lines). Solid lines indicate the value of Pearson linear Correlation Coefficient (PCC) whereas its 95% confidence intervals for each coefficient are also depicted by fainter lines. The upper frame figures yielded from the entire data set, whereas the figure below by taking into account only those cells experiencing positive ΔCFF . Reference seismicity rate corresponds to the period 1985-1995.

2.3.1.5 Contribution to Seismic Hazard Assessment

The expected seismicity rates after 2008 were estimated by considering the influence of coseismic (due to $M \geq 5.9$ earthquakes) and tectonic stress changes on the reference seismicity rates during 1970-1981 ($M \geq 3.7$, Fig. H1). The unbounded non-parametric magnitude distribution of the 2438 events ($M \geq 3.7$ during 1970-2012) was then considered in connection with the averaged estimated expected seismicity rate, to calculate the exceedance probabilities for the next decade. These probabilities were found equal to 75.7% (with 95% confidence bounds at 73.8% - 77.9%) and 42.6% (with 95% confidence bounds at 39.2% - 48.8%) for an earthquake with magnitude higher than 6.0 and 6.5, respectively. As shown in figure H1, the expected rates and consequently the exceedance probabilities are not spatially uniform. The highest probabilities are calculated for the western part of the area, whereas in the central and eastern part these probabilities are expected

considerably lower. The stress changes associated with the mostly recent and strongest events (1995, $M=6.5$; 2008, $M=6.4$) have produced a characteristic pattern of expected rates (both increased and decreased) in the eastern part of Corinth Gulf. It is noteworthy that the epicenter of the first strong ($M=5.5$) earthquake of the 2010, Efpalio sequence (see chapter 3) was located in enhanced predicted rate (and high probability) area.

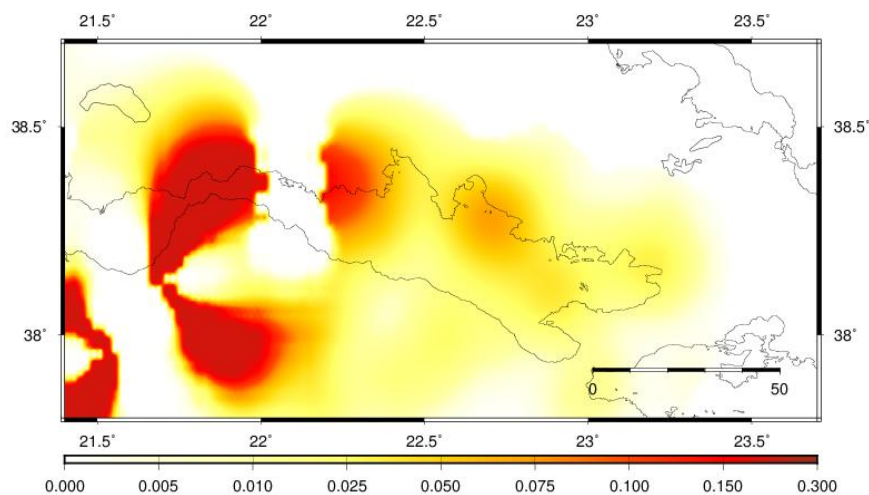


Fig. H1. Snapshot of the expected seismicity rates ($M \geq 3.7$) estimated for the period after 2008 in the Corinth Gulf.

2.3.2 Area 2 – Central Ionian Sea

2.3.2.1 Introduction

The Central Ionian area (Fig. 2.8), namely the Cephalonia and Lefkada Islands, constitutes the most active zone of shallow seismic activity in the Aegean and nearby regions. It consists of the transition zone between the Hellenic subduction to the south and the continental collision between the Apulian and the Aegean plates to the north. [McKenzie \(1978\)](#) indicated the existence of transform motions, mainly interpreting the orientation of slip vectors from a few focal mechanisms that were available at that time. The dextral strike-slip character of the Cephalonia Transform Fault Zone (CTFZ) was first evidenced by [Scordilis et al. \(1985\)](#) and then was further supported by [Kiritzi and Langston \(1991\)](#) and [Papadimitriou \(1993\)](#).

The CTFZ is the most prominent feature of tectonic origin in the study area sustaining a dextral strike-slip fault system that accommodates frequent strong earthquakes, clustered in space and time possibly due to the stress transfer between adjacent fault segments (Papadimitriou 2002; Karakostas and Papadimitriou, 2010). It consists of two main segments, namely the Cephalonia and Lefkada segments (Papazachos *et al.* 1998, Louvari *et al.* 1999) that differ slightly in their strike and the magnitude of the maximum observed earthquake. CTFZ follows the submarine Cephalonia valley west of the island chain from Lefkada to Cephalonia and separates the slowly northward- and northwestward-moving (<5 mm/yr with respect to Eurasia) northern Ionian Islands from the rapidly southwestward moving (7–30 mm/yr) central Ionian Islands (Peter *et al.*, 1998; Hollenstein, 2006; Hollenstein, 2008). Papadimitriou and Papazachos, (1985) showed that the occurrence frequency for the stronger ($M > 6.5$) events in the study area is almost constant during the last four centuries with one such shock per decade. The maximum observed earthquake magnitude in Cephalonia equals to 7.4 and in Lefkada to 6.7 (Papazachos and Papazachou, 2003). Moreover moderate magnitude events are also very frequent, oftentimes located onshore, constituting an additional threat from the seismic hazard view point.

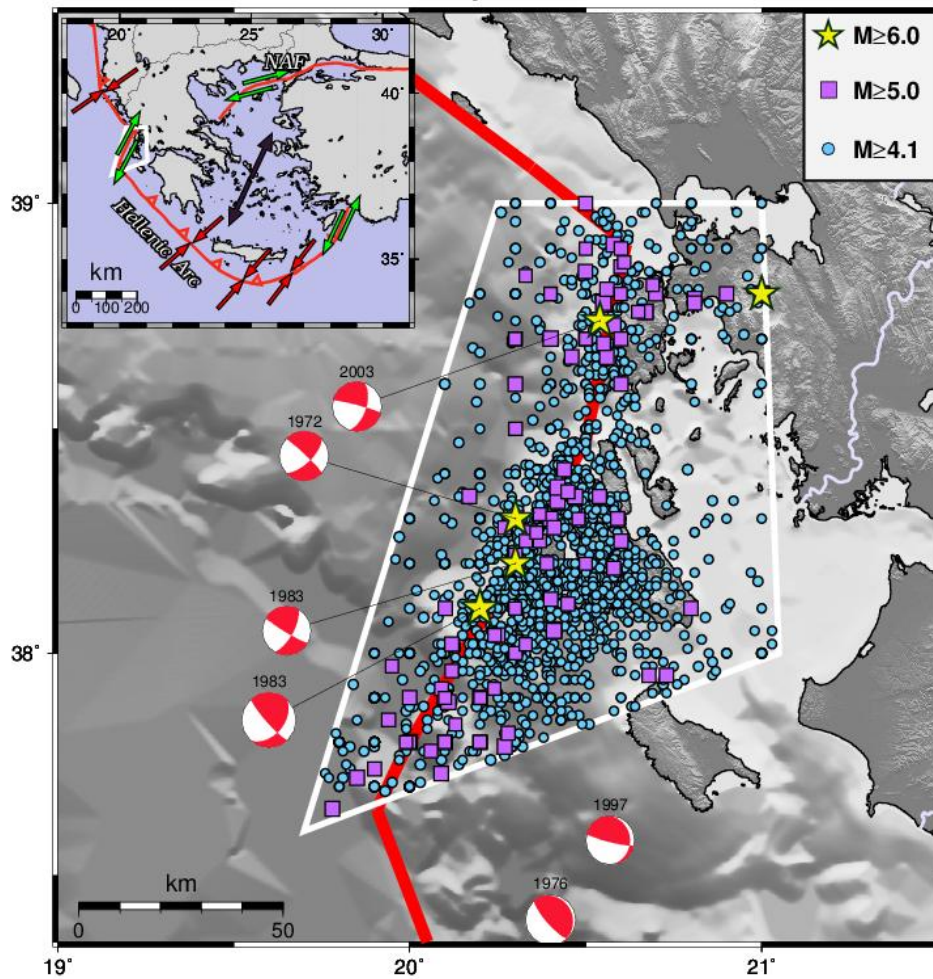


Fig. 2.8. Morphological map of the study area (indicated by the white polygon). Seismicity with $M \geq 4.1$ in the study area since 1970 is shown along with the fault plane solutions of the strongest shocks (their epicenters are depicted by yellow stars) that were taken into account for the ΔCFF calculations incorporated in the Rate/State model. Note that two of the main shocks occurred outside the study area and they are connected with thrust faulting, but they took place close enough to alter the regional stress field.

2.3.2.2 Data

The data used in the following analysis come from the catalog of the Hellenic Unified Seismological Network (HUSN). This catalog demonstrates diverse completeness magnitude thresholds since 1964 due to the continuous evolution and expansion of the National seismological network. M_c was estimated for overlapping 10-year time windows (per 5 years) by the means of the MGFT technique (Leptokaropoulos et al., 2013). According to the results derived from this method, 2 datasets were selected for seismicity rate change calculations, exhibiting different sample size and duration: The first dataset is

complete above $M=4.3$ since 1973 (875 events during 40 years) whereas the second one includes earthquakes since 1989 with $M_c=3.6$ (2071 events during 24 years). Information on the source models of the strongest ($M \geq 6.0$) events that were taken into account for Coulomb stress changes calculations is given in Table 2.4. The forecasting periods correspond to the inter-event time intervals between successive strong main shocks (1983-1997, 1997-2003), except for the last one that starts after the 14th August 2003 Lefkada earthquakes and terminates on 31st of December 2012.

Table 2.4. Source parameters of the 11 earthquakes with $M \geq 6.0$ modeled for coseismic static Coulomb stress changes calculations.

Event	Date	Epicentral Coordinates	M_w	M_0 ($\cdot 10^{25}$ dyn·cm)	Focal Mechanism			Reference
					Strike($^\circ$)	Dip($^\circ$)	Rake($^\circ$)	
1983	17JAN	38.030°N 20.220°E	6.8	20.8	39	45	175	1
1983	23MAR	38.290°N 20.260°E	6.1	1.92	31	69	174	1
1997a	18NOV	37.420°N 20.619°E	6.6	6.46	354	20	159	2
1997b	18NOV	37.360°N 20.650°E	6.1	1.70	354	20	159	2
2003	14AUG	38.744°N 20.539°E	6.3	2.90	15	80	170	3

1. Papadimitriou et al. (1993); 2. Kiratzi and Louvari (2003); 3. Papadimitriou et al. (2006)

2.3.2.3 Parameters values

The stressing rate was considered as constant and uniformly distributed throughout the seismogenic layer. The estimated values of the stressing rate at the center of each one of the major fault segments (fig. 2.9), were calculated from the respective slip rates as they were defined from geodetic data analysis (McClusky et al., 2000; Reilinger et al., 2006). These stressing rates exhibit a significant variation between 0.06bar/yr to 0.16bar/yr (Table 2.5). Following this observation, the values of $\dot{\tau}$ applied in Rate/State modeling were selected to cover a range from 0.025 – 0.15 bar/yr. The characteristic relaxation time is ranging between 2–30 years (see section 2.2.4). The previously mentioned values of stressing rate and characteristic time yield product $A\sigma$ values ranging between 0.05 and 4.5 bars. The smoothing parameter was given values from 0.04 $^\circ$ to 0.24 $^\circ$ (or alternatively radii of 4.5km

to 26.7km), whereas according to equation (2.17) an $h \sim 0.13$ for $M \geq 4.3$ and $h \sim 0.06$ for $M > 3.6$ was suggested. All ΔCFF calculations were accomplished at the depth of 8 km in agreement with [Karakostas et al. \(2004\)](#). The effective friction coefficient was set $\mu' = 0.4$ whereas the shear modulus, G , and Poisson's ratio, ν , were fixed at $3.3 \cdot 10^5$ bar and 0.25, respectively.

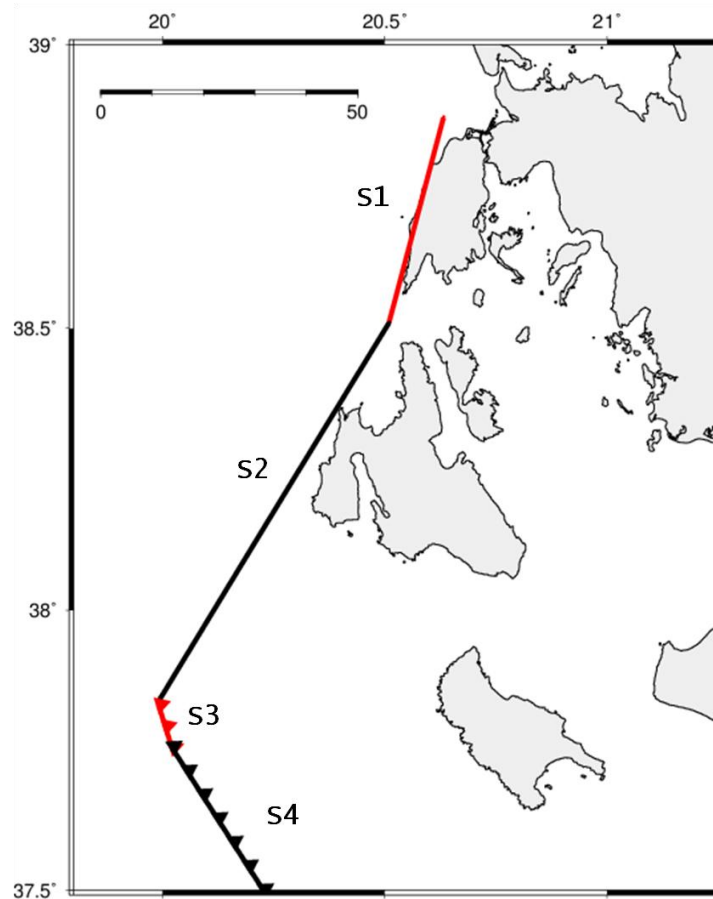


Fig. 2.9. Major fault segments in Cephalonia Transform Fault Zone and their code names (Table 2.5.).

Table 2.5. Information on the major regional fault segments (figure 2.9) on which tectonic loading is considered for the Rate/State model calculations. Columns represent: the code name of segment, its boundaries, strike, dip, rake, length, width, sense of slip (T: for Thrust, RL: for Right Lateral), slip components along strike (positive for sinistral slip) and vertical to it (positive for normal slip) and the stressing rate.

SN	Fault Boundaries				Strike (°)	Dip (°)	Rake (°)	Length (km)	Width (km)	Type of slip	SS (mm/y)	DS (mm/yr)	Stressing Rate (bar/yr)
	°N	°E	°N	°E									
S1	38.871	20.632	38.509	23.509	18	59	-180	43.2	17.9	RL	6.0	0.0	0.1257
S2	38.509	23.509	37.838	19.991	39	45	-180	89.5	23.3	RL	2.5	0.0	0.1620
S3	37.838	19.991	37.755	20.021	336	45	-85	11.0	21.6	T	2.0	-11.0	0.0871
S4	37.755	20.021	37.497	20.229	295	30	-80	35.6	21.2	T	1.0	-9.0	0.0606

2.3.2.4 Results – Discussion

First the results derived considering reference seismicity rate during 1973-1983 are presented (Fig. 2.10) In the first testing period (1983-1997) there is significant overestimation of the expected seismicity rates in the northern part of the study area, whereas a generally good agreement between observed and simulated seismicity rates is evident in the central part. The PCC (Fig. 2.11) in this period (1983-1997) is between 0.4-0.6 and it roughly exceeds 0.6 if only positive Δ CFF areas are considered. The second period (1997-2003) indicates overestimation of the simulated seismicity rates in significant part of the study area, mostly on the north and central region. The correlation coefficient is also fluctuating between 0.4-0.6 and it does not seem to get improved when positive Δ CFF cells approach is followed. For the last period the expected seismicity rates are once more generally higher than the observed ones, with some exceptions in the central part of the area. The correlation is also weak with the PPC values close to 0.4 which are getting even lower when areas inside positive stress changes lobes are taken into account.

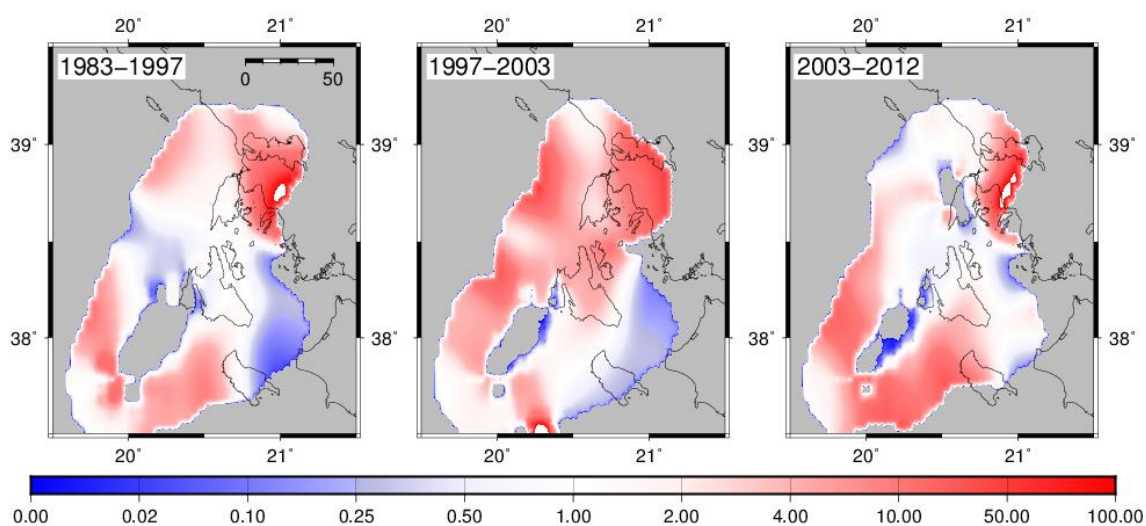


Fig. 2.10. Ratio of expected/observed seismicity rates for Cephalonia Transform Fault Zone, with reference seismicity rate obtained from 1973-1983 ($M>4.3$). Red colors show that the expected values are overestimated in comparison with the observed ones whereas blue colors show higher observed seismicity rates than the simulated ones. White areas correspond to ratio value between 0.5-2, suggesting sufficient model performance. Parameter values applied are: $h=0.13^\circ$, $t_a=5$ yrs and $\dot{\tau}_r=0.03$ bar \cdot yr $^{-1}$ ($\Delta\sigma=0.15$ bar).

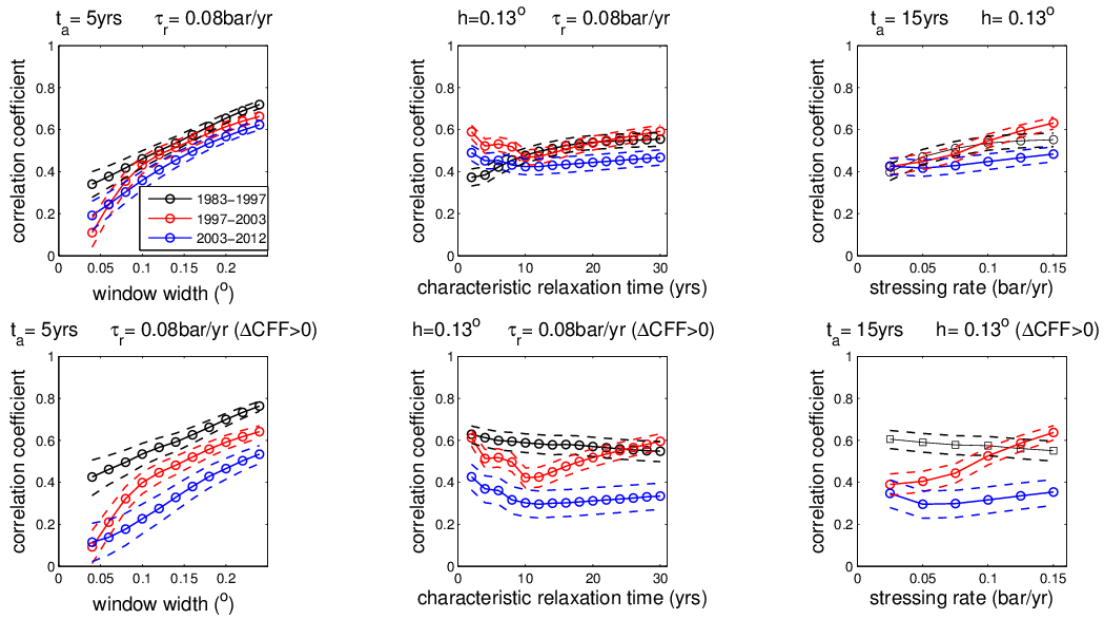


Fig. 2.11. Quantitative evaluation of the difference between observed-synthetic seismicity rates during the inter-event time periods for Cephalonia Transform Fault Zone (colored lines). Solid lines indicate the value of Pearson linear Correlation Coefficient (PCC) whereas its 95% confidence intervals for each coefficient are also depicted by fainter lines. The upper frame figures yielded from the entire data set, whereas the figure below by taking into account only those cells experiencing positive ΔCFF . Reference seismicity rate corresponds to the period 1973-1983.

However, the model performance is much more different when reference seismicity rate with $M \geq 3.6$ for the period 1989-1997, is assumed (Fig. 2.12). In this approach the areas where the ratio expected/observed seismicity rate is approximately 1 are significantly extended and even if a bias towards lower values is present, it is still much lower than in figure 2.10. This is also confirmed from the quantitative analysis (Fig. 2.13) where the PCC exceeds 70% and 80% for the first (1997-2003) and the second (2003-2012) period, respectively, regardless the influence of negative stress changes. These results indicate that smaller magnitude seismicity leads to sufficient forecasting ability, even if the influence on stress changes of past strong events (before 1997) is neglected. On the other hand, it seems that an 11-year period (1973-1983) cannot be considered to retrieve reliable reference seismicity rate (Fig. 2.10). This is because the catalog corresponds to this period does not contain an adequate number of $M \geq 4.3$ earthquakes, so that it cannot be considered as representative for the regional seismic activity.

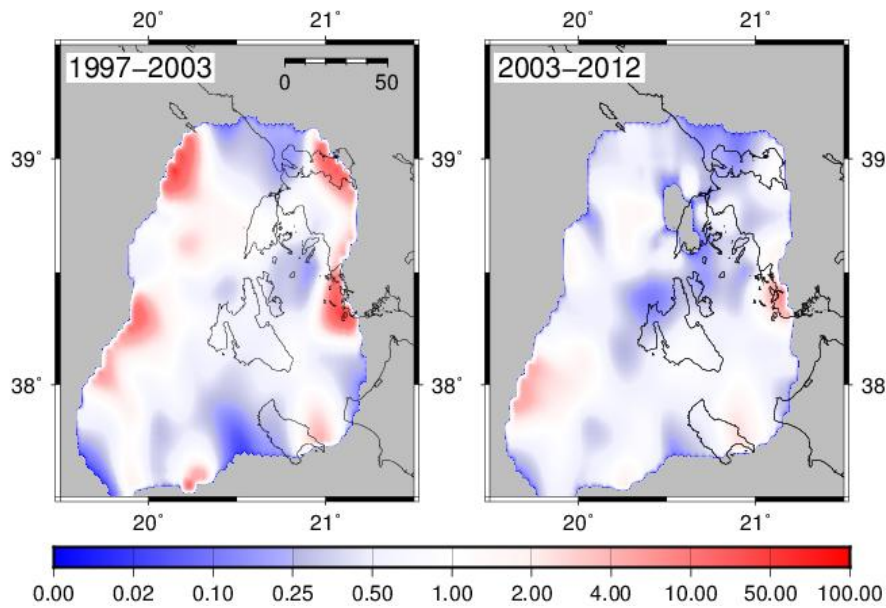


Fig. 2.12. Ratio of expected/observed seismicity rates for Cephalonia Transform Fault Zone, with reference seismicity rate obtained from 1989-1997 ($M>3.6$). Red colors show that the expected values are overestimated in comparison with the observed ones whereas blue colors show higher observed seismicity rates than the simulated ones. White areas correspond to ratio value between 0.5-2, suggesting sufficient model performance. Parameter values applied are: $h=0.07^\circ$, $t_a=5\text{yrs}$ and $\dot{\tau}_r=0.03\text{bar}\cdot\text{yr}^{-1}$ ($A\sigma=0.15\text{bar}$).

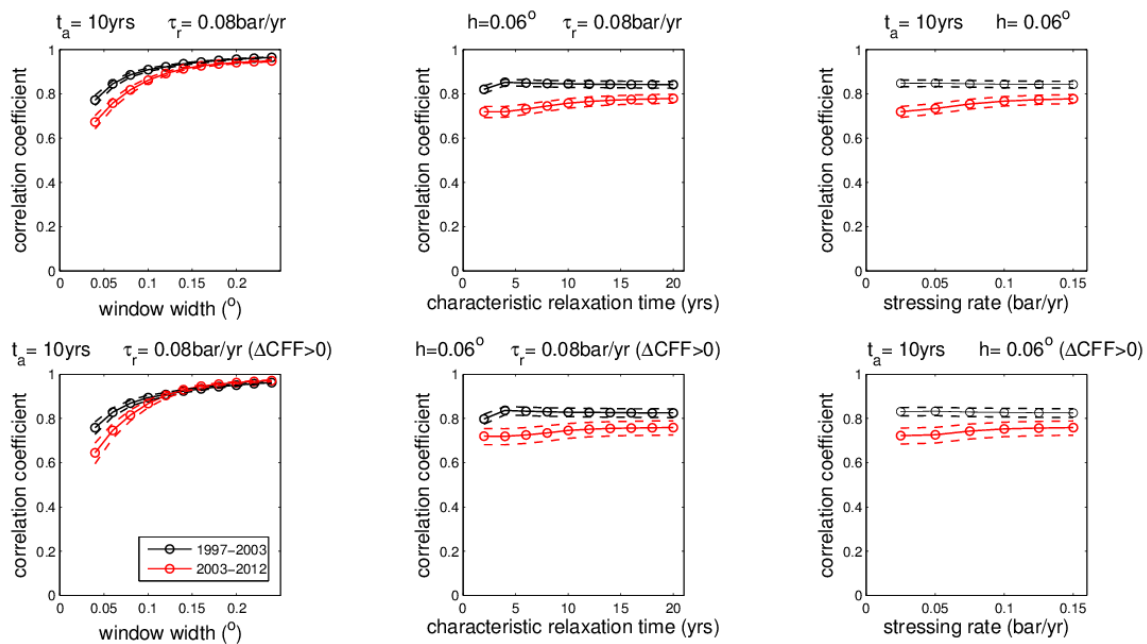


Fig. 2.13. Quantitative evaluation of the difference between observed-synthetic seismicity rates during the inter-event time periods for Cephalonia Transform Fault Zone (colored lines). Solid lines indicate the value of Pearson linear Correlation Coefficient (PCC) whereas its 95% confidence intervals for each coefficient are also depicted by faint lines. The upper frame figures yielded from the entire data set, whereas the figure below by taking into account only those cells experiencing positive ΔCFF . Reference seismicity rate corresponds to the period 1989-1997.

2.3.2.5 Contribution to Seismic Hazard Assessment

The expected seismicity rates after 2012 were estimated by considering the influence of coseismic (due to $M \geq 6.0$ earthquakes) and long term stress changes on the reference seismicity rates during 1989-1997 ($M \geq 3.6$, Fig. H2). The unbounded non-parametric magnitude distribution of the 2070 events ($M \geq 3.6$ during 1989-2012) was then considered in connection with the averaged estimated expected seismicity rate, to calculate the exceedence probabilities for the next decade. These probabilities were found equal to 49.0% (with 95% confidence bounds at 25.8% -68.2%) and 23.2% (with 95% confidence bounds at 5.0% - 40.1%) for an earthquake with magnitude higher than 6.0 and 6.5, respectively. As shown in figure H2, the expected rates are estimated to be high in the entire region. However, the highest probabilities are expected close to the western shore of Lefkada and Cephalonia Islands. Both areas accommodate fault segments that have repeatedly failed during the last centuries causing major damage and numerous casualties. In section 2.4 it is shown that the recent $M=6.1$ January 2014 earthquake took place in such enhanced seismicity rate areas in Cephalonia Island.

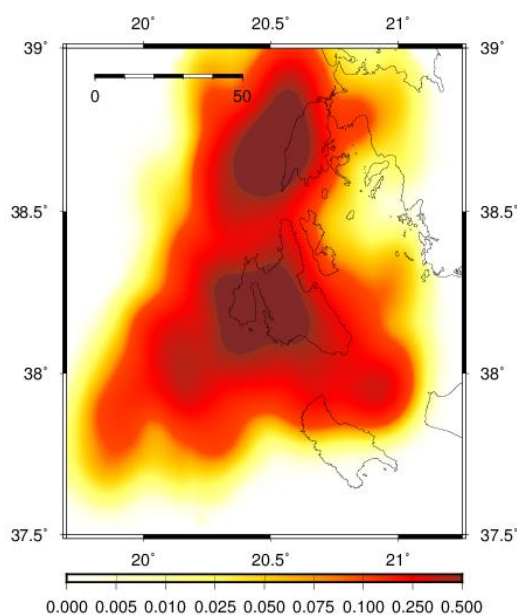


Fig. H2. Snapshot of the expected seismicity rates ($M \geq 3.6$) estimated for the period after 2012 in the Central Ionian Area.

2.3.3 Area 3 – South Aegean (4 sub-areas)

2.3.3.1 Introduction

The investigation of earthquake production rate changes resulted from the regional stress field evolution in the seismogenic sources along the Hellenic Arc is attempted in this section. The Hellenic Arc constitutes one of the most rapidly deforming parts of the Alpine-Himalayan belt. Intense shallow and intermediate depth seismic activity is known from both historical reports and instrumental recordings encompassing frequent devastating earthquakes (Fig. 2.14). The strongest earthquake (M8.3) ever reported in the Mediterranean region is associated with the southwestern part of the Hellenic Arc, near Crete Island, in AD 365 (Papazachos and Papazachou, 2003; Papadimitriou and Karakostas, 2008; Shaw, 2012).

The subduction zone extends over a distance of approximately 1000km between the two Subduction-Transform Edge Propagators (STEP) of the dextral Cephalonia Transform Fault Zone to the northwest (Scordilis et al., 1985) and the sinistral Rhodos fault to the east (Papazachos and Papazachou, 2003). The existence of a Wadati-Benioff zone along the Hellenic Arc was first recognized by Papazachos and Comninakis (1971) and it was further confirmed from seismic hypocenter studies (Hatzfeld and Martin, 1992; Papazachos et al., 2000; Piromallo and Morelli, 2003; Suckale et al., 2009; Pearce et al., 2012). This zone is gently dipping at an angle of 30° at its shallow part until 100km depth and then is descending with a steeper angle of 45°. Seismic tomography studies also illustrated the deeper branches of the subducted lithosphere down to a depth of 600 km (Spakman et al., 1988, Papazachos and Nolet, 1997). Both compressive and extensional regimes are evident in this seismotectonically complex region. Thrust faulting prevails because of the convergence between Eurasian and African lithospheric plates, (Papazachos et al., 1998) at a rate of about 4cm/yr (Clarke et al., 1998;

McClusky et al., 2000), with the maximum compression axis being oriented NE-SW. The high deformation rates are adequate to induce a roll-back at the Hellenic Trench leading to significant extension of the overriding plate with the back-arc stretching direction being oblique to the trench roll-back direction (LePichon and Angelier, 1979). As a result, E-W striking normal faulting with N-S oriented T-axis also occurs in the back-arc region, whereas N-S striking normal faulting with E-W extension is present parallel to the arc. Finally, strike slip faults with reverse components are evident in the subducting plate with the T-axis trending parallel to the dip of the Wadati-Benioff zone and the maximum compression being parallel to the arc (Taymaz et al., 1991; Papazachos and Kiratzi, 1996; Papazachos et al., 1998; Yolsal-Çevikbilen and Taymaz, 2012).

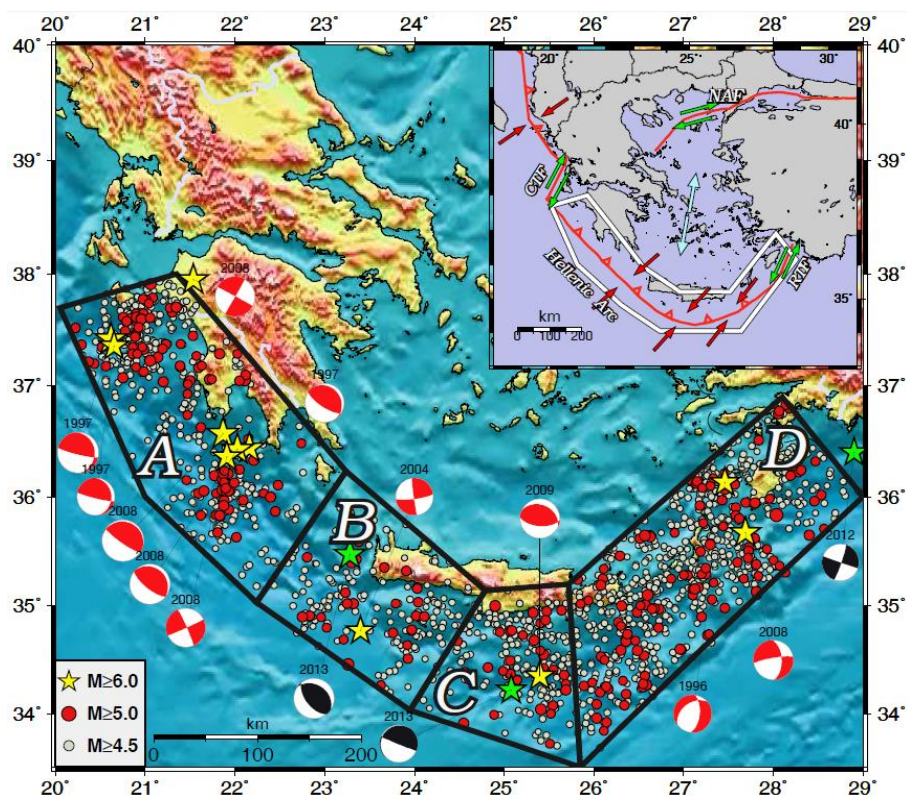


Fig. 2.14. Morphology and spatial distribution of earthquake epicenters since 1971 along the Hellenic Subduction Zone. The 4 sub-areas (A-D) demonstrate different data density and completeness level. The strongest ($M \geq 6.0$) earthquakes' fault plane solutions are also shown as lower hemisphere (red - before June 2012, black - after June 2012) projection and their epicenters are depicted by stars. The inset shows the main regional seismotectonic features: The subduction zone (Hellenic Arc), the Rhodes Transform Fault - RTF and the Cephalonia Transform Fault - CTF at the southeastern and western termination of the Hellenic arc and the North Anatolian Fault - NAF. The white polygon indicates the study area.

2.3.3.2 Data

The study area (Fig. 2.14) was too large to be treated throughout as one, for two reasons: Firstly, it comprises areas where deformation style is spatially differentiating and secondly because the smoothing technique we adopted in our analysis cannot be applied in large areas with significantly diverse data density. To compromise both constraints explained in Section 2.3, the study region was divided into 4 sub-areas (A-D in Fig. 2.14), which exhibit identical seismotectonic features and seismicity density. In order to overcome uncertainties regarding the epicentral locations especially before 1981 (when the first telemetric seismic National Network was enhanced) and secure lower completeness magnitude threshold, two reference rate periods (or learning periods) are tested in each one of the 4 selected sub-areas: one period with longer duration and higher magnitude threshold (and thus smaller sample size) and another one exhibiting shorter duration but lower completeness magnitude. Shallow seismicity at focal depths of less than 60km that occurred in the study area since 1971 was considered. Then the completeness magnitude, M_c , was separately evaluated for each sub-area and for 10-year time windows since 1971, by the MGFT method proposed by [Leptokaropoulos et al. \(2013\)](#). The older periods (1971-1981) were preferred unless there was significantly higher number of events in a more recent period (after 1981), such that the finally selected datasets containing sufficient data and having as long duration as possible for being more representative for seismicity properties manifestation. Eventually two learning periods, shown in grey cells in Table 2.6, with different duration and M_c were considered to calculate the reference seismicity rates for each sub-area to balance between large sample size and adequate time span. The source parameters of the 11 earthquakes used to compute coseismic ΔCFF in the current analysis are shown in Table 2.7.

Table 2.6. Properties of the data sets selected for each sub-area. Model applications were performed for the periods shown in gray cells.

Area A	Mc	Events	Area B	Mc	Events	Area C	Mc	Events	Area D	Mc	Events
1971-1980	4.0	3430	1971-1980	4.3	496	1971-1980	4.4	372	1971-1980	4.4	1334
1981-1990	3.7	7308	1981-1990	4.2	493	1981-1990	4.4	297	1981-1990	4.4	1128
1991-2000	3.6	7089	1991-2000	3.9	974	1991-2000	4.1	567	1991-2000	4.1	1810
2001-2012	3.6	5037	2001-2012	3.7	1068	2001-2012	3.7	904	2001-2012	3.7	1742

Table 2.7. Source parameters of the 11 earthquakes with $M \geq 6.0$ modeled for coseismic static Coulomb stress changes calculations.

Event	Date	Epicentral Coordinates	M_w	M_0 ($\cdot 10^{25}$ dyn-cm)	Focal Mechanism			Reference
					Strike($^\circ$)	Dip($^\circ$)	Rake($^\circ$)	
1996	20JUL	36.131 $^\circ$ N 27.460 $^\circ$ E	6.1	1.53	6	58	-119	1
1997a	13OCT	36.440 $^\circ$ N 22.160 $^\circ$ E	6.3	3.19	322	19	108	1
1997b	18NOV	37.420 $^\circ$ N 20.619 $^\circ$ E	6.6	6.46	354	20	159	1
1997c	18NOV	37.360 $^\circ$ N 20.650 $^\circ$ E	6.1	1.70	354	20	159	1
2004	17MAR	34.770 $^\circ$ N 23.397 $^\circ$ E	6.0	1.10	82	80	177	2
2008a	14FEB	36.570 $^\circ$ N 21.868 $^\circ$ E	6.7	14.65	288	10	73	3
2008b	14FEB	36.430 $^\circ$ N 22.026 $^\circ$ E	6.1	1.67	312	18	93	3
2008c	20FEB	36.360 $^\circ$ N 21.907 $^\circ$ E	6.0	1.36	344	88	-155	3
2008d	08JUN	37.950 $^\circ$ N 21.537 $^\circ$ E	6.4	4.60	301	74	7	2
2008e	15JUL	35.670 $^\circ$ N 27.690 $^\circ$ E	6.4	4.80	261	81	-36	2
2009	01JUL	34.350 $^\circ$ N 25.400 $^\circ$ E	6.4	5.85	295	32	108	2

1 Kiratzi and Louvari (2003); 2 Global CMT; 3 Roumelioti et al. (2009);

2.3.3.3 Parameters values

All Δ CFF calculations were performed at the depths of 10km, 15km, and 20km which correspond to majority of focal depths in the study area (Fig. 2.15). Note also that the depth of 20km is shown to represent the shallow seismogenic layer along the Hellenic trench (Papazachos et al., 2000). Two values of the shear modulus, G , were tested, $3.3 \cdot 10^5$ bars and $5.0 \cdot 10^5$ bars. According to Bird and Kagan (2004) this later value encompasses both crustal and mantle values and therefore it is more appropriate for oceanic convergent boundaries and subduction zones. The receiver faults were selected to have the focal mechanisms of the strongest events occurred in each one of the study sub-areas. Finally, the apparent coefficient of friction, μ' , and the Poisson ratio, ν , were considered equal to 0.4 and 0.25, respectively.

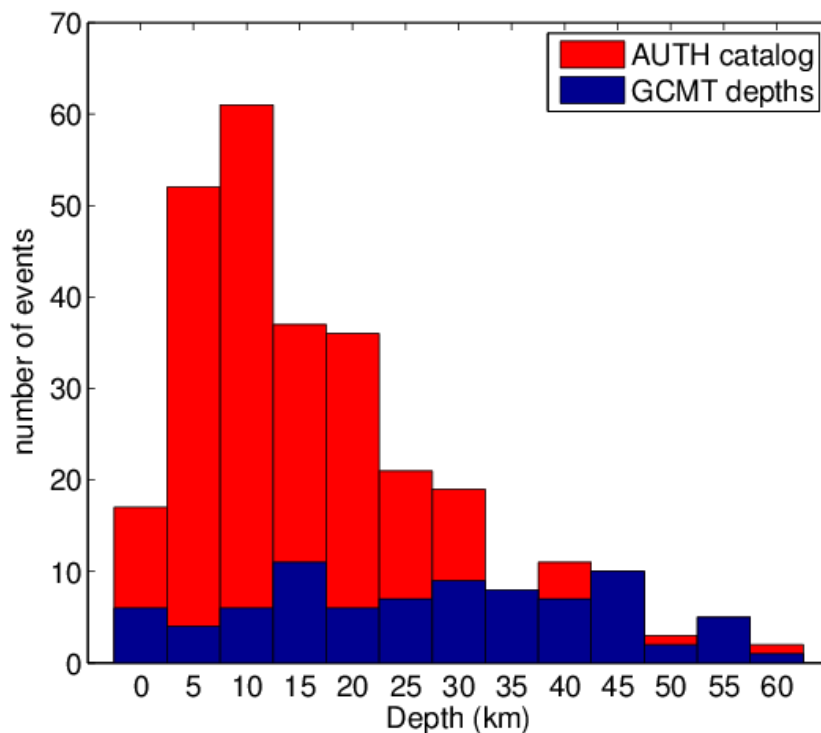


Fig. 2.15. Histogram of the vertical distribution of the stronger ($M > 4.5$) earthquake foci in the study area, as determined by AUTH (red) and GCMT (blue).

For the expected seismicity rates evaluation the characteristic relaxation time, t_a , was considered to take values between 2.5yr-25yrs. The tectonic loading was found ranging from 0.005bar/yr to 0.06bar/yr, as determined by Paradisopoulou (2009), who elaborated GPS data (Reilinger et al., 2006). The aforementioned values of t_a and $\dot{\tau}_r$, lead to an $A\sigma$ to be in the range between 0.0125 – 1.5 bars. Finally, the values of the bandwidth, h , were selected ranging from 0.04° – 0.24° (or equivalently 4.5km – 27km).

2.3.3.4 Results – Discussion

Once the modeled seismicity rates were calculated, they were compared with the observed ones for the respective inter-event time windows constituting the study periods. Regarding the depth, it was shown that selecting 15km for ΔCFF calculations leads to slightly better correlation in all areas except area B, where the computation at 10km depth yields considerably better results. Calculations at 20km depth provide almost identical results with the ones performed at 15km depth. Finally, correlation

is improved for a small average value of ~3% when the larger shear modulus of 50GPa is applied instead of 33GPa. A summary of the datasets and parameter values used for the quantitative analysis in each sub-area is given in Table 2.3.

Table 2.8. Information on learning (or reference rate) and testing periods selected for each sub-area

Sub-area	Learning Periods	Testing Periods	Δ CFF Calculations	Shear Modulus
A	1971-1997	1997-2008		
	1981-1997	2008 (February-June)		
		2008-2012		
B	1971-2004	2004-2007	10km	33GPa
	1991-2004	2007-2012	15km	
			25km	
C	1991-2009	2009-2012		50Gpa
	2001-2009			
D	1971-1996	1996-2008		
	1991-1996	2008-2012		

Seismicity rate evaluation after 1997 was attempted for sub-area A, where 7 strong ($M > 6.0$) earthquakes (3 in 1997 and 4 in 2008) took place. The June 2008 event occurred outside the area borders but it was close enough to influence the regional stress field. Firstly, the reference seismicity rate was calculated for the time interval 1971-1997 ($M_c=4.0$, Fig. 2.16). In the first period (1997-2008) the correlation is strong with most of the area demonstrating an expected/observed seismicity rate ratio close to unity. The period 2008-2012 is not long enough to contain sufficient earthquakes number and therefore the correlation coefficient is relatively lower. Areas where the modeled rates are either overestimated or underestimated are both evident in this case. Slight improvement of the results for the first period (1997-2008) were derived when reference seismicity rates were evaluated from 1981-1997 ($M_c=3.7$ – Fig. 2.17), whereas for the second period (2008-2012), although even more events are available, the correlation does not show any improvement with a significant number of earthquakes taking place in stress shadows. The quantitative analysis (Fig. 2.18 and Fig. 2.19) shows that there is a relatively high

correlation between observed and modeled seismicity rates for the first of the study periods. This correlation is even stronger in areas experiencing positive ΔCFF values and reaches over 70% in most cases. For the period between 20 February 2008 and 8 June 2008 correlation is null (~ 0) most probably due to the very small span of the time window, and consequently insufficient data number for the statistical analysis to be carried out. Finally, moderate correlation appears for the period 2008-2012, especially for positive ΔCFF areas. This relatively low correlation seems to be independent of the reference seismicity rate period selection, since PCC value is similar in both cases. It is rather because most of the earthquakes occurred after the main shocks were onto fault aftershocks, that took place in the close vicinity of the fault segments connected with these main events and therefore it is very likely that the correlation will be improved in the future.

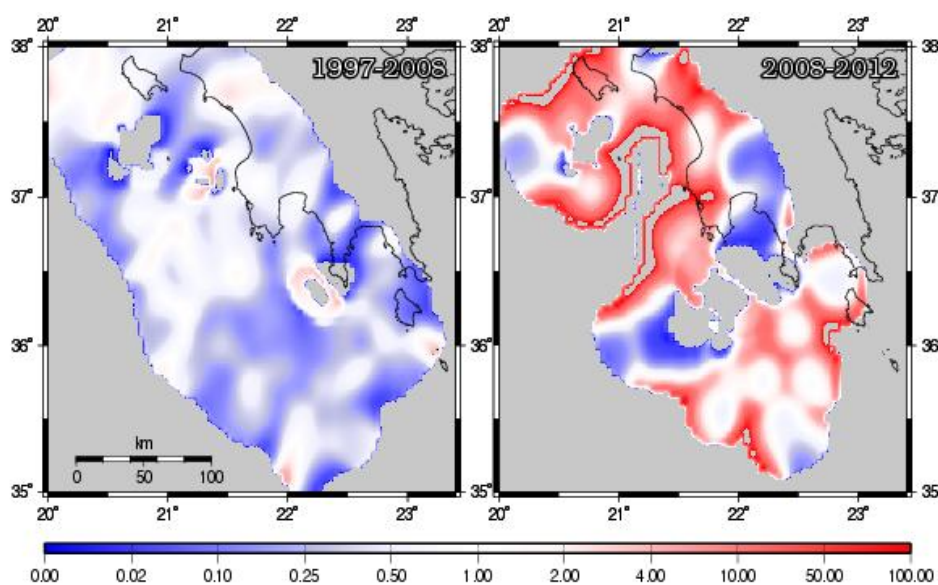


Fig 2.16. Ratio of expected/observed seismicity rates for sub-area A, given the reference seismicity rate calculated during 1971-1997 ($M > 4.0$). Red colors show that the expected values are overestimated in comparison with the observed ones whereas blue colors show higher observed seismicity rates than the simulated ones. White areas correspond to ratio value between 0.5-2, suggesting sufficient model performance. Calculations are not performed in gray areas because of data insufficiency. Parameters values applied are: $h=0.08^\circ$, $t_a=10\text{yrs}$, $\tau_r=0.01\text{ bar/yr}$.

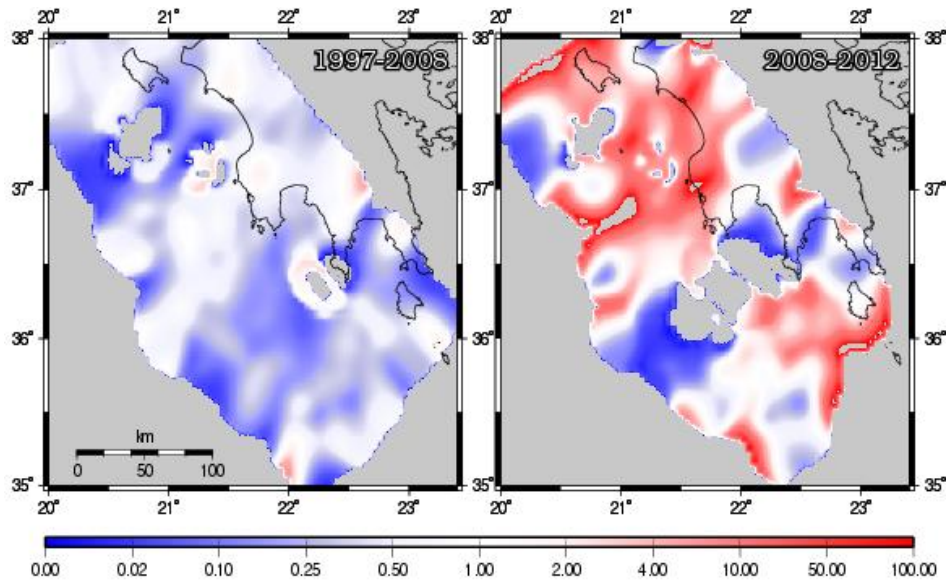


Fig. 2.17. Ratio of expected/observed seismicity rates for sub-area A, given the reference seismicity rate calculated during 1981-1997 ($M>3.7$). Red colors show that the expected values are overestimated in comparison with the observed ones whereas blue colors show higher observed seismicity rates than the simulated ones. White areas correspond to ratio value between 0.5-2, suggesting sufficient model performance. Calculations are not performed in gray areas because of data insufficiency. Parameters values applied are: $h=0.08^\circ$, $t_a=10$ yrs, $\tau_r=0.01$ bar/yr.

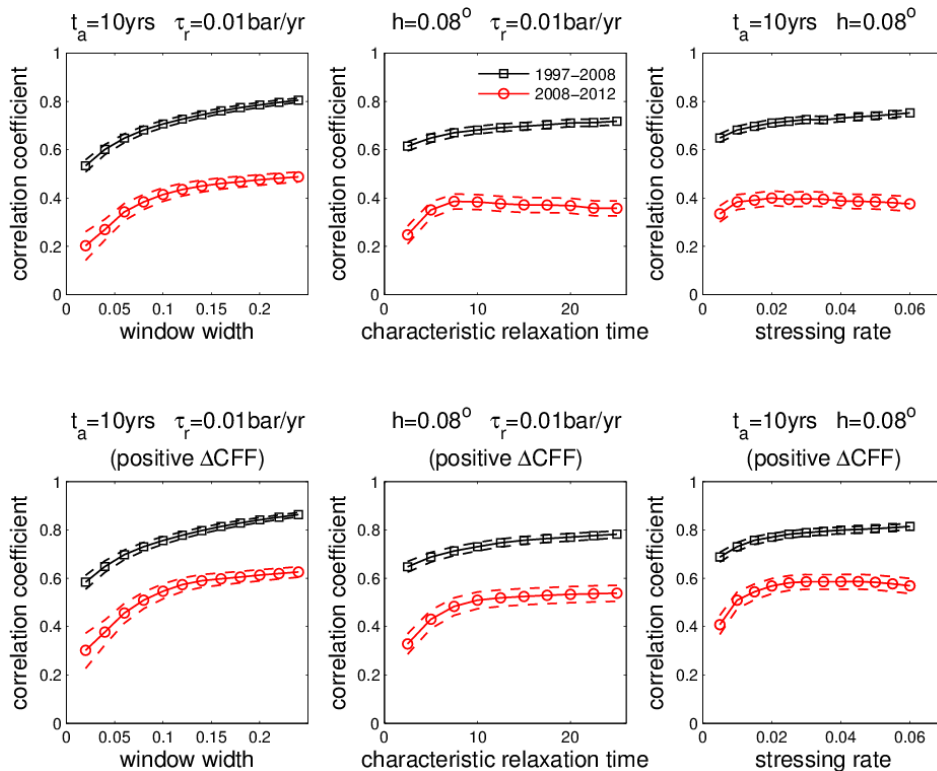


Fig. 2.18. Quantitative evaluation of the difference between observed-synthetic seismicity rates during the inter-event time periods for sub-area A (colored lines). Solid lines indicate the value of Pearson linear Correlation Coefficient (PCC) whereas its 95% confidence intervals for each coefficient are also depicted by fainter lines. The upper frame figures yielded from the entire data set, whereas the figure below by taking into account only those cells experiencing positive ΔCFF . Reference seismicity rate corresponds to the period 1971-1997.

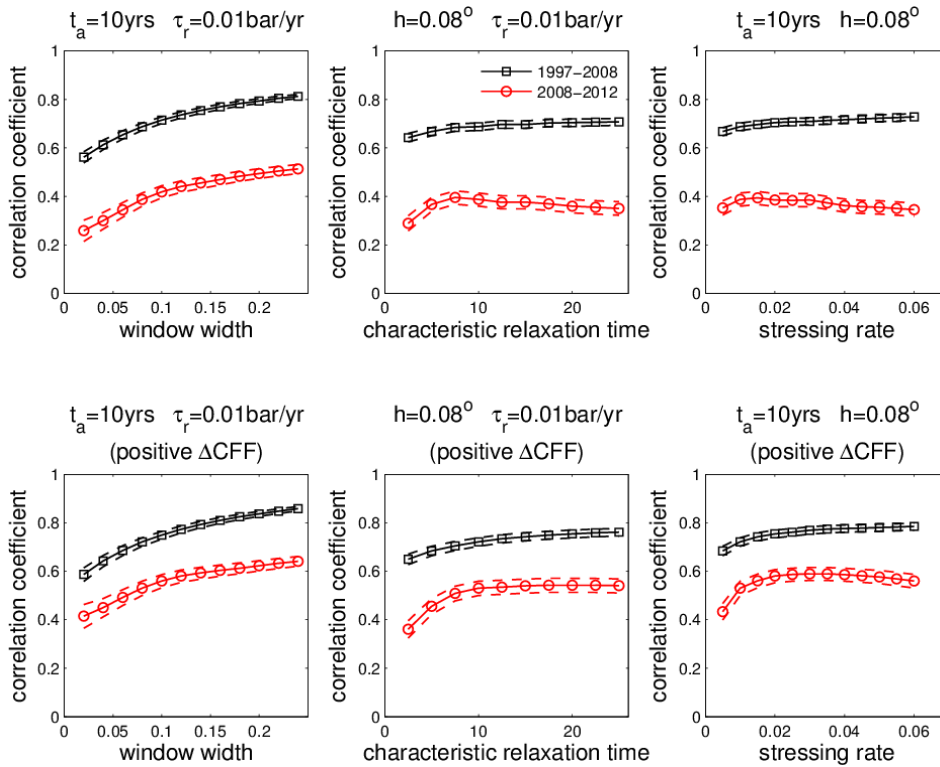


Fig. 2.19. Quantitative evaluation of the difference between observed-synthetic seismicity rates during the inter-event time periods for sub-area A (colored lines). Solid lines indicate the value of Pearson linear Correlation Coefficient (PCC) whereas its 95% confidence intervals for each coefficient are also depicted by faint lines. The upper frame figures yielded from the entire data set, whereas the figure below by taking into account only those cells experiencing positive ΔCFF . Reference seismicity rate corresponds to the period 1981-1997.

Figures 2.20 and 2.21 show the ratio of expected/observed seismicity rates for sub-area B, with reference seismicity rates evaluated from 1971-2004 and 1991-2004, respectively. Although calculations were performed for a smaller number of cells in figure 2.20, due to higher completeness threshold, the ratio is found to be closer to 1 in a broader area. This is also confirmed from the quantitative analysis (Figs. 22 & 23), where it is shown that the correlation in all cases is 0.10-0.20 units higher when reference rate since 1971 is considered. This fact suggests that the 34-year period is more representative for the reference seismicity rate to be calculated than the 14-year period (1991-2004), although it contains smaller number of earthquakes. Regarding the correlation in respect to ΔCFF , it is shown that for the first testing period (2004-2008) the PCC is only slightly improved when positive ΔCFF areas are

considered regardless the selected learning period. The accumulating co-seismic slip due to the 2008 events spread stress shadow all over the study area, thus PCC was not calculated for the second period, in the lower frames of figures 2.22 and 2.23.

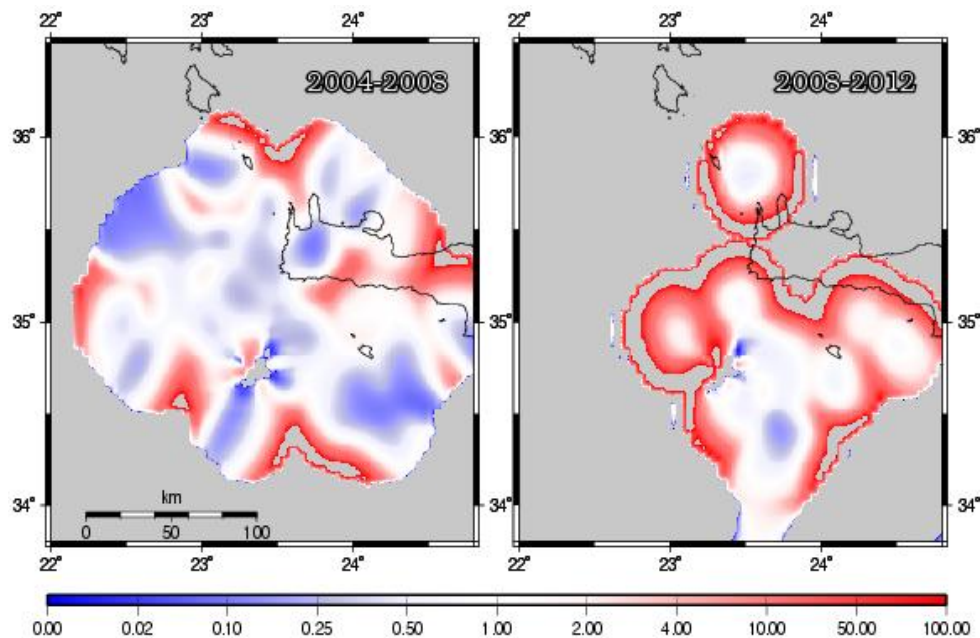


Fig. 2.20. Ratio of expected/observed seismicity rates for sub-area B, given the reference seismicity rate calculated during 1971-2004 ($M > 4.3$). Red colors show that the expected values are overestimated in comparison with the observed ones whereas blue colors show higher observed seismicity rates than the simulated ones. White areas correspond to ratio value between 0.5-2, suggesting sufficient model performance. Calculations are not performed in gray areas because of data insufficiency. Parameters values applied are: $h=0.08^\circ$, $t_a=10\text{yrs}$, $\tau_r=0.02\text{ bar/yr}$.

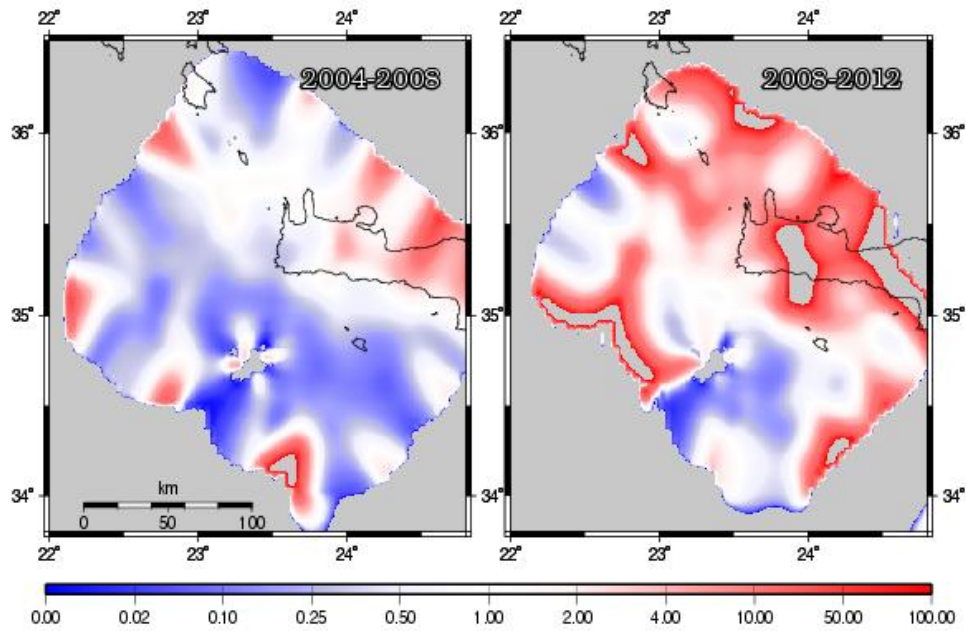


Fig. 2.21. Ratio of expected/observed seismicity rates for sub-area B, given the reference seismicity rate calculated during 1991-2004 ($M > 3.9$). Red colors show that the expected values are overestimated in comparison with the observed ones whereas blue colors show higher observed seismicity rates than the simulated ones. White areas correspond to ratio value between 0.5-2, suggesting sufficient model performance. Calculations are not performed in gray areas because of data insufficiency. Parameters values applied are: $h=0.08^\circ$, $t_a=10\text{yrs}$, $\tau_r=0.02\text{ bar/yr}$.

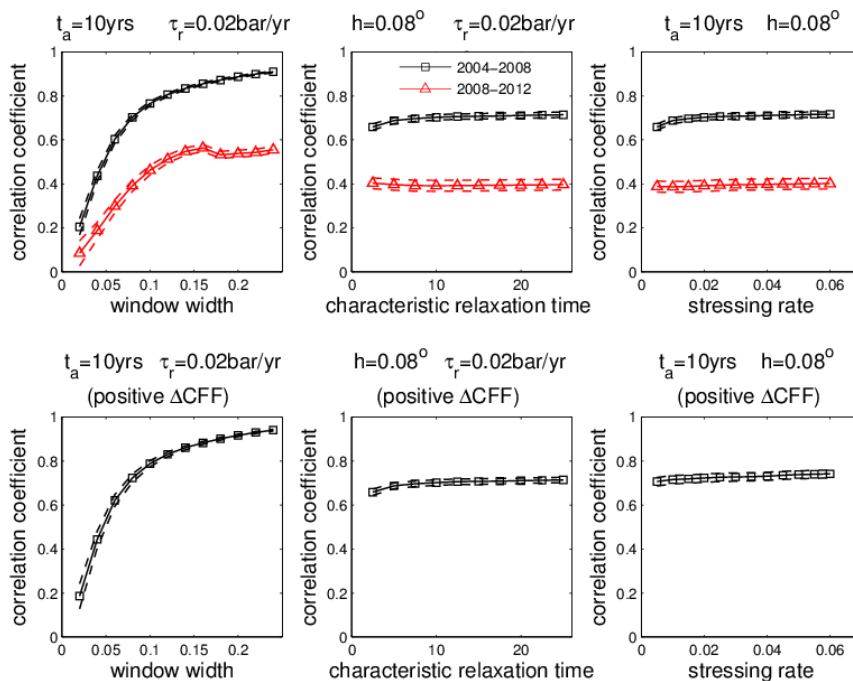


Fig. 2.22. Quantitative evaluation of the difference between observed-synthetic seismicity rates during the inter-event time periods for sub-area B (colored lines). Solid lines indicate the value of Pearson linear Correlation Coefficient (PCC) whereas its 95% confidence intervals for each coefficient are also depicted by fainter lines. The upper frame figures yielded from the entire data set, whereas the figure below by taking into account only those cells experiencing positive ΔCFF . Reference seismicity rate corresponds to the period 1971-2004.

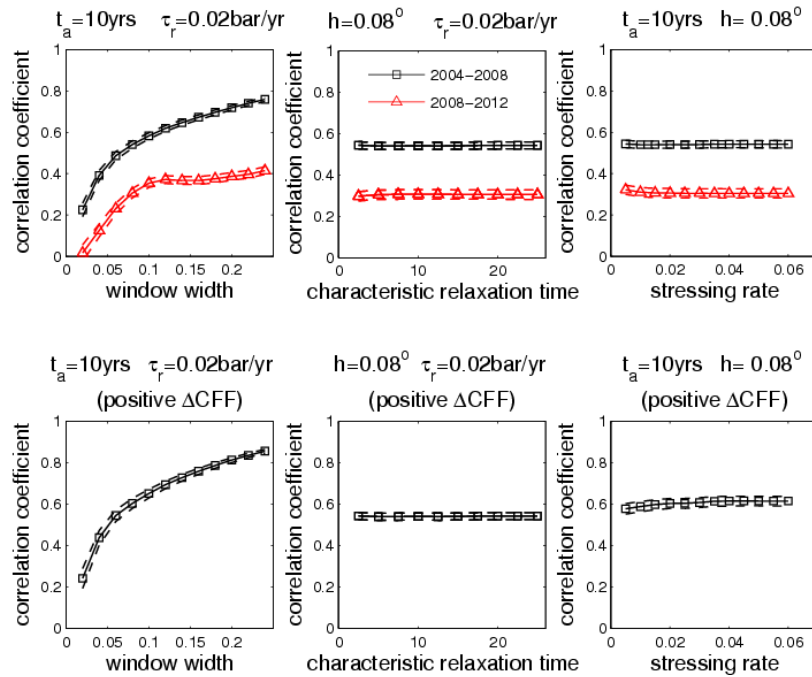


Fig. 2.23. Quantitative evaluation of the difference between observed-synthetic seismicity rates during the inter-event time periods for sub-area B (colored lines). Solid lines indicate the value of Pearson linear Correlation Coefficient (PCC) whereas its 95% confidence intervals for each coefficient are also depicted by fainted lines. The upper frame figures yielded from the entire data set, whereas the figure below by taking into account only those cells experiencing positive ΔCFF . Reference seismicity rate corresponds to the period 1991-2004.

The 1 July 2009 event was the only $M \geq 6.0$ shallow event that occurred in sub-area C during the study period. This area is also remotely located from the closest stations of the regional seismic network, resulting to a completeness magnitude higher than in sub-areas A and B ($M_c=4.1$ after 1991, $M_c=3.7$ after 2001). Therefore, calculations were only performed in approximately half of the region where the data set was adequate. There is a significant number of cells though, where the ratio of expected/observed seismicity rate is close to 1 (Fig. 2.24) for both reference data sets considered (1991-2009, left frame; 2001-2009, right frame). The modeled rates are generally overestimated in the northern part of the area (where the reference seismicity rates were higher) and underestimated in the southern part. Nevertheless, the quantitative analysis (Fig. 2.25 and Fig. 2.26) implies that the 19-year learning period (1991-2009) lead to a PCC which is up to 0.25 units higher than the respective values derived from the 9-year learning period

(2001-2009). If a reference rate before 1991 was considered, then the completeness magnitude would be raised to 4.4 and therefore the earthquake number in the data sample would be dramatically decreased (Table 2.6). This implies that not only a low magnitude threshold is necessary for such analysis, but also an adequate time span, relatively representative of the normal regional (reference) activity should be selected. Finally, in all approaches there is a distinct improvement of correlation when only cells experiencing $\Delta CFF > 0$ are taken into consideration leading to a PCC higher than 60% in some cases.

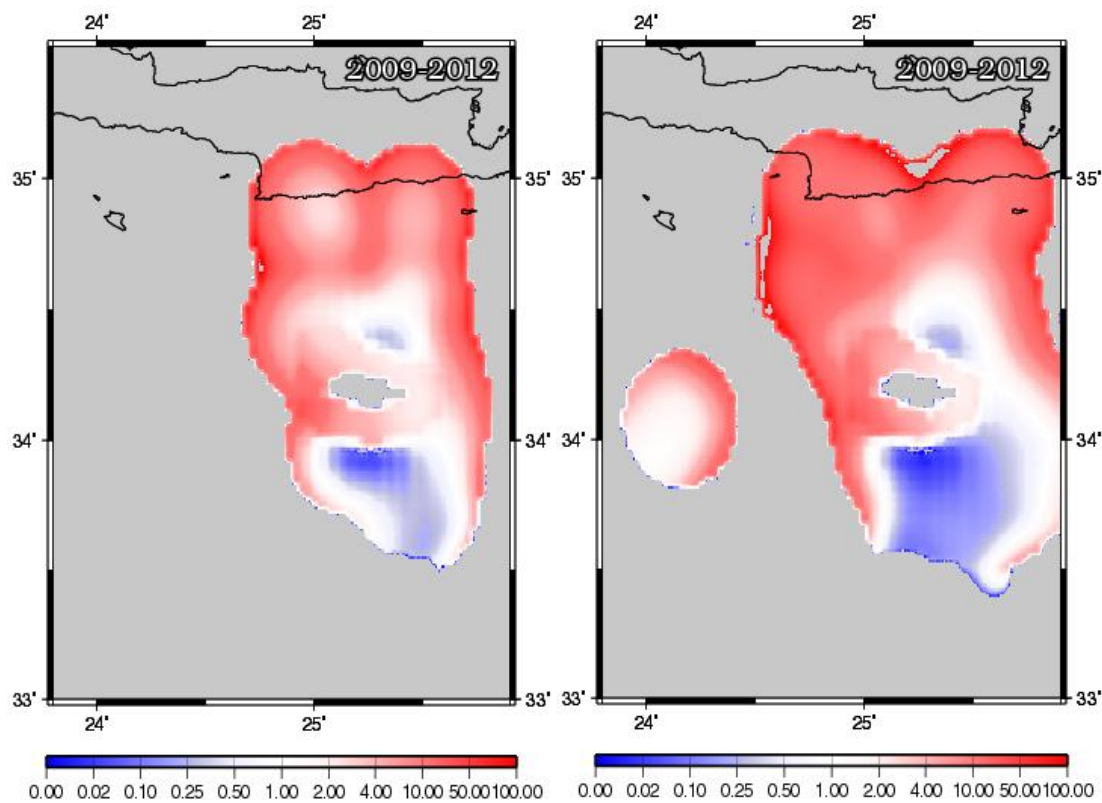


Fig. 2.24. Ratio of expected/observed seismicity rates for sub-area C, given the reference seismicity rate calculated during 1991-2009 ($M > 4.1$, left frame) and 2001-2009 ($M > 3.7$, right frame). Red colors show that the expected values are overestimated in comparison with the observed ones whereas blue colors show higher observed seismicity rates than the simulated ones. White areas correspond to ratio value between 0.5-2, suggesting sufficient model performance. Calculations are not performed in gray areas because of data insufficiency. Parameters values applied are: $h=0.1^\circ$, $t_a=10\text{yrs}$, $\tau=0.01\text{ bar/yr}$.

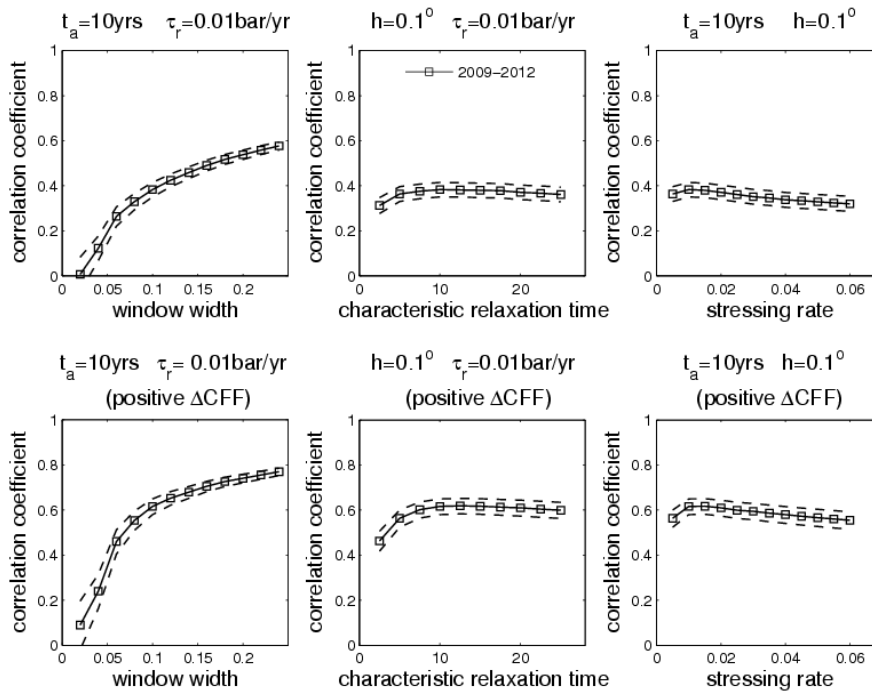


Fig. 2.25. Quantitative evaluation of the difference between observed-synthetic seismicity rates during the inter-event time periods for sub-area C (colored lines). Solid lines indicate the value of Pearson linear Correlation Coefficient (PCC) whereas its 95% confidence intervals for each coefficient are also depicted by fainted lines. The upper frame figures yielded from the entire data set, whereas the figure below by taking into account only those cells experiencing positive ΔCFF . Reference seismicity rate corresponds to the period 1991-2009.

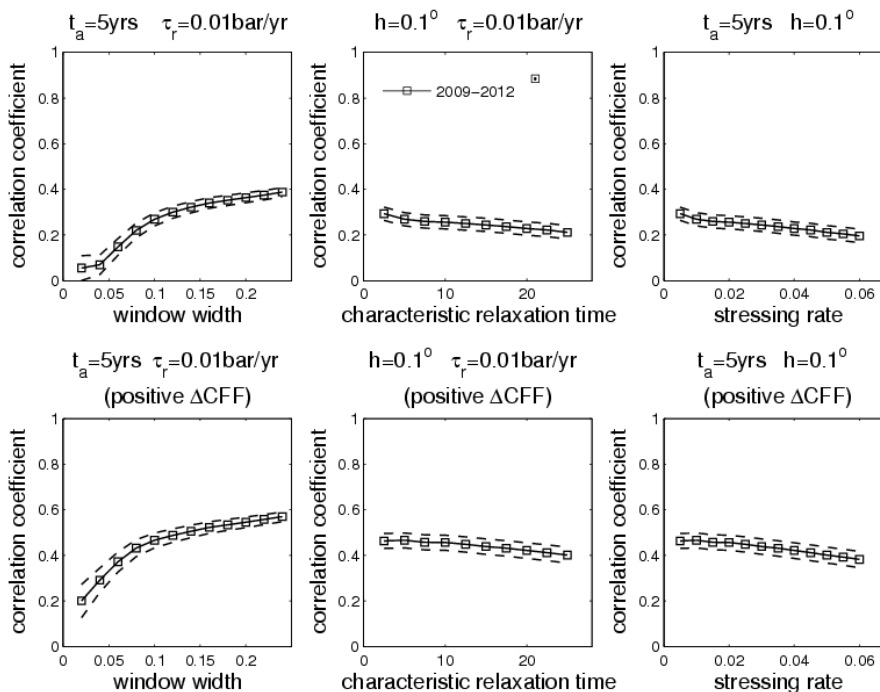


Fig. 2.26. Quantitative evaluation of the difference between observed-synthetic seismicity rates during the inter-event time periods for sub-area C (colored lines). Solid lines indicate the value of Pearson linear Correlation Coefficient (PCC) whereas its 95% confidence intervals for each coefficient are also depicted by fainted lines. The upper frame figures yielded from the entire data set, whereas the figure below by taking into account only those cells experiencing positive ΔCFF . Reference seismicity rate corresponds to the period 2001-2009.

The influence of 2 strong earthquakes (20 July 20 1996 and 15 July 2008) to the reference seismicity rates estimated from 1971-1996 (Fig. 2.27) and 1991-1996 (Fig. 2.28) was examined for area D. The completeness magnitude of the catalog is also high as in area C (Table 2.6) and therefore there is a limited number of cells where calculations could be performed for the second study period (2008-2012). On the contrary the simulated seismicity rate results seem to be satisfactory for the 1st testing period (1996-2008) when a large part of the study area demonstrates ratios of expected/observed seismicity rates between 0.5-2.0, for both learning periods considered. The PCC as a function of bandwidth, characteristic time and stressing rate is shown in Figure 2.29 and Figure 2.30. The first testing period (1996-2008) exhibits high correlation (>60%) when all data are considered and it remains almost identical when calculations concern only positive Δ CFF cells. The correlation is somewhat improved when the reference seismicity rate from 1991-1996 is considered and becomes even stronger when positive Δ CFF areas are only taken into account. The second study period (2008-2012) demonstrates lack of correlation, in all tested aforementioned approaches, probably because of the short duration and the data shortage.

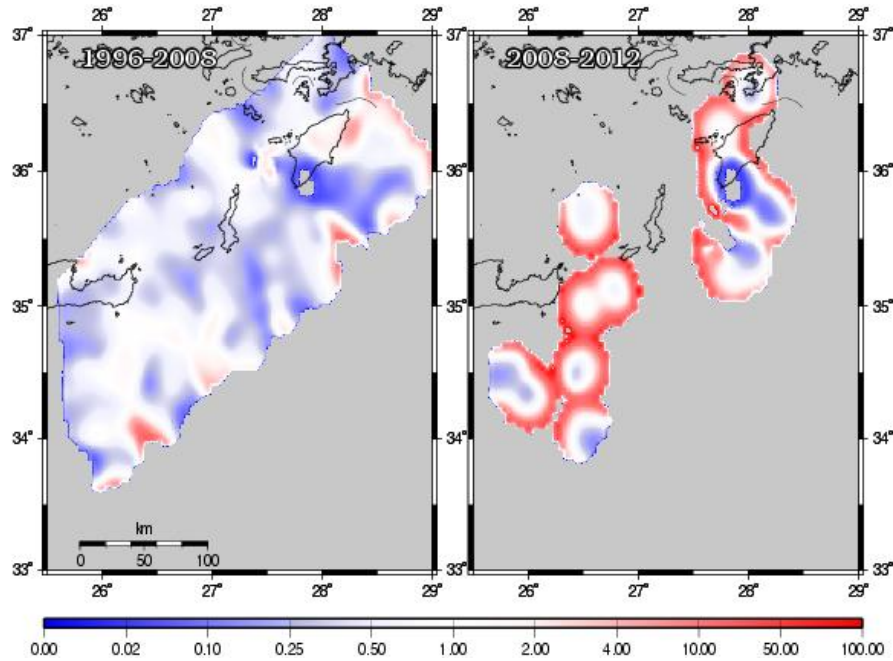


Fig. 2.27. Ratio of expected/observed seismicity rates for sub-area D, given the reference seismicity rate calculated during 1971-1996 ($M > 4.4$). Red colors show that the expected values are overestimated in comparison with the observed ones whereas blue colors show higher observed seismicity rates than the simulated ones. White areas correspond to ratio value between 0.5-2, suggesting sufficient model performance. Calculations are not performed in gray areas because of data insufficiency. Parameters values applied are: $h=0.08^\circ$, $t_a=10\text{yrs}$, $\tau=0.02\text{ bar/yr}$. Parameters values applied are: $h=0.08^\circ$, $t_a=10\text{yrs}$, $\tau=0.02\text{ bar/yr}$.

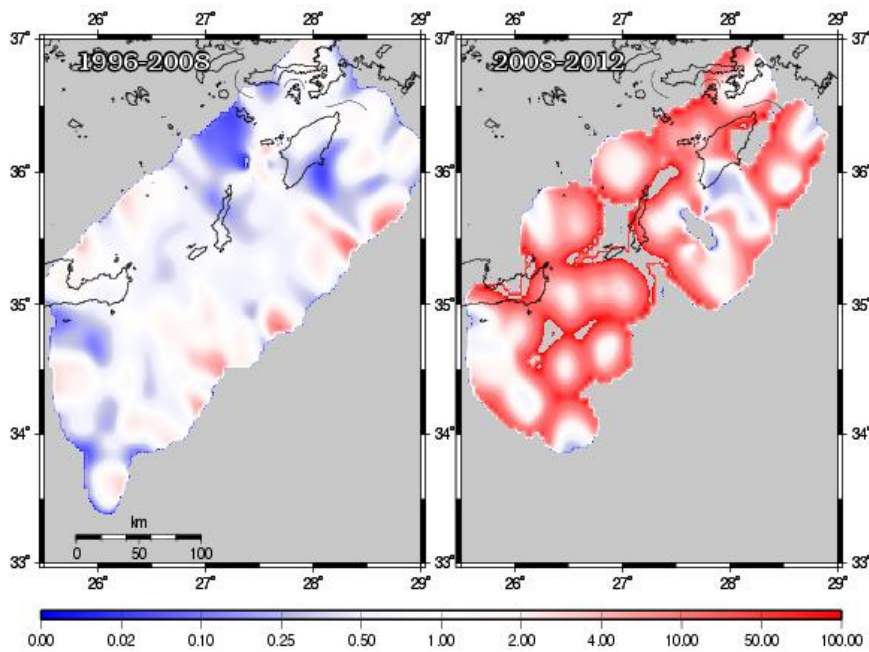


Fig. 2.28. Ratio of expected/observed seismicity rates for sub-area D, given the reference seismicity rate calculated during 1991-1996 ($M > 4.1$). Red colors show that the expected values are overestimated in comparison with the observed ones whereas blue colors show higher observed seismicity rates than the simulated ones. White areas correspond to ratio value between 0.5-2, suggesting sufficient model performance. Calculations are not performed in gray areas because of data insufficiency. Parameters values applied are: $h=0.08^\circ$, $t_a=10\text{yrs}$, $\tau=0.02\text{ bar/yr}$. Parameters values applied are: $h=0.08^\circ$, $t_a=10\text{yrs}$, $\tau=0.02\text{ bar/yr}$.

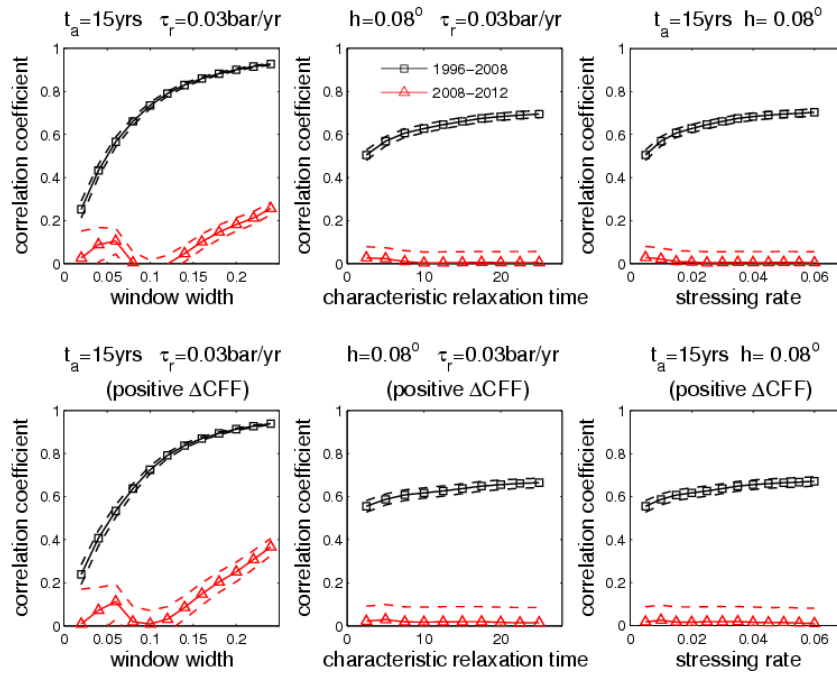


Fig. 2.29. Quantitative evaluation of the difference between observed-synthetic seismicity rates during the inter-event time periods for sub-area D (colored lines). Solid lines indicate the value of Pearson linear Correlation Coefficient (PCC) whereas its 95% confidence intervals for each coefficient are also depicted by fainter lines. The upper frame figures yielded from the entire data set, whereas the figure below by taking into account only those cells experiencing positive ΔCFF . Reference seismicity rate corresponds to the period 1971-1996.

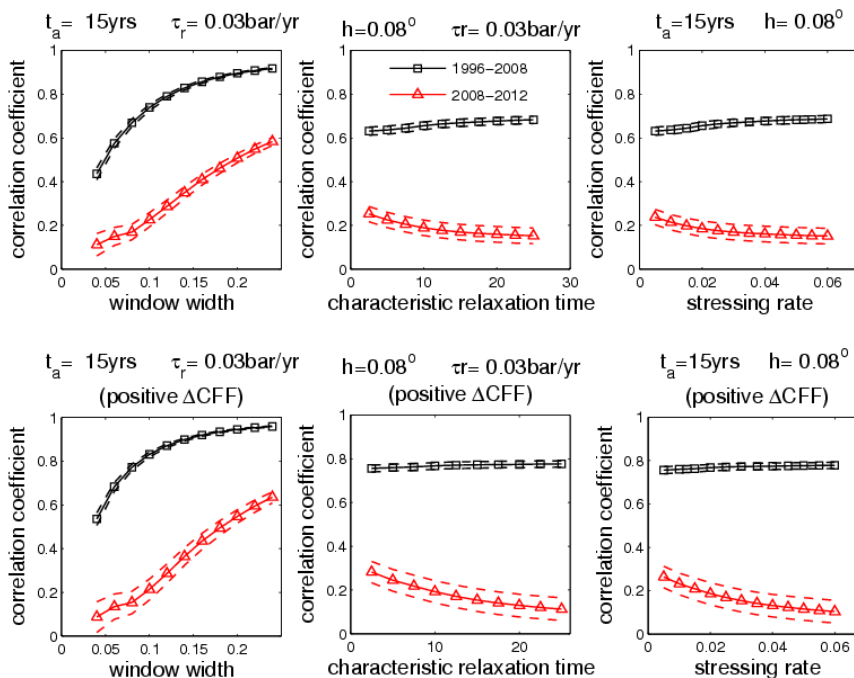


Fig. 2.30. Quantitative evaluation of the difference between observed-synthetic seismicity rates during the inter-event time periods for sub-area D (colored lines). Solid lines indicate the value of Pearson linear Correlation Coefficient (PCC) whereas its 95% confidence intervals for each coefficient are also depicted by fainter lines. The upper frame figures yielded from the entire data set, whereas the figure below by taking into account only those cells experiencing positive ΔCFF . Reference seismicity rate corresponds to the period 1991-1996.

2.3.3.5 Contribution to Seismic Hazard Assessment

This part of the analysis was also performed separately for each sub-area due to the diversity of data properties and assumptions. Figure H3 shows the expected seismicity rates after 2012 in sub-area A of South Aegean. These rates were estimated by considering the influence of coseismic (due to $M \geq 6.0$ earthquakes) and long term stress changes on the reference seismicity rates during 1981-1997 ($M \geq 3.7$). The unbounded non-parametric magnitude distribution of the 7308 events ($M \geq 3.7$ during 1981-2012) was then considered in connection with the averaged estimated expected seismicity rate, to calculate the exceedance probabilities for the next decade. These probabilities were found equal to 79.4% (with 95% confidence bounds at 73.9% - 87.9%) and 44.7% (with 95% confidence bounds at 35.7% - 61.2%) for an earthquake with magnitude higher than 6.0 and 6.5, respectively. The expected rate pattern has been considerably influenced by all strong ($M \geq 6.0$) earthquakes occurred in 2008. Moreover, the signature of the previously events that took place in 1997 can be still distinguished. The highest earthquake probabilities are expected in the central and northern part of sub-area A. Contrarily at the southern part, there is a sequence of areas where the seismicity rates are expected to be both high and low.

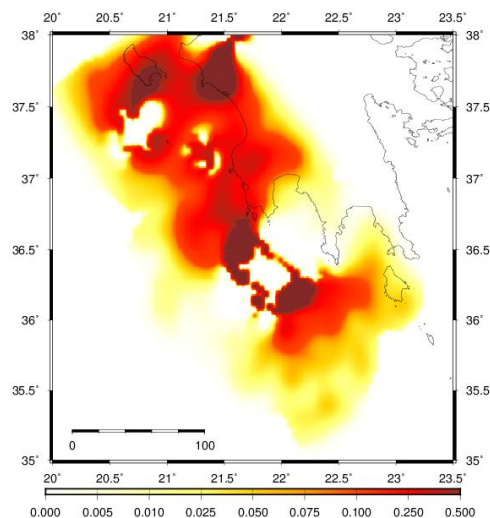


Fig. H3. Snapshot of the expected seismicity rates ($M \geq 3.7$) estimated for the period after 2012 in the Sub-Area A of South Aegean.

The expected seismicity rates after 2012 were estimated for sub-area B, by considering the influence of coseismic (due to $M \geq 6.0$ earthquakes) and long term (tectonic) stress changes on the reference seismicity rates during 1991-2004 ($M \geq 3.9$, Fig. H4). The unbounded non-parametric magnitude distribution of the 974 events ($M \geq 3.9$ during 1991-2012) was then considered in connection with the averaged estimated expected seismicity rate, in order to calculate the exceedance probabilities for the next decade. These probabilities were found equal to 60.4% (with 95% confidence bounds at 55.8% - 66.4%) and 34.4% (with 95% confidence bounds at 16.1% - 43.0%) for an earthquake with magnitude higher than 6.0 and 6.5, respectively. Figure H4 shows that the highest expected rate areas are located at the north-east part of sub-area B, close to the shores of Crete. It is noted that high probability values are expected in the vicinity of the fault that ruptured during the 365, $M=8.3$ earthquake. In addition the October 2013, $M=6.5$ earthquake took place in such high estimated probability area (see section 2.4).

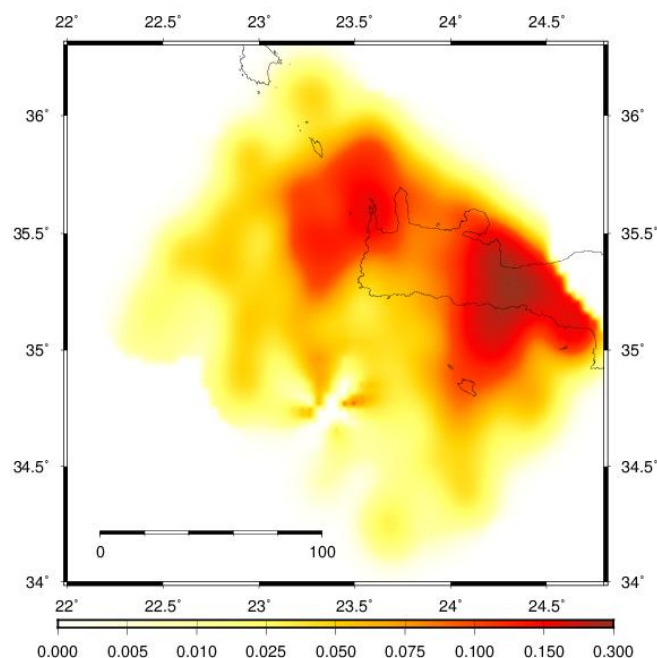


Fig. H4. Snapshot of the expected seismicity rates ($M \geq 3.9$) estimated for the period after 2012 in sub-area B of South Aegean.

The low amount of available seismic data resulted to a spatially limited seismicity rate forecast for sub-area C of South Aegean. The expected seismicity rates after 2009 are shown in Figure H5. These rates were estimated after considering the influence of coseismic (due to $M \geq 6.0$ earthquakes) and tectonic stress variations on the reference seismicity rates, calculated from the period 2001-2009 ($M \geq 3.7$). The unbounded non-parametric magnitude distribution of the 904 events ($M \geq 3.7$ during 2001-2012) was then considered in connection with the averaged estimated expected seismicity rate, to calculate the exceedance probabilities for the next decade. These probabilities were found equal to 80.1% (with 95% confidence bounds at 66.5% - 86.1%) and 55.1% (with 95% confidence bounds at 39.4% - 67.6%) for an earthquake with magnitude higher than 6.0 and 6.5, respectively. The inadequate data corresponding to the western part of the area didn't allow robust expected rate calculations. On the other hand, the reference rates are expected to be considerably enhanced in the south-eastern part of sub-area C. In section 2.4 is demonstrated that an $M=6.1$ event that took place on June 2013, was located inside an increased earthquake probability area.

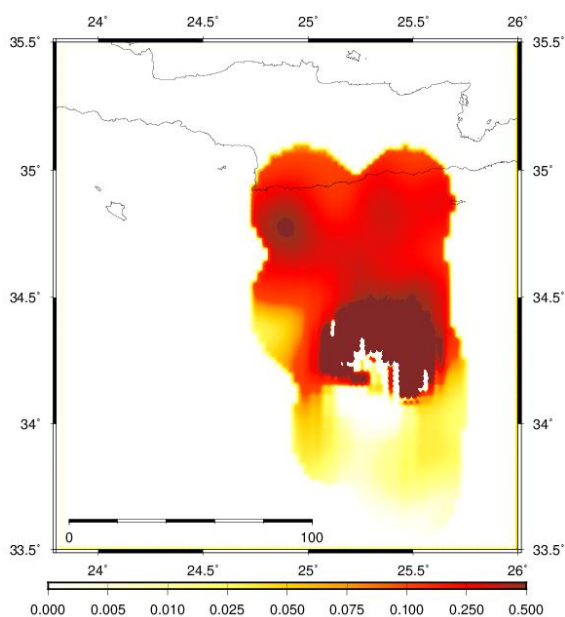


Fig. H5. Snapshot of the expected seismicity rates ($M \geq 3.7$) estimated for the period after 2012 in sub-area C of South Aegean.

The expected seismicity rates after 2012 were estimated for sub-area D of South Aegean, by considering the influence of coseismic (due to $M \geq 6.0$ earthquakes) and tectonic stress changes on the reference seismicity rates during 1991-1996 ($M \geq 4.1$, Fig. H6). The unbounded non-parametric magnitude distribution of the 1810 events ($M \geq 4.1$ during 1991-2012) was then considered in connection with the averaged estimated expected seismicity rate, in order to calculate the exceedance probabilities for the next decade. These probabilities were found equal to 78.0% (with 95% confidence bounds at 65.4% - 83.4%) and 49.4% (with 95% confidence bounds at 29.2% - 58.0%) for an earthquake with magnitude higher than 6.0 and 6.5, respectively. Figure H6 illustrates that the highest expected rate areas are located at the central and western part area D, with significantly increased probabilities expected close to the coasts of Karpathos Island. On the other hand, decreased seismicity rates are expected eastern of Rhodes Island.

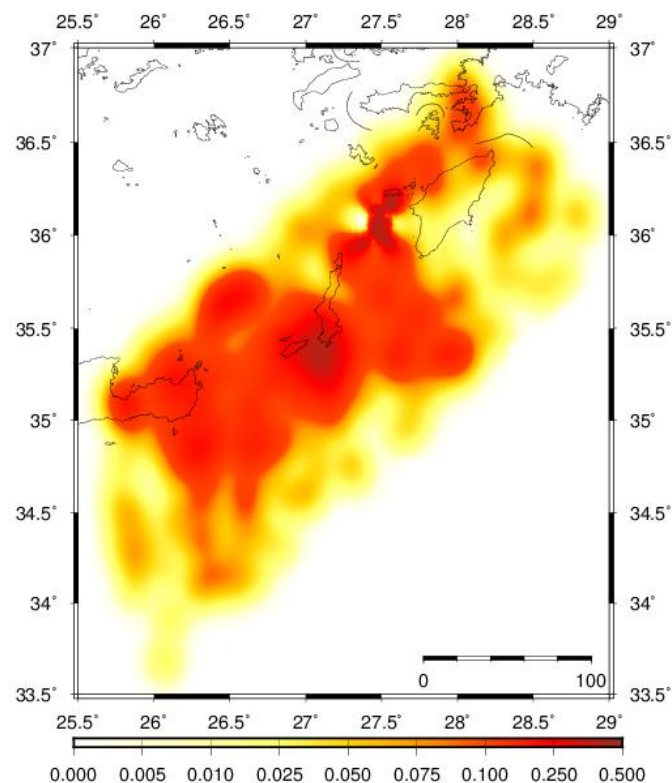


Fig. H6. Snapshot of the expected seismicity rates ($M \geq 4.1$) estimated for the period after 2012 in sub-area D of South Aegean.

2.3.4 Area 4 – Western Turkey (4 sub-areas)

2.3.4.1 Introduction

The study area in this section comprises Western Turkey (Fig. 2.31), a region where the complex interaction of Eurasian, Arabian, and African lithospheric plates has resulted to high deformation and consequently seismicity rates. The most prominent tectonic characteristic of the broader area is the subduction and rollback of the Eastern Mediterranean plate beneath the Aegean microplate along the Hellenic Arc since the early Miocene (Papazachos and Comninakis, 1969, 1971), which has resulted to a significant N-S oriented extension regime in the Aegean and the adjacent areas. The second geodynamic process that affects the study area is the westward propagation of the Anatolian block away from the Arabian-Eurasian plate collision zone along the North and East Anatolian Fault Systems (McKenzie, 1972; Şengör et al., 1985; Bozkurt, 2001). This geodynamic development is also confirmed by GPS studies (e. g. Reilinger et al., 2006; Aktuğ et al., 2009). These interactions have produced a broad and complex system of normal faults, usually bounding the E-W trending extensional basins that are characteristically placed in parallel, with current rate of extension equal to 6 mm/yr (McClusky et al., 2000; Noquet, 2012). Secondary structures with NE-SW trending basins are also evident (Taymaz and Price, 1992; Westaway, 1993). Dextral strike-slip faulting is dominant along the North Anatolian Fault (NAF), one of the longest active right lateral fault systems, which extends for approximately 1,500 km, from eastern Turkey, through the Marmara Sea where it bifurcates into sub-parallel branches.

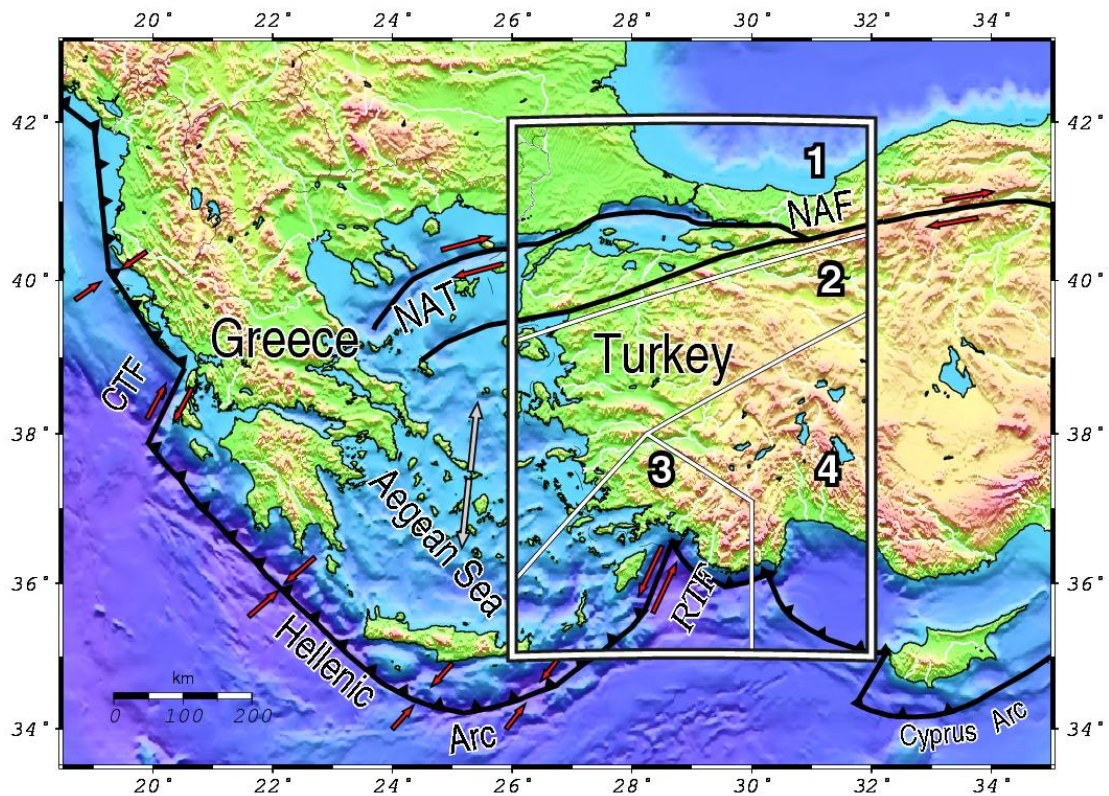


Fig. 2.31. Morphological map and main seismotectonic properties of the study area and its surroundings. Black lines indicate the major active boundaries: the subduction zone (Hellenic Arc) and the North Anatolian Fault – NAF with its westernmost extension, the North Aegean Trough (NAT). The Collision Zone between the Apulian and Eurasian plates along with the Rhodes Transform Fault - RTF and the Cephalonia Transform Fault – CTF at the southeastern and western termination of the Hellenic arc, respectively, are also indicated along with the Cyprus Arc at the southeast corner of the map. The white rectangle indicates the study area divided into 4 sub-areas.

2.3.4.2 Data

We attempt to study seismicity rate variation in terms of the stress field evolution during time and therefore we need to initiate our analysis as back in time as possible. The most appropriate constraint for such task deals with the earthquake data availability and quality. A major problem of the published regional catalogs is connected with the magnitude inhomogeneity, since different magnitude scales are assigned from different institutions and periods. To overcome this obstacle we used a recently compiled equivalent moment magnitude, M^*_w , catalog (Leptokaropoulos et al., 2013), available at (<ftp://geophysics.geo.auth.gr/pub/users/kleptoka/BSSA-D-12-00174-esupp.html>) for the study area. This catalog includes earthquakes occurred from 1964 to 2010

with M_w^* ranging from 3.5 to 7.5, with the distribution of these events being non-homogeneous in both space and time. Therefore, we divided the study area into 4 individual sub-areas (Figure 2.32) exhibiting relatively uniform seismotectonic features (similar faulting type, seismicity level) and also similar data quality, as suggested by [Leptokaropoulos et al. \(2013\)](#).

Table 2.10. Source parameters of the 12 earthquakes with $M \geq 5.8$ modeled for coseismic static Coulomb stress changes calculations.

Event	Date	Sub-area of occurrence	M_w	M_0 ($\cdot 10^{25}$ dyn·cm)	Focal Mechanism			Reference
					Strike($^\circ$)	Dip($^\circ$)	Rake($^\circ$)	
1992	NOV 06	2	6.0	1.09	238	85	-167	1
1995	OCT 01	4	6.3	2.10	309	51	-94	2
1996	JUL 20	3	6.2	2.40	196	38	-102	1
1999a	AUG 17	1	7.6	131.0	268	84	180	3
1999b	NOV 12	1	7.2	47.0	262	53	-177	4
2000	DEC 15	4	6.0	1.20	285	41	-100	1
2002a	FEB 03	4	6.4	6.00	269	37	-71	1
2002b	FEB 03	4	5.8	0.61	236	45	-58	1
2003	MAR 10	2	5.7	0.43	250	76	-159	1
2005a	OCT 17	2	5.8	0.60	228	79	-171	5
2005b	OCT 20	2	5.8	0.70	231	66	-162	5
2008	JUL 15	3	6.4	4.73	357	65	-179	1

1: Global CMT, 2: Pinar (1998), 3: Barka et al. (2002), 4: Kiratzi and Louvari (2001), 5: Benetatos et al. (2006)

The next task was to distinguish the starting point and duration of the reference and forecast periods for each region, in order to utilize as larger dataset as possible, for the seismicity rate analysis. The completeness magnitude was calculated for different time windows by applying the modified goodness of fit test (MGFT) proposed by [Leptokaropoulos et al. \(2013\)](#). This processing led to different starting year, number of events and M_c for each sub-area, as shown in Table 2.11. The reference seismicity rate periods were selected to last until the origin time of the first strong ($M_w^* \geq 5.8$) event occurrence. The testing periods were set to be equal with the inter-seismic periods between two successive main shocks occurred individually in each one of the study subareas. Nevertheless, the two 1999 ($M_w^* > 7.0$) events, occurred inside sub-area 1, caused such large and extensive stress changes

that significantly influenced seismicity rates also in sub-area 4. Consequently the ΔCFF 's associated with these events were also taken into consideration for the seismicity rate changes variation in this sub-area. Note that instead of truncating the dataset by declustering, in order to avoid along-fault aftershock influence, we preferred using the entire data set and focus our attention to specific target areas of major interest. Such areas are located close to the epicenter of the subsequent events, or extending inside positive ΔCFF lobes (Toda et al., 2003; Cocco et al., 2010; Leptokaropoulos et al., 2012).

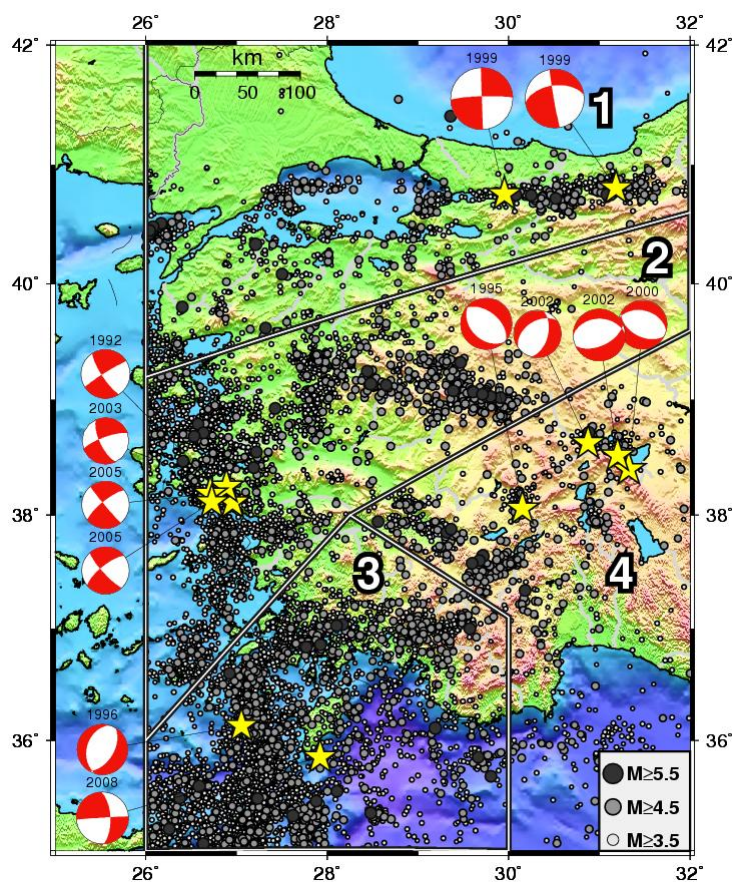


Fig. 2.32. Spatial distribution of earthquake epicenters during 1964-2010 in the study area with magnitudes expressed as M^*w . The 4 sub-areas (also indicated here) demonstrate different data density and completeness level. The fault plane solutions of $M \geq 5.8$ events are shown as lower hemisphere equal area projection and their epicenters are depicted by stars. Information on these strong earthquakes is provided in Table 2.10.

Table 2.11. Properties of the datasets utilized for each sub-area.

Sub-area	Duration	Reference Seismicity	M_c	Number of events
1	20 yrs	1991-1999	3.7	898
2	32 yrs	1979-1992	3.8	1782
3	24 yrs	1987-1996	4.1	1439
4	20 yrs	1991-1995	3.7	627

2.3.4.3 Parameters values

In this area, stressing rates, were obtained from [Paradisopoulou et al. \(2010\)](#), who calculated $\dot{\tau}_r$ as derived from slip rates in each fault segment, considered the seismic coupling ([King et al., 2001](#)) and concluded to values that were in agreement with those from [Stein et al. \(1997\)](#) and [Parsons et al. \(2004\)](#). The average values computed for these segments were applied in the present study for each sub-area i.e. 0.10, 0.04, 0.025 and 0.03 bars/yr for sub-areas 1 to 4 respectively. Trials with additional stressing rate values were performed ranging from 0.04-0.25 for sub-area 1 and 0.01-0.08 for the other 3 sub-areas, which represent the minimum and maximum values computed in each case. Calculations were performed by considering t_a fluctuation between 2.5-30 yrs. A wide range of $A\sigma$ results from the aforementioned values of characteristic relaxation time stressing rate, varying from 0.25-2.5 bars for sub-area 1 and 0.15-1.2 bars for sub-areas 2, 3 and 4. The applying values of bandwidth though, fluctuate between 0.04° to 0.28° . Silverman's (1986) formula for appropriate h estimation in respect to the data number and distribution provides values between 0.08-0.11 for the three sub-areas. Finally, we adopted the value of $\mu'=0.4$ as applied by [Stein et al. \(1997\)](#), [Nalbant et al. \(1998\)](#) and [Paradisopoulou et al. \(2010\)](#) for NAF and western Turkey. The Poisson's ratio, ν , and shear modulus, G , were set equal to 0.25 and $3.3 \cdot 10^5$ bar, respectively and the seismogenic layer in the study area was assumed extending from 3-15 km depth ([Papadimitriou and Sykes, 2001](#); [Paradisopoulou et al., 2010](#)).

2.3.4.4 Results – Discussion

The resulted seismicity rates for the study periods, as derived from Rate/State model application and their comparison with the observed ones for the respective periods are now presented. The impact of 2 strong earthquakes

(17th August 1999, M7.6 and 12th November 1999, M7.2) on regional seismicity rates is studied here. As shown in figures 2.33 and 2.34, there is a poor observed/expected seismicity rate correlation for the ~100 days period between the occurrence of the two strong events. Nevertheless it is evident in figure 2.34 that relatively high PCC values (>0.5) are achieved when characteristic relaxation time or stressing rate take lower values (<5 yrs and <0.05bar/yr, respectively). Given that the stressing rate is well constrained along the NAF with values usually much higher than 0.05, it follows from the model that t_a may be lower than initially assumed. On the other hand, the second period (1999b-2010) demonstrates a much stronger correlation between real and modeled seismicity rate values, with $PCC > 0.7$. Figure 2.33b shows that off-fault seismicity that took place west of the two main shocks rupture areas is well simulated by the Rate/State model although some local deviations are still present. Note that the influence of these events is not modeled for the area beyond the 32 meridian due to the catalog geographical limitation. Finally the results are identical if only positive ΔCFF bins are considered.

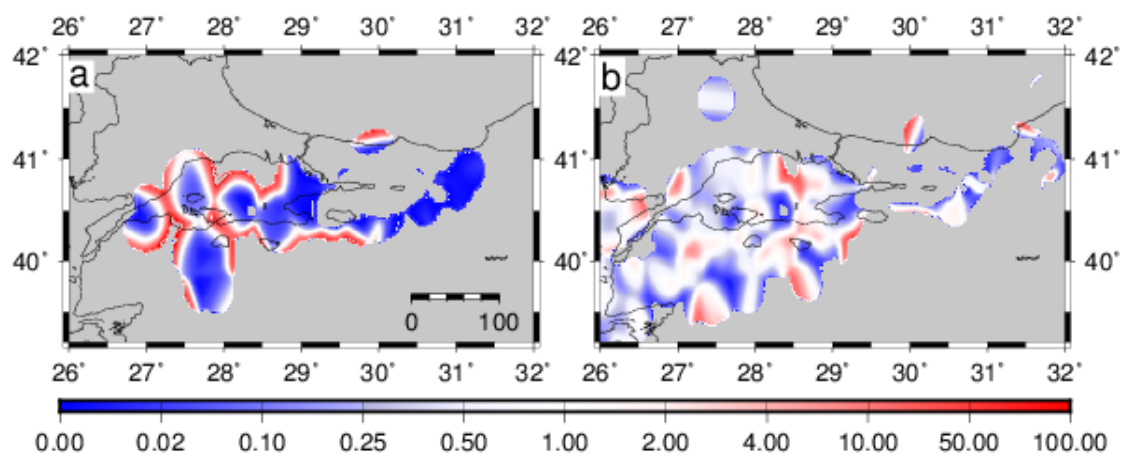


Figure 2.33. Ratio of expected/observed seismicity rates for sub-area 1, for 1999a-1999b (left frame $\Delta t=0.24$ yrs) and 1999b-2010 (right frame $\Delta t=11.1$ yrs). Red colors show that the expected values are overestimated in comparison with the observed ones whereas blue colors show higher observed seismicity rates than the simulated ones. White areas correspond to ratio value between 0.5-2, suggesting sufficient model performance. Calculations are not performed in gray areas because of data insufficiency. Parameter values were taken as: $h=0.08^\circ$, $t_a=10$ yrs and $\dot{\tau}_r=0.10$ bar \cdot yr $^{-1}$ ($A\sigma=1.0$ bar).

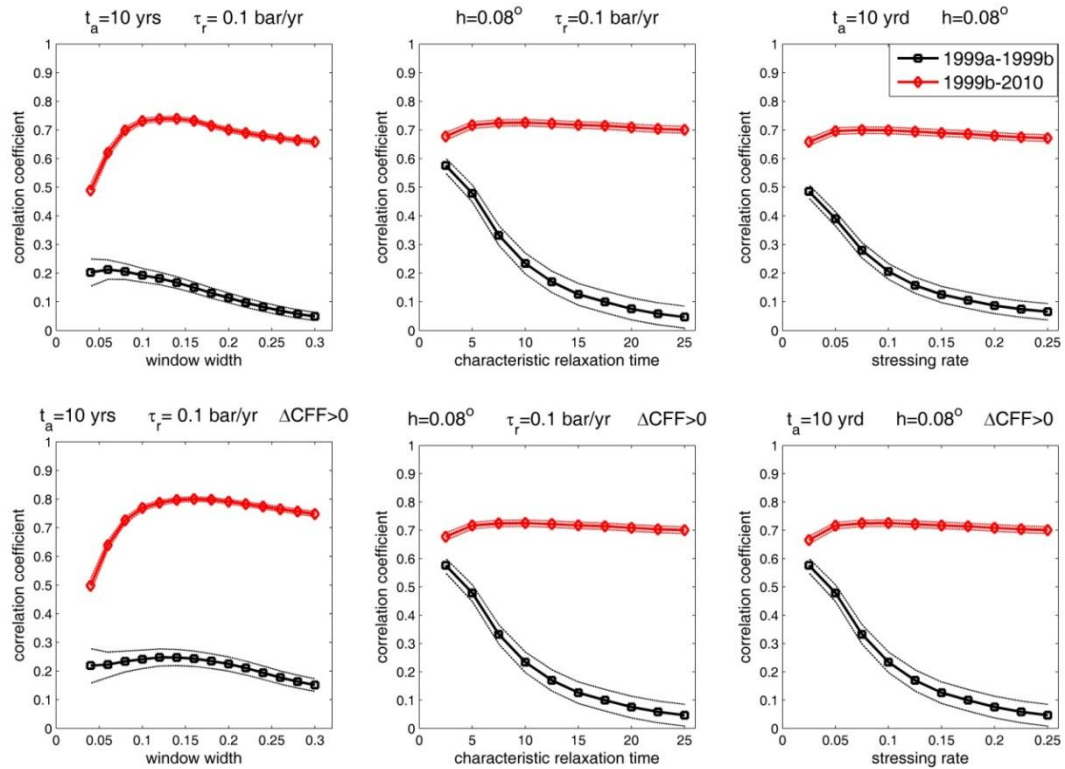


Fig. 2.34. Pearson Correlation Coefficient (PCC) estimation (solid lines) and its 95% confidence interval (fainted lines) for subarea 1. Upper frames were obtained from the entire dataset, whereas the lower frames yielded by taking into account only those cells experiencing positive ΔCFF .

Considering sub-area 2, four strong events are taken into account for the Rate/State modeling: The 6th November 1992, M6.0, the 10th March 2003, M5.8, the 17th October 2005, M5.8 and the 20th October 2005, M5.8 shocks. The forecasted periods correspond to the respective inter-seismic time intervals. Significant variations regarding the selection of parameter values are here observed (Fig. 2.35 and 2.36). The model seems to perform well for the first testing period which has a quite long duration of over 10 years (Fig 2.35a), but the PCC is notably lower regarding the subsequent, shorter periods (Fig 2.36). Especially for the third period there is no linear correlation obtained during this 3-days time increment. Because of the relatively high completeness threshold, it is necessary for a testing period to last for several years in order for the respective dataset to contain sufficient number of events. Correlation is though significantly improved when positive ΔCFF areas are only considered (Fig. 2.40, lower frames) and stressing rate together with characteristic time

are given lower values. Figure 2.39 evidences that expected rates are usually lower than the real ones, a fact that also suggests that the actual seismicity recovers faster at its reference level (1979-1992).

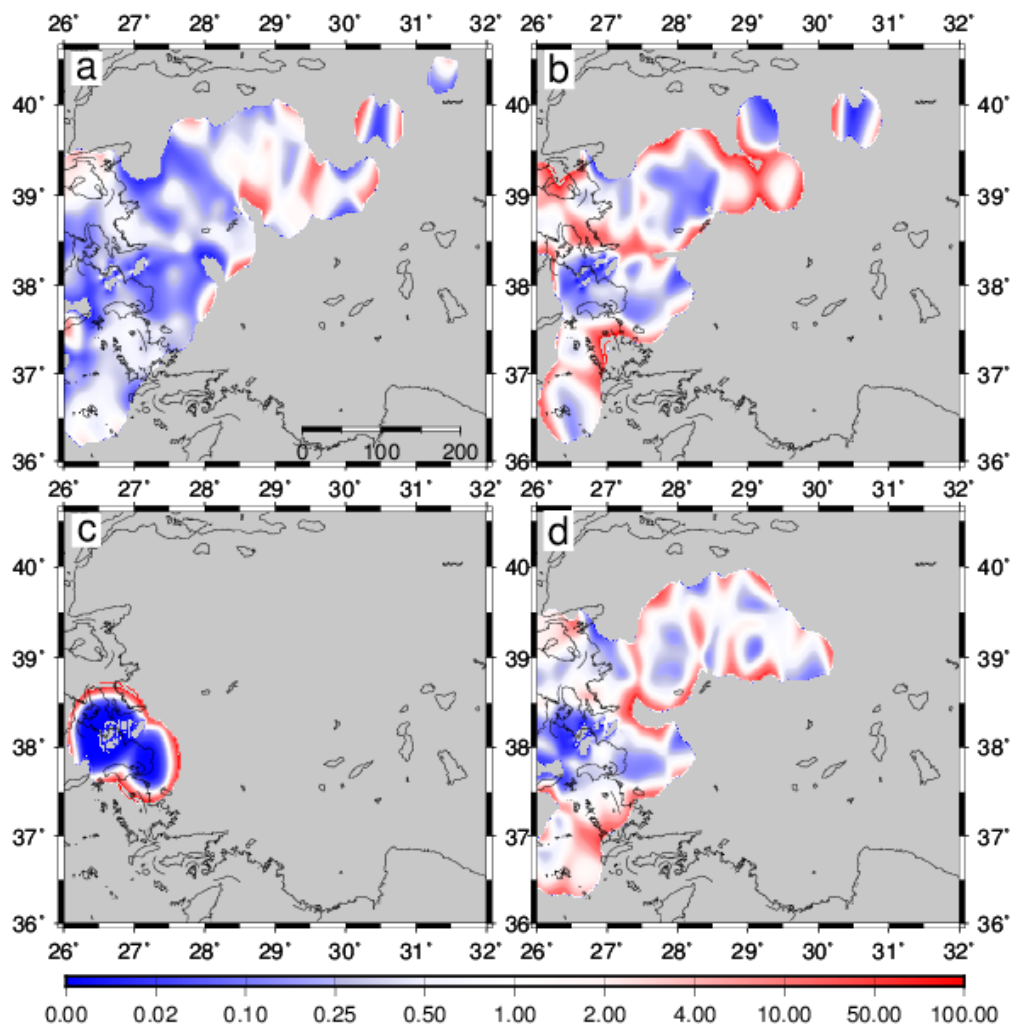


Figure 2.35. Ratio of expected/observed seismicity rates for sub-area 2, for 1992-2003 (upper left frame $\Delta t=10.4$ yrs), 2003-2005a (upper right frame $\Delta t=2.5$ yrs), 2005a-2005b (lower left frame $\Delta t=0.01$ yrs) and 2005b-2010 (lower right frame $\Delta t=5.2$ yrs), with $h=0.10^\circ$, $t_a=15$ yrs and $\dot{\tau}_r=0.04$ bar \cdot yr $^{-1}$ ($A\sigma=0.6$ bar). Red colors show that the expected values are overestimated in comparison with the observed ones whereas blue colors show higher observed seismicity rates than the simulated ones. White areas correspond to ratio value between 0.5-2, suggesting sufficient model performance. Calculations are not performed in gray areas because of data insufficiency.

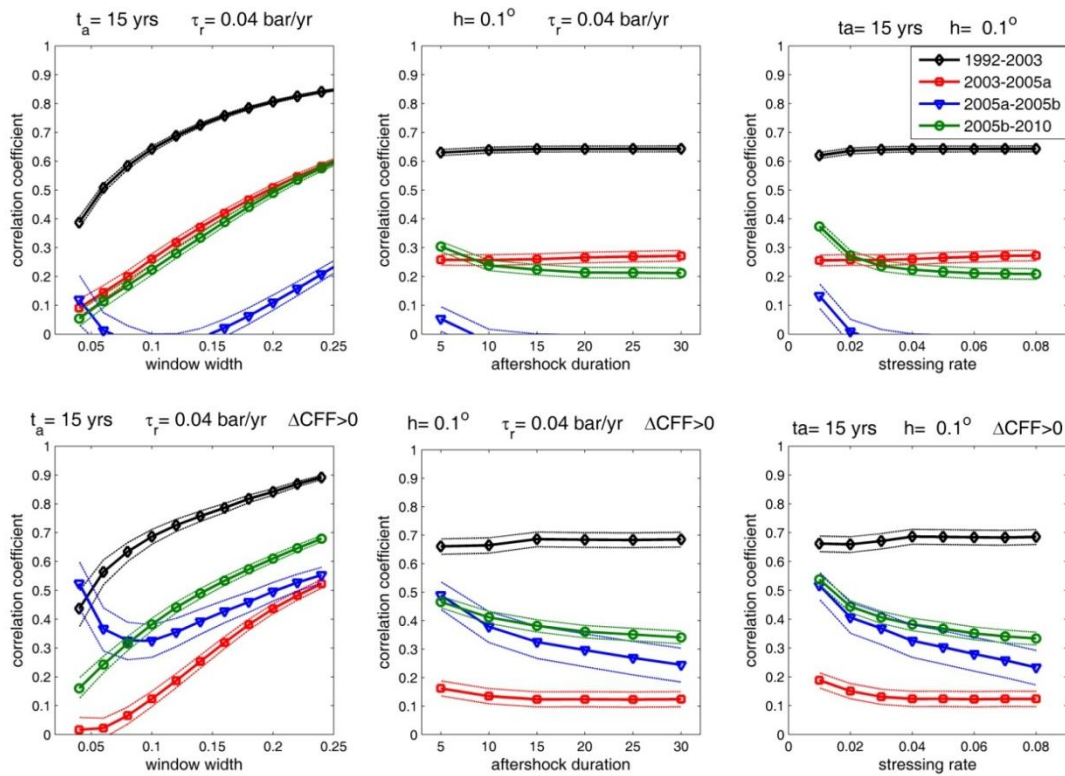


Figure 2.36 Pearson Correlation Coefficient (PCC) estimation (solid lines) and its 95% confidence interval (fainted lines) for subarea 2. Upper frames were obtained from the entire dataset, whereas the lower frames yielded by taking into account only those cells experiencing positive ΔCFF .

In sub-area 3 the coseismic stress changes associated with the 20th July 1996, M6.0 and the 15th July 2008, M6.4 are incorporated to Rate/State model. The first forecast period (1996-2008) exhibits high correlation coefficient especially regarding the cells with positive Coulomb stress changes (Fig. 2.38). Although the next event occurred in stress shadow zone caused by the 1996 mainshock, the observed, smaller magnitude seismicity rates, appear to correlate well with the simulated ones, with many cells having expected/observed seismicity rate ratio close to unity (Fig. 2.37a). The second period (2008-2010) exhibits almost no linear correlation. This is due to the short duration of the time interval (~2.5 years) and the respective small dataset (only 85 events) available. Note that the 2008 event and many of the following ones were located at depths larger than 30km. Many cells that overestimate and underestimate real seismicity are both detected for this period.

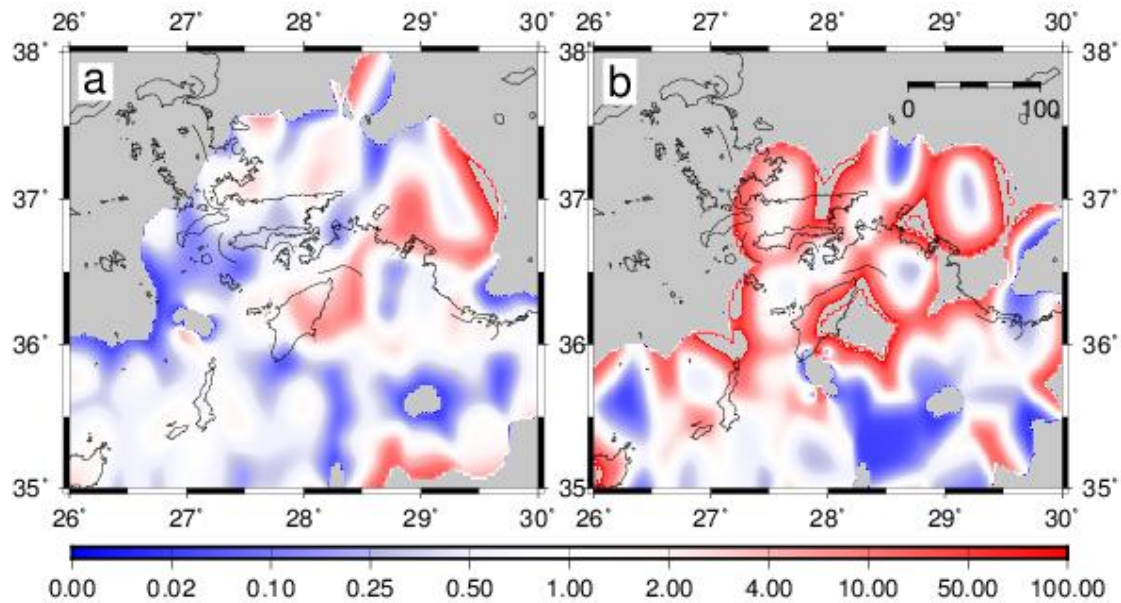


Figure 2.37. Ratio of expected/observed seismicity rates for sub-area 3, for 1996-2008 (left frame $\Delta t=12$ yrs) and 2008-2010 (right frame $\Delta t=2.4$ yrs). Red colors show that the expected values are overestimated in comparison with the observed ones whereas blue colors show higher observed seismicity rates than the simulated ones. White areas correspond to ratio value between 0.5-2, suggesting sufficient model performance. Calculations are not performed in gray areas because of data insufficiency. Parameter values were taken as: $h=0.10^\circ$, $t_a=20$ yrs and $\dot{\tau}_r=0.03$ bar \cdot yr $^{-1}$ ($A\sigma=0.6$ bar).

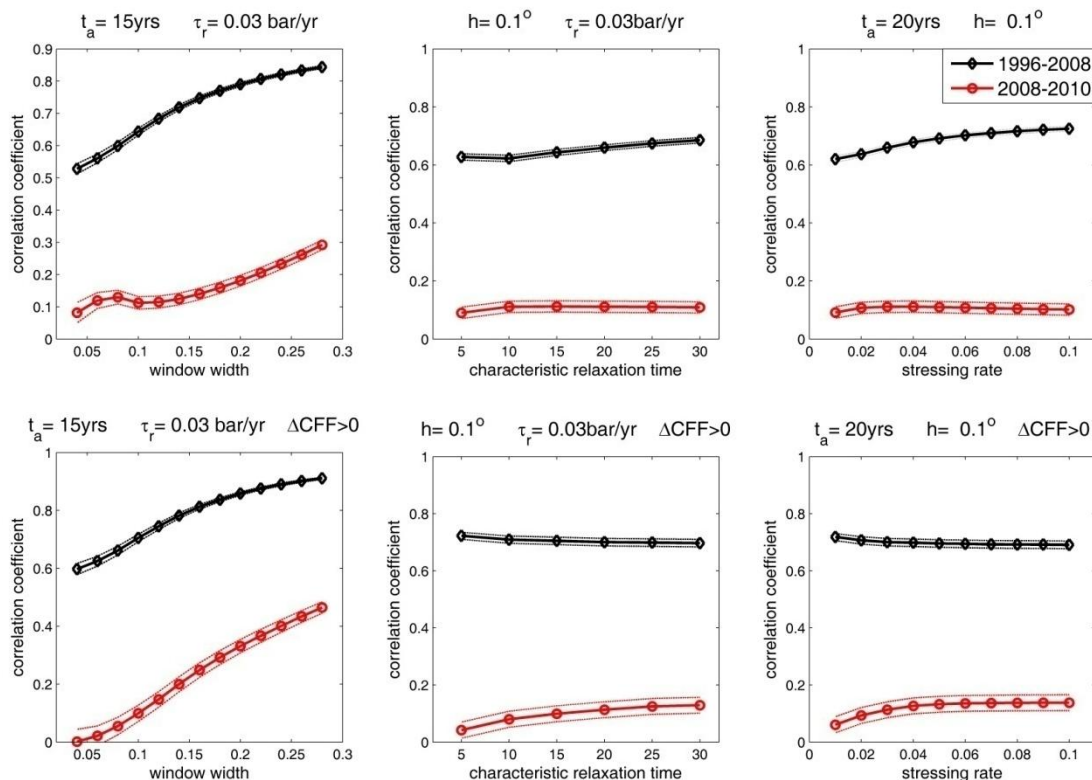


Figure 2.38. Pearson Correlation Coefficient (PCC) estimation (solid lines) and its 95% confidence interval (fainted lines) for subarea 3. Upper frames were obtained from the entire dataset, whereas the lower frames yielded by taking into account only those cells experiencing positive ΔCFF .

Four strong events occurred in sub-area 4 since 1995: The 1st October 1995, M6.3, the 15th December 2000, M6.0, and two events that occurred on the 3rd February 2002 with M6.4 and M5.8, respectively. These 4 events, together with the 2 strong 1999 earthquakes that took place in sub-area 1 are considered to influence seismicity rates here. The spatial distribution of the expected/observed seismicity rates ratios derived for the 4 testing periods are illustrated in Fig. 2.39. The first two periods (1995-1999 & 1999-2000) exhibit relatively strong correlation ($PCC > 0.5$) when the entire data set is considered (Fig. 2.40, upper frames). When calculations are performed only for positive ΔCFF cells (lower frames of Fig. 2.40), the first period (1995-1999) demonstrates even higher efficiency whereas the second one fails to describe at all seismicity that occurred in positive stress lobes. This is one of the rare cases that Rate/State model performs better in stress shadows rather than modeling seismicity enhancements. This may be probably because of the short duration (1.3 years) of this testing period (mostly concerning aftershock productivity), which was abruptly interrupted from the 2000 event. The next two periods (2000-2002 and 2002-2010) demonstrate low correlation which becomes slightly higher for positive ΔCFF (Fig. 2.40).

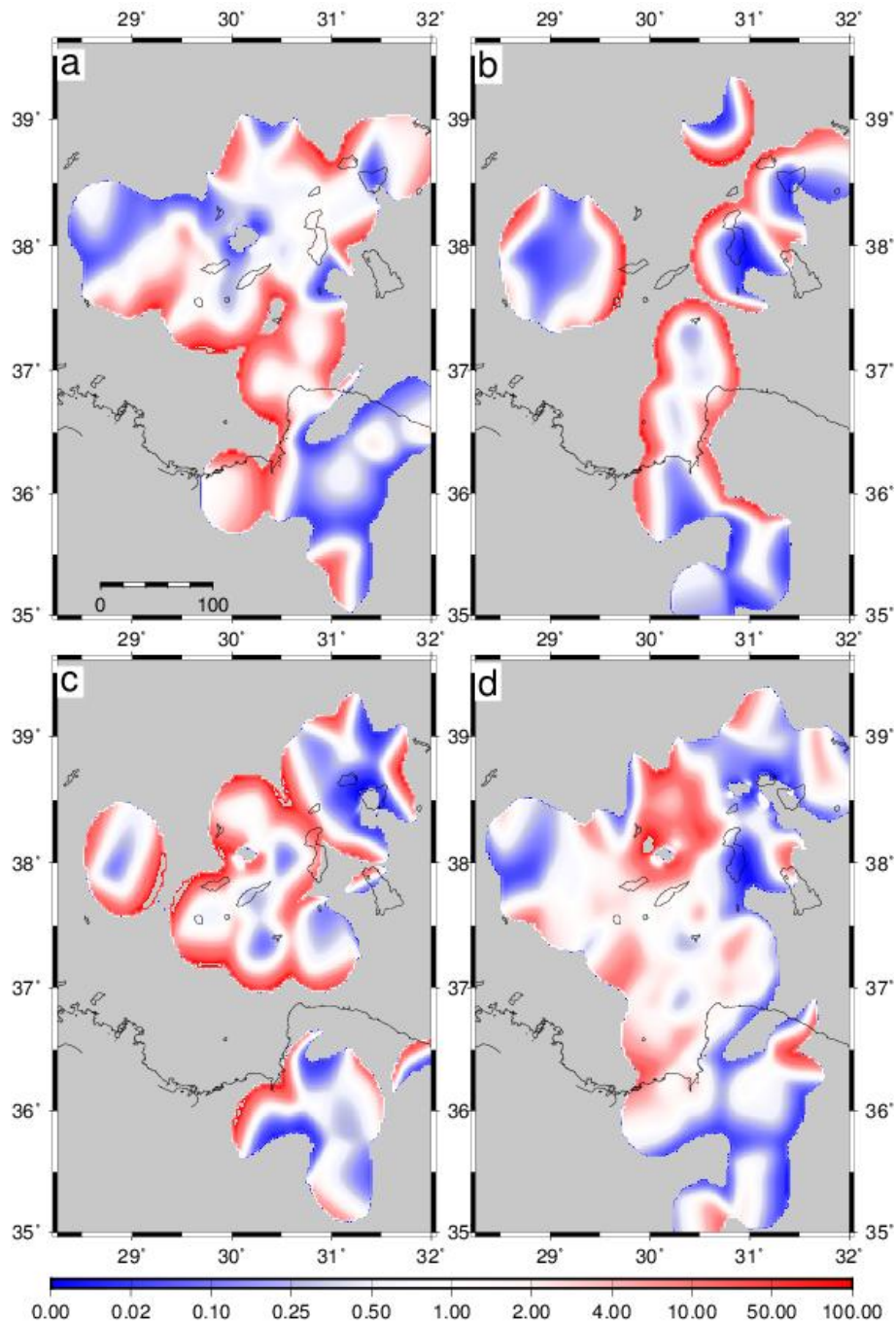


Figure 2.39. Ratio of expected/observed seismicity rates for sub-area 4, for 1995-1999a (upper left frame $\Delta t=3.8$ yrs) and 1999b-2000 (upper right frame $\Delta t=1.3$ yrs), 2000-2002b (lower left frame $\Delta t=1.1$ yrs) and 2002b-2010 (lower right frame $\Delta t=8.9$ yrs). Red colors show that the expected values are overestimated in comparison with the observed ones whereas blue colors show higher observed seismicity rates than the simulated ones. White areas correspond to ratio value between 0.5-2, suggesting sufficient model performance. Calculations are not performed in gray areas because of data insufficiency. Parameters values are taken as: $h=0.11^\circ$, $t_a=20$ yr and $\dot{\tau}_r=0.03$ bar \cdot yr $^{-1}$ ($A\sigma=0.6$ bar).

Once again the model performance is getting better as we go towards lower t_a values (<10 yrs). Note that in 2nd and 3rd periods (1999-2000 and 2000-

2002) the available data are so sparse that calculations have only been performed for approximately half of the entire area. The last period (2002-2010) actually shows many cells with comparable observed and expected seismicity rates, but there are still several bins with large differences which reduce the total correlation coefficient although the simulation is adequate for a considerable part of the region (Fig. 2.43d). The actual PCC for the cells with ratio between 0.4 and 2.5, which occupy the half of the area's cells with calculated values, is 0.864.

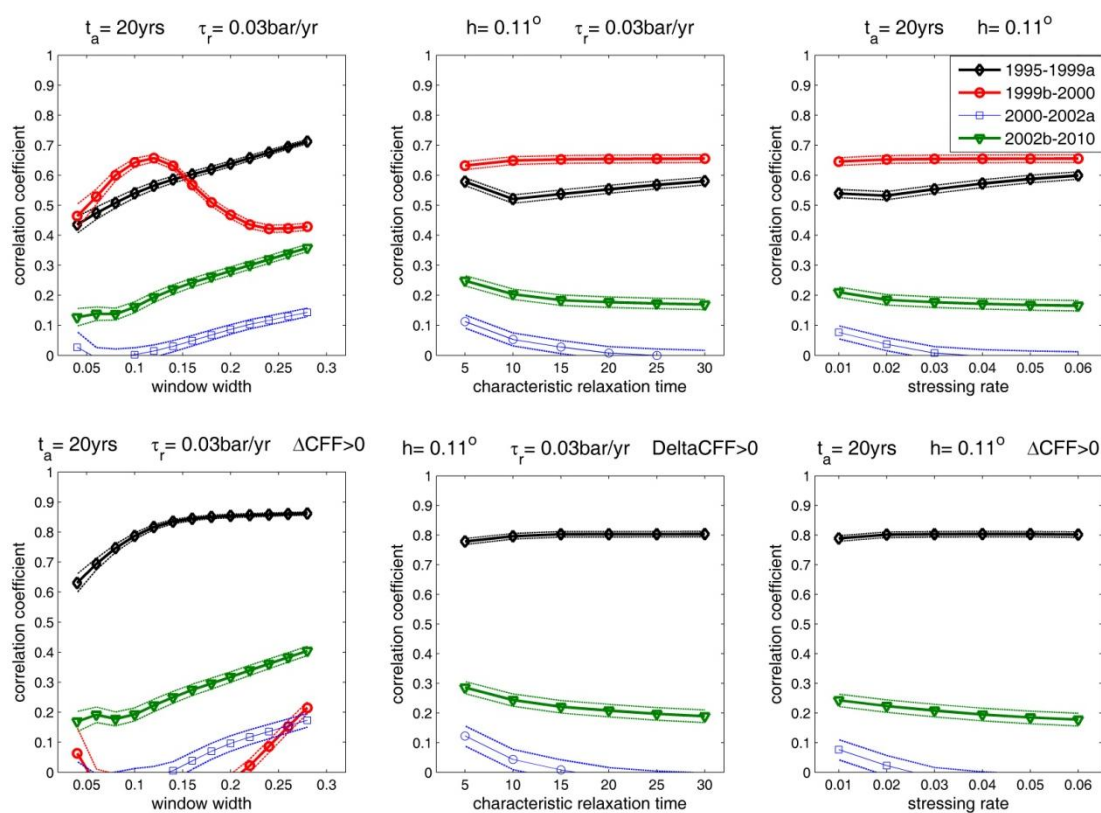


Figure 2.40. Pearson Correlation Coefficient (PCC) estimation (solid lines) and its 95% confidence interval (faint lines) for subarea 4. Upper frames were obtained from the entire dataset, whereas the lower frames yielded by taking into account only those cells experiencing positive ΔCFF .

2.3.4.5 Contribution to Seismic Hazard Assessment

The calculation of exceedance probabilities for earthquakes with $M \geq 6.0$ and $M \geq 6.5$ was also performed separately for each sub-area due to the different completeness threshold of the corresponding datasets. Figure H7 shows the expected seismicity rates after 2010 in sub-area 1 of Western

Turkey. These rates were determined after considering the influence of coseismic (due to $M \geq 6.0$ earthquakes) and long term (tectonic) stress changes on the reference seismicity rates during 1991-1999 ($M \geq 3.7$). The unbounded non-parametric magnitude distribution of the 898 events ($M \geq 3.7$ during 1991-2010) was then considered in connection with the averaged estimated expected seismicity rate, to calculate the exceedance probabilities for the next decade. These probabilities were found equal to 44.8% (with 95% confidence bounds at 34.2% - 49.3%) and 32.6% (with 95% confidence bounds at 30.1% - 33.9%) for an earthquake with magnitude higher than 6.0 and 6.5, respectively. In the eastern part of the area the forecasted seismicity rates are expected to be low because of the stress shadow induced by the 2 strong ($M=7.6$ and $M=7.2$) 1999 events and/or the low reference rate. Contrarily, in the western part of the area the reference seismicity rates have been amplified due to positive stress changes and the earthquake probabilities are high at specified sites.

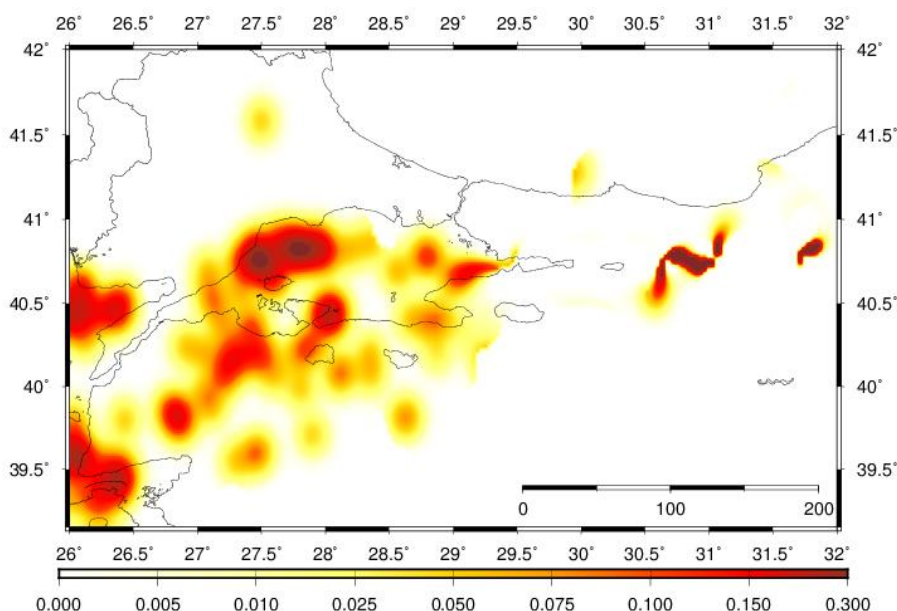


Fig. H7. Snapshot of the expected seismicity rates ($M \geq 3.7$) estimated for the period after 2010 in sub-area 1 of Western Turkey.

The low amount of available seismic data resulted to a spatially limited seismicity rate forecast for sub-area 2 of Western Turkey. The expected

seismicity rates after 2010 are shown in Figure H8. These rates were estimated after considering the influence of coseismic (due to $M \geq 5.8$ earthquakes) and tectonic stress variations on the reference seismicity rates, calculated from the period 1979-1992 ($M \geq 3.8$). The unbounded non-parametric magnitude distribution of the 1782 events ($M \geq 3.8$ during 1979-2010) was then considered in connection with the averaged estimated expected seismicity rate, to calculate the exceedance probabilities for the next decade. These probabilities were found equal to 32.9% (with 95% confidence bounds at 9.5% -46.4%) and 9.5% (with 95% confidence bounds at 1.0% - 18.9%) for an earthquake with magnitude higher than 6.0 and 6.5, respectively. The inadequate data corresponding to the eastern part of the area didn't allow robust expected rate calculations. On the other hand, the reference rates are expected to be considerably enhanced in the western and south-western part of sub-area 2. Nevertheless the calculated probabilities are lower in comparison with the sub-area 1, because strong earthquakes ($M > 6.0$) are not so frequent here.

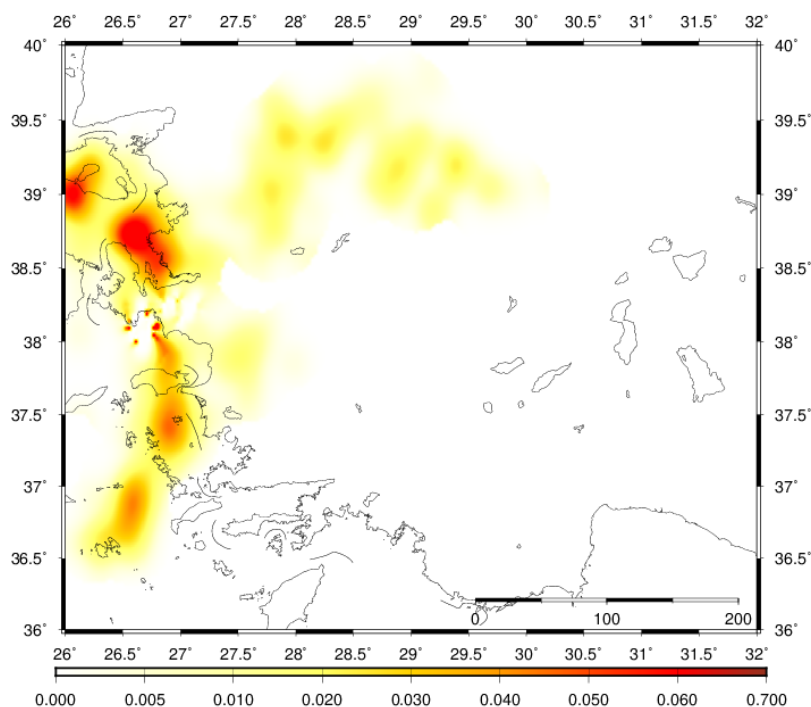


Fig. H8. Snapshot of the expected seismicity rates ($M \geq 3.8$) estimated for the period after 2010 in sub-area 2 of Western Turkey.

The expected seismicity rates after 2010 were estimated for sub-area 3 by considering the influence of coseismic (due to $M \geq 6.0$ earthquakes) and tectonic stress changes on the reference seismicity rates during 1987-1996 ($M \geq 4.1$, Fig. H9). The unbounded non-parametric magnitude distribution of the 1439 events ($M \geq 4.1$ during 1987-2010) was then considered in connection with the averaged estimated expected seismicity rate, to calculate the exceedance probabilities for the next decade. These probabilities were found equal to 58.9% (with 95% confidence bounds at 44.5% - 75.0%) and 30.7% (with 95% confidence bounds at 20.1% - 42.9%) for an earthquake with magnitude higher than 6.0 and 6.5, respectively. As shown in figure H9, the expected rates and consequently the exceedance probabilities are not spatially uniform. The highest probabilities are concentrated in areas in the south coast of Turkey and also in the north, east and south of Karpathos island, whereas in the vicinity of Rhodes Island the estimated probabilities are expected considerably lower.

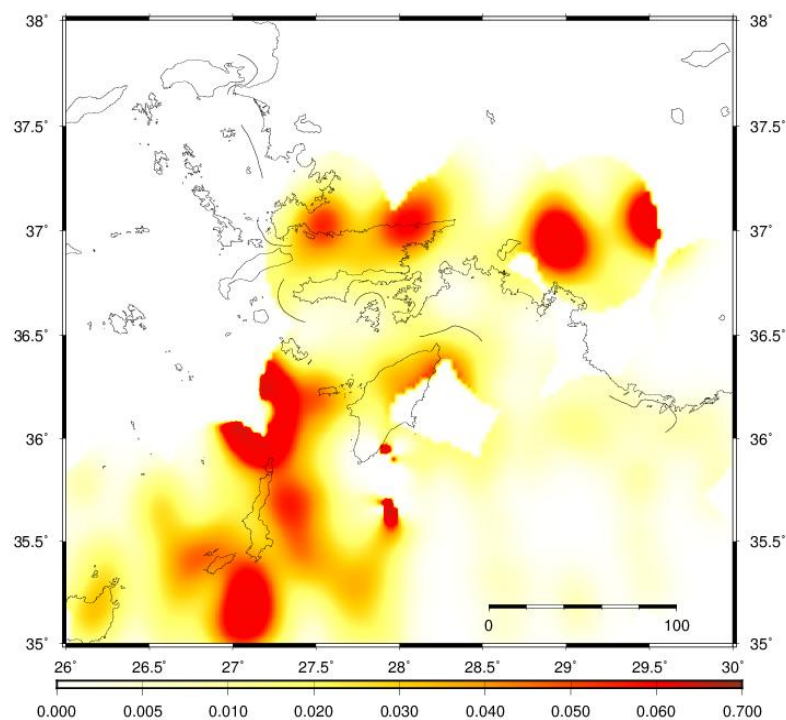


Fig. H9. Snapshot of the expected seismicity rates ($M \geq 4.1$) estimated for the period after 2010 in sub-area 3 of Western Turkey.

Figure H10 shows the expected seismicity rates after 2010 in sub-area 4 of Western Turkey. These rates were determined after considering the influence of coseismic (due to $M \geq 5.8$ earthquakes) and tectonic stress changes on the reference seismicity rates during 1991-1995 ($M \geq 3.7$). The unbounded non-parametric magnitude distribution of the 627 events ($M \geq 3.7$ during 1991-2010) was then considered in connection with the averaged estimated expected seismicity rate, to calculate the exceedance probabilities for the next decade. The expected seismicity rates are very low in this sub-area in comparison with the rest of Western Turkey because the recording levels of seismicity are generally lower here. Nevertheless the frequent occurrence of strong events ($M \geq 5.8$) led to relatively increased earthquake probabilities in comparison with the adjacent areas. These probabilities were found equal to 58.8% (with 95% confidence bounds at 55.4% - 60.9%) and 24.3% (with 95% confidence bounds at 7.8% - 30.8%) for an earthquake with magnitude higher than 6.0 and 6.5, respectively. As evident in Figure 10, the highest expected rates and probabilities are estimated for the central part of the study area.

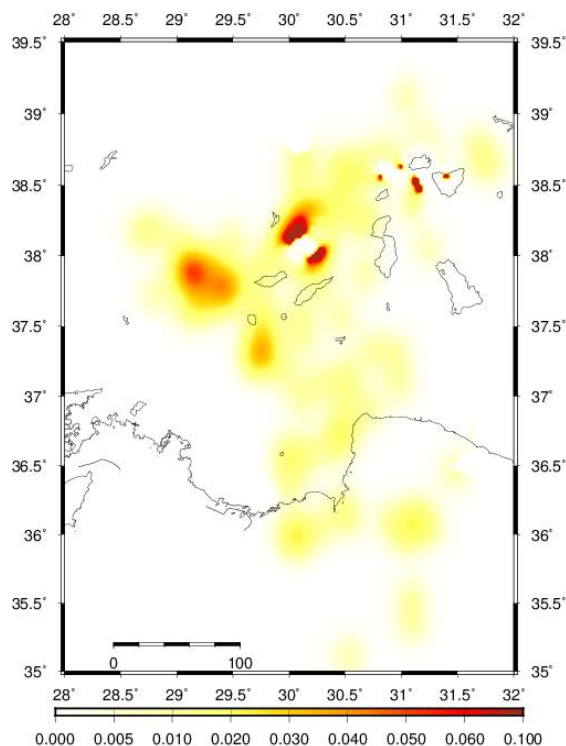


Fig. H10. Snapshot of the expected seismicity rates ($M \geq 3.7$) estimated for the period after 2010 in sub-area 4 of Western Turkey.

2.3.5 Area 5 – North Aegean (4 sub-areas)

2.3.5.1 Introduction

The area of interest in this section comprises the North Aegean Sea, part of the back arc Aegean region (Fig.2.41). The propagation of the North Anatolian fault to the west, sustains the existence of strike slip faults, most of them dextral with NE-SW striking, along the North Aegean Trough (NAT) and parallel fault branches. McKenzie (1970, 1972, 1978) showed that the northward motion of the Arabian plate pushes the smaller Anatolian plate westwards along the North Anatolian fault. The rotation of the Anatolian plate is transferred in the Aegean area as a simple translation, indicated by the subparallel deformational field in this area. This translation occurs along the central and southern part of the coasts of Turkey and the neighboring Greek islands (Karakostas et al., 2010). The back-arc extension of the Aegean due to the subduction of the Eastern Mediterranean oceanic plate under the Eurasian (Papazachos and Comninakis, 1971) is the second but most prominent dominant effect in the region. Superposition of these two deformation fields yields an extension increase in the back arc region, leaving almost no significant contraction and reverse faulting in the Aegean. The region exhibits the highest deformation rates and seismicity, moving rapidly towards the SW, due to the combined effect of Anatolia westward motion and subduction rollback (Armijo et al., 2003; Flerit et al., 2004; Papazachos et al., 2006).

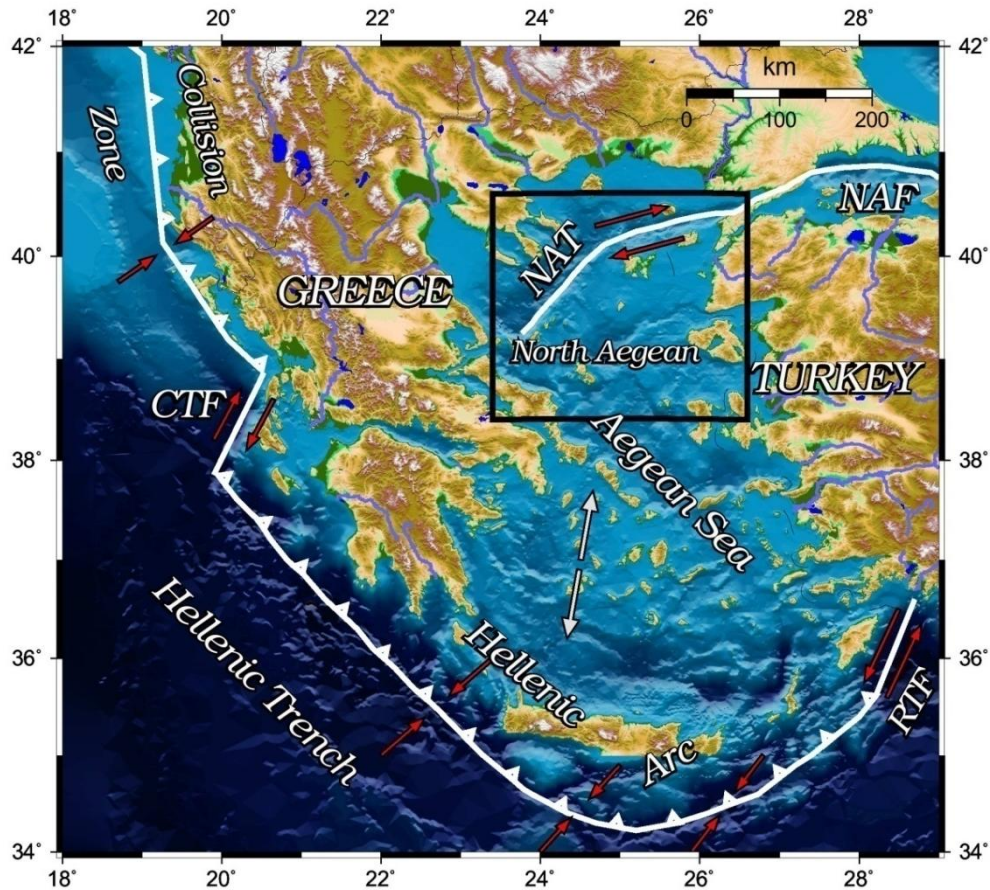


Fig. 2.41. Main seismotectonic properties of the Aegean Sea and the surrounding area. NAF, North Anatolian Fault; NAT, North Aegean Trough; CTF, Cephalonia Transform Fault; RTF, Rhodes Transform Fault. Rectangle indicates the study area.

Frequent strong earthquakes in the study area are known from both instrumental and historical data. Since 1964, 11 strong earthquakes ($M \geq 5.8$) occurred in the study area with eight of them being associated with dextral strike slip faulting, two with oblique normal faulting and one with sinistral strike slip fault. As it is shown in figure 2.42, most of these earthquakes are associated with the regional major faults. The keen interest for the area's seismic hazard assessment led to the several studies accomplished, among them being the ones based upon the stress field changes and evolution, which proved to be appropriate to explain the strong events occurrence (Nalbant et al., 1998; Papadimitriou and Sykes, 2001, Leptokarpoulos et al., 2012, among others). These stress changes are also expected to influence the occurrence rates of smaller magnitude seismicity, mostly concentrated along the North

Aegean Trough and onto the well defined sub-parallel branches, as well as in the south-eastern part where the seismicity is more diffused (Fig. 2.42).

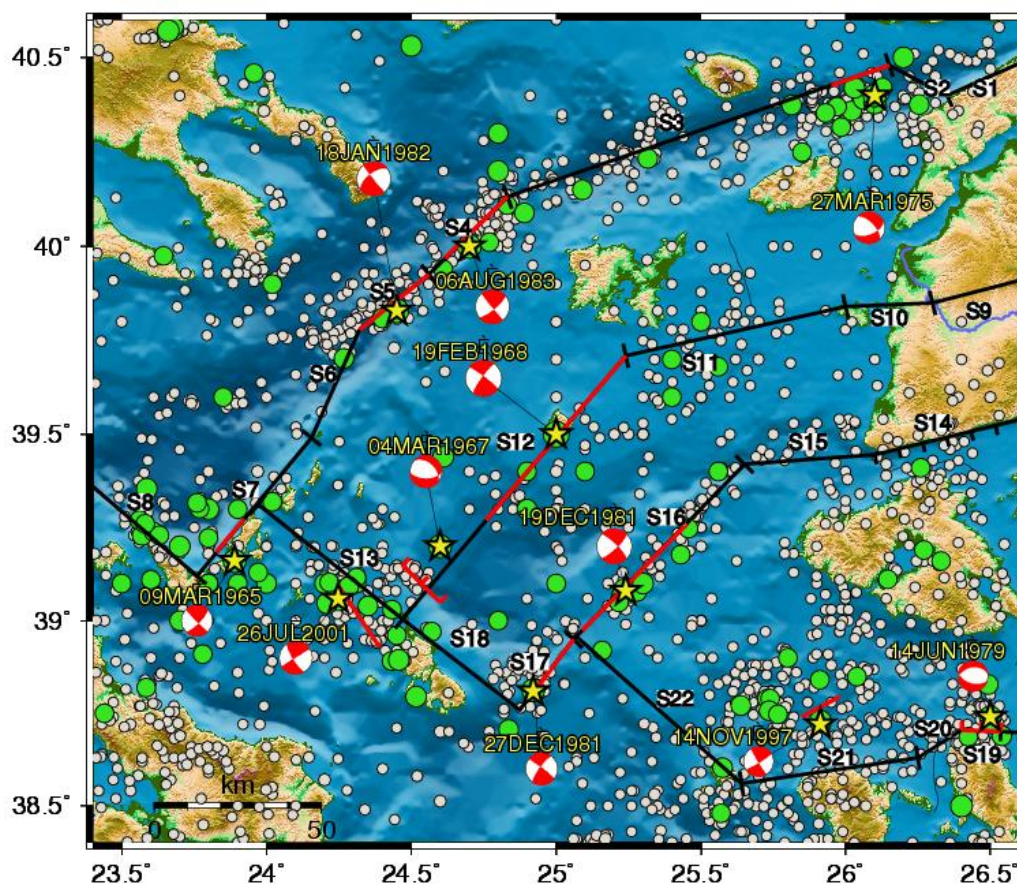


Fig. 2.42. Major faults of the northern Aegean along with $M \geq 4.1$ seismicity from 1970-2010 (indicated as grey circles). Stronger earthquakes with $M \geq 5.0$ are denoted as green circles. The focal mechanisms of $M \geq 5.8$ earthquakes (yellow asterisks indicate their epicenters) are also shown. The occurrence date of each one of the strongest events is shown above the beach balls. Black lines represent the major fault segments with their code names. Geometric and kinematic properties of these segments are shown at Table 2.12. Red lines show the fault segments that have been ruptured since 1965, and are associated with $M \geq 5.8$ earthquakes.

2.3.5.2 Data

The data utilized in this section were taken from the Hellenic Unified Seismological Network (HUSN). The time interval of investigation covers a period of approximately 33 years (19 December 1981 - 31 December 2012), with a reference seismicity from the beginning of 1970 up to 19 December 1981 (12 years learning period), when an increased activity started with multiple strong ($M \geq 6.0$) main shocks. It is well accepted that going back in time leads to lower quality and adequacy of data in comparison with the

more recently obtained ones. Past data have to be treated with caution in order to ensure their reliable completeness magnitude, M_c , and at the same time to certify the largest possible data sample. For this reason the calculations were performed separately on data coming from each sub-area. The division of these sub-areas was done by taking into account their particular features (M_c , fault orientation and slip direction, stressing rate). Figure 2.43 shows the selected sub-areas along with the seismicity distribution ($M \geq M_c$) from 1970 to 2010.

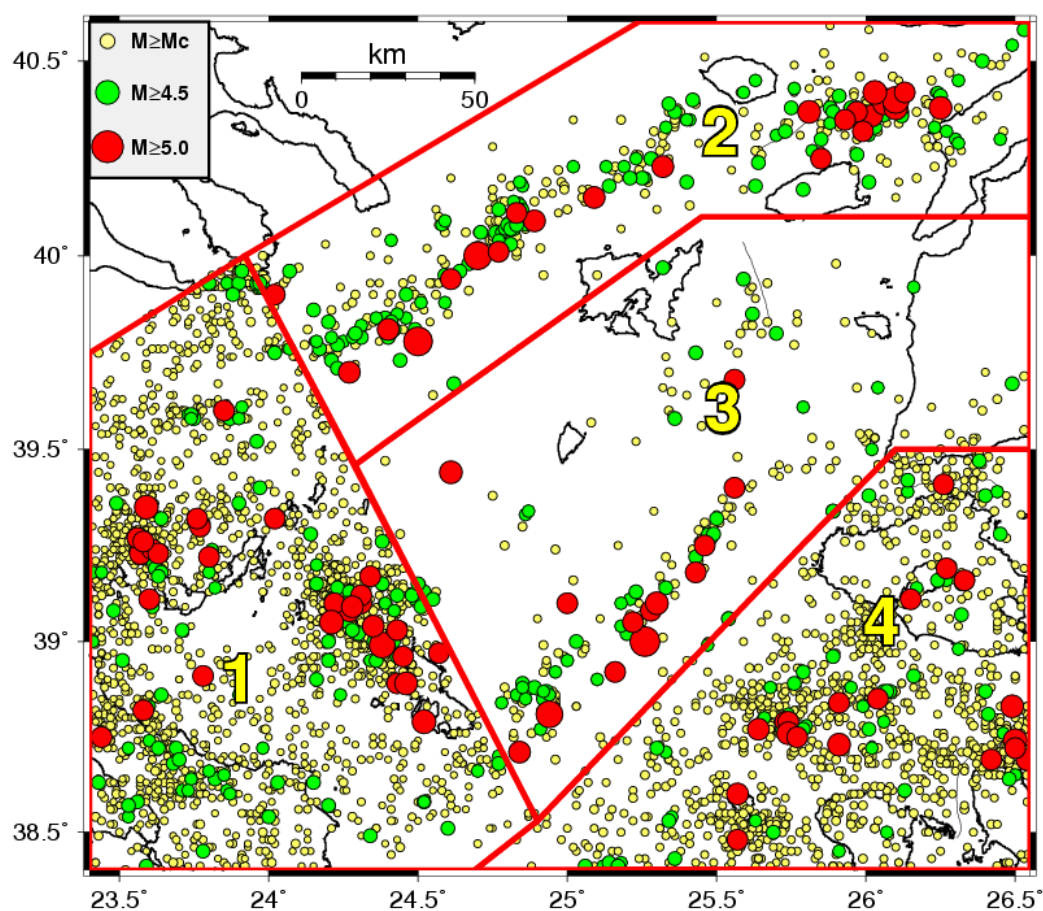


Fig. 2.43. Division of the North Aegean into 4 sub-areas according to seismotectonic similarities: 1: Sporades, 2: North Aegean Trough (NAT), 3: Central Area, 4: Chios – Lesvos. Seismicity between 1970–2010 with $M \geq 5.0$ is indicated as red circles, $4.5 \leq M < 5.0$ as green circles and $M_c \leq M < 4.5$ as yellow circles. M_c was individually estimated in each case and is $M_{1c}=3.5$, $M_{2c}=4.1$, $M_{3c}=4.1$, $M_{4c}=3.8$, respectively.

The magnitude of completeness was evaluated separately by the modified Goodness-of-Fit test (MGFT) proposed by [Leptokaropoulos et al](#),

2013. This method was applied for the learning period and for posterior periods, in order to investigate the time dependency of the FMD. The examination of the FMD for different periods showed that there is an obvious difference between the number of events (individual and cumulative) during the learning period, and the consequent ones for all the 4 sub-areas with the learning period contains less events than the following ones of the same duration (12-year periods), although the gradients of the decay (b-values) are almost identical. This procedure resulted to a $M_c=3.5$ in sub-area 1, $M_c=4.1$ in sub-areas 2 and 3 and $M_c=3.8$ in sub-area 4. Coulomb stress changes were calculated from the coseismic displacements of the stronger ($M \geq 5.8$) events that occurred in the study area during the testing period (19 December 1981 – 31 December 2012), for which information on the source parameters is given in Table 2.12.

Table 2.12. Source parameters of the 6 earthquakes with $M \geq 5.8$ modeled for coseismic Coulomb static stress changes calculations.

Event	Date	Epicentral Coordinates	M_w	M_0 ($\cdot 10^{25}$ dyn·cm)	Focal Mechanism			Reference
					Strike($^\circ$)	Dip($^\circ$)	Rake($^\circ$)	
1981	Dec 19	39.000 $^\circ$ N 25.600 $^\circ$ E	7.2	22.4	47	77	-167	1
1981	Dec 27	38.313 $^\circ$ N 24.941 $^\circ$ E	6.5	3.82	216	79	175	2
1982	Jan 18	38.780 $^\circ$ N 24.500 $^\circ$ E	7.0	7.32	233	62	-177	2
1983	Aug 06	40.700 $^\circ$ N 24.600 $^\circ$ E	6.8	12.1	50	76	177	1
1997	Nov 14	38.729 $^\circ$ N 25.913 $^\circ$ E	5.8	0.404	58	83	175	3
2001	Jul 26	39.066 $^\circ$ N 24.248 $^\circ$ E	6.4	5.61	148	76	-1	4

1: Kiratzi et al. (1991), 2: Taymaz et al. (1991), 3: Louvari et al. (2000), 4: Global CMT

2.3.5.3 Parameters values

In this application we considered a steady stressing rate on each fault segment, uniform throughout the seismogenic layer (both along strike and dip direction). The estimated values of the stressing rate at the center of each fault segment (Table 2.13) vary from 0.0093bar/yr to 0.14bar/yr, as they were defined from geodetic data analysis (McClusky et al., 2000; Reilinger et al., 2006) assuming 60% of the geodetic slip value to account for the seismic part of the secular tectonic motion (Fig. 2.44). This comparatively narrow range is

due to the fact that the geometric and kinematic properties of the fault segments were set as constraint in the division of the area and therefore each one of the sub-areas includes faults with similar values of stressing rate. The average values of $\dot{\tau}$ were found to be 0.03, 0.10, 0.04 and 0.025 bar/yr for the subareas 1 through 4, respectively. The aforementioned values appear to be in agreement with the ones estimated by [Straub et al. \(1997\)](#), [Stein et al. \(1997\)](#) and [Parsons et al. \(2004\)](#), which range between 0.01-0.15 bar/yr, for the NAF segments. Moreover, a larger range of values (0.005 bar/yr – 0.15 bar/yr) was applied in order to test the sensitivity of the Rate/State model in stressing rate fluctuation and also to take into consideration a different potential value of seismic coupling. The characteristic relaxation time was selected to be between 5–25 years (see section 2.2.4). The previously mentioned values of stressing rate and characteristic time yield to a wide range of $A\sigma$ values, between 0.025 and 3.75 bars. In the following calculations h-values between 0.04° to 0.24° were considered (or alternatively radii of 4.5km to 26.7km). Seismogenic layer in the study area was found lying between 3–15 km, as it comes from the strongest, well located events in the HUSN catalogue and also from studies of aftershock sequences with accurate depth determinations ([Karakostas et al., 2010](#)). All ΔCFF calculations were done at the depth of 8 km, which represents approximately the nucleation depth. The apparent friction coefficient was set $\mu'=0.4$ whereas the shear modulus, G , and Poisson's ratio, ν , were fixed at $3.3 \cdot 10^5$ bar and 0.25, respectively.

Table 2.13. Information on the major regional fault segments (Fig. 2.44) on which tectonic loading is considered for the Rate/State model calculations. Columns represent in turn: the code name of segment, its boundaries, strike, dip, rake, length, width, sense of slip (RL for right lateral, LL for left lateral, Ob: for oblique), slip components along strike (positive for sinistral slip) and vertical to it (positive for normal slip) and the stressing rate.

SN	Fault Boundaries				Strike (°)	Dip (°)	Rake (°)	Length (km)	Width (km)	Type of slip	SS (mm/y)	DS (mm/yr)	Stressing Rate (bar/yr)
	°N	°E	°N	°E									
S1	40.49	26.60	40.40	26.35	68	55	-145	33	19	RL	-12.0	0.6	0.074153
S2	40.40	26.35	40.48	26.15	119	60	-145	19	17	RL	-12.0	3.0	0.072104
S3	40.48	26.15	40.132	24.832	68	55	-145	121	18	RL	-12.0	3.0	0.064454
S4	40.132	24.832	39.926	24.56	50	76	177	33	15.5	RL	-12.0	-0.6	0.086432
S5	39.926	24.56	39.78	24.322	233	62	-177	26	17	RL	-12.0	-0.6	0.086432
S6	39.78	24.322	39.49	24.155	204	75	-175	34	15.5	RL	0.0;	6.6;	0.013454
S7	39.49	24.155	39.12	23.76	44	75	175	55	15.5	RL	0.0;	6.6;	0.002511
S8	39.12	23.76	39.36	23.40	130	68	-6	41	16	LL	0.0	5.4	0.014618
S9	39.91	26.60	39.85	26.30	76	90	177	26	15	RL	-0.6	1.2	0.007993
S10	39.85	26.30	39.84	26.00	89	90	177	26	15	RL	-0.6	1.2	0.007993
S11	39.84	26.00	39.71	25.24	78	68	-156	67	16	RL	-0.6	1.2	0.009311
S12	39.71	25.24	39.005	24.47	216	81	173	102	15	RL	-1.5	0.0	0.014660
S13	39.005	24.47	39.312	23.97	128	76	-1	57	15.5	LL	0.0	4.8	0.005885
S14	39.539	26.60	39.445	26.10	76	46	-70	43	21	Ob	-0.6	1.2	0.005797
S15	39.445	26.10	39.42	25.65	86	46	180	38	21	RL	-0.6	1.2	0.005933
S16	39.42	25.65	38.95	25.06	47	77	-167	72	15	RL	-7.2	1.2	0.067970
S17	38.95	25.06	38.758	24.874	216	79	175	26	15	RL	-7.2	1.2	0.080075
S18	38.758	24.878	39.005	24.47	128	76	-1	44	15.5	LL	0.0	4.8	0.006189
S19	38.698	26.61	38.705	26.40	91	55	-108	17	14	Ob	0.0	3.6	0.024650
S20	38.705	26.40	38.63	26.25	59	74	-168	14	15.5	RL	0.7	3.6	0.003201
S21	38.63	26.25	38.56	25.64	81	69	-168	54	16	RL	0.7	3.6	0.004018
S22	38.56	25.64	38.96	25.065	131	73	-12	66	15.5	LL	0.0	4.8	0.013728

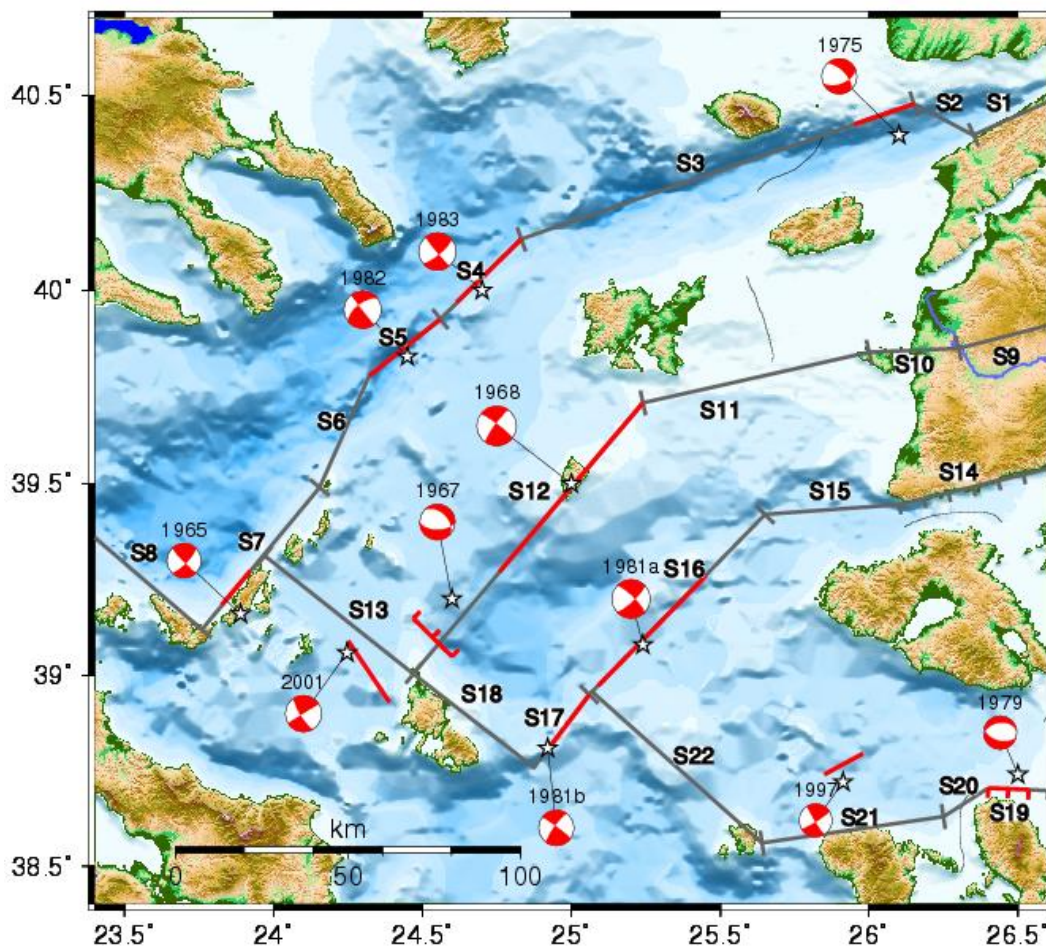


Figure 2.44. Major fault segments in North Aegean area and their code names (Table 2.12).

2.3.5.4 Results – Discussion

Rate/State formulation as it was discussed in Section 2.2, provided the values of expected seismicity rates after a main shock, which were compared with the real seismicity rates in the interevent periods as they yielded from PDF equations. Qualitative and quantitative correlations in the four sub-areas are shown in figures 2.45 through 2.52. Some interesting conclusions can be retrieved for sub-areas 1 and 4, where much more data are available. In general, regions with high observed rates can be modeled, as it appears that they are expected to accommodate events on higher rates. Areas with higher expected rates as resulted from model application seem to fit well with characteristic earthquake clusters shown in real seismicity figures. There are still some areas of low seismicity rate expectance where much higher activity

was observed. Most of these cases are either related with regions of low reference seismicity rates or found very close to faults that failed i.e. areas of loosely constrained ΔCFF . Regarding sub-areas 2 and 3, some sort of correlation can be obtained locally (especially in sub-area 2), but in general the data are insufficient to provide a reliable comparison.

More interesting are the figures showing the quantitative correlation, as they provide a measure for comparison between the real and synthetic data sets. Figures 2.46, 2.48, 2.50 and 2.52 show the values of PCC along with their 95% confidence intervals derived for the interevent times for different sets of parameter values. The upper frames show the correlation yielded by taking into consideration all the cells of the grid, except those with extremely low values of seismicity rates (< 0.0005 events/cell·yr), whereas their lower frames show the respective values of correlation coefficients by taking into account only those cells with positive Coulomb stress changes after a strong event. The correlation coefficient is generally increasing as the bandwidth value is getting higher, a fact rather expected, because high values of h tend to smooth the seismicity rates in the entire area, with the differences between the cells gradually disappearing. Regarding the characteristic time and stressing rate (or $A\sigma$), it yields that their influence is minor, except perhaps at their lowest values.

Seismicity rate simulation results for sub-area 1 are shown in figures 2.45 and 2.46. This sub-area exhibits the lowest completeness level of seismicity data ($M_c=3.5$) and is expected to provide the higher quality results. The first two periods demonstrate low correlation coefficient because of the inadequate data contained in the short time increments (20 days and 1.5 year, respectively). However, improved correlation is demonstrated for the two later periods especially the last one (2001-2010). For this period the correlation coefficients are also much higher for cells that experience positive ΔCFF . This means that the method can adequately predict seismicity rate enhancement in

areas with increased stress. There is still a significant number of earthquakes that occurred in regions with stress decrease. Such events seem to be better modeled in the third period (1983-2001) where the mean PCC was higher when applied to the whole dataset, rather than for positive ΔCFF areas.

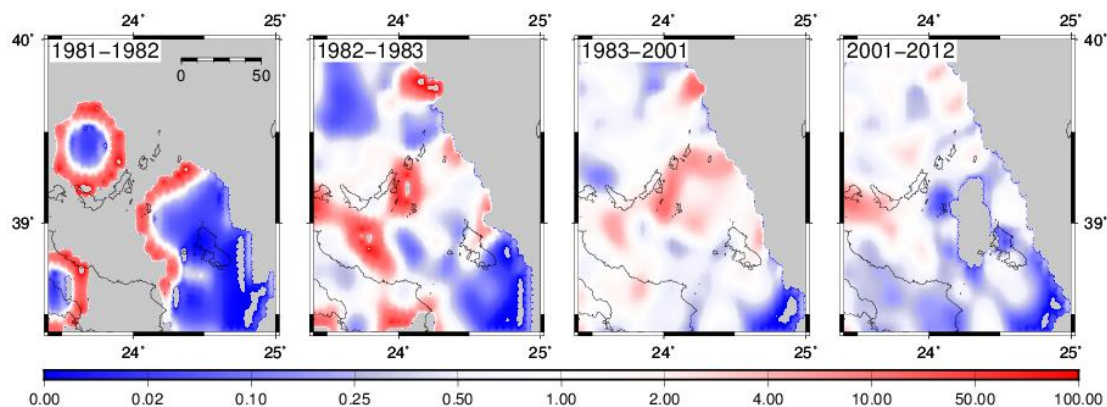


Fig. 2.45. Ratio of expected/observed seismicity rates for North Aegean sub-area 1 for the 4 study periods tested. Red colors show that the expected values are overestimated in comparison with the observed ones whereas blue colors show higher observed seismicity rates than the simulated ones. White areas correspond to ratio value between 0.5-2, suggesting sufficient model performance. Calculations are not performed in gray areas because of data insufficiency. Parameters values are taken as: $h=0.06^\circ$, $t_a=15\text{yr}$, $\dot{\tau}_r=0.03\text{bar/yr}$ ($A\sigma=0.45\text{bar}$). Seismicity data used includes events with $M\geq 3.5$.

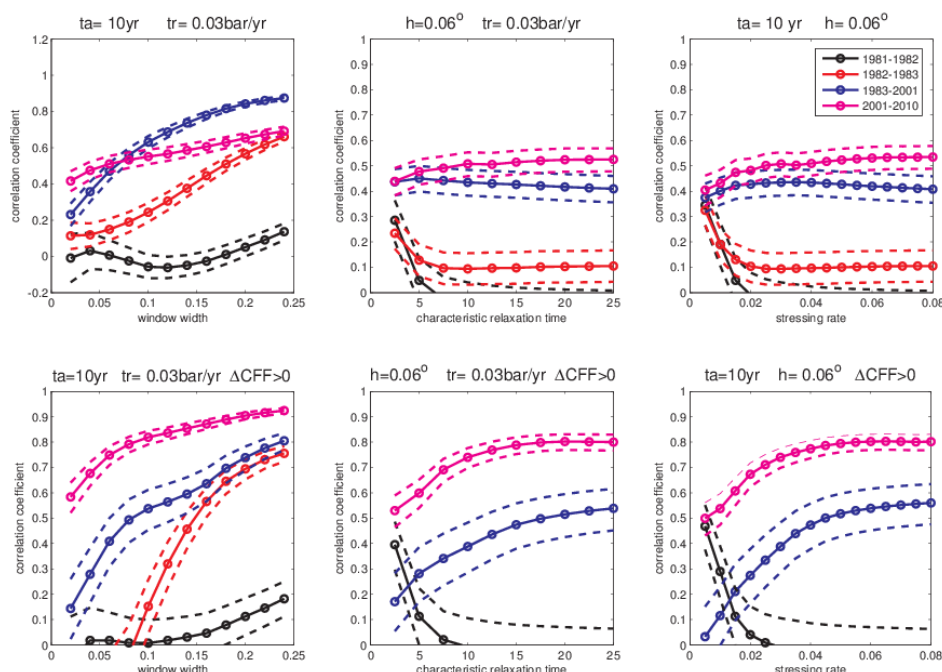


Fig. 2.46. Quantitative evaluation of the difference between observed-synthetic seismicity rates in sub-area 1, (Sporades), during the interevent periods (colored lines). Solid lines indicate the value of Pearson linear Correlation Coefficient (PCC) while dashed lines indicate its lower and upper bounds for a 95% confidence interval for each coefficient. Sub-figures a, b, and c, yielded from the whole data, while sub-figures d, e and f, by taking into account only those cells which experience positive ΔCFF .

In sub-area 2, there is moderate to low correlation for the two earlier periods (Fig. 2.47 and Fig. 2.48). The third period provides better correlation with the PCC being stably higher than 0.70 and remains almost unaffected from the selection of positive Δ CFF cells or all cells. For cells experiencing positive stress changes the correlation is improved for the second period although the confidence intervals are wider. Lower correlations were derived from sub-area 3 (Fig. 2.49 and Fig 2.50), the area with the smallest data sample. This fact is reflected to the results demonstrating correlation coefficients values below 0.4 in almost all the cases. The confidence intervals are also much wider because of the smaller sample size. Even for positive Δ CFF cells the maximum value of the achieved correlation coefficient is very low. Therefore, the model fails to simulate the seismicity rate changes into this specific sub-area. These weakly correlated results in sub-area 3 are probably due to the limited data sample ($M_c=4.1$). However, in sub-area 2 there is a larger number of available data than in sub-area 3, because the respective fault segments exhibit 2.5 times higher stressing rates and consequently seismicity rates are higher in the same magnitude increments. This explains the fact that the mean correlation coefficient is quite higher in sub-area 2, although data with the same magnitude of completeness is applied.

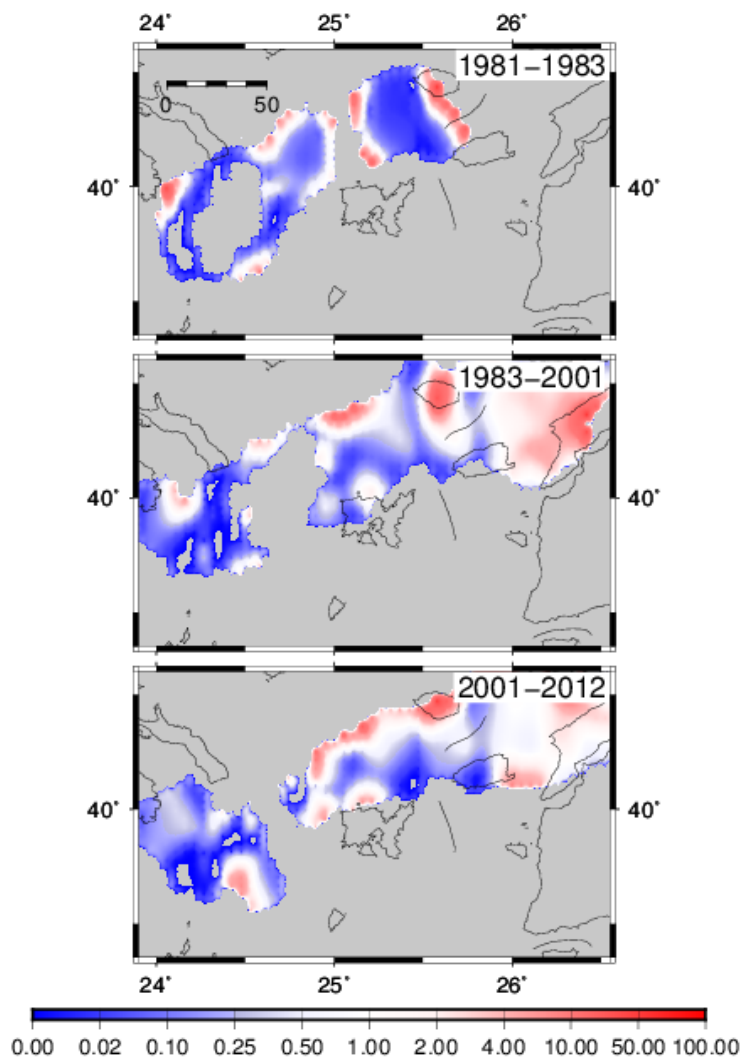


Fig. 2.47. Ratio of expected/observed seismicity rates for North Aegean sub-area 2 for the 3 study periods tested. Red colors show that the expected values are overestimated in comparison with the observed ones whereas blue colors show higher observed seismicity rates than the simulated ones. White areas correspond to ratio value between 0.5-2, suggesting sufficient model performance. Calculations are not performed in gray areas because of data insufficiency. Parameters values are taken as: $h=0.06^\circ$, $t_a=5\text{yr}$, $\dot{\tau}_r=0.10\text{bar/yr}$ ($A\sigma=0.5\text{bar}$). Seismicity data used includes events with $M\geq 4.1$.

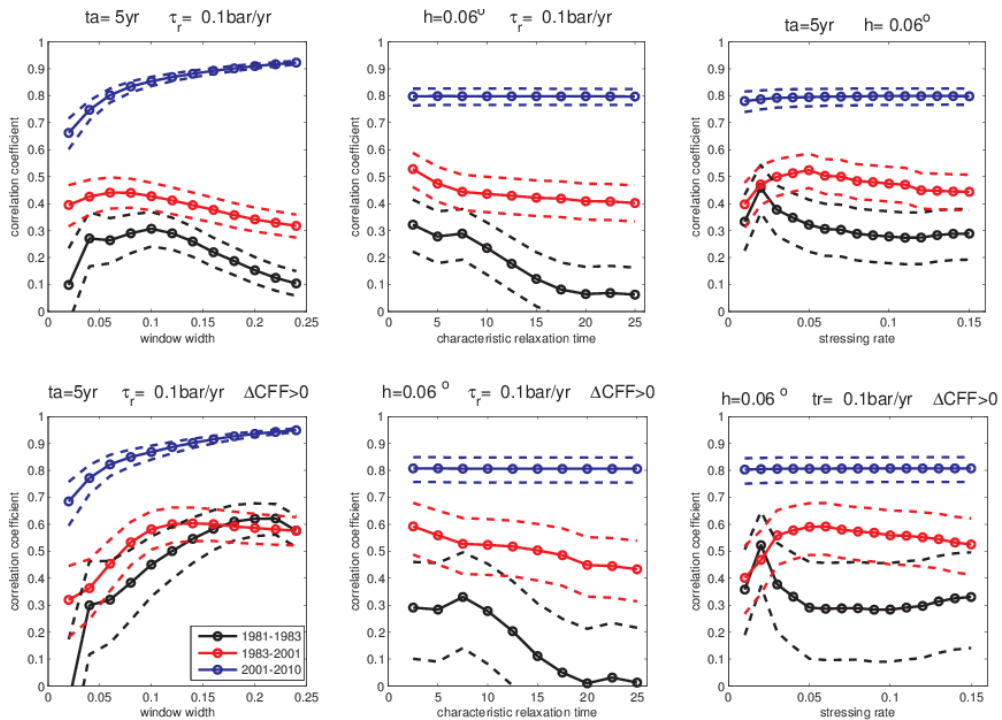


Fig. 2.48. Quantitative evaluation of the difference between observed-synthetic seismicity rates in sub-area 2, (NAT), during the interevent periods (colored lines). Solid lines indicate the value of Pearson linear Correlation Coefficient (PCC) while dashed lines indicate its lower and upper bounds for a 95% confidence interval for each coefficient. Sub-figures a, b, and c, yielded from the whole data, while sub-figures d, e and f, by taking into account only those cells which experience positive ΔCFF .

In the 4th sub-area only two periods were tested because the influence of 1982, 1983 and 2001 strong earthquakes is negligible. Absence of $M \geq 6.0$ event since 1949 gives significant stress changes being connected with the 1997, $M=5.8$ earthquake. Strong events that took place in adjacent fault systems (1981 events, sub-area 3) also seem to simulate well seismicity rate changes. Results (Fig. 2.51 and 2.52) show a quite high correlation coefficient especially regarding the cells which experience positive Coulomb stress changes and even higher correlation after the 1997 shock. Once more, there are still many earthquakes that occurred in stress shadows during both study periods.

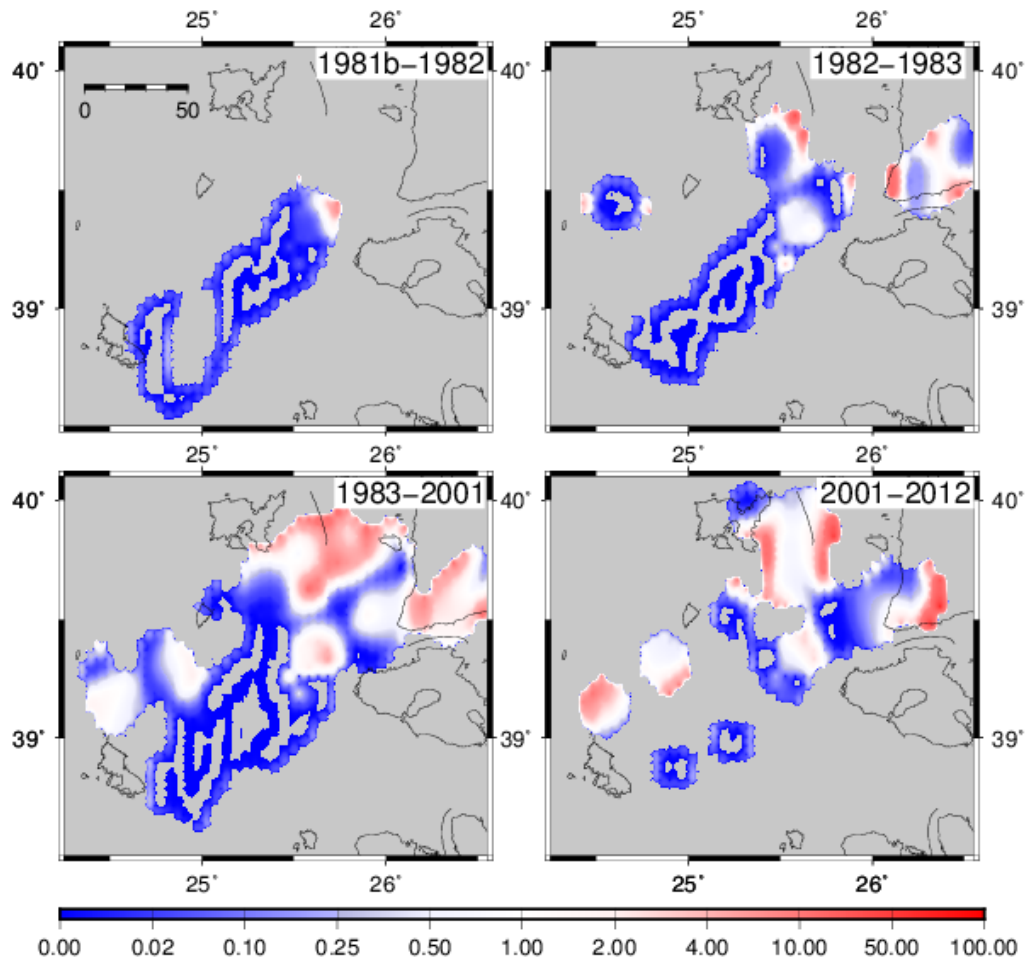


Fig. 2.49. Ratio of expected/observed seismicity rates for North Aegean sub-area 3 for the 4 study periods tested. Red colors show that the expected values are overestimated in comparison with the observed ones whereas blue colors show higher observed seismicity rates than the simulated ones. White areas correspond to ratio value between 0.5-2, suggesting sufficient model performance. Calculations are not performed in gray areas because of data insufficiency. Parameters values are taken as: Parameters applied are $h=0.06^\circ$, $t_a=10\text{yr}$, $\tau_r=0.04\text{bar/yr}$ ($A\sigma=0.4\text{bar}$). Seismicity data used includes events with $M\geq 4.1$.

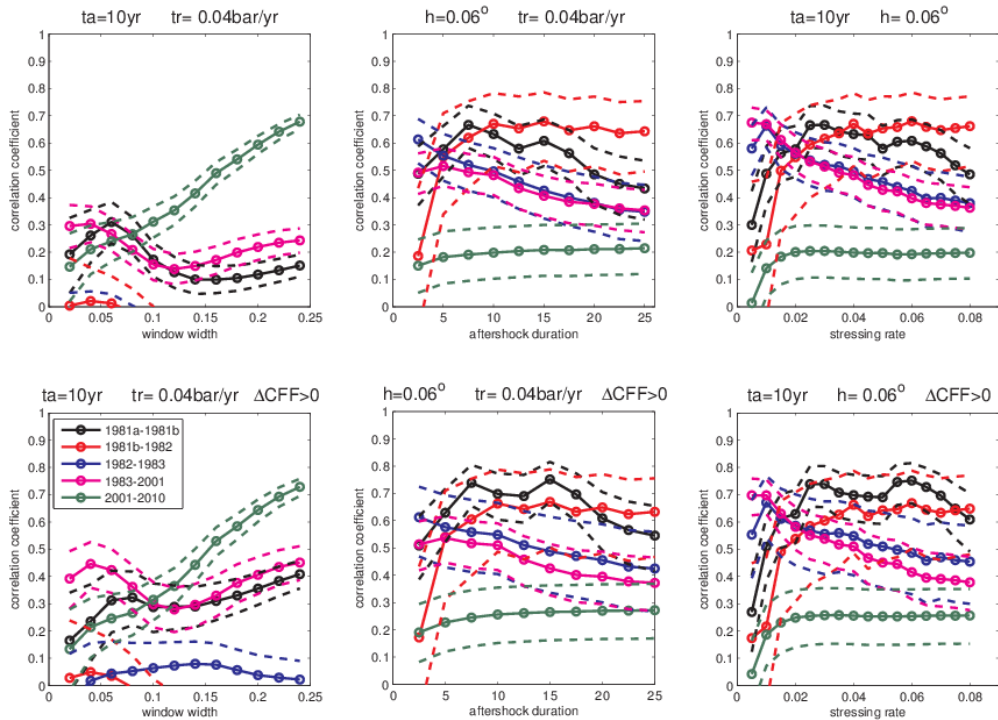


Fig. 2.50. Quantitative evaluation of the difference between observed-synthetic seismicity rates in sub-area 3, (Central Area), during the interevent periods (colored lines). Solid lines indicate the value of Pearson linear Correlation Coefficient (PCC) while dashed lines indicate its lower and upper bounds for a 95% confidence interval for each coefficient. Sub-figures a, b, and c, yielded from the whole data, while sub-figures d, e and f, by taking into account only those cells which experience positive ΔCFF .

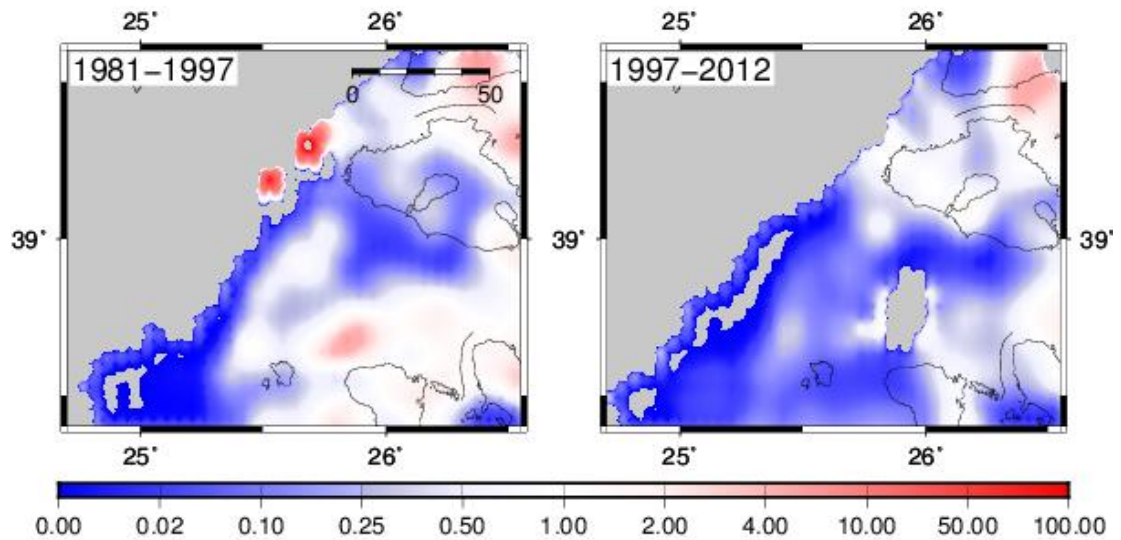


Figure 2.51. Ratio of expected/observed seismicity rates for North Aegean sub-area 4 for the 2 study periods tested. Red colors show that the expected values are overestimated in comparison with the observed ones whereas blue colors show higher observed seismicity rates than the simulated ones. White areas correspond to ratio value between 0.5-2, suggesting sufficient model performance. Calculations are not performed in gray areas because of data insufficiency. Parameters values are taken as: $h=0.06^\circ$, $t_a=5\text{yr}$, $\tau_r=0.025\text{bar/yr}$ ($A\sigma=0.125\text{bar}$). Seismicity data used includes events with $M \geq 3.8$.

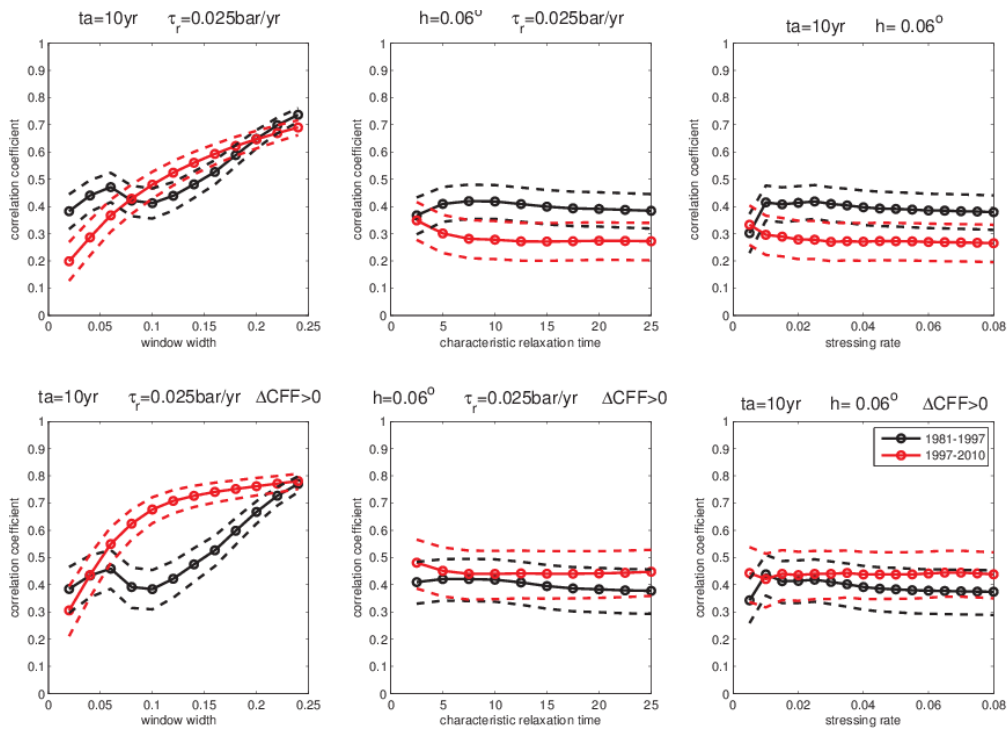


Fig. 2.52. Quantitative evaluation of the difference between observed-synthetic seismicity rates in sub-area 4, (Chios - Lesvos), during the interevent periods (colored lines). Solid lines indicate the value of Pearson linear Correlation Coefficient (PCC) while dashed lines indicate its lower and upper bounds for a 95% confidence interval for each coefficient. Sub-figures a, b, and c, yielded from the whole data, while sub-figures d, e and f, by taking into account only those cells which experience positive ΔCFF .

In all previous cases, characteristic time and stressing rate have not significant impact on correlation coefficient values. This happens because these parameters affect the values of seismicity rates but do not influence their spatial distribution, a feature that mostly depends on reference seismicity rate values and the bandwidth selection. From this point of view an alternative approach is attempted in sub-areas 1 and 4. Since the other parameters slightly affect the results, the reference seismicity rate influence was tested. Reference seismicity rate was considered from 1970 to just before the occurrence of the strongest event in the respective sub-area, namely 2001 for sub-area 1 and 1997 for sub-area 4. This assumption resulted to a somewhat lower PCC in comparison with the previous approach. Two major conclusions can be obtained from this test. Firstly, seismicity in between 1970-

1981 ($M_c=3.5$ for sub-area 1 and $M_c=3.8$ for sub-area 4), is proved to be sufficient enough for investigating the seismicity evolution in these two sub-areas, as it leads to a better correlation than an extended reference rate period. Secondly, it is shown that strong events outside the specific areas, do affect seismicity rates, providing better results and therefore have to be taken into account, rather than assuming only the influence of the strong shocks occurred inside these sub-areas.

2.3.5.5 Contribution to Seismic Hazard Assessment

The expected seismicity rates after 2012 were estimated for sub-area 1 (North Aegean) by considering the influence of coseismic (due to $M \geq 6.0$ earthquakes) and long term (tectonic) stress changes on the reference seismicity rates during 1970-1981 ($M \geq 3.5$, Fig. H11). The unbounded non-parametric magnitude distribution of the 1865 events ($M \geq 3.5$ during 1970-2012) was then considered in connection with the averaged estimated expected seismicity rate, to calculate the exceedance probabilities for the next decade. These probabilities were found equal to 20.6% (with 95% confidence bounds at 14.5% -25.2%) and 5.4% (with 95% confidence bounds at 0.9% - 7.5%) for an earthquake with magnitude higher than 6.0 and 6.5, respectively. As shown in figure H11, the expected rates for seismicity with $M \geq 3.5$ are estimated to be high in the entire region, except maybe its south-eastern part. However, the calculated probabilities for strong ($M \geq 6.0$) earthquake occurrence are considerably lower in comparison with the other areas of the broader Aegean region because of the particular magnitude distribution.

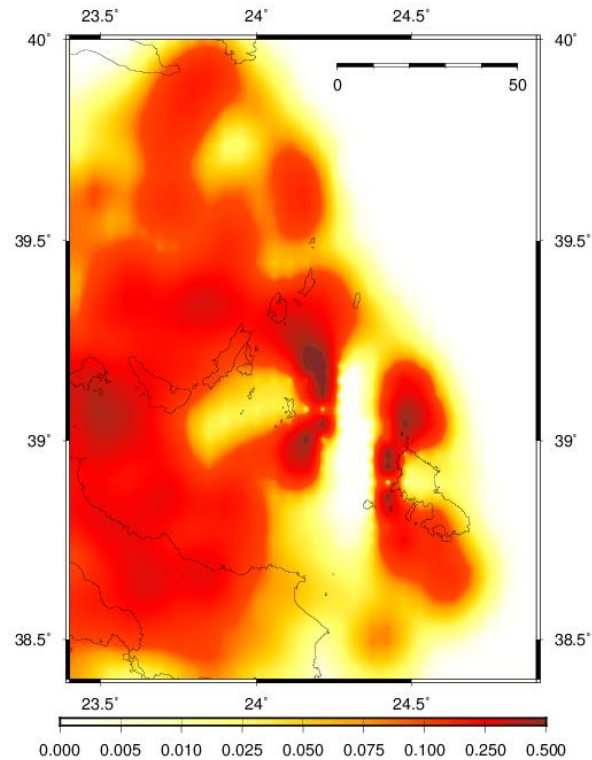


Fig. H11. Snapshot of the expected seismicity rates ($M \geq 3.5$) estimated for the period after 2012 in sub-area 1 of North Aegean.

Figure H12 shows the expected seismicity rates after 2010 in sub-area 2 of North Aegean. These rates were determined after considering the influence of coseismic (due to $M \geq 6.0$ earthquakes) and tectonic stress changes on the reference seismicity rates during 1970-1981 ($M \geq 4.1$). The unbounded non-parametric magnitude distribution of the 442 events ($M \geq 4.1$ during 1970-2012) was then considered in connection with the averaged estimated expected seismicity rate, to calculate the exceedance probabilities for the next decade. The expected seismicity rates are quite low in this sub-area because of the relatively high completeness threshold of the catalog. Nevertheless the magnitude distribution that the catalog follows led to the highest strong ($M \geq 6.0$) earthquake probabilities in comparison with the adjacent areas of North Aegean. These probabilities were found equal to 43.6% (with 95% confidence bounds at 36.5% - 47.2%) and 28.6% (with 95% confidence bounds at 27.0% - 32.3%) for an earthquake with magnitude higher than 6.0 and 6.5, respectively. The spatial distribution of the expected rates shown in figure

H12 suggests that the highest probabilities correspond to the north-eastern part of the area.

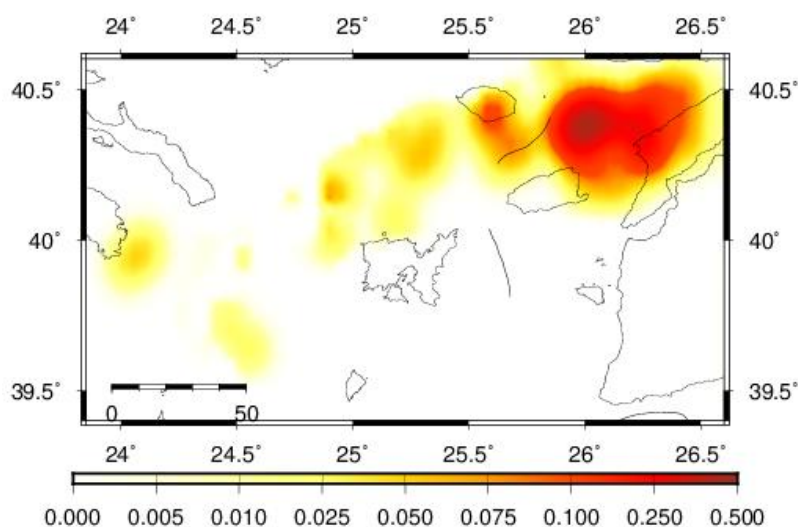


Fig. H12. Snapshot of the expected seismicity rates ($M \geq 4.1$) estimated for the period after 2012 in sub-area 2 of North Aegean.

The expected seismicity rates after 2012 were estimated for sub-area 3, by considering the influence of coseismic (due to $M \geq 6.0$ earthquakes) and long term (tectonic) stress changes on the reference seismicity rates during 1970-1981 ($M \geq 4.1$, Fig. H13). The unbounded non-parametric magnitude distribution of the 218 events ($M \geq 4.1$ during 1970-2012) was then considered in connection with the averaged estimated expected seismicity rate, in order to calculate the exceedance probabilities for the next decade. Most of the area is expected to accommodate low seismicity rates. This is because of the high completeness magnitude of the available catalog. The highest rates are expected to take place north of Skyros Island and close to the eastern coasts of Lemnos Island. The corresponding probabilities were found equal to 18.4% (with 95% confidence bounds at 17.5% - 20.3%) and 13.2% (with 95% confidence bounds at 12.1% - 14.4%) for an earthquake with magnitude higher than 6.0 and 6.5, respectively. It is noted that high expected probability were calculated for the area where the epicenter of the January 2013 strong ($M=5.8$) earthquake was located (see section 2.4).

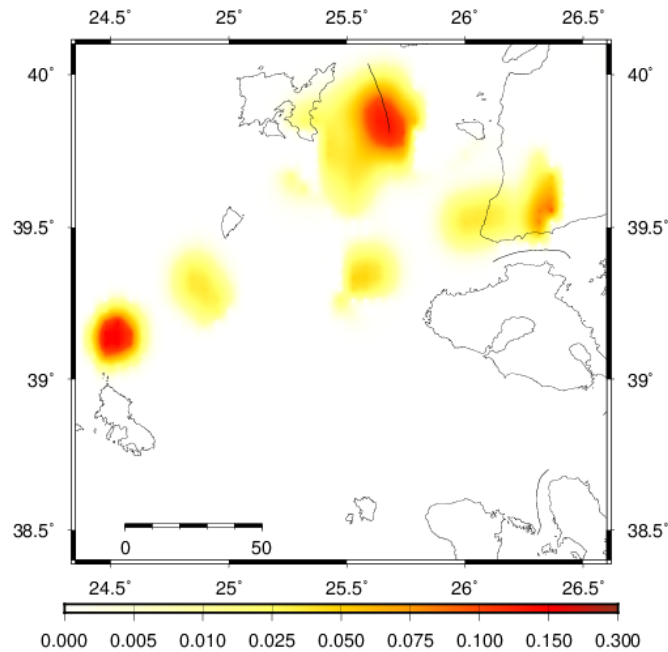


Fig. H13. Snapshot of the expected seismicity rates ($M \geq 4.1$) estimated for the period after 2012 in sub-area 3 of North Aegean

Figure H14 shows the expected seismicity rates after 2012 in sub-area 4 of North Aegean. These rates were determined after considering the influence of coseismic (due to $M \geq 5.8$ earthquakes) and tectonic stress changes on the reference seismicity rates during 1970-1987 ($M \geq 3.8$). The unbounded non-parametric magnitude distribution of the 1182 events ($M \geq 3.8$ during 1970-2012) was then considered in connection with the averaged estimated expected seismicity rate, to calculate the exceedance probabilities for the next decade. The absence of strong events ($M \geq 6.0$) in the area and the magnitude distribution of the available dataset led to very low probabilities for an $M \geq 6.0$ in the sub-area 4. These probabilities were found equal to 5.7% (with 95% confidence bounds at 1.4% - 10.4%) and 0.6% (with 95% confidence bounds at 0.2% - 2.1%) for an earthquake with magnitude higher than 6.0 and 6.5, respectively. The northern coasts of Lesbos Island and the south eastern part of the area, north of Karaburun peninsula are expected to experience the highest seismicity rates according to Rate/State model applied here.

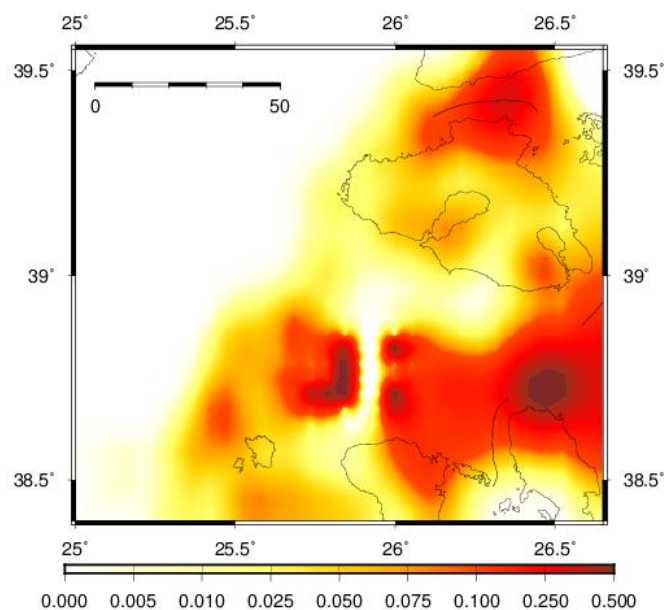


Fig. H14. Snapshot of the expected seismicity rates ($M \geq 3.8$) estimated for the period after 2012 in sub-area 4 of North Aegean

2.3.6 Area 6 – Thessalia (Central Greece)

2.3.6.1 Introduction

Thessalia (Fig. 2.53) constitutes a part of the extensional backarc Aegean region and is characterized by extension on sub-parallel E–W striking normal faults (Papazachos et al., 2001). The southern part of the study area comprises the Sperchios basin with two active faults known to be associated with events of $M > 6.5$ during the last five centuries, namely the Lamia fault and the Skarfeia fault (Papazachos et al., 2001). In the northern part, the NW–SE trending normal faults in the Late Miocene – Early Pliocene (Caputo and Pavlides, 1993) control the local morphology and bound two parallel basins and probably the coastline. An old dextral strike-slip motion along the fault zone during the Miocene was followed by two normal reactivations was identified, suggesting possible initial connection of the western extension of the North Anatolian fault with the southern Thessalia fault zone. This zone maybe constitutes an active boundary and for this reason larger earthquakes occur there than in its northern margin (Mountrakis et al., 1993;

Papadimitriou and Karakostas, 2003). The contemporary N–S extension is revealed by the fault plane solutions of both strong (Papazachos et al., 1998) and small earthquakes (Hatzfeld et al., 1999). A NW–SE trend is dominant at a regional scale, but it is not so well defined by major faults although the basins in the Thessalia area are generated by this fault set. In contrast, a E–W to ESE–WNW trending fault system was clearly observed in the field. Its large-scale morphological features are much less prominent than the NW–SE trending ones but equally evident. There is evidence that many faults belonging to this latter group experienced recent movements and are imposed onto the NW–SE trending structures inherited from the earlier tectonic phases.

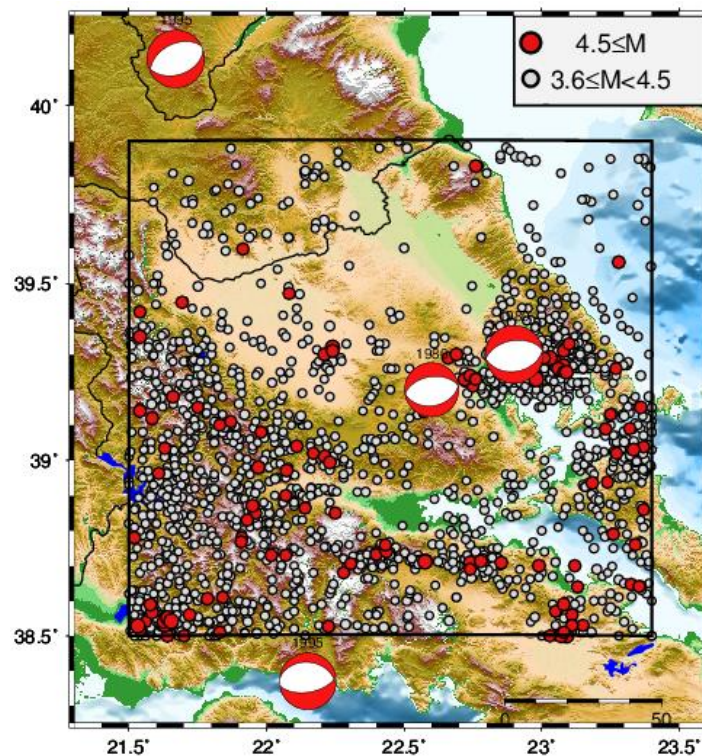


Fig. 2.53. Morphological map of Central Greece (indicated by the rectangle). Seismicity with $M \geq 3.6$ that occurred in the study area since 1970 is shown along with the fault plane solutions of the strongest shocks that were taken into account for the Δ CFF calculations incorporated in the Rate/State model

Seismological data indicate that strong earthquakes are associated with these fault systems. From 1954 until 1958, five strong ($6.1 < M < 7.0$) earthquakes devastated towns and villages located along the southwestern border of the Thessalia basin. This remarkable sequence took place on along strike normal

faults interacting through their stress fields (Papadimitriou and Karakostas, 2003). The 30 April 1954 Sofades earthquake in Thessaly (Papastamatiou and Mouyiaris, 1986a, 1986b; Ambraseys and Jackson, 1990; Papathanassiou et al., 2007) occurred in a multi-fractured setting (Pavlidis, 1993) and was accompanied by sporadic and locally complex ground ruptures (Palyvos et al., 2010). On July 9th 1980 an earthquake of magnitude M=6.5 occurred in the Magnesia region of Central Greece. The epicenter of the earthquake was located in the Pagasitikos gulf and the associated seismic sequence was studied by Papazachos et al. (1983) and Drakos et al. (2001).

2.3.6.2 Data

For seismicity rate change analysis in Thessalia the data from the Hellenic Unified Seismological Network (HUSN) were utilized. Seismicity since 1964 was considered and elaborated for estimation of its completeness threshold during time. M_c was estimated for overlapping 10-year windows by the Modified Goodness-of-Fit Test (MGFT – Leptokaropoulos et al., 2013) and found equal to 3.6 since 1970 (1953 events during 43 years). The source parameters of the events that were taken into account for Coulomb stress changes calculations are shown in Table 2.14 and the forecasting periods correspond to the inter-event time periods between them, except for the last one that ends in December 2012.

Table 2.14. Source parameters of the 11 earthquakes with $M \geq 6.0$ modeled for coseismic static Coulomb stress changes calculations.

Event	Date	Epicentral Coordinates	M_w	M_0 ($\cdot 10^{25}$ dyn-cm)	Focal Mechanism			Reference
					Strike($^\circ$)	Dip($^\circ$)	Rake($^\circ$)	
1980	09JUL	39.300°N 22.900°E	6.5	8.67 ¹	81	40	-90	2
1980	09JUL	39.200°N 22.600°E	6.1	5.52 ³	81	40	-90	2
1995	13MA	40.160°N 21.670°E	6.5	7.64	243	47	-97	1
1995	15JUN	38.370°N 22.150°E	6.5	6.10	277	33	-76	4

1. Global CMT; 2. Papazachos et al. (1983); 3. Drakos et al., 2001; 4. Bernard et al. (1996);

2.3.6.3 Parameters values

Stressing rate values for the major regional fault segments were estimated by considering the long term slip rate (Papadimitriou and Karakostas, 2003; Paradisopoulou, 2011) and found equal to 0.032bar/year. Nevertheless the values applied here were between 0.010 bar/year and 0.08 bar/year, whereas the characteristic relaxation time was selected fluctuating from 2.5 years to 30 years. The aforementioned values of $\dot{\tau}$ and t_a , lead to $0.025 \text{ bar} < \Delta\sigma < 2.4 \text{ bar}$. The smoothing parameter was given values between 0.04° to 0.24° (or alternatively radii of 4.5km to 26.7km), whereas according to equation 2.17 an $h \sim 0.12^\circ$ was suggested. All ΔCFF calculations were done at the depth of 8 km, which approximates the average regional seismicity nucleation depth. The effective friction coefficient was set $\mu' = 0.4$ whereas the shear modulus, G , and Poisson's ratio, ν , were fixed at $3.3 \cdot 10^5 \text{ bar}$ and 0.25, respectively.

2.3.6.4 Results – Discussion

Two study periods are tested in this area (Fig. 2.54). For the first one (1980-1995) a good agreement found between forecasted and observed seismicity rates in the western part of the area, whereas for the second period (1995-2012) the respective area is smaller. In quantification terms (Fig. 2.54) a maximum of ~60% of real seismicity rates are forecasted sufficiently for the first period (1980-1995) with these results being sensitive in bandwidth selection. On the other hand, a maximum of ~40% of observed seismicity during 1995-2012 is well simulated by the Rate/State model with t_a and $\dot{\tau}$, influencing these percentage more than the bandwidth. Note that both the 1995 events caused stress shadow in the entire study area, so there are no results for positive ΔCFF cells (lower frames of Fig. 2.55). This low correlation coefficient can be therefore explained due to the inherent model weakness to forecast seismicity rate decreases. For 1980-1995 period the PCC for stress increase areas is considerably improved reaching up to approximately 80%.

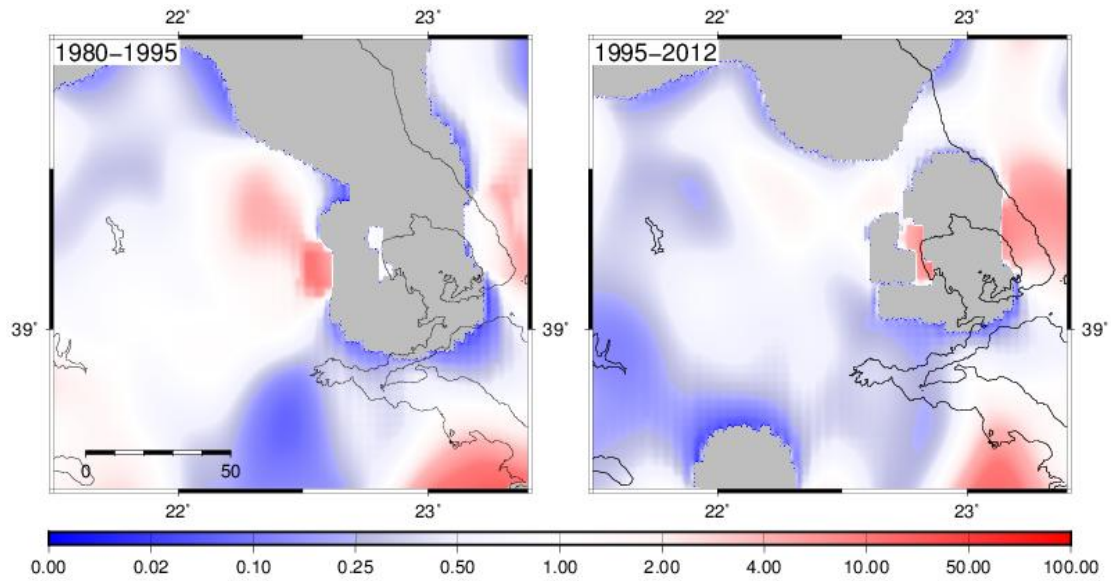


Fig. 2.54. Ratio of expected/observed seismicity rates for Thessalia, with reference seismicity rate obtained from 1970-1980 ($M>3.6$). Red colors show that the expected values are overestimated in comparison with the observed ones whereas blue colors show higher observed seismicity rates than the simulated ones. White areas correspond to ratio value between 0.5-2, suggesting sufficient model performance. Parameter values applied are: $h=0.15^\circ$, $t_a=5\text{yrs}$ and $\dot{\tau}_r=0.03\text{bar}\cdot\text{yr}^{-1}$ ($A\sigma=0.15\text{bar}$).

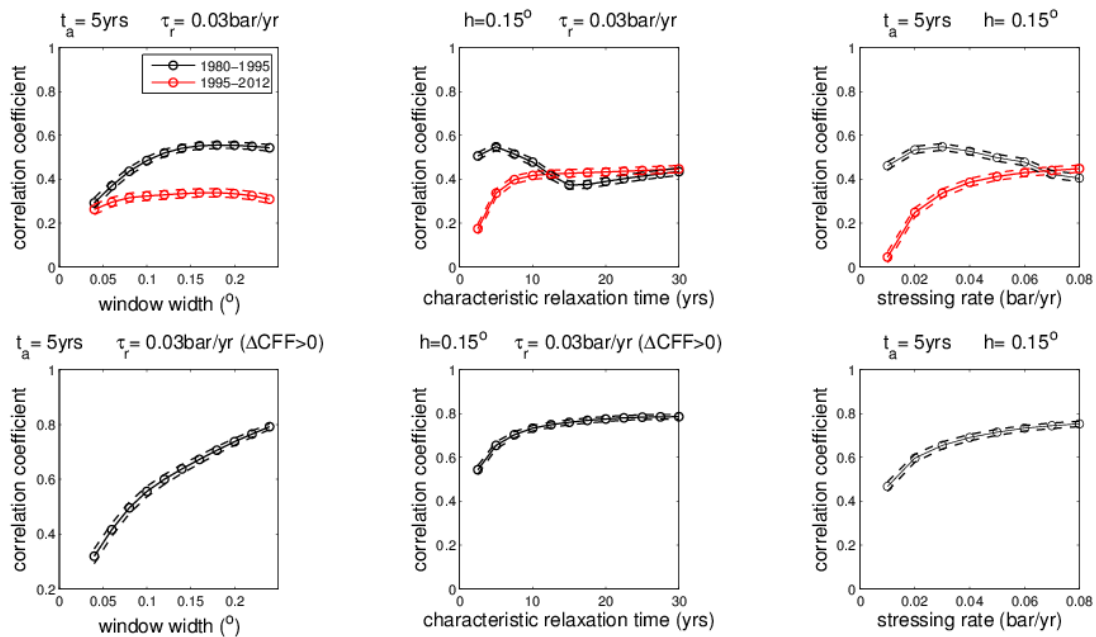


Fig. 2.55. Quantitative evaluation of the difference between observed-synthetic seismicity rates during the inter-event time periods for Thessalia (colored lines). Solid lines indicate the value of Pearson linear Correlation Coefficient (PCC) whereas its 95% confidence intervals for each coefficient are also depicted by fainter lines. The upper frame figures yielded from the whole data set, while the figure below by taking into account only those cells experiencing positive ΔCFF . Reference seismicity rate corresponds to the period 1970-1980.

2.3.6.5 Contribution to Seismic Hazard Assessment

The expected seismicity rates after 2012 were estimated for Thessalia region after considering the influence of coseismic (due to $M \geq 6.0$ earthquakes) and long term (tectonic) stress changes on the reference seismicity rates during 1970-1980 ($M \geq 3.6$, Fig. H15). The unbounded non-parametric magnitude distribution of the 1953 events ($M \geq 3.6$ during 1989-2012) was then considered in connection with the averaged estimated expected seismicity rate, to calculate the exceedance probabilities for the next decade. These probabilities were found equal to 28.2% (with 95% confidence bounds at 21.9% - 35.0%) and 12.4% (with 95% confidence bounds at 6.4% - 17.4%) for an earthquake with magnitude higher than 6.0 and 6.5, respectively. As shown in figure H15, the expected rates (and consequently probabilities) are estimated to be high in specified areas in the central and eastern parts, which were influenced by the 2 strong 1980 ($M=6.5$ and $M=6.1$) events. Contrarily, the western sites are expected to accommodate seismicity at lower rates and an $M \geq 6.0$ earthquake is much less likely to occur there.

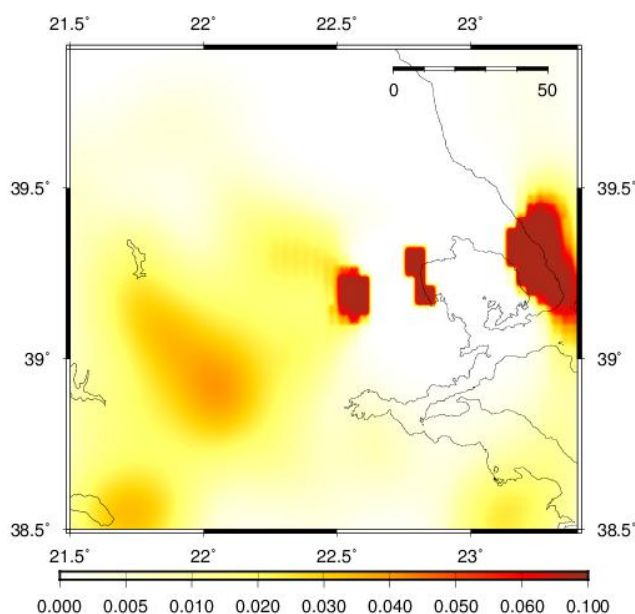


Fig. H15. Snapshot of the expected seismicity rates ($M \geq 3.6$) estimated for the period after 2012 in Thessalia.

2.4 Integration of Results – Contribution of the Study to Probabilistic Seismic Hazard Assessment

An overview of the obtained results is now demonstrated along with an attempt to verify the model performance in connection with the most recent strong earthquakes ($M \geq 5.8$) that took place in the broader Aegean region since June 2012. The impact of parameter values on correlation coefficient was explicitly investigated in this chapter. An evaluation of the model performance in respect to the input data statistical properties is presented. Figure 2.56 shows the mean values of PCC (averaged for different Rate/State parameter values combinations) as a function of the time span that each forecasting period covers. The distribution is quite diffused, nevertheless it is shown that for time intervals smaller than ~ 1000 days the value of PCC is generally low and does not exceed 0.5. On the other hand, as the duration of the testing periods increases over approximately 4-5 years, PCC values range is extended. There are still several cases with low PCC, but high values up to 0.85 also exist.

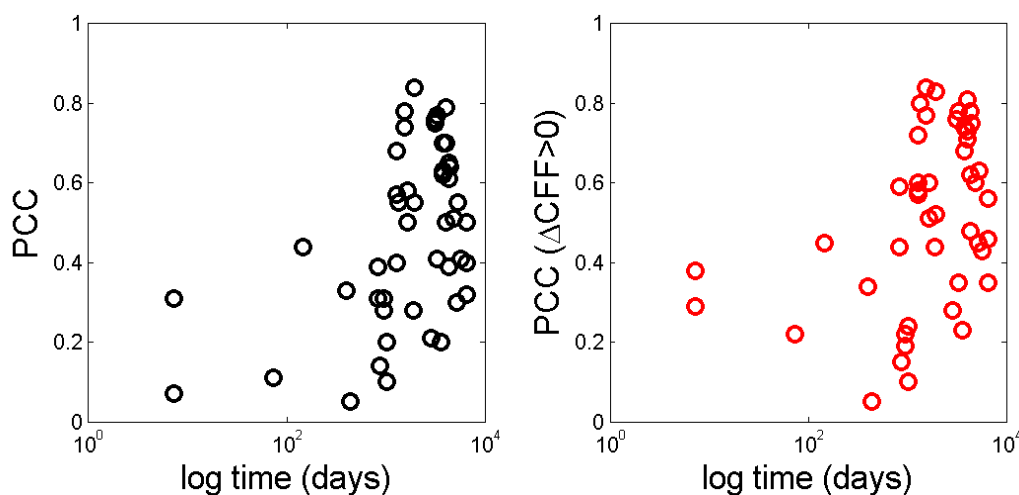


Fig. 2.56. Average correlation coefficient plots versus the duration of the data sets corresponding to the learning periods (in logarithmic scale) for the entire study areas (left frame) and only in cells experiencing positive Coulomb stress changes (right frame).

More important is the influence of the amount of data on correlation coefficient. The datasets corresponding to the study periods include event counts from some tenths up to thousands of events, depending upon the time period they cover, the completeness magnitude threshold and the regional degree of seismic activity. Such comparison of the average PCC in association with sample size is demonstrated in figure 2.57. In this case the plot is also quite diffuse but an increasing trend is evident. When datasets are consisted of small number of events the correlation coefficient is generally lower and vice versa. It is noteworthy that there are no very high PCC for very small datasets and respectively, there are no very low PCC values corresponding to the largest datasets.

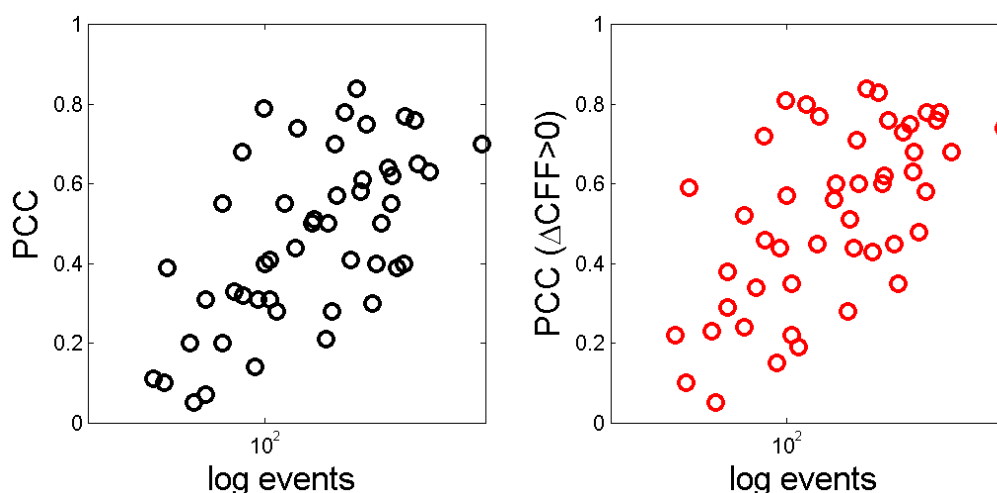


Fig. 2.57. Average correlation coefficient plots versus the number of the events in each data set corresponding to the learning periods (in logarithmic scale) for the entire study areas (left frame) and only in cells experiencing positive Coulomb stress changes (right frame).

In order to seek for a more comprehensive connection between PCC and both dataset duration and size, the following plotting technique was followed: The data pairs (PCC-duration) were sorted according to their duration (or data number) and the mean of the first 5 PCC values were plotted versus the mean of the 5 first values of duration. Then the same procedure was repeated after shifting the 5-pair set by 1 event, so that overlapping 5-pair averaged sets were created. By this smoothed plotting it

becomes more visible that there is a correlation between PCC and dataset properties. Figure 2.58 shows that PCC tends to take higher values as time windows increase despite the large fluctuations which are shown as error bars. The pattern is identical for considering only positive ΔCFF cells, although shifted towards higher PCC values. A more clear view is obtained for the association between PCC and data number (fig. 2.59). In this case, despite a second order fluctuation there is an obvious increasing trend of PCC as the sample size becomes larger. These results illustrate that data number is a crucial parameter for the model application since it directly affects its performance regardless the other parameters influence. Therefore, the failure of the model to sufficiently forecast the real seismicity rates is in several cases, arises as a result of insufficient data's negative influence rather than due to an inherent model weakness.

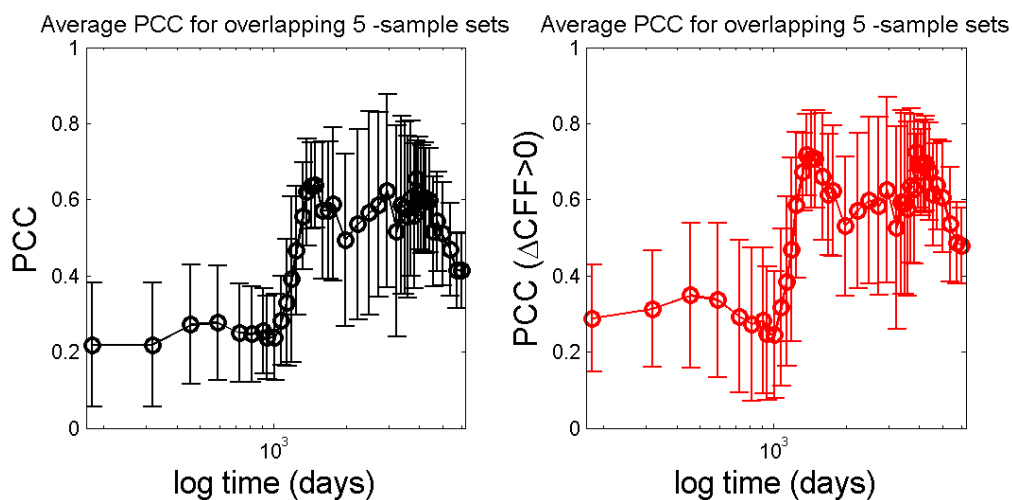


Fig. 2.58. Average correlation coefficient plots, smoothed by overlapping 5-sample sets versus the duration of the data sets corresponding to the learning periods (in logarithmic scale) for the entire study areas (left frame) and only in cells experiencing positive Coulomb stress changes (right frame).

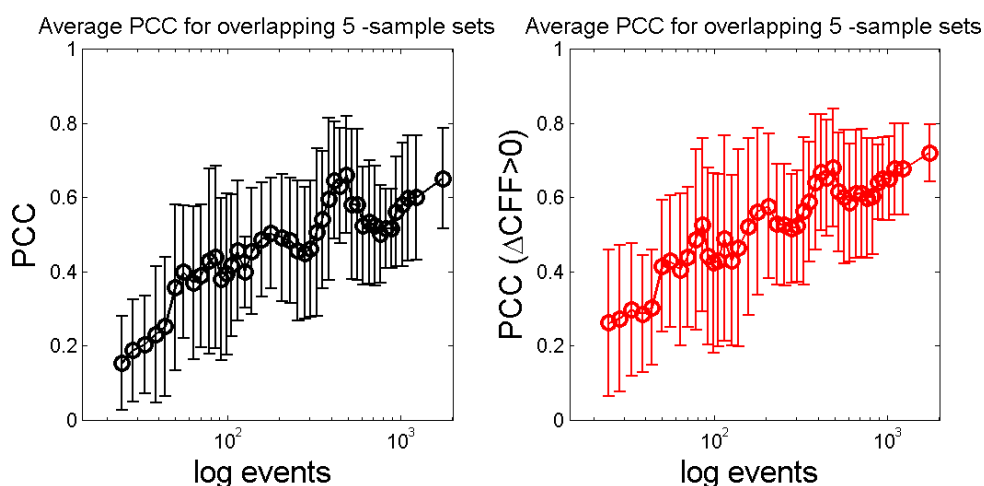


Fig. 2.59. Average correlation coefficient plots smoothed by overlapping 5-sample sets versus the number of the data sets corresponding to the learning periods (in logarithmic scale) for the entire study areas (left frame) and only in cells experiencing positive Coulomb stress changes (right frame).

In the next step an attempt to verify the model results in respect with strong earthquakes $M > 5.8$ occurrence since June 2012 is attempted. Eight such events took place in the broader Aegean region (Table 2.13) and we are going to investigate if their foci were located in areas that Rate/State model forecasted to experience seismicity rate enhancements. The first event occurred on 10 June 2012 very close to sub-area D of South Aegean (Area 4). Its epicenter is though outside the borders of the study site and therefore no seismicity rates were modeled in this case. We could only reproduce the Coulomb stress changes associated with the 2008 event (Fig. 2.60) and confirm that the 2012 event took place in a positive ΔCFF lobe.

Table 2.13. Source parameters of the 8 strong earthquakes ($M \geq 5.8$) occurred in the Aegean region since June 2012

Event	Date	Epicentral Coordinates	M_w	M_0 ($\cdot 10^{25}$ dyn-cm)	Focal Mechanism			Reference
					Strike($^\circ$)	Dip($^\circ$)	Rake($^\circ$)	
2012	10JUN	36.441°N 28.904°E	5.9	0.69	19	85	-1	1
2013	08JAN	39.641°N 25.611°E	5.8	0.64	241	86	175	2
2013	16JUN	34.220°N 25.080°E	6.1	1.90	222	7	20	3
2013	12OCT	35.472°N 23.280°E	6.5	6.20	305	33	76	1
2013	28DEC	35.960°N 31.290°E	5.9	0.98	137	61	87	3
2014	26JAN	38.160°N 20.340°E	6.1	1.38	286	90	-5	1
2014	03FEB	38.270°N 20.320°E	6.0	0.96	287	87	-3	1
2014	24MAY	40.296°E 24.403°E	6.3	4.15	245	72	171	1

1 AUTH; 2; Kiratzi and Svirgkas (2013); 3 Global CMT

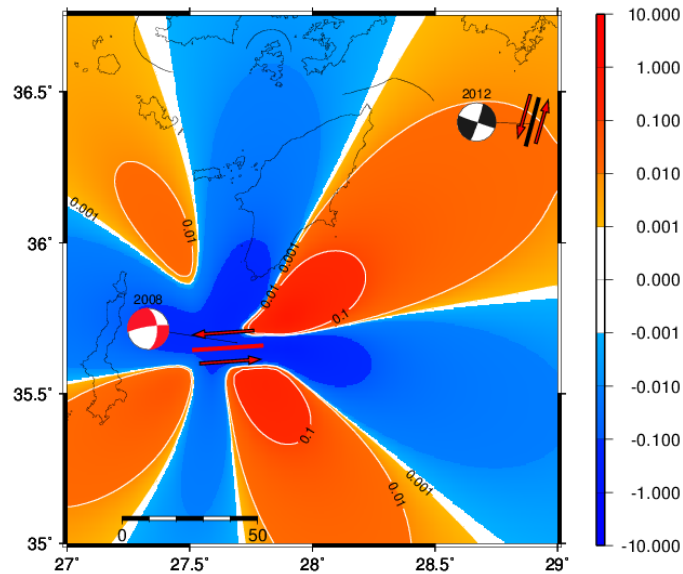


Fig. 2.60. Coulomb stress changes associated with the 2008 earthquake, resolved according to the fault plane and focal depth of the June 2012 strong earthquake. The color map indicates the stress changes in bars.

Two strong earthquakes occurred in South Aegean (Area 4): The 16 June 2013 event, occurred in sub-area C and is located in an area surrounded by cells with high forecasted seismicity rates (Fig. 2.61 left frame), in a relatively short distance from the 2009 earthquake. Similarly, the 12 October 2013 shock, took place in a region (sub-area B of Area 4) where the reference seismicity rates were significantly amplified by the coseismic stress changes caused by the 2008 earthquakes (Fig 2.61 right frame). To quantify these observations we plotted the empirical Cumulative Distribution Function (CDF) of expected seismicity in each cell and spotted the rank of the cells corresponding to the epicenter of each earthquake (Figures 2.62 and 2.63). To cope with the uncertainties in epicentral location we averaged the seismicity rate values of the cells in a radius of 5km from the epicenter. Histograms of the number of cells with specified values of modeled seismicity rates are also provided in the same figures. It is shown that in both cases less than 10% of the cells (8.4% and 9.8%, respectively) are expected to accommodate seismic activity at higher rates than the ones calculated close to the two epicenters. This provides strong evidence of the proposed model sufficiency, supporting

the concept of seeking strong earthquake occurrence at sites where increased seismicity rates are expected according to Rate/State modeling.

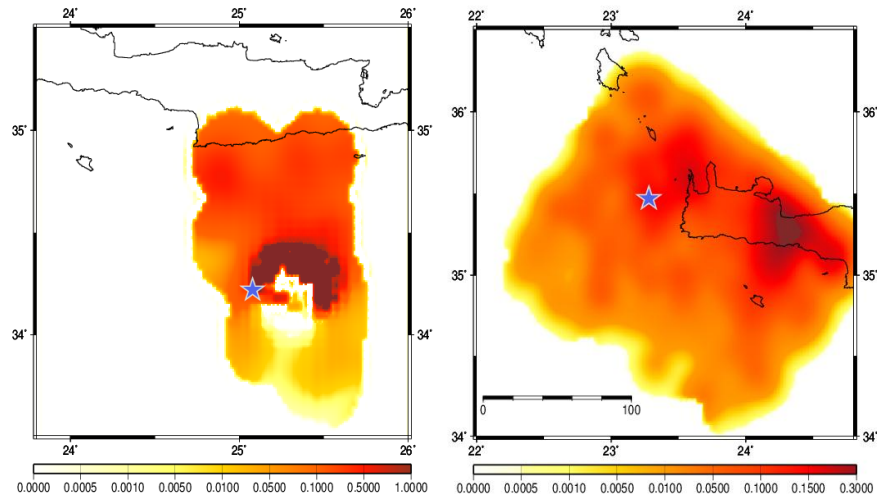


Fig. 2.61. Forecasted seismicity rates just before the June 2013 (left frame) and the October 2013 earthquakes. Δ CFF calculations are performed at their focal depth and according to their focal mechanism. Shear modulus is fixed at 50GPa and bandwidth is 0.08° .

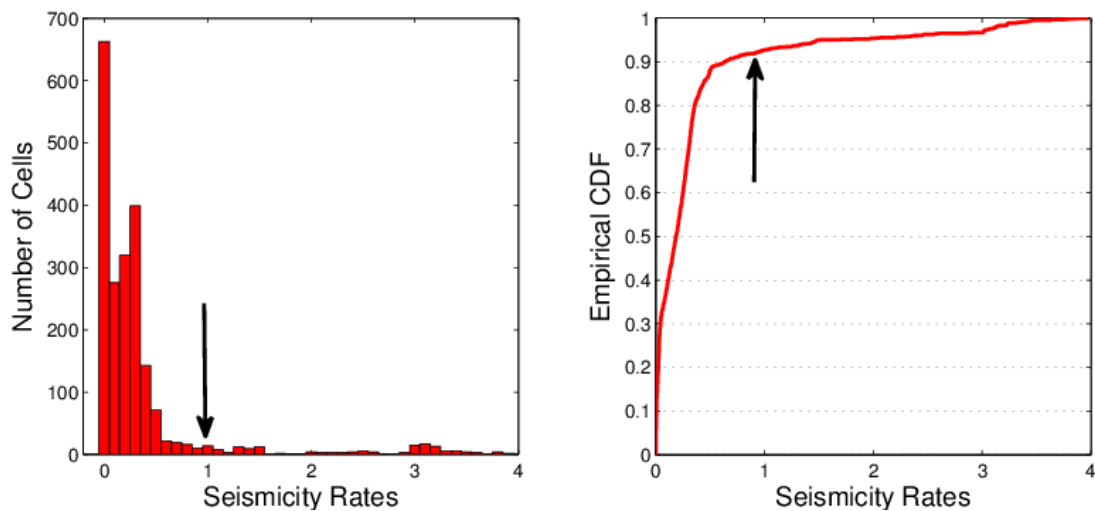


Fig. 2.62. Histogram of the number of cells in sub-area C that are expected to have a specified seismicity value (left frame) and the cumulative distribution function (CDF) of those rates just before the June 2013 earthquake (right frame). The arrow indicates the average rate close to the epicenter. Reference seismicity rate is evaluated since 1991 ($M_c=3.9$).

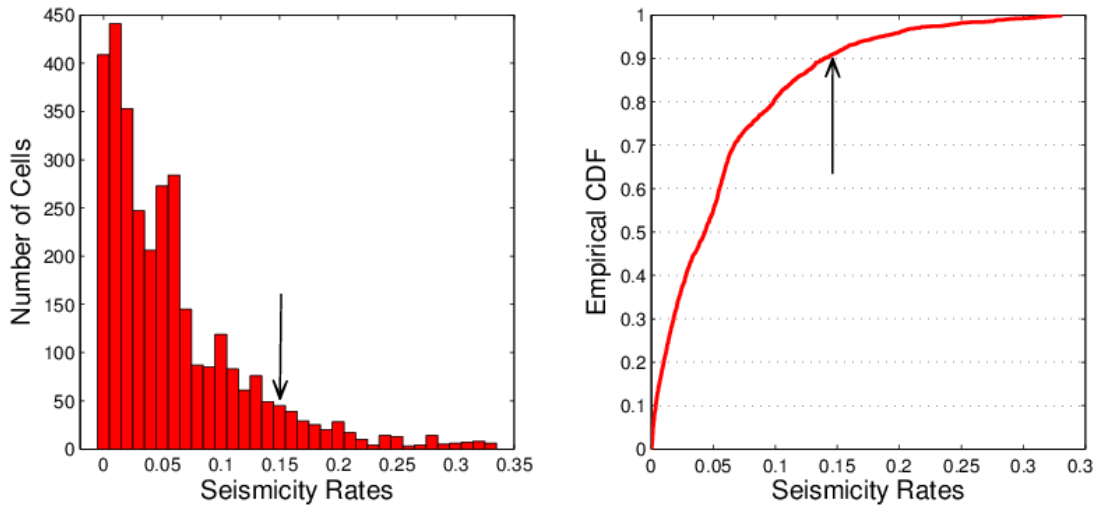


Fig. 2.63. Histogram of the number of cells in sub-area C that are expected to have a specified seismicity value (left frame) and the cumulative distribution function (CDF) of those rates just before the October 2013 earthquake (right frame). The arrow indicates the average rate close to the epicenter. Reference seismicity rate is evaluated since 1971 ($M_c=4.0$).

The same procedure was followed to investigate the $M=5.8$ earthquake occurred close to Lemnos island, North Aegean (Area 5) on the 8th January 2013. Because of the relatively sparse data due to high completeness threshold considered ($M_c=4.1$), expected seismicity rates were only calculated for a limited fraction of the study area (Fig. 2.64). Nevertheless the epicenter of the 2013 earthquake is located in an area where the expected rates have not only been calculated but also their values are very high. As shown in Figure 2.65, only $\frac{1}{4}$ of the area was expected to suffer higher seismicity rates than the close vicinity of this earthquake. Note that this proportion refers to the cells where calculations were performed and not to the entire area. Given that the main reason for not performing seismicity rate forecast is data insufficiency, mostly due to low seismicity rates, it becomes obvious that the actual percentage could be even higher for the entire area.

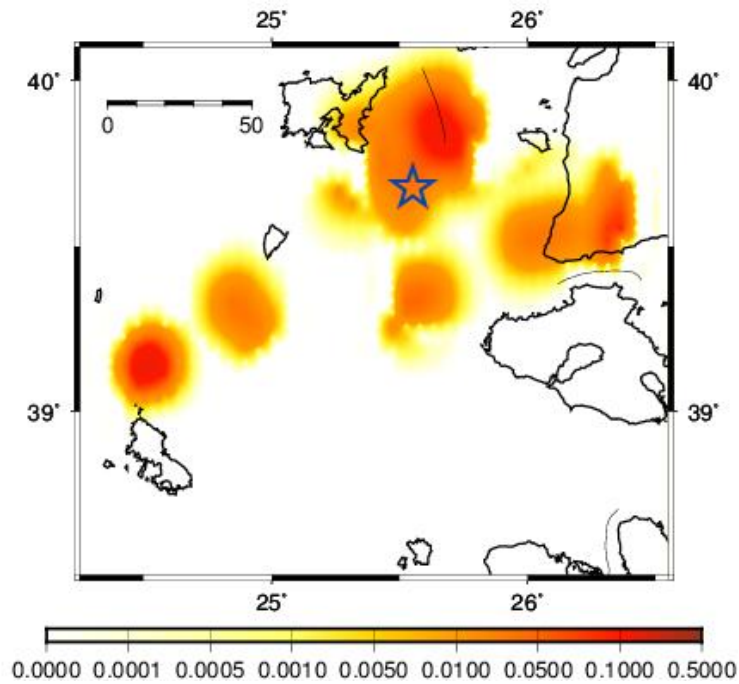


Fig. 2.64. Forecasted seismicity rates just before the January 2013 earthquake. The expected seismicity rates have been calculated for $M \geq 4.1$ events. Shear modulus is fixed at 33GPa and bandwidth is 0.10° .

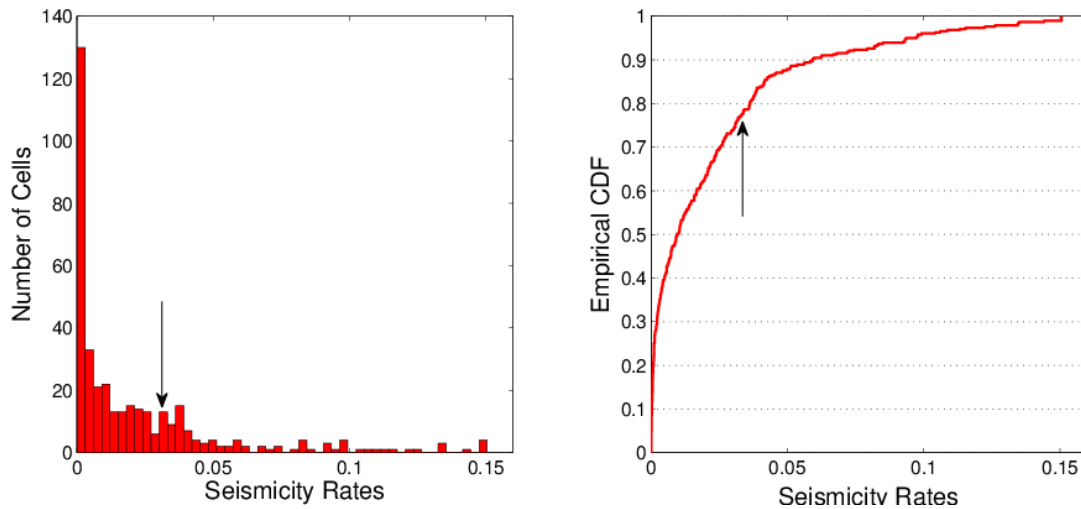


Fig. 2.65. Histogram of the number of cells in sub-area 3 of North Aegean, that are expected to have a specified seismicity value (left frame) and the cumulative distribution function (CDF) of those rates just before the January 2013 earthquake (right frame). The arrow indicates the average rate in a radius of 5km from the epicenter. Reference seismicity rate is evaluated since 1970 ($M_c=4.1$).

The final test that was attempted concerns the $M_w=6.1$ January 26th 2014 earthquake that took place on Paliki peninsula, the western part of Cephalonia island (Area 2) and was followed one week later by a second main shock ($M_w=6.0$). The Rate/State model was tested here according to two approaches concerning the data utilized (Fig. 2.66). The first one assumes

reference seismicity rates estimated from the period 1973-1983 ($M_c=4.3$) and resulted to moderate performance and in the second one the reference seismicity rates were estimated from the period 1989-1997 ($M_c=3.6$) and yielded high correlation (both approaches are described in section 2.3.2.4). In the first approach the epicenter was located in an area where the expected seismicity rates are very close to the average for the total area (Fig. 2.67). Approximately 63% of the cells are expected to accommodate seismicity at lower rates than in the close vicinity of the January 2014 epicenter. This is of course higher than 50% but does not imply a strong connection. On the other hand when dataset with lower completeness threshold is considered (reference rate from 1989-1997) the forecasted seismicity rate spatial distribution is significantly different (Fig 2.66 right frame). In this case the Rate/State model application suggests that only ~5% of the area is expected to experience higher seismicity rates than the 5km radius from the epicenter of the M6.1 earthquake. This provides additional evidence that the model is more sufficient when adequate data are taken into account even if these data correspond to shorted time intervals.

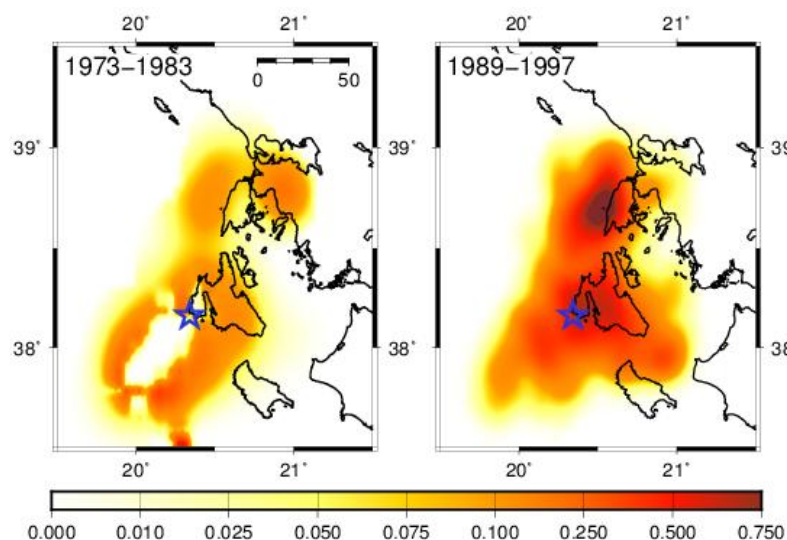


Fig. 2.66. Forecasted seismicity rates just before the January 2014 earthquake. The expected seismicity rates were calculated from two datasets: Reference seismicity rate estimated since 1973 with $M \geq 4.3$ and bandwidth equal to 0.13° (left frame) and reference seismicity rate estimated since 1989 with $M \geq 3.6$ and bandwidth equal to 0.08° (right frame). Shear modulus is fixed at 33GPa.

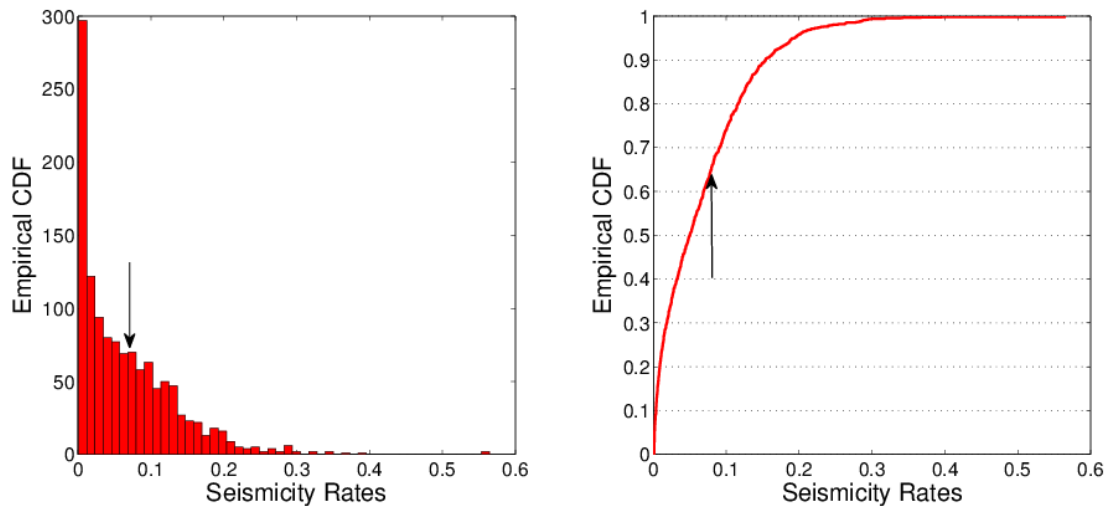


Fig. 2.67. Histogram of the number of cells in Cephalonia Transform Fault Zone (Area 2), that are expected to have a specified seismicity value (left frame) and the cumulative distribution function (CDF) of those rates just before the January 2014 earthquake (right frame). The arrow indicates the average rate in a radius of 5km from the epicenter. Reference seismicity rate is evaluated since 1973 ($M_c=4.3$).

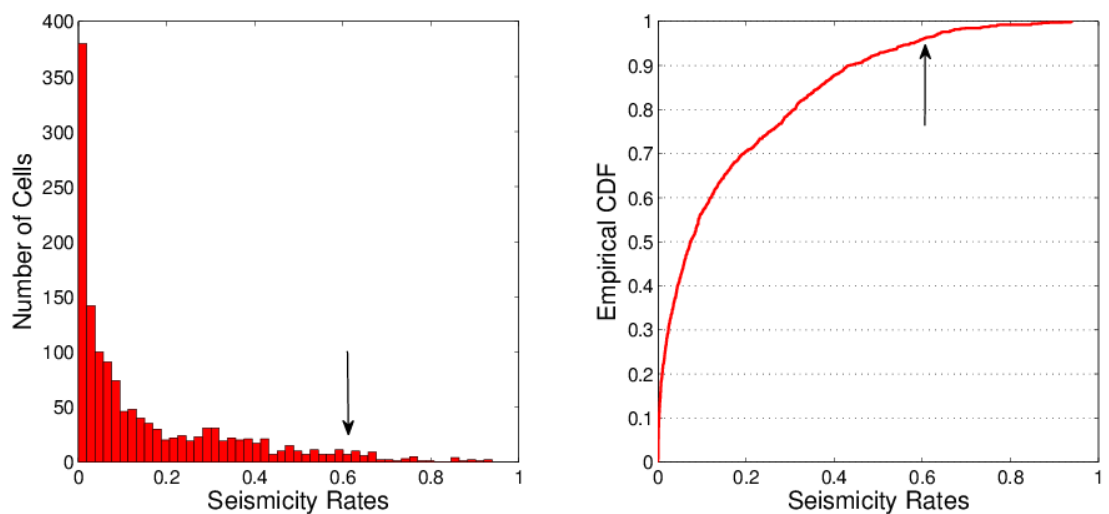


Fig. 2.68. Histogram of the number of cells in Cephalonia Transform Fault Zone (Area 2), that are expected to have a specified seismicity value (left frame) and the cumulative distribution function (CDF) of those rates just before the January 2014 earthquake (right frame). The arrow indicates the average rate in a radius of 5km from the epicenter. Reference seismicity rate is evaluated since 1989 ($M_c=3.6$).

The contribution of this thesis to PSHA is to provide the exceedance probabilities of a predefined magnitude during a specified time period in particular sites of the broader Aegean region. As an implementation to seismic hazard assessment the following map is presented which integrates all the results described in this chapter (Fig. 2.69). This figure shows the expected

seismicity rate values that correspond to 25% (orange) and 10% (red) of the highest reference seismicity rate amplifications calculated for each sub-area. Note that these results do not correspond to seismicity rate values: Since each area not only demonstrates different reference activity but also the respective datasets exhibit diverse completeness magnitude, it is profound that the expected rates should vary by several orders of magnitude. Therefore it was necessary to cope with data inhomogeneity and spatial variability of the earthquake production reference rates. In doing so, the expected rates were normalized by the regional reference rate for each area and their highest values were illustrated in a single figure. It should be also emphasized that the aforementioned percentages (of 25% and 10%) do not correspond to the percentage of each area's entire surface, but to the fraction of each area that calculations were performed (where adequate data were available). Recall that no forecasted rates were evaluated where reference or expected rates found to be lower than a predefined rate ($0.0001 \text{ event}\cdot\text{cell}^{-1}\cdot\text{year}^{-1}$). It is noteworthy that 7 out of 8 strong events ($M \geq 5.8$) occurred since June 2012 are located inside (6 events) or very close (1 event) these enhanced expected areas. Candidates to expect high earthquake occurrence rates and even a strong event in the future according to the analysis presented here are: Some of the western segments of North Anatolian Fault in the Marmara Sea, Sporades Islands and their vicinity, several sites along the Hellenic arc, the western Gulf of Corinth, the islands and Asia Minor coasts located in the central-eastern part of the Aegean Sea and several sites of south-western Turkey.

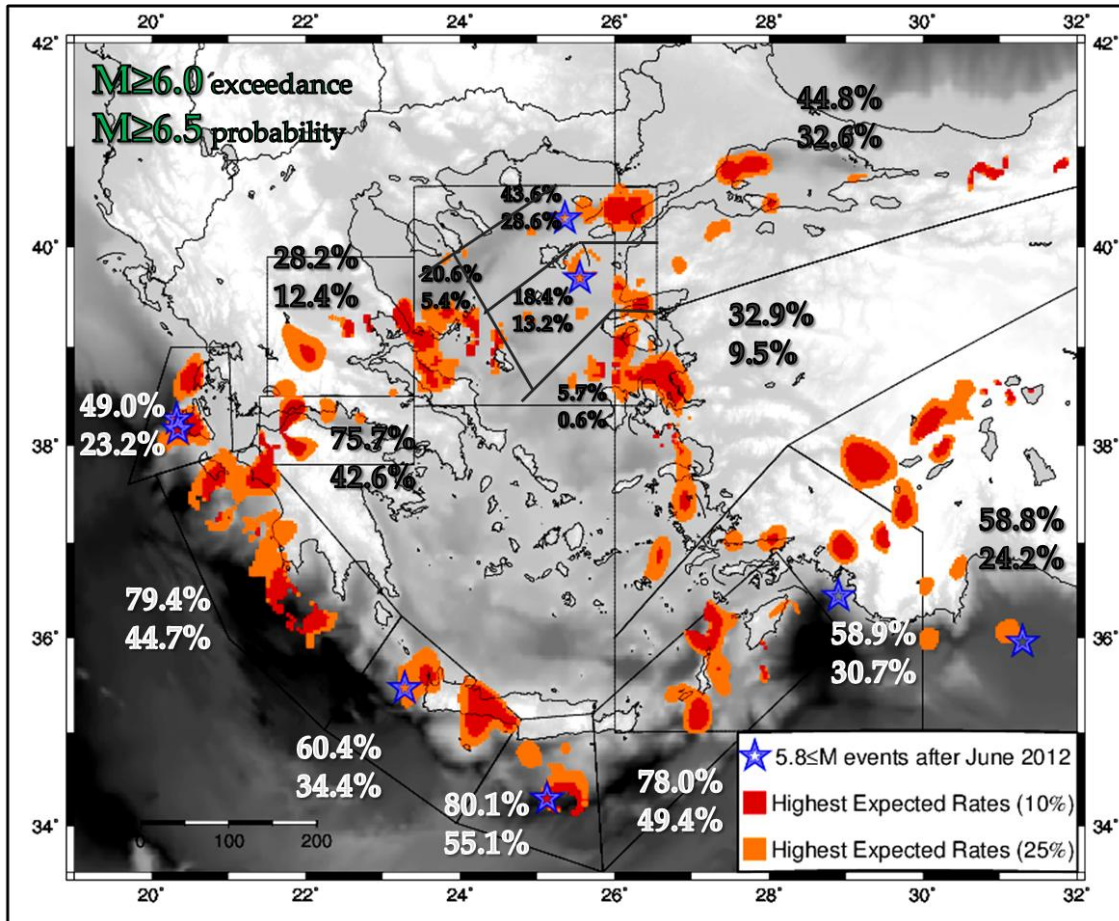


Fig. 2.69. Integration of the forecasted seismicity rate results after June, 2012: Expected seismicity rates for each study area normalized by the respective reference seismicity rate. The orange and red areas indicate the highest 25% and 10% of the total seismicity rate values calculated per region, respectively. Equivalently, the remaining 75% and 90% of each area is expected to accommodate seismicity at lower rates than the mapped one, respectively (cells with very low rates did not account for this calculations). Blue stars illustrate the epicenters of the most recent (since June 2012) strong events ($M \geq 5.8$) that took place in the broader Aegean region. In each area, the exceedance probability for a $M \geq 6.0$ and a $M \geq 6.5$ earthquake for a 10-year period is denoted by the upper and lower number, respectively. The black lines show the boundaries of each study area, as they were defined in this Thesis.

In this study the exceedance probability of an $M \geq M_i$ event is estimated in the selected study areas for a predefined time period. The model free, unbounded estimation of magnitude distribution (Kijko et al., 2001; Lasocki and Orlecka-Sikora, 2008) applied in this study ensures a satisfactory agreement between the average return period estimates and actual observations (description and formulation is given in Appendix D). The exceedance probability for $M \geq 6.0$ and $M \geq 6.5$ was estimated in each sub-area of the study area for a time horizon of a decade, given the expected seismicity

rates as estimated in Chapter 2. The 95% confidence intervals of probabilities were established by estimating the 95% confidence bounds for the non-parametric kernel estimator of cumulative distribution function of magnitude by the means of bootstrap resampling. The values of these exceedance probabilities and their respective confidence bounds are shown in Table (2.13) and correspond to the entire sub-area in each case.

Table 2.13. Exceedance probabilities for $M \geq 6.0$ (2nd column) and $M \geq 6.5$ (3rd column) earthquakes in the 14 areas studied in this Thesis, estimated for a 10-year horizon. The bold number in the parenthesis gives the average value, whereas its 95% confidence bounds are also provided. The number of events that were used to retrieve the unbounded, non-parametric frequency magnitude distribution parameters is given in the forth column.

Area	Probability for $M \geq 6.0$	Probability for $M \geq 6.5$	N (events)
A1	73.8-0.77.9 (75.7)	32.9-48.8 (42.6)	2438
A2	25.8-0.68.2 (49.0)	5.0-40.1 (23.2)	2069
A31	73.9-0.87.9 (79.4)	35.7-61.2 (44.7)	7308
A32	55.8-0.66.4 (60.4)	16.1-43.0 (34.4)	974
A33	66.5-0.86.1(80.1)	39.4-67.6 (55.1)	904
A34	65.4-0.83.9 (78.0)	29.2-58.0 (49.4)	1810
A41	34.2-0.49.3 (44.8)	30.1-33.9 (32.6)	774
A42	9.5-0.46.4 (32.9)	1.0-18.9 (9.5)	1781
A43	44.5-0.75.0 (58.9)	20.1-42.9 (30.7)	1438
A44	55.4-0.60.9 (58.8)	7.8-30.8 (24.2)	626
A51	14.5-0.25.2 (20.6)	0.9-7.5 (5.4)	1865
A52	36.5-0.47.2 (43.6)	27.1-32.3 (28.6)	440
A53	17.5-0.20.3 (18.4)	12.4-14.4 (13.2)	218
A54	1.4-0.10.4 (5.7)	0.1-2.1 (0.6)	1182
A6	21.9-0.35.0 (28.2)	6.4-17.5 (12.4)	1953

It should be pointed out that these probability values are not equally distributed along the study areas. For more comprehensive results, these values should be combined with figure (2.69) in order to obtain a more realistic view of how these probabilities are spatially distributed. The gridding approach adopted in this study for seismicity rate calculations does not allow a more detailed probability estimate, nevertheless the average estimated values for the 15 seismic sources together with the distribution of high-expected rate areas (Fig. 2.69) provide an integrated and explicit illustration of hazard assessment. It should be also noted that the uncertainties incorporated in the Rate/State modeling and deal with

parameter values (e.g. stressing rate, characteristic relaxation time), rupture models (e.g. friction coefficient, fault geometry) and reference rate period selection were not included in the probabilities confidence bound construction. This sustains a challenge for future research: To incorporate both Rate/State model and Frequency-Magnitude parameters uncertainties for well defined seismic sources, in order to establish robust probabilistic hazard estimates for given periods.

2.5 Discussion and Summary

Seismicity rate changes in the broader Aegean region were investigated in this thesis on the basis of Dieterich (1994) Rate/State dependent friction concept. After optimally defining the study areas according to seismotectonic criteria and data homogeneity, the respective earthquake catalogs were selected and sought for their completeness magnitude thresholds and their temporal variations. Starting from selected “learning periods”, the reference seismicity rates were evaluated for each study area. The forecasting periods (study periods) were chosen to be the interseismic time intervals between two successive strong main shocks ($M_w > 5.8$). The influence of the Coulomb stress changes due to the coseismic slip of these strong events was examined in connection with the occurrence rates of small events ($M > M_c$ for each study area) for the interevent periods. The impact of the constant tectonic loading (stressing rate) during the inter-seismic periods was also embodied to the modeled seismic rates. Summarizing, the simulated rates of earthquake occurrence were estimated as a result of the effect of the successive coseismic ΔCFF and the steady-rate tectonic loading on the reference rates evaluated from the learning periods seismicity.

The results obtained by the Rate/State model application were afterwards qualitatively and quantitatively compared with the ones observed during the respective periods, in order to seek for correlation between

observed and expected seismic rates and improve the modeling by appropriately tuning the parameter values. All model parameters evaluation and data processing was done individually in each one of the study areas, regarding their particular geophysical (stressing rate, focal mechanisms) and statistical (seismicity data number and distribution) properties. The quantitative correlation between the expected and observed seismicity rates was evaluated by the means of Pearson linear correlation coefficient (and its 95% confidence bounds) and tested for its significance. In every case where PCC was larger than 0.4 the significance of correlation was high, with the p-value being less than 10^{-6} giving ground to reject the null hypothesis and accept that there is a linear relationship (weaker or stronger) between estimated and observed seismicity rate. This test was performed for the entire data set, excluding cells with extremely low seismicity rate values (lower than $0.0001 \text{ events}\cdot\text{cell}^{-1}\cdot\text{year}^{-1}$), which correspond to areas with very low seismic activity associated with minor faults or even large epicentral location errors. This assumption provides statistically more robust results because comparison of seismicity rates in comparatively less active areas is avoided.

Tests were performed once again only for cells with positive values of Coulomb stress changes. Previous studies (Toda et al., 2005; Mallman and Parsons, 2008) concluded that detection of seismicity enhancement in such areas is better manifested than depression of seismicity rates in areas with stress shadows. For detecting decreases of earthquake occurrence rates, in particular, a high value of reference seismicity is essential. Our data were not sufficient for obtaining visible evidence of such seismicity rate reductions. Therefore it is worth to focus on positive ΔCFF areas instead, not only because the results might be more advantageous, but also because most of the strongest ($M \geq 5.8$) earthquakes after 1965, occurred in those areas (e.g. Papadimitriou and Sykes, 2001). Correlation is also usually improved when

the calculation concern cells where $\Delta CFF > 0$, in agreement with the previously studied observation that it is easier to detect seismicity bursts in such areas rather than rate depression in stress shadows. Sample size is also a crucial precondition for this analysis; in all the tested cases where data was sparse due to the short time window and/or high corresponding completeness magnitude, the correlation was negligible.

A thorough investigation on parameter values was performed in the present study. Rate/State parameter values depend on physical rock properties which can be non-uniform over the area. [Catalli et al. \(2008\)](#) pointed out that although it is likely to expect that all considered parameters are spatially variable, it is extremely difficult to constrain realistic patterns for Rate/State modeling. This is the main reason for considering these parameters as spatially uniform and constant in most of the applications available in the literature. At this point we should emphasize that the explicit determination of physical rock properties is not an issue of this study. In general, these values are not known and have to be estimated from the observed seismicity data or using some approximate physical relations ([Hainzl et al., 2009](#)). [Dieterich \(1994\)](#) formulation actual power is lying upon indirectly incorporating these properties despite the uncertainties that they exhibit in order to simulate and forecast seismicity rate changes. [Toda et al. \(1998\)](#) for example, estimated $A\sigma$ by fitting the observed dependence of the seismicity rate change (R/r) on stress change predicted for Rate/State dependent fault properties, i. e. by using indirect mean instead of recalling laboratory experimental results. The model parameters are strongly correlated with each other for both physical and statistical reasons and in this study is verified that different sets of model parameters can yield to the same expected seismicity rate variations, in agreement with [Cocco et al. \(2010\)](#). The selection of the

range of parameter values in this study was adequate to improve the modeling of the physical processes that take place in the earth's crust.

Concerning the bandwidth, higher values of h , result to higher correlation but from physical aspect too high values should be avoided because they oversmooth seismicity patterns and balance the differences among broader areas obtaining to misleading results. On the contrary, smaller values are preferable because in this case each earthquake has a limited area of influence and consequently low seismicity areas should be better distinguished. Referring to the Rate/State parameters, the model seems to perform better when lower $A\sigma$ values are applied. This in turn means that lower values of the selected range of characteristic relaxation time or stressing rate are more appropriate. Stressing rate was determined with sufficient accuracy, thus it is very unlikely that the $\dot{\tau}_r$ has obtained values almost one order of magnitude lower. Hence, a probable scenario is that in most of the study regions the constitutive properties of the fault zones exhibit lower $A\sigma$ values, and consequently lower characteristic relaxation time (eq. 2.8). These results seem to be in better agreement with Dieterich (1994) who estimate t_a values varying between 0.5 – 5 years in some cases, putting into question the selection of higher t_a values, as stated in the literature, for application in our study area. In addition, it was also shown in our trials that the previously mentioned parameter values usually have a minor impact on the resulting correlation. This is due to the fact that these parameters amplify or depress seismicity rates expected but do not influence their spatial pattern, a property that almost exclusively depends on reference seismicity rate, stress changes and bandwidth selection.

Consequently, it is of major importance that the data set and the rupture models of the strong events to be defined as precisely as possible. The accuracy of the evaluated epicentral coordinates and focal depth of the

earthquake data has a significant impact on the model results. This is confirmed by our results, showing that the best fitting to the real data takes place in areas with adequate azimuthal network coverage such as Corinth Gulf and North Aegean. On the contrary, as it happens to the subduction zones, the geographical shape of the Hellenic Arc, yields to sparsely recorded seismicity due to the insufficient azimuthal coverage and high completeness magnitude threshold, leading to relatively lower correlation coefficient. However, even in these areas the results demonstrate that the present formulation and the available data sets are quite sufficient to model adequately the observed seismicity rates, even when data during the last 5 decades are considered.

The methodology we followed provided satisfactory results in general, taking into account the uncertainties, assumptions and simplifications that we performed in order to construct a more flexible and easy to apply model. The uncertainties arise from the accuracy of the focal coordinates determination of the earthquakes used in the current analysis. They are also related with the parameter values speculation although a wide range of them was considered. Different kind of uncertainties embodied in our study deal with the determination of the rupture models, especially of the smaller magnitudes main shocks. Moreover strong event influence (e.g. 1956 M=7.7 in Southern Aegean, 1967 M=7.2 in NAF, 1905 M=7.1, 1912 M=7.6, 1968 M=7.1, in Northern Aegean, 1953 M7.2 in Cephalonia, 1954 M7.0 in Thessalia) was not taken into account because of the insufficient data available before 1980 for a robust seismicity rate investigation. Therefore, it is inevitable that the state of stress remains unknown at the beginning of our analysis, since data adequacy and reliability are not appropriate when going back in time (e.g. [Papadimitriou and Sykes, 2001](#)). Nevertheless, note that we utilized non-declustered data sets, which contain triggered events or seismicity depression that persist in time and are related with the stress perturbations produced by previous

strong main shocks (Leptokaropoulos et al., 2012). Therefore, the reference seismicity rates pattern contain in a way some of the effects associated with these non-modeled stress perturbations. Moreover, diverse reference rate periods were tested in several cases: one period with longer duration and higher magnitude threshold (and thus smaller sample size) and another one exhibiting shorter duration but lower completeness magnitude. By this procedure the model sensitivity is tested, and the parameter values that appear to simulate more realistically the regional tectonic procedures are evaluated. The results notably depend on data sufficiency and it was shown here that the model application provided satisfactory results despite the inherent ambiguities embodied in the process as previously mentioned.

For the calculations of stress perturbations the use of rupture models of the major shocks, introduced additional uncertainties. The highest decreases of ΔCFF are evident in the near field, along the causative fault and in small distances of it, i.e. where the higher aftershock activity is observed. This intense seismic activity cannot be simulated because these aftershocks are regarded to be generated by short-scale slip variations while the applied rupture model considers uniform slip along the fault and cannot model the Coulomb stress changes in the near field. Therefore, one more reason to avoid seismicity rate estimation in negative ΔCFF areas regards the ambiguities concerning the stress calculations. Other features such as aftershock interactions and variability of their mechanisms, post-seismic deformations and rheological properties, introduce more uncertainties into the study on the rupture surface and its close vicinity (Helmstetter and Shaw, 2006; Helmstetter et al., 2006; Hainzl et al., 2010). These ambiguities can be overcome by comparison between off-fault observed and synthetic seismicity rates, in areas with well constrained ΔCFF values (Toda and Stein, 2003).

Even under these assumptions and inherent weaknesses of the data and the model, the results show that modeling seismicity rate changes through this approach is a feasible goal. The results indicate that the correlation between observed and simulated seismicity rate values is quite high when the study periods last enough for the respective dataset exhibiting sufficient size and including adequate number of off-fault earthquakes. More important is also the fact that the recent strong earthquakes ($M_w \geq 5.8$) since 2013 took place in areas that were modeled to experience increased earthquake occurrence rates, given the regional reference seismicity rates and stressing history. These results may be improved in future applications because of more accurate location and lower completeness magnitude threshold achieved, following the regional seismological network evolution in number of stations and azimuthal coverage. Implication of the current analysis to earthquake probabilities is expected to prove a promising tool for time dependent seismic hazard assessment. Given a magnitude-frequency relation, the strongest events occurrence rates can be transformed to probability of earthquake occurrence for mid-term earthquake forecasting and hazard assessment (Toda et al., 2003) and this could be an interesting perspective for future research. Other issues related with the future improvement of the current methodology deal with the smoothing technique. The adaptive seismicity smoothing around each epicenter rather than in each cell (e.g. Helmstetter et al., 2006; Werner et al., 2010; Botev et al., 2010) may provide flexibility in investigating larger areas. More generally the spatial determination of parameter values (bandwidth, $A\sigma$, stressing rate), introduction of new perspectives (viscoelastic phenomena, afterslip) and combination of Rate/State physical based approach with statistical models (such as the ETAS) constitute significant challenge for the future research.

Chapter 3. Stress Changes Inverted from Seismicity Rates

3.1 Introduction

The purpose of this chapter is to investigate seismicity rate changes in both space and time domain and to employ these changes in order to obtain information concerning the stress field variations. In doing so, the highest accuracy most recent and large sized regional datasets are utilized in order to invert seismicity rate changes into stress variation through a Rate/State dependent friction model, focusing in stress changes before and after recent strong earthquake occurrence. After explicitly determining the physical quantities incorporating in the modeling (characteristic relaxation time, reference seismicity rates) we sought for stress changes in both space and time and their possible connection with earthquake clustering and fault interactions. The spatial stress changes distribution were evaluated after smoothing the seismological data by the means of a probability density function (PDF). These inverted stress results were also compared with the ones derived from an independent approach (elastic dislocation model) and their correlation was quantified.

Usually, the impact of stressing history to the reference seismicity rates in specific areas is studied in order to forecast future seismicity rates. During the last fifteen years an attempt has been made to take advantage of the well determined seismicity rates in order to estimate the stress field variation. The calculation of stress changes from earthquake occurrence rates obtained from catalogues (achieving adequate spatial and temporal resolution) was firstly led to successful results by [Dieterich et al. \(2000\)](#), despite of the non-linearity of earthquake rate changes with respect to both stress and time. The same authors proposed and applied two methods using data from Kilauea volcano region, the results of which yielded sufficient agreement with independent

estimates of stress changes (boundary element/ elastic dislocation models). They discretized the space, with a grid size of about 1 km, and assume that the stress is uniform in each cell. This assumption that the stress is uniform at scales of a few km is reasonable for the stress change induced by a dyke intrusion, as in [Dieterich et al. \(2003\)](#), or for the coseismic stress change induced by a large earthquake in the far field. Although short term stress fluctuations could not be investigated because of random seismicity rate changes and possible catalogue inconsistencies, the long term stressing rate evolution and sudden stress steps appeared well resolved. The aforementioned studies assumed that the stress induced by dyke intrusion or the coseismic stress change in the far field is uniform at scales of a few km. However, the coseismic stress change on the main shock fault plane, where most of the aftershocks are located, is most probable being heterogeneous at all scales ([Herrero and Bernard, 1994](#); [Helmstetter and Shaw, 2005; 2006](#))

[Ogata \(2005\)](#) proposed a method of exploratory seismic data analysis using the epidemic-type aftershock sequence (ETAS) model, providing examples of how this method might indicate changes in stress. He detected and utilized anomalous seismic activity (such as quiescence and excitation) by a systematic deviation of seismic rates from the predicted by ETAS rate. These results were consistent with the coseismic changes of Coulomb failure stress in the corresponding regions, transferred from certain strong earthquakes. Few results in his paper agreed with the claim that there should be a threshold value of ΔCFF capable of affecting seismic changes. Thus he supports the idea that the anomaly in seismic activity, including the case of a single aftershock sequence relative to the model's rates, can sensitively reveal small stress changes caused by seismic or aseismic slips. Such a seismic anomaly could be a highly sensitive measure for exogenous stress changes in a wide region, comparable to, or possibly more sensitive than, various geodetic measurements.

Helmstetter and Shaw (2005, 2006) attempted to estimate the stress distribution on the fault plane from the aftershock rate, using the rate-and-state dependent friction model. They assumed that stress changes instantaneously after a mainshock, and they neglected the stress relaxation on the fault due to aseismic slip or viscous relaxation. Moreover, they neglected the stress/seismicity rate change induced by aftershocks. They interpreted their results assuming significant spatial heterogeneity in the stress distribution and explained in this way why aftershocks occur on the main rupture area. Concluding they noticed that heterogeneous stress distribution may not be the only mechanism that affects the temporal seismicity rate evolution: Heterogeneity of the friction law parameter A , effective normal stress, and stressing rate, multiple interactions between aftershocks, and postseismic relaxation may also cause considerable earthquake rate variations.

Following the Dieterich et al. (2000) methodology Toda and Matsumura (2006) studied a large scale silent slip in Tokai region. This slow slip event from 2001-2004 released total moment of $5 \times 10^{19} \text{Nm}$, roughly equivalent with a $M=7.0$ earthquake and took place in an area exhibiting unusual silent crustal movement. Their purpose was to investigate whether this phenomenon was uniquely associated with the 'Expected Tokai Earthquake', or sustained ordinary activity, repeatedly occurring for the region. The time series of microseismicity were used as an in situ stress sensor to estimate the crustal movements that are too small for the surface GPS network to detect until the cumulative movement becomes sufficient large. They calculated stress changes inverted from micro seismicity ($M \geq 1.5$) but they were still able to detect only moderate to large slippage rather than short term motions. These inverted stress changes values strongly depended on slip direction and fault orientation and their results could be interpreted only after revisiting the regional seismotectonic setting. They finally presented a new

delineation of plate coupling for the Tokai region, proposing a slip distribution on the plate interface.

[Ghimire et al. \(2008\)](#) attempted an estimation of spatio-temporal evolution of Coulomb stress from the analysis of seismicity rate changes within the subducted Pacific slab in Hokkaido. They found that the change of stress pattern inverted from seismicity rate changes was comparable with the one estimated from dislocation models. They divided their study area into 4 sub-regions according to their tectonic environment and in order to convert seismicity rates into ΔCFF they assumed the annual rate of earthquake occurrence averaged from the reference seismicity calculated for the period between 1994 and 2006. Their inversion analysis also revealed that stressing events with $M_w < 7.0$ appear to have minimal impact on Coulomb stress change in the Pacific slab and that deep focused large earthquakes could not also change Coulomb stress significantly in the shallower layers.

3.2 Stress Inversion Methodology

In this study we follow the [Dieterich et al. \(2000\)](#) methodology for various implications regarding the stress regime evolution in both space and time and the associated seismotectonics, such as fault interaction and earthquake clustering. Spatial and temporal evolution of the stress field changes are evaluated for datasets corresponding to different time increments and areas of major interest such as those located close to ruptured fault segments. As already presented in Chapter 2, [Dieterich \(1994\)](#) formulation implies that there is a causative relationship between the evolution of the stress field and the deviation of the earthquake production rates from their unperturbed, reference state. Despite the inherent uncertainties embodied in such an approach, dealing with parameter values determination, random seismic fluctuation and fault orientation ([Stein, 1999](#); [Harris, 2000](#)), its application often succeeds satisfactory results. A very important precondition

is that the local seismicity should be continuously high and well recorded. In such way the seismicity rate information contained in the earthquake catalogues may be interpreted as a stress meter (Toda and Matsumura, 2006). Dieterich et al. (2000) developed and applied two methods to estimate stress perturbations from seismicity rate changes. The first gives the stress as a function of time in a specified volume as

$$\Delta S = A\sigma \ln \left[\frac{\gamma_i + \frac{\Delta t}{2A\sigma}}{\gamma_{i+1} - \frac{\Delta t}{2A\sigma}} \right] , \quad (3.1)$$

where γ_i and γ_{i+1} are the estimated values of state variable, γ , at the beginning and the end of the time step, Δt , respectively. This equation expresses the stress changes over successive time intervals for a stress step at the mid-point of a time interval. In this study we apply the second one, which uses the solution of (2.2) for an initial assumption of constant stressing rate. This solution provides the spatial distribution of stress changes, ΔS , for a stress event

$$\Delta S = A\sigma \ln \left[\frac{\dot{S}(\exp(N_2 \dot{S}_r t_1 / N_1 A\sigma) - 1)}{\dot{S}_r (\exp(\dot{S} t_2 / A\sigma) - 1)} \right] , \quad (3.2)$$

where, \dot{S}_r and \dot{S} , are the background stressing rate and the Coulomb stressing rate on the fault, respectively, N_1 , is the count of earthquakes in the time interval, t_1 , immediately before the stress event and N_2 , is the count of earthquakes in the time interval, t_2 , immediately after the stress event. ΔS is therefore estimated from the observed time-dependent seismicity, by counting the number of earthquakes occurred during specified time intervals (t_1 , t_2). As “stress event”, one can refer to a magmatic intrusion or eruption (Dieterich et al., 2000; Dieterich et al., 2003), a silent slip event (slow creep that may lead to dynamic instability – Toda and Matsumura, 2006 and references within) or an earthquake (Helmstetter and Shaw, 2006; Mallman and Zoback, 2007; Ghimire et al., 2008). In the application of this formulation in Corinth

Gulf, it is assumed that the stressing rate remains constant in time and it is independent of the sudden stress events (earthquakes). Moreover, in our analysis similar fault geometry (faulting mechanism) is assumed within a small volume in earth (Ghimire et al., 2008). This assumption can be considered as valid, since the average focal mechanism of 31 events in the area suggests small variation in geometry, ($258^{\circ}\pm 22^{\circ}$ strike, $41^{\circ}\pm 11^{\circ}$ dip and $-80\pm 22^{\circ}$ rake), implying $\dot{S}_r = \dot{S}$. Note that parameter $A\sigma$ and stressing rate are connected with each other through the equation (2.8).

3.3 Applications and Results

In this section there is an effort to investigate stress changes in selected areas of the Aegean region characterized by high seismicity rates, for periods with relatively high recording level of seismicity. The results derived from the stress inversion analysis are demonstrated for the areas shown in Table 3.1, selected on the basis of data sufficiency and accuracy. To achieve this task well recorded seismicity catalogues at low completeness magnitude thresholds should be available for large time interval. This is the reason that led us to study these specific areas although stronger earthquakes occur along other rupture zones in the broader Aegean area.

Table 3.1. Datasets used in the stress inversion study and their properties. The three first datasets are characterized by better quality as far as the focal parameters accuracy and data density concerns.

No	Area	Duration	Events	Events/ (yr·100km ²)	Mc
1	Efpalio	4.4yrs (2008-2012)	988	17.20	2.4
2a	Samos-Kusadasi	5.2yrs (2007-2012)	2814	53.50	1.6
2b	Karaburun	5.2yrs (2007-2012)	1876	49.50	1.6
3	Corinth Gulf	~38yrs (1975-2013)	1613	1.92	3.5
4	Lefkada	~14yrs (1999-2013)	744	0.53	3.2
5	Western Crete	5.2 yrs (2009-2014)	666	0.64	2.8

The association of the stress changes results with various implications regarding seismic clustering and tectonics and stress changes are shown in each case in the following sub-sections as:

- Temporal evolution of stress field changes inverted from seismicity rate variations since August 2008 to December 2012 (dataset 1)
- Comparison between inverted stress changes associated with the coseismic slip due to the two strongest events of the 2010 sequence ($M=5.5$ and $M=5.4$), with ΔCFF derived from elastic dislocation model applied for the January 2010 main shocks (dataset 1)
- Spatial distribution of stress changes inverted from seismicity rate variations before and after the January 2010 main shocks (dataset 1)
- Stress changes close to the two fault segments that failed in the 2010 doublet (dataset 1 excluding events located approximately 1 fault length farther from the ruptured segments)
- Stress changes associated with spatio-temporal earthquake clustering (dataset 1)
- Temporal analysis of stress field variations inverted from seismicity rate changes since 1975 (dataset 2)

All of these analyses were performed for the first three datasets shown in Table 3.1 (Efpalio & Karaburun-Kusadasi). For the remaining 3 datasets, shown with italics in Table 3.1 (Corinth Gulf, Lefkada and western Crete) only the first step of analysis (i.e. temporal variation of stress field) was accomplished. It was not feasible to perform further analysis (comparison with ΔCFF derived from independent approaches, earthquake clustering, spatial variation of stress changes) due to data insufficiency resulting from high completeness catalog magnitude thresholds and/or the limited time span these data correspond to.

3.3.1 Area 1 – Efpalio 2008-2012 (Corinth Gulf)

3.3.1.1 Introduction-Overview

The area of interest is located in western Corinth Gulf, Central Greece, a region characterized by strong extensional deformation and exhibiting intense seismic activity, since it consists one of the most rapidly deforming continental extension areas in the Mediterranean domain (Fig. 3.1). This rift has been generalized as an East-West oriented, asymmetric half-graben with North-South striking extension controlled by a series of en-echelon north dipping normal faults along the southern coast together with minor south dipping antithetic faults along its northern boundary (Roberts and Jackson, 1991; Armijo et al., 1996; Bell et al., 2008). The available fault plane solutions of the strongest ($M \geq 6.0$) earthquakes determined in the last decades by waveform modeling (Taymaz et al., 1991; Braunmiller and Nabelek, 1996; Baker et al., 1997; Kiratzi and Louvari, 2003) along with solutions of moderate size events occurred during the most recent sequence of January 2010 (Karakostas et al., 2012) verify the pattern of East–West trending normal faulting, having one north dipping plane. The aforementioned features are also consistent with microseismic observations obtained by dense temporary networks (Hatzfeld et al., 1990; Rigo et al., 1996). The regional fault segments are associated with many devastating earthquakes reported since the ancient times (Papazachos and Papazachou, 2003) and recorded during the instrumental era, causing extensive damage and several casualties. Moderate magnitude events ($M \geq 5.0$) are also quite frequent in the area.

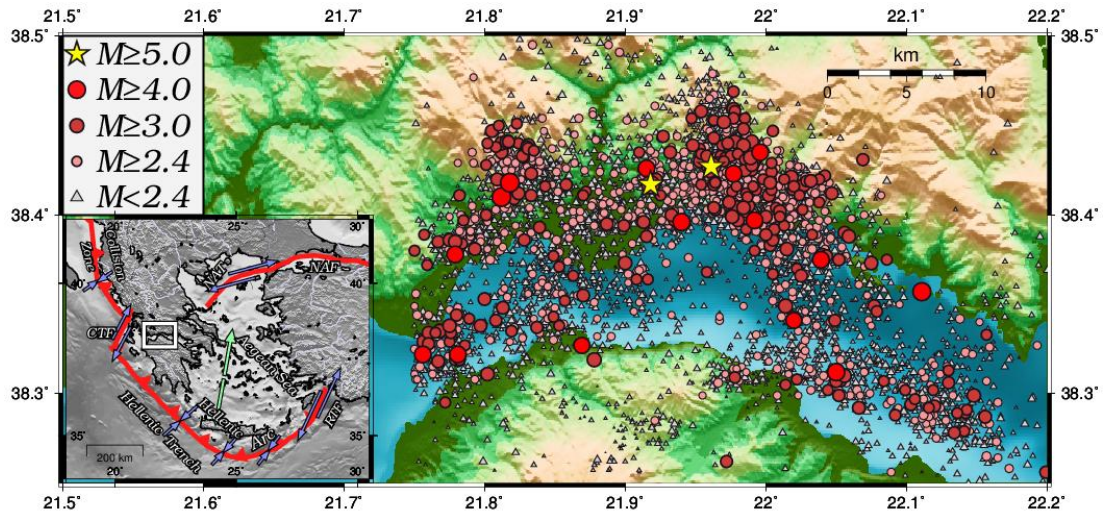


Fig. 3.1. Morphological map of the study area with seismicity occurred between August 2008 – December 2012. Stars denote the two main-shock epicenters. The inlaid figure shows the broader Aegean region and its major tectonic features. White box indicates the study area.

In the analysis presented below we follow the [Dieterich et al. \(2000\)](#) methodology for various implications regarding the stress regime evolution and the associated seismotectonics. Spatial and temporal evolution of the stress field changes are evaluated for datasets corresponding to different time increments and areas of major interest such as close to ruptured fault segments: On January 18th, 2010, an $M=5.5$ earthquake struck the northern coast of the western part of Corinth Gulf (Fig. 3.1), close to the town of Efpalio. The intense aftershock activity was culminated 4 days later with a second moderate magnitude ($M=5.4$) earthquake, and then continued for several weeks. The spatio-temporal evolution of the sequence along with seismotectonic implementations such as coseismic shifts and crustal structure have already been studied by several previous researches ([Jansky et al., 2011](#); [Ganas et al., 2012](#); [Karakostas et al., 2012](#); [Kostecky and Dousa, 2012](#); [Novotny et al., 2012](#); [Sokos et al., 2012](#)). The aim here is to take advantage of the large number of well recorded earthquakes both before and after the 2010 sequence in order to derive the spatial and temporal distribution of stress variations. We performed a more detailed analysis close in space and time to the fault segments associated with the 2010 doublet and we also attempt to

connect earthquake clustering with stress field variation. The stress changes inverted from seismicity rates are then compared with the ones derived from the elastic dislocation model application and quantification of their correlation is also demonstrated.

3.3.1.2 Data

Corinth Gulf sustains one of the best monitored areas of the Aegean region, since the adequately dense National seismological network and the local morphology conduce to satisfactory azimuthal coverage, and thus low completeness magnitude and considerable hypocentral accuracy. The data available from the Hellenic Unified Seismological Network (HUSN) was used (available at <http://geophysics.geo.auth.gr/ss/>) between August 2008 – December 2012 which demonstrate homogeneity in respect to magnitude estimation and detection level. We excluded from this catalogue the earthquakes located deeper than 20km which correspond to either poorly determined hypocenters or to intermediate depth events along the subducting Eastern Mediterranean plate underneath Peloponnese at this site.

The reliable determination of the completeness magnitude, M_c , for this dataset is of major importance for any seismicity rate based analysis. For M_c determination the Modified Goodness of Fit Test (MGFT) proposed by [Leptokaropoulos et al. \(2013\)](#) was followed. Although a relatively stable detection level of seismicity is achieved since August 2008, a temporal analysis of M_c should be carried out in order to ensure the appropriate completeness threshold. Therefore, annual and 2-year data sets were sought for M_c determination and the final selection was the highest of the resulting M_c 's. This was found equal to 2.4 (Figure 3.2) and it is observed, as expected, during the aftershock sequence of January 2010, because a fraction of smaller magnitude earthquakes cannot be distinguished within the coda of larger events ([Woessner and Wiemer, 2005](#)). This magnitude is 0.1-0.5 units higher

than the corresponding M_c calculated for the other tested data sets that correspond to periods prior and after the sequence. The b -value was found in the range $0.96 < b < 1.03$ in all the sub sets examined with an average value of $b = 0.98 \pm 0.025$ as shown in Figure 3.3.

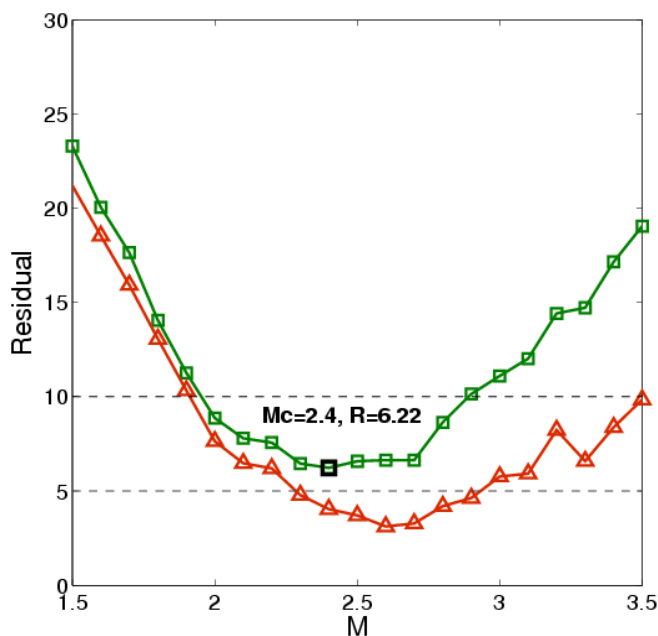


Fig. 3.2. Modified Goodness of Fit Test (MGFT) for M_c determination for the original data set during 2010. The residuals yielded as a function of minimum magnitude from the application of the original and the modified GFT are shown with green and red colors respectively.

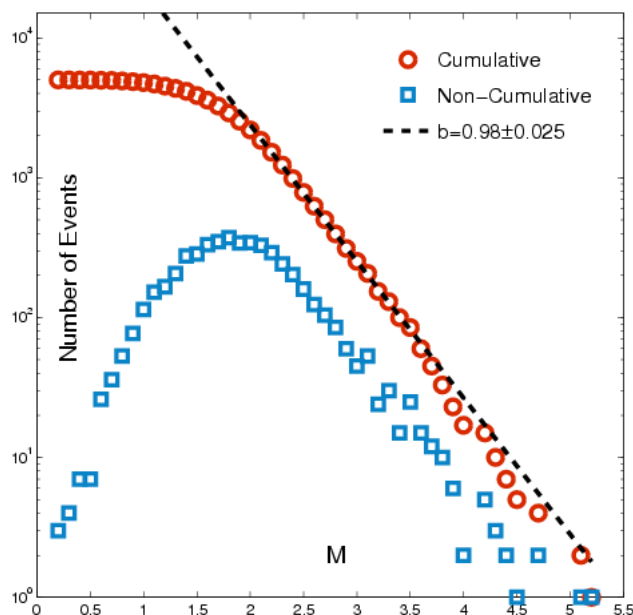


Fig. 3.3. Frequency-Magnitude distribution of the events recorder by the National Seismological Network from August 2008 until December 2012. The b -value and its standard error, σ_b , was calculated by following the maximum likelihood estimate (Aki, 1965) for 1-year and 2-year duration sub-sets and did not show significant fluctuations from 0.98. On the contrary, M_c , was fluctuating from 1.9 to 2.4 depending on the selected dataset.

3.3.1.3 Parameterization

In this section the determination process of the Rate/State model parameter values is described, i.e. reference and background seismicity rates, stressing rate, characteristic relaxation time and product $A\sigma$.

3.3.1.3.1 Reference and Background Seismicity Rates

We need to evaluate reference seismicity rate for the comparison of stress changes with the elastic dislocation modeling results but also to calculate an average background seismicity rate in order to estimate t_a from the Omori-Utsu law. The definitions based on [Cocco et al., 2010](#) for reference and background rates as were stated in Chapter 1 are recalled here. Reference seismicity rates were estimated in terms of earthquake probabilities by spatially smoothing the seismicity using a probability density function (PDF) as it was defined in Chapter 2 (eq. 2.13 through 2.16 - [Silverman, 1986](#)). The region was divided into a grid of rectangular cells and PDF determined the $M \geq M_c$ earthquake probabilities at the center of each cell.

For estimating background seismicity rates the depended events (aftershocks) were removed from the original dataset by applying a declustering algorithm based upon [Reasenber \(1985\)](#) approach. The seismicity rates were temporally smoothed for 30-event windows and an average background rate equal to 0.48 ± 0.17 events/day was estimated. Given the fact that declustering methods commonly apply subjective criteria, it is likely that a fraction of the total aftershocks still remains in the declustered dataset. For this reason, we preferred an even more conservative background rate evaluation derived from the declustered seismicity from August 2008 to January 15th, 2010, a period during which there was no noticeable (enhanced) seismic activity recorded in the study area. In such way we ensure that even less dependent events are included in the derived dataset. By this procedure we derived a background seismicity rate equal to 0.32 ± 0.04 events/day (Fig

3.4). This rate varies in both space and time but it is assumed to be representative for the unperturbed regional rate, since these fluctuations are not significant because they exhibit identical order of magnitude. In addition this rate is relatively stable during the period prior to the seismicity enhancement since its standard error (0.04) is less than 1/4 of the respective error for the entire dataset (0.17). Note also that the study area is relatively small and spatial rate variations do not significantly influence the results of our analysis, since most of the events are concentrated in specified areas, which mostly contribute to the derived background seismicity rate value.

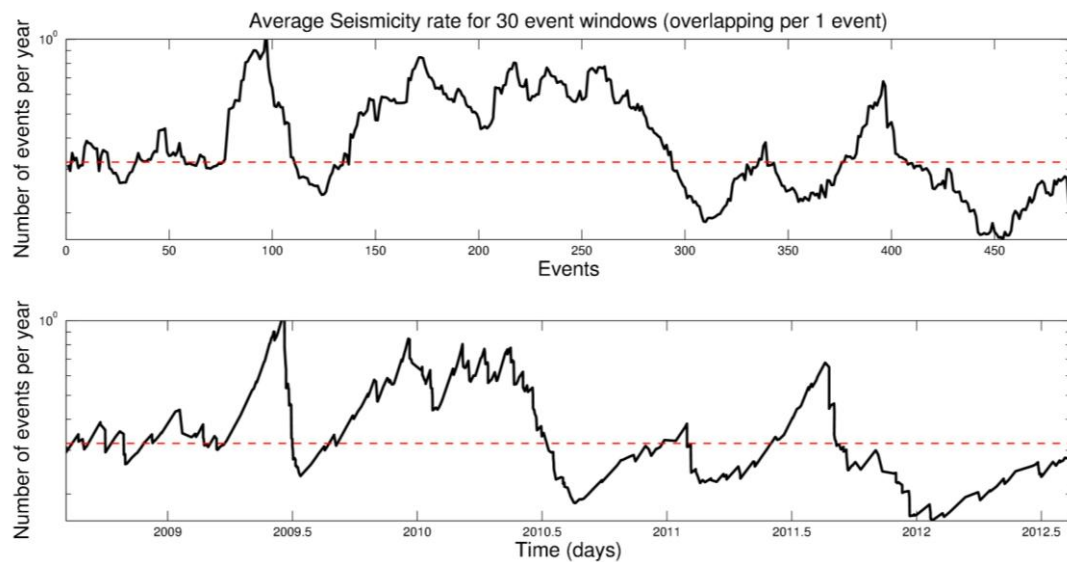


Fig 3.4. Background seismicity rate estimate from the declustered catalogue in event domain (upper frame) and time domain (lower frame) for 30-event sub-sets (overlapping per 1 event). The averaged background seismicity rate was estimated equal to 0.32 events/day from the period just before the January 2010 sequence (dashed line).

3.3.1.3.2 Characteristic Relaxation Time (t_a)

After determining the background seismicity rate, we estimated characteristic relaxation time in two different ways. The first approach is based upon the temporal variation of the inter event time between successive events since August 2008 (Fig. 3.5) and the second is estimating t_a from the parameters of the Omori-Utsu formula for the January 2010 sequence (Fig. 3.6)

$$\lambda(t) = \frac{K}{(c+t)^p} \quad (3.3)$$

Omori-Utsu decay law parameters were estimated as $K=87.5\pm 4.5$, $p=1.05\pm 0.05$, $c=0$, which suggest a characteristic relaxation time equal to 223 days (166 - 307 days at 95% confidence level). We also fitted the decay law to the aftershock sequence followed the June, 15th, 1995, Aigion ($M=6.4$, 38.36°N , 22.20°E) earthquake. For this purpose we considered seismic activity since 1975 with $M\geq 3.5$ since then (M_c was calculated for overlapping 10-year datasets and found equal to 3.5). The average background seismicity rate was estimated at 0.1 events/day and the Omori-Utsu law parameters were found equal to $K=45.2\pm 11.7$, $p=1.12\pm 0.09$, $c=0.725\pm 0.16$. These values lead to a characteristic relaxation time of 230 days with the 95% confidence bounds lie between 115 and 473 days. This result is in very good agreement with the ones yielded from the previously mentioned methods for the 2010 sequence (226 days from inter event time plots and 223 days from Omori-Utsu law fitting in the Efpalio sequence data). Considering these results we adopted a $t_a=225$ days (or 7.5 months) in the following calculations.

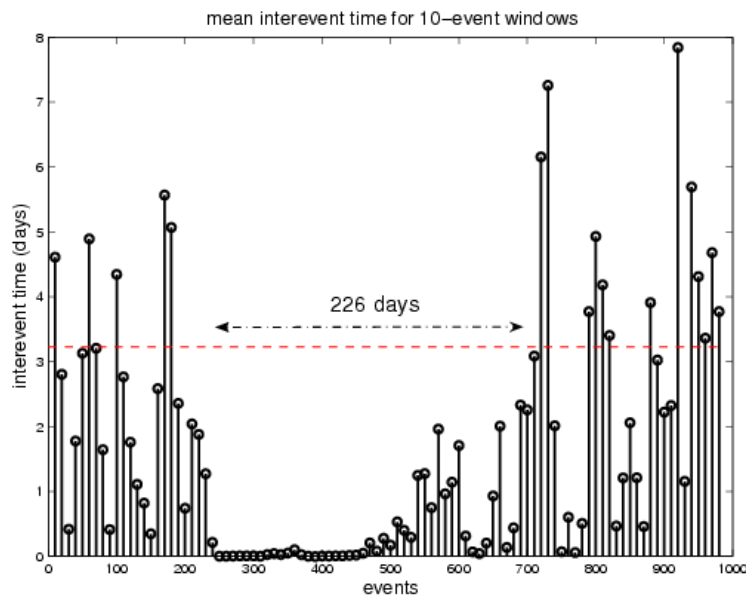


Fig. 3.5. The inter-event time plot shows that seismicity rate is returning to the background rate after approximately 226 days. These times yielded from averaging the times of overlapping 10-event windows. Dashed line shows the average inter-event time which is the inverse of the average background seismicity rate as it was estimated in the previous section.

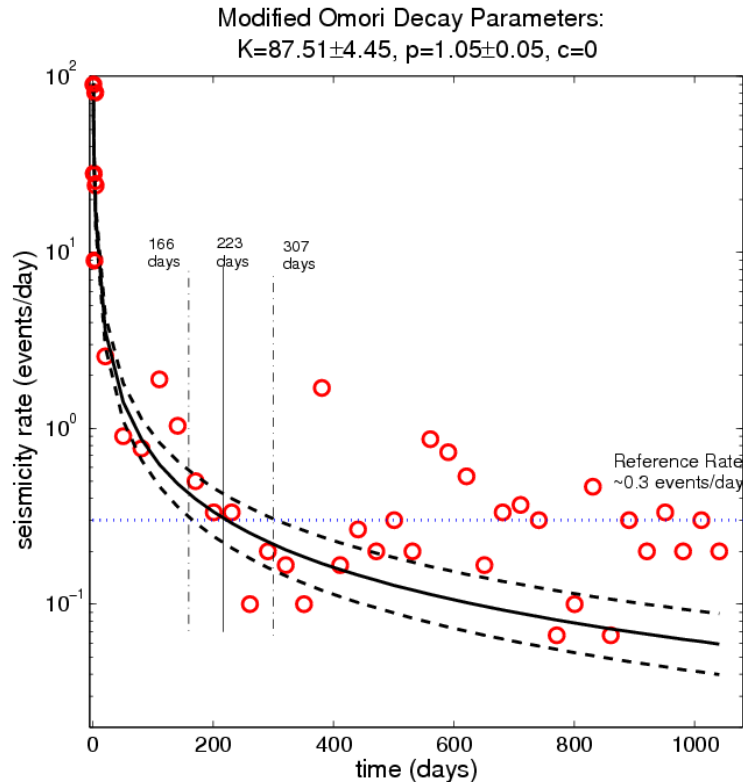


Fig. 3.6. Seismicity rate decay over time (circles) and Omori-Utsu law fitting (solid line) with its 95% confidence interval (dashed lines) after the January, 18th, 2010 sequence (Dataset 1). The first five points (solid circles) show the daily seismicity rates for the first five days after the main shock. The rest of the circles represent the daily seismicity rates smoothed over 1-month non-overlapping periods. The horizontal dotted line demonstrates the background seismic activity as derived from the declustered Dataset 1, intersecting with the Omori-Utsu law curve at $t_a \sim 223$ days.

3.3.1.3.3 $A\sigma$ and Stressing Rate (\dot{S}_r)

In the following applications t_a along with \dot{S}_r , were used to estimate $A\sigma$. For this purpose we first derived \dot{S}_r , which was assumed to be spatially uniform and constant over time (section 2.2.3). A stressing rate equal to ~ 0.06 bars/yr was estimated in such way, or equivalently $\sim 1.68 \cdot 10^{-4}$ bars/day. This value together with $t_a = 225$ days, were applied in equation 2.8 for obtaining the product $A\sigma$. The previously mentioned values of stressing rate and characteristic time yield to $A\sigma = 0.04$ bars (~ 0.03 - 0.05 bars considering the t_a uncertainties), which is relatively low, but still inside the proposed accepted values ($A\sigma = 0.01$ - 9 bars, [Harris and Simpson, 1998](#)) and also in agreement with recent studies (e. g. [Hainzl et al., 2013](#) – 0.0016 - 0.16 bar). [Maccaferi et al. \(2013\)](#)

accepted a value of 0.05 bars for their analysis in the extensional regime of Iceland which is quite similar with the one estimated in this study.

3.3.1.4 Results – Discussion

3.3.1.4.1 Temporal evolution of stress field derived from seismicity rate changes

We applied equation (3.2) in order to calculate stress changes from seismicity rate variations and how they evolve through time. The obtained results are illustrated in two ways: Firstly we followed an equal-event number approach (Fig. 3.7) and then an equal-time approach (Fig. 3.8). In the equal event approach seismicity rates were calculated for unequal moving time windows which though included a constant predefined number of earthquakes. Since all datasets contain the same event number, positive ΔCFF occurred when a time window has shorter duration than the previous one. These stress changes are plotted versus time in Fig. 3.7. We first selected a 20-event window overlapping per 1 event (Fig. 3.7 left frame). The occurrence times of the strongest shocks ($M \geq 4.5$) are denoted by asterisks. Stress changes associated with these events are clearly demonstrated, especially regarding the January 2010 doublet, when the highest ΔCFF values are computed. There are also some distinctive stress steps that do not seem to be connected with an $M \geq 4.5$ event, but they rather being a product of a swarm like activity. It is clear that in this approach that each positive stress step is followed by a negative one due to the depression of seismicity rates. This is rather expected on the basis of this concept because we compare the seismicity rate occurred in each time (or equivalently event) step, with the one occurred immediately beforehand. Therefore, instead of using a uniform and not explicitly determined, constant background rate as reference activity, we compare the observed seismic rate differences between subsequent time increments. Every time when a dataset correspond to lower rates than the preceding one

(equivalently, decrease of the slope of cumulative events number, figure 3.8) this is interpreted as a stress drop in figure 3.7. The tuning parameter for illustrating stress changes in this case is the size of the time (or event) window. We then selected a broader 100-event window overlapping per 5 events (Fig. 3.7 right frame). In this case the temporal range of the obtained results and their resolution is reduced but it is clear that the only significant stress jump is related with the strongest earthquake occurrence in the study region. This stress step was followed by a long-term gradual stress decrease, which almost stabilized after August 2010. All minor stress changes are not distinguished in this figure.

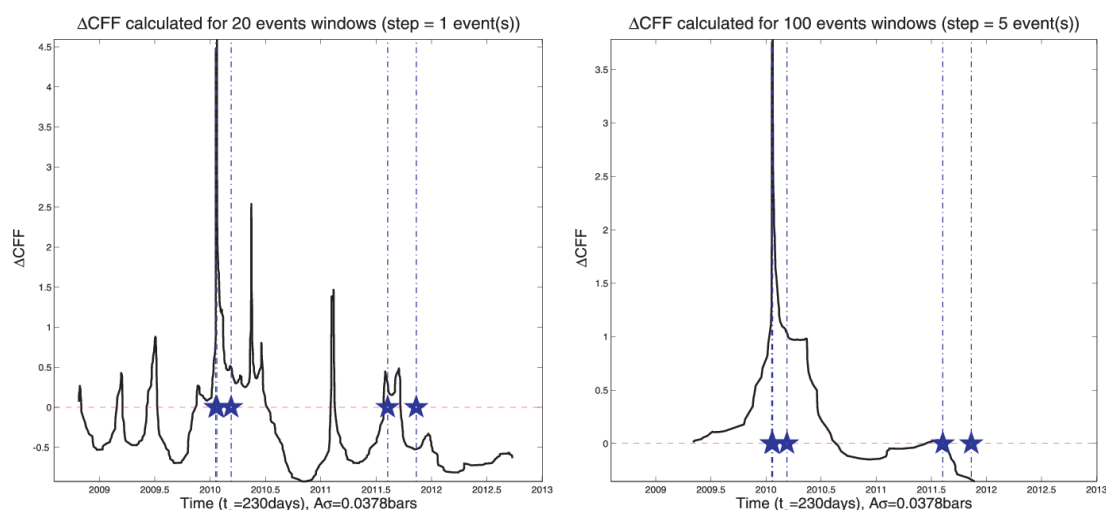


Fig. 3.7. Stress changes inverted from seismicity rate variation considering overlapping datasets of 20 (left frame) and 100 (right frame) events. The size of the event window determines the resolution of ΔCFF : Small windows reveal more stress variations whereas broader windows only demonstrate stress changes associated with the aftershock sequence followed the January 18th 2010, $M=5.5$ event. Blue asterisks denote the $M \geq 4.5$ events.

In the second approach tested stress changes were calculated by considering fixed time windows before and after successive calculation points (Fig. 3.8). Positive ΔCFF therefore appear when the dataset following a calculation point includes more events than the one preceding this point. The left frame of Figure 3.8 shows the stress derived from 1-month time windows whereas the right frame of figure 3.8 displays the respective results yielded for 3-month time windows. The cumulative number of events as a function of

time is also plotted in the same figures. Stress changes associated with the larger magnitude events are obvious but there are still considerable stress steps due to seismic enhancement that are not directly connected with a significantly larger magnitude event. These changes are evident both before and after the January 2010 doublet. The application of the 90 days time window reveals that in addition to the stress jumps associated with a “main-shock” there are also two notable positive stress steps, one before and one after the January 2010 seismicity burst, that are connected with swarm-like activity rather than a typical main shock - aftershock sequence. Nevertheless there is also an M=4.5 earthquake (close to event 1200) that does not seem to induce remarkable stress changes and this is shown in both cases where the time window is equal to 30 and 90 days, respectively.

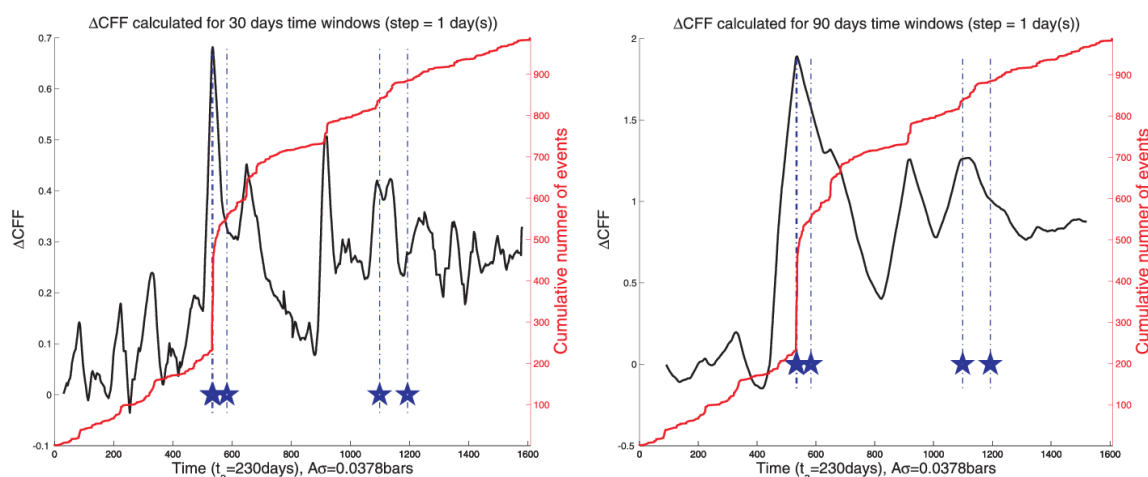


Fig. 3.8. Stress changes inverted from seismicity rate variation considering overlapping datasets of 1month (left frame) and 3 months (right frame) time windows.

3.3.1.4.2 Comparison with ΔCFF derived from elastic dislocation model

The stress results as they were inverted from seismicity rate changes are here compared with the ones obtained from the elastic dislocation model application. This later approach was firstly applied to calculate Coulomb stress changes caused by the coseismic slip of the two strong earthquakes. Then, reference rates and seismicity rates of the small magnitude events for

different time increments after the main shock were spatially smoothed by the application of the selected PDF (eq. 2.15). The differences between the earthquake occurrence rates before and after the main shock were compared and used as input data in the stress inversion algorithm in order to provide an independent estimation of stress changes. Eventually we investigated the quantitative correlation among the results derived from the two methods. Stressing rate is assumed to be constant throughout the study period and therefore, long term changes in tectonic loading are not investigated here. Even if some variation in the stressing rate does exist, it is expected too short to influence substantial changes.

The analysis we performed here is based upon the observation that even small static stress changes result to considerable seismicity rate changes (Harris, 2000; Steacy et al., 2005 and references therein). Thus we examine the proportion of the area where there is agreement in the sign of ΔCFF derived by the two methods. Following this point of view, the values of stressing rate and characteristic relaxation time do not affect the spatial distribution of the stress changes, but only their absolute value, such that the results we seek being insensitive to these parameter values fluctuation. We focus on the agreement of the ΔCFF sign instead and therefore we fix parameter values as mentioned in the previous sections: $\dot{S}_r = 0.06 \text{bar/yr}$, $A\sigma = 0.04 \text{bar}$ and $t_a = 225 \text{days}$. The only parameter that does affect the spatial pattern of the derived stress changes is the bandwidth, and thus the examination is carried out with respect to bandwidth fluctuation. Note that the epicentral error in the catalog is 3-5km and therefore the bandwidth selection was done according to this criterion.

For the calculation of Coulomb stress changes due to the coseismic slip of 2 main shocks by the elastic dislocation approach, we adopted the rupture model proposed by Karakostas et al. (2012). The calculations were performed

at a depth of 9km which is approximately the average depth determined for both regional (7.8 ± 3.5) and relocated (8.9 ± 1.6). Figure 9 shows the distribution of ΔCFF in the study area after the combined influence of both main shocks, along with their aftershocks. The aftershocks spatial distribution suggests that there are important spatial clusters beyond both the east and west tips of the ruptured fault segment, where the largest positive ΔCFF are observed. Nevertheless, there is a significant fraction of seismicity located inside the negative ΔCFF lobes, mostly comprising onto fault aftershocks.

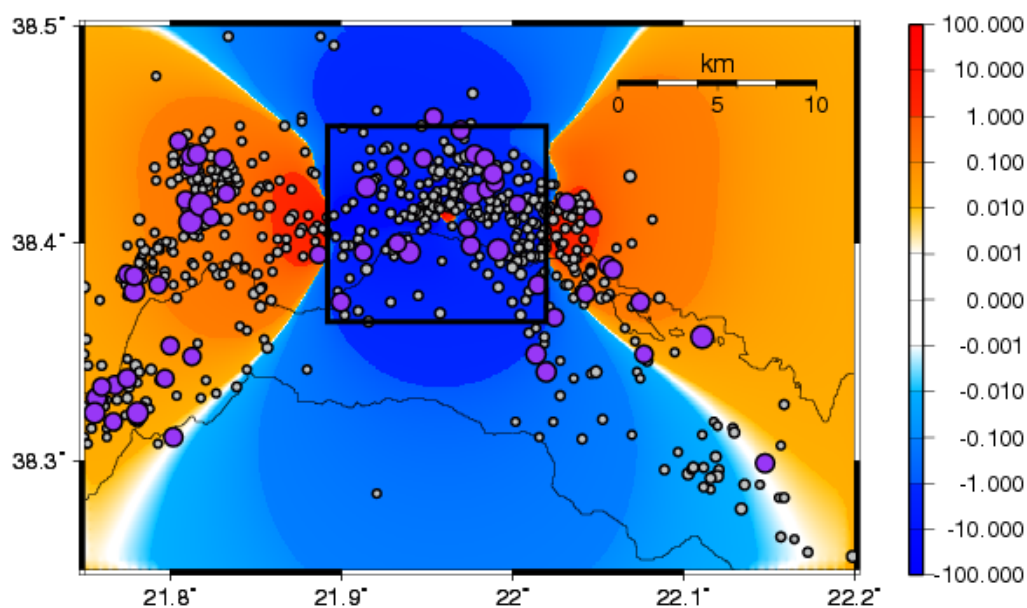


Fig. 3.9. Stress pattern due to the combined coseismic slip of the two main shocks, resolved according to the faulting type of the first main shock at 9km depth. Gray circles show the epicenters of subsequent events above $M_c=2.4$ that occurred until December 2012, whereas the strongest of them ($M>3.5$) are depicted by purple circles. The black box indicates approximately the area located in a distance closer than one fault length ($\sim 5.5\text{km} - 6\text{km}$) across the ruptured zone.

In Figure 3.10 the agreement percentage between the two methods is plotted as a function of bandwidth, h . The average sign agreement is generally not sensitive in the bandwidth fluctuation between $0.01^\circ - 0.05^\circ$, demonstrating an almost stable value between 60%-65%. This means that nearly $2/3$ of the coseismic stress changes are compatible with the observed seismicity rate variations after the main shocks. Positive stress changes are better forecasted though, with the sign agreement in such areas reaching up

to 78% and being directly proportional to the bandwidth value. On the contrary, negative stress changes are inversely proportional to the smoothing parameter. The sign agreement in this case falls below 60% for $h > 0.03^\circ$.

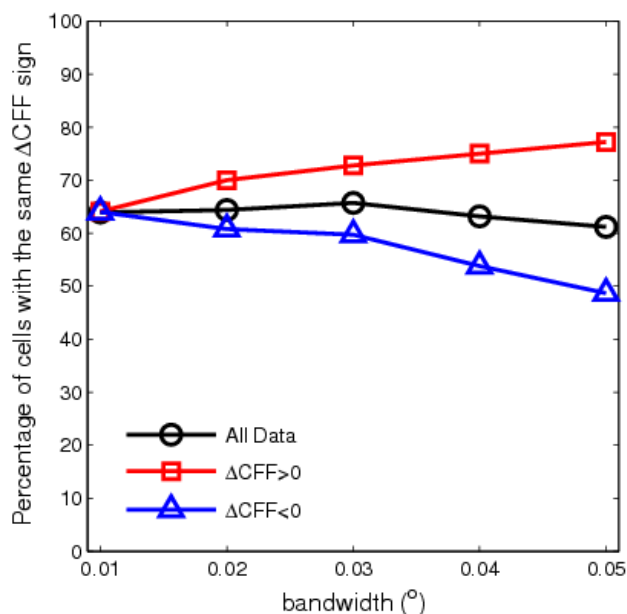


Fig. 3.10. Percentage of cells having common ΔCFF sign derived from both methods. The elastic dislocation model takes into account the combined influence of both main shocks. Reference seismicity rate is derived by the events occurred from August 2008 to January 18th 2010. Solid lines demonstrate the results derived from the local catalogue until the end of 2012. Red and blue lines indicate the percentage of cells with positive and negative ΔCFF , calculated from both the elastic dislocation model and the stress inversion technique, respectively.

Our next step deals with off-fault seismicity rate changes, where the elastic dislocation model calculates ΔCFF with significantly higher accuracy than in the near field, where unavailability of slip details influences the stress pattern. The stress values derived by this method are compared with the ones inverted from earthquake rate changes after excluding the area inside the box shown in figure 9. We selected this constraint in order to concentrate on the off-fault aftershocks distribution, which occupies areas where the ΔCFF is well determined by the elastic dislocation model. Therefore, the consistency between the two methods is based upon results that do not suffer from significant uncertainties. The obtained results (Fig. 3.11) illustrate that higher correlation in comparison with the previously described approach is achieved by this way: The two methods provide the same ΔCFF sign for approximately

75% of the area beyond the near field. Generally, as shown in figures 3.10 and 3.11, lower bandwidth values lead to better agreement for negative ΔCFF cells, whereas higher values of h , bring out higher percentage of agreement for positive ΔCFF areas. Nevertheless, higher bandwidth values should be avoided, because they oversmooth the calculated ΔCFF and therefore local fluctuations cannot be distinguished anymore, a fact that may lead to erroneous interpretation. Silverman (1986) equation (eq. 2.17) leads to $h \sim 0.03$ which as shown in figures 10 and 11 leads to the higher percentage of sign agreement and also balances the differences between positive and negative ΔCFF cells. This bandwidth value also leads to the highest correlation between observed and synthetic seismicity rates yielding from the forward Rate/State modeling (see Appendix E).

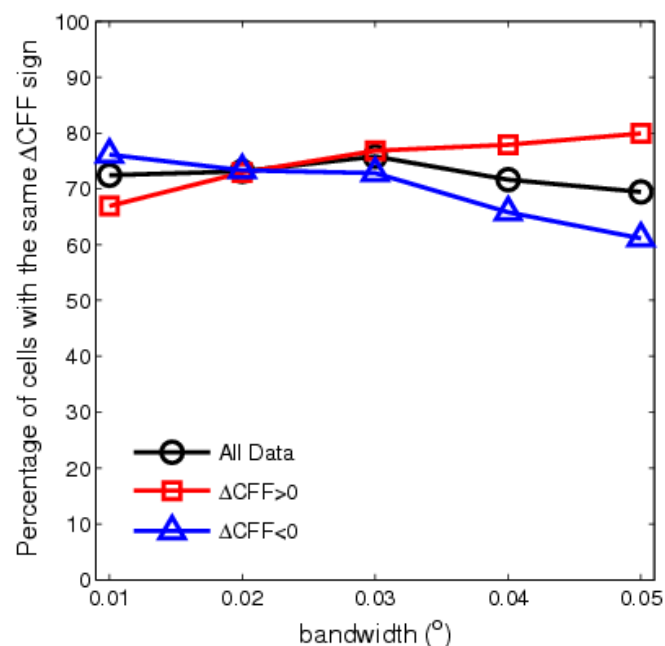


Fig. 3.11. Percentage of cells having common ΔCFF sign derived from both methods only outside the square area indicated in figure 9. The elastic dislocation model takes into account the influence of both main shocks. Reference seismicity rate is derived by the events occurred from August 2008 to January 18th 2010. Solid lines demonstrate the results derived from the local catalogue until the end of 2012. Red and blue lines indicate the percentage of cells with positive and negative ΔCFF , calculated from both the elastic dislocation model and the stress inversion technique, respectively.

The comparison of the stress results implies that in general there is a good agreement between the elastic dislocation and the inversion methods (>50% in almost all cases) especially in the far field (reaching up to 80%). It is therefore verified to be of major importance that significant seismicity rates should also be available both prior and after the stress events for the analysis to provide conspicuous results. Finally approximately 3/4 of the stress changes in the far fields as they were calculated by the elastic dislocation model can be successfully reproduced by the stress inversion methodology followed here.

3.3.1.4.3 Spatial distribution of stress changes

In this section an attempt is performed to derive the stress changes caused by the strongest earthquakes ($M \geq 5.4$) in the study area since August 2008. In doing so, various time-windows preceding and following the January 18th, $M=5.5$ earthquake were selected and the stress changes derived from eq. (3.1) were mapped. This application was performed in a dense grid superimposed onto the study area, consisting of cells with 0.001° side (Fig. 3.12a-d). The stress values in each cell were smoothed by a Gaussian filter with radius 0.02° , in all cases except in figure 3.12c where the bandwidth value applied was $h=0.04^\circ$. In the approaches described below, the condition that each cell contains at least 2 events before or after the main shock was fulfilled. The parameter values applied were the same we used in the previous subsection and equal to $A\sigma=0.04\text{bars}$, $t_a=225\text{days}$ and $\dot{S}_r=0.06\text{bars/year}$. In figure 3.12a the stress changes were inverted from 1-year time intervals both before and after the first main shock. In this approach positive stress changes up to 0.6bars were detected close to the activated fault segments but also to the west of it.

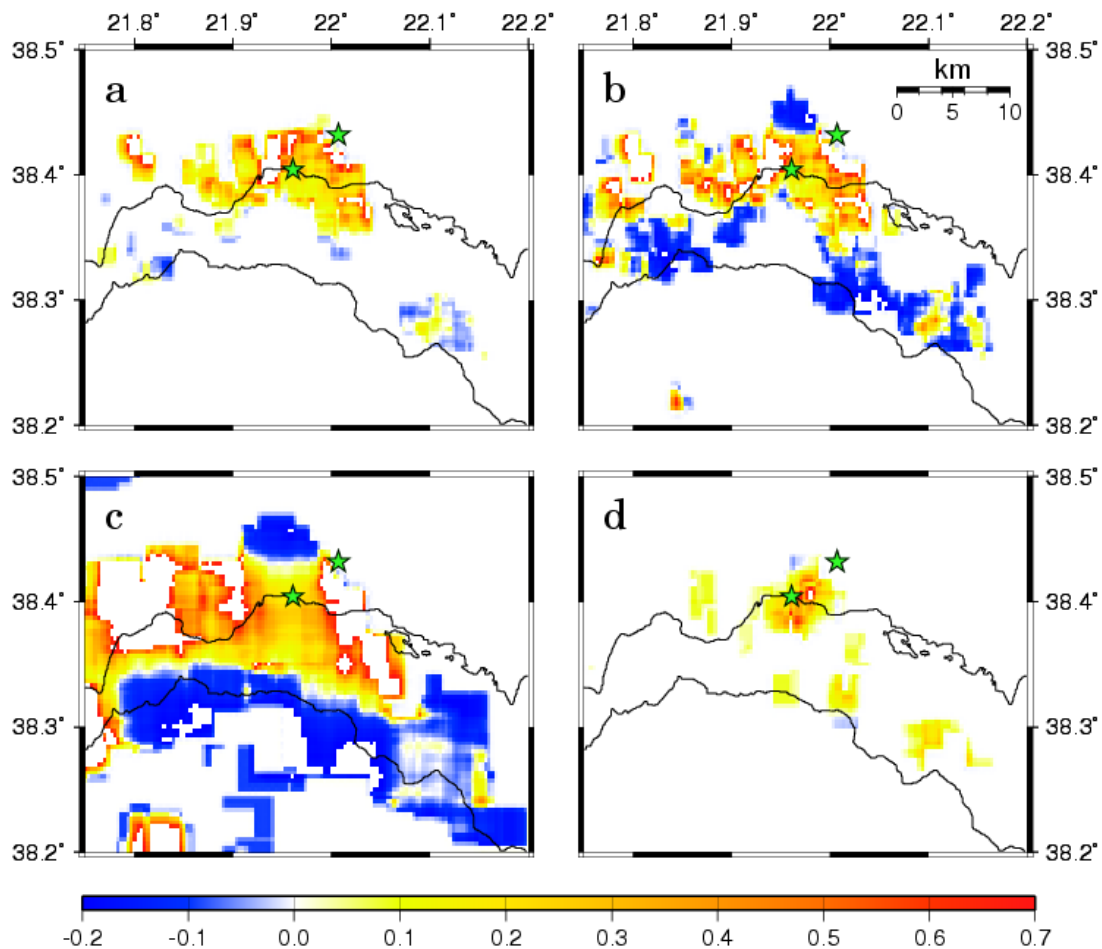


Fig. 3.12. Spatial variation of Coulomb stress derived from seismicity rate changes in different time windows before and after the January 2010 doublet: a) 1 year before and 1 year after, $h=0.02^\circ$, b) 532 days before and 1077 days after (entire dataset), $h=0.02^\circ$, c) 532 days before and 1077 days after (entire dataset), $h=0.04^\circ$, d) 100 days before and 100 days after, $h=0.02^\circ$. White cells represent areas with insufficient data. Spatial step in all cases is 0.001° .

Minor stress changes, both positive and negative in the southern part of the region are evident although the data in this area do not provide sufficient resolution. A more detailed stress pattern is revealed when longer time spans are considered and the entire dataset is utilized (Fig 3.12b&c). The entire dataset includes 232 events within 532 days before and 755 events within 1077 days after the January, 18th, earthquake. Positive stress changes up to 0.7bars are accommodated in approximately the same areas with the previous case. Stress drops down to 0.2bars are detected opposing to figure 3.12a which are amplified in figure 3.12c where the bandwidth value is doubled. Positive stress changes that are persistent at the location of the first main shock can be attributed to the stress transfer from the second mainshock

and possibly, to the numerous strong ($M > 4.0$) aftershocks located to the east of the firstly failed fault segment. The resulting stress pattern seems to be consistent with the one derived from the elastic dislocation model when onto-fault areas are excluded (Fig. 3.9). A narrow time window of 100 days before and after the main shock is able to provide only local, low amplitude positive stress changes, despite the fact that some of these variations are located in considerable distances of the activated faults (Fig. 3.12d).

3.3.1.4.4 Δ CFF changes close to the fault segments associated with the 2010 doublet

The analysis is now focused in the close vicinity of the fault segments associated with the January 2010 doublet, in an area approximately one fault length further from the rupture zone. The aim is to seek for anomalies in earthquake occurrence rates prior to the sequence and their possible connection with stress changes. These anomalies are detected by the means of the inter-event time distribution (the inverse quantity of seismicity rate) and how this time deviates from the average inter-event time as it is derived from the declustered catalogue (dotted horizontal line in figure 3.13). 2 months before the 5.5 event, an $M=3.9$ earthquake took place, followed by an extraordinary seismicity burst at a rate more than 10 times higher than the background activity. The seismic activity was depressed for a couple of weeks and then another burst occurred 25 days before the beginning of the Efpalio sequence. This second earthquake cluster had no distinctive magnitude earthquake and the strongest event of the sequence had $M=3.1$. After this seismic enhancement only 2 earthquakes occurred during the 25 days period that passed until the initiation of the seismic sequence on January 18th.

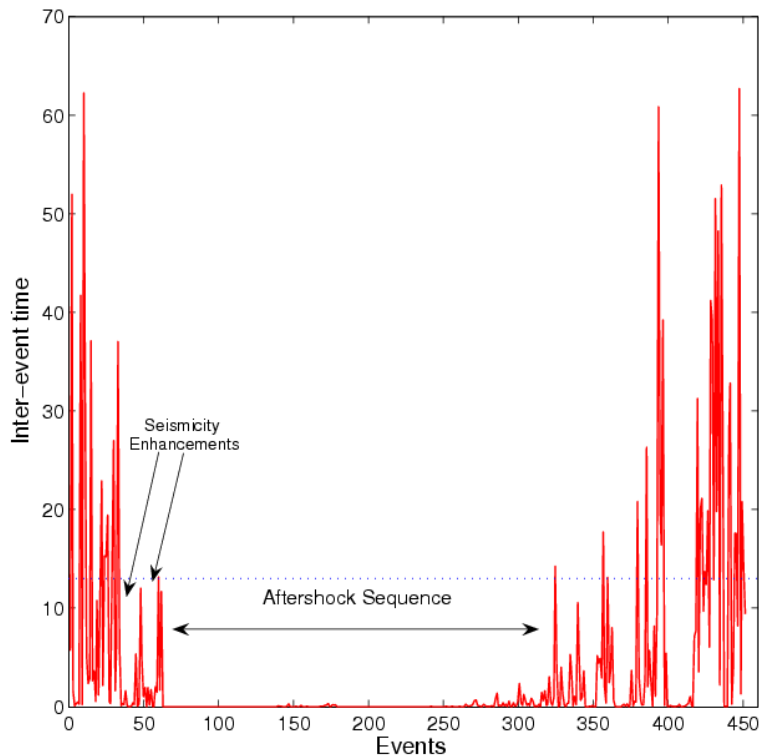


Fig. 3.13. Seismicity rates in the close vicinity of the fault segments associated with the January 2010 doublet. Evidence of anomalous activity prior to the 1st strong event is shown here. We interpret this activity in terms of stress increase that finally led to the seismic burst less than one month later.

Both clusters occurred very close to the epicenter of the second strong shock of the sequence. An effort is now attempted to derive stress changes from these rate enhancements and to associate these changes with the Efpalio sequence. The regional data relocated by [Karakostas et al. \(2012\)](#) indicate an average focal depth of 9km. Here it is shown that a focal depth close to 9km produces a stress pattern more consistent with the location of the cluster preceded the M=5.5 main shock, which is also located in positive Δ CFF lobe. The stress field variation is resolved according to the 18th January, 2013, M=5.5 earthquake. If an h=2km is adopted for the M=3.9 event (Fig. 3.14a) most of the events in the cluster are located into a negative Δ CFF lobe. At a depth of 12km (Fig. 3.14c) the southernmost of the events fall inside a positive stress lobe, but there are still some shocks found in stress shadows. Moreover the depth of 12km is at the lower bound of the regional seismogenic layer which roughly reaches 15km ([Karakostas et al., 2012](#)). Obviously the depth

selection of 9km (Fig. 3.14b) appears to reproduce the most consistent stress pattern since the entire cluster is found in an area of increased stress.

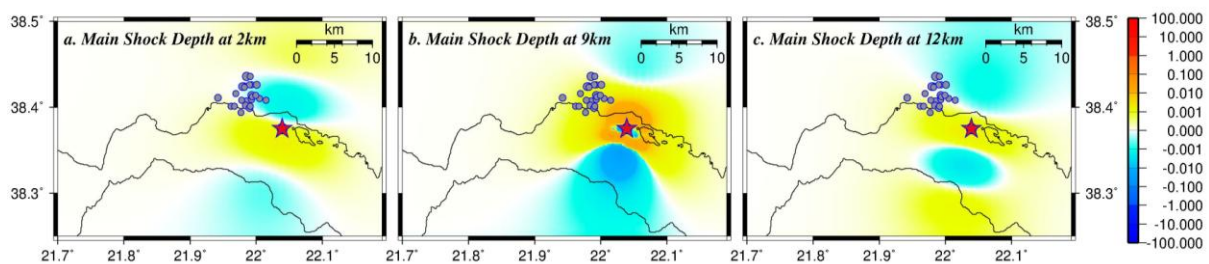


Fig. 3.14. Coulomb stress changes caused by the $M_L=3.9$ event resolved according to the focal mechanism of January 18th, 2010, $M=5.5$ event, considering the nucleation depth of the causative fault at 2, 9 and 12 km (a, b and c respectively).

3.3.1.4.5 Stress changes associated with spatio-temporal earthquake clustering

Earthquake clustering in western Corinth Gulf appears quite frequently, attracting the interest of several researchers. [Mesimeri et al. \(2013\)](#) identified 18 earthquake clusters in NW Peloponnese since 1980 and classified them in three categories (main-shock – aftershocks, swarms and swarm-like sequence) according to their history of moment release and the occurrence time of the main event. [Karagianni et al. \(2013\)](#) also studied spatio-temporal earthquake clustering in western Corinth Gulf during 2010 and 2011 and demonstrated the swarms evolution with space-time plots. Taking advantage from the availability and adequate number of the observed clusters we attempt their identification by the stress changes they induce (Fig. 3.15). The eight clusters that were detected are shown in Figure 3.16. Their properties are also presented in table 3.2. The first three of them occurred prior the Efpalio doublet whereas the next five followed the 2010 sequence and they are all located in positive ΔCFF lobes.

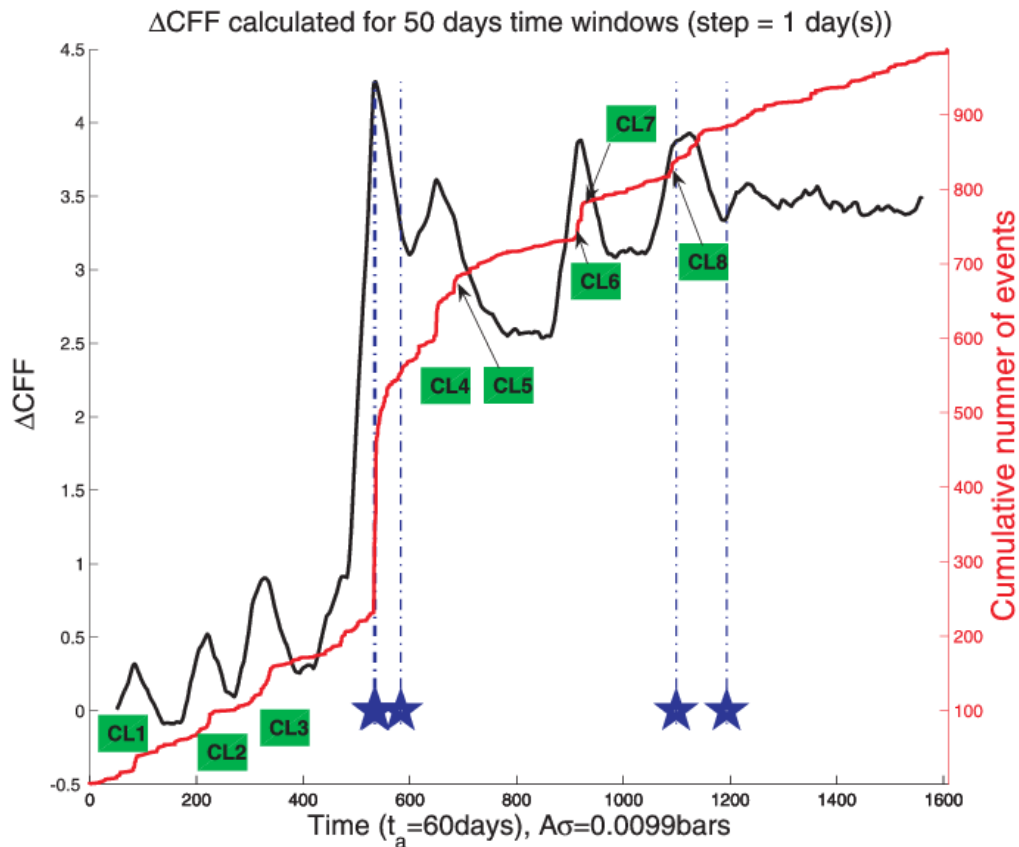


Fig. 3.15. Cluster identification by stress changes associated with their occurrence. Apart from the larger stress changes connected with January 2010 sequence, 8 more clusters are shown to produce remarkable stress changes.

Table 3.2 evidences that most of these clusters exhibit swarm-like behavior since the largest magnitude event occurred when the activity was already in progress in several cases. Even when the strongest shock took place at the beginning of the sequences, the magnitude difference from the second strongest event was less than 0.4 units, except in cluster 7, in which this difference was equal to 0.6 units. This sustains an additional evidence that the associated fault segments came closer to failure by remote stress triggering rather than producing aftershock sequences, induced by a near field main shock. Figure 3.17 shows the locations of these 5 clusters in relation to ΔCFF as calculated by elastic dislocation model application. Although there are several events occurred inside negative lobes, only spatio-temporal clusters characterized by increased seismicity rates are located in increased stress

areas. This suggests that non-clustered activity is probably related to reference seismicity whereas the enhanced-rated clusters are plausibly considered to be associated with stress triggering.

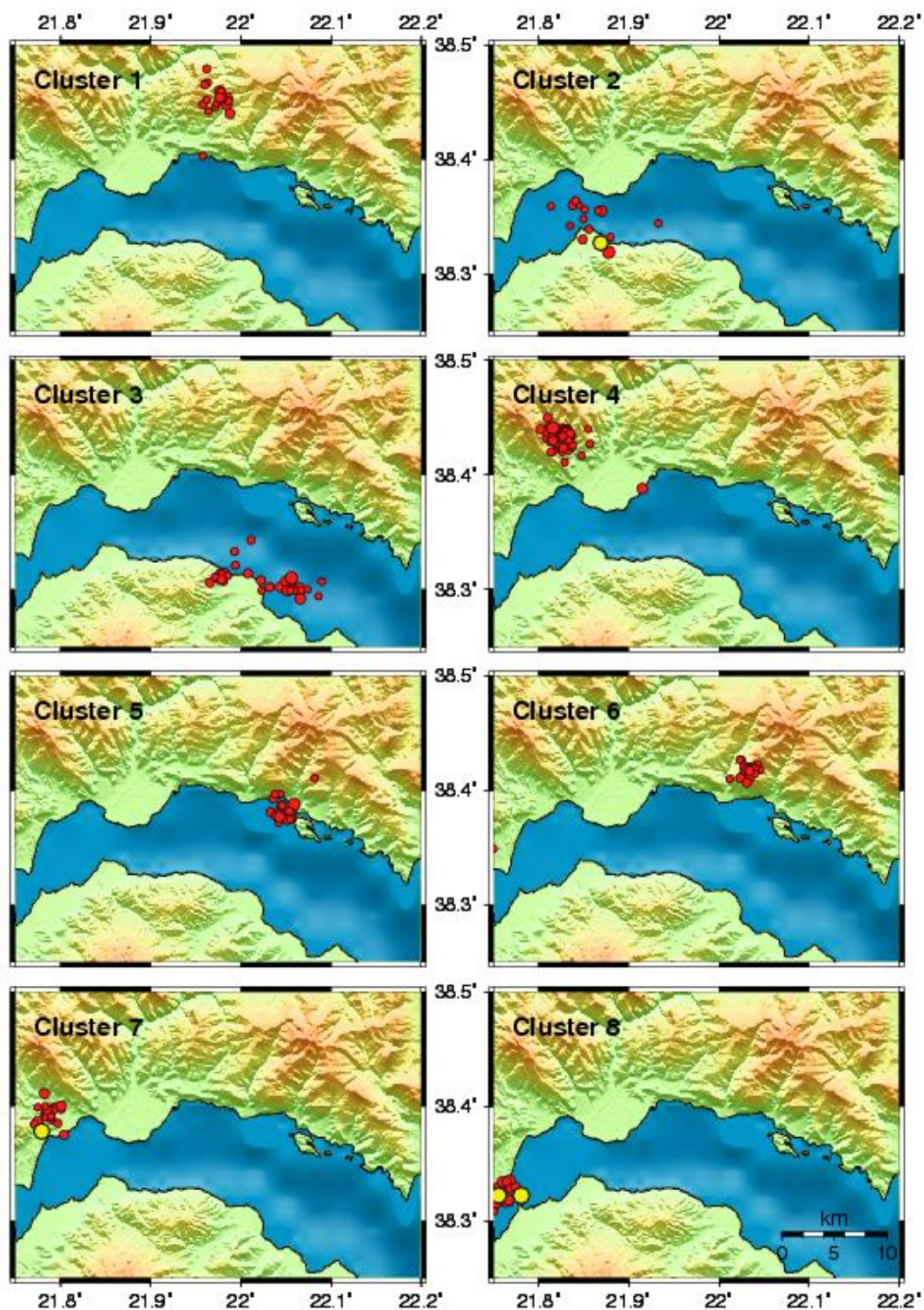


Fig. 3.16. Seismicity clusters associated with minor Δ CFF changes. Yellow circles illustrate $M \geq 4.0$ events.

Table 3.2. Properties of the 8 clusters associated with stress changes in the study area (excluding the 18th January sequence).

Cluster	Number of Events	Duration (days)	1 st Event's Magnitude	Largest Magnitude	ΔM between 2 strongest events	M_{max} Event
1	18	7.5	3.7	3.7	0.3	1 st
2	15	5	4.0	4.0	0.1	1 st
3	29	20	2.8	3.8	0.3	23 th
4	42	4	3.5	3.9	0.1	34 th
5	19	5.5	2.9	3.8	0.3	5 th
6	20	2.5	2.5	3.5	0.3	11 th
7	23	3.5	2.4	4.2	0.6	2 nd
8	18	7	2.5	4.3	0.1	8 th

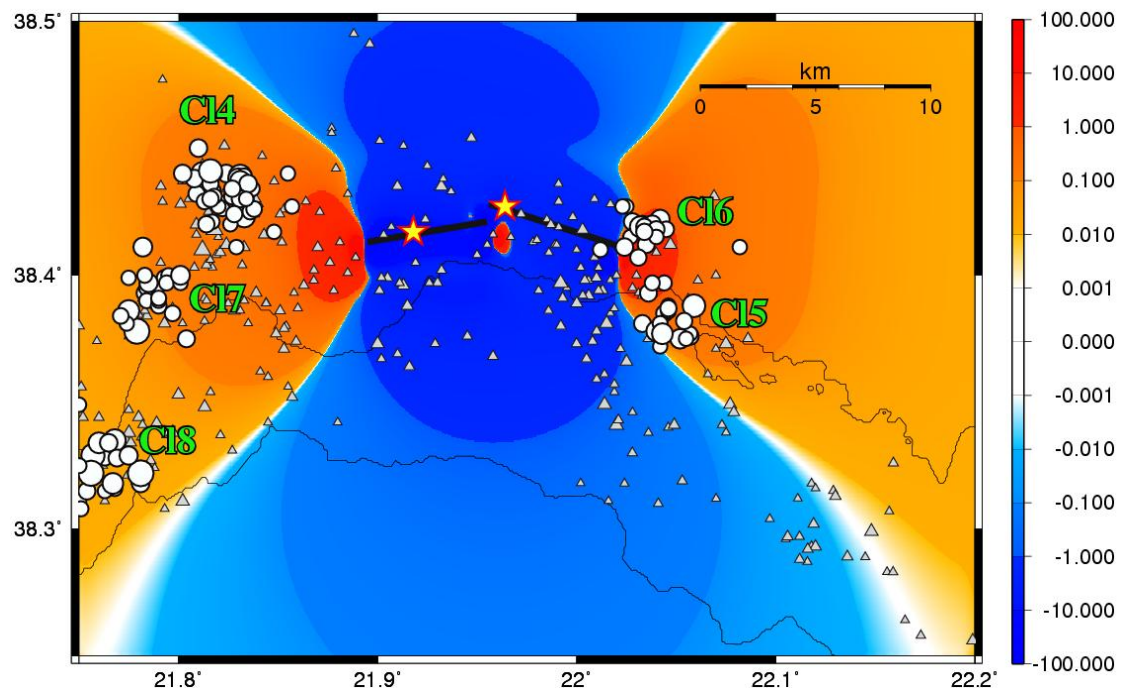


Fig. 3.17. Map with ΔCFF caused by the January 2010 doublet. Aftershocks that followed since April 2010 are also plotted. Non clustered activity is indicated by gray triangles. Seismicity Locations of the spatio-temporal earthquake clusters are depicted as white circles. It is shown that almost all the clustered epicenters are found in increased stress areas. Cluster codes correspond to the ones provided in Table 3.2 and shown in Figure 3.16.

3.3.2 Area 2 – Samos-Kusadasi/ Karaburun Peninsula 2007-2012

3.3.2.1 Introduction

The study area (Fig. 3.18) constitutes part of the back arc Aegean area, the most important feature of seismotectonic origin in the eastern Mediterranean. The area of eastern Aegean has repeatedly suffered from devastating earthquakes, known from both historical reports and instrumental recordings. In the Aegean region an additional N–S movement due to the inner deformation is observed and therefore the resultant extension demonstrates a NE-SW orientation. In northern Aegean the dominant type of faulting is dextral strike slip with NW striking, which is also verified by several reliable fault plane solutions of recent strong earthquakes and neotectonic observations.

The onshore deformation in western Turkey is dominated by crustal extension and confirmed by rather frequent earthquakes along grabens, the formation of which is attributed either to the N-S extensional regime and subsequently they are coeval, or they are produced by successive events and have been formed under different tectonic regimes (Genç et al. 2001). Nevertheless, strike slip faulting is also present, which onshore results in oblique normal faults and becomes more evident in the Karaburun peninsula and offshore area. The strike-slip faulting, that has previously been thought only to accommodate variations in extension between adjacent normal faults, is now suggested to be of greater importance because there is considerable evidence of zones of deformation, some of which may be linked to the strike-slip faulting onshore (Ocakoglu et al. 2004).

Several previous studies focused in seismotectonic properties of the study area concerned either mapping of active faults and neotectonic analysis of the study area (e.g., Bozkurt, 2001, 2003; Mountrakis et al. 2003; Çiftçi and Bozkurt 2009), study of seismic sequences (e.g., Benetatos et al. 2006; Aktar et al., 2007), seismic prospecting (Kurt et al. 1999; Ocakoğlu et al. 2004). or

microseismicity analysis (e.g., Tan 2013). Tan et al. (2014) illuminated the subsurface structure of the mapped faults and analyzed the seismicity and identify faults that appear related to certain clusters using hypocenter locations of crustal seismicity registered with a dense local network.

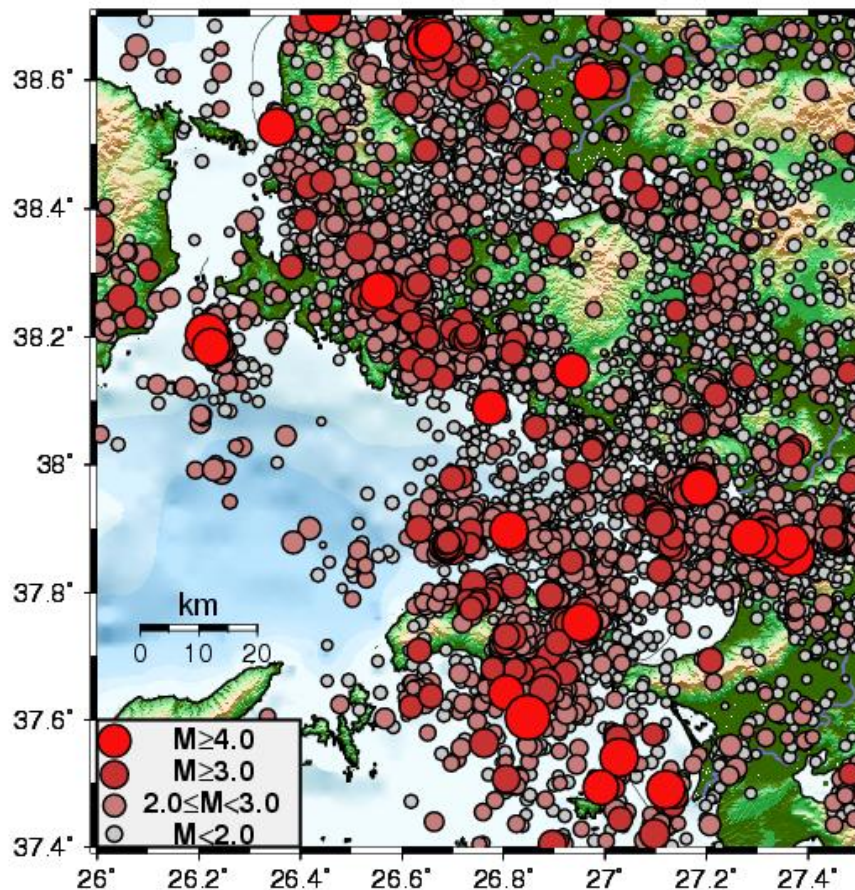
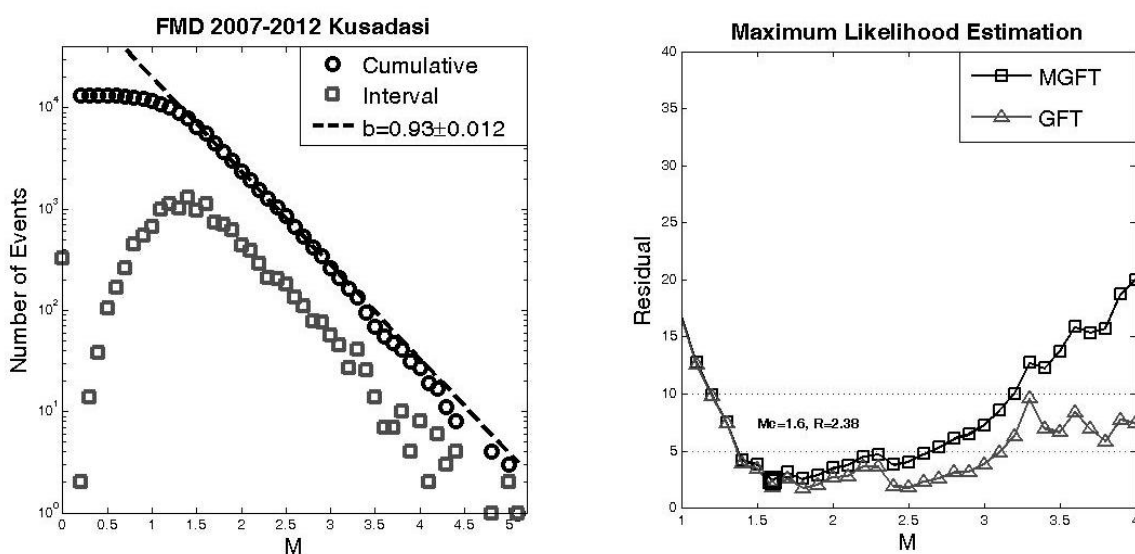


Fig. 3.18. Spatial distribution of 13,592 earthquakes recorder and analyzed between July 4th 2007 - September 15th 2012 in the study area (Latitude: 37.400°N - 38.700°N, Longitude: 26.000°E – 27.500°E). An intense seismic activity is observed at the eastern part of the Samos island, the marine area north-north east of the island close to the mainland and also in Karaburun peninsula

3.3.2.2 Data

On 31st of July 2007 online seismological stations were deployed in the central part of the Aegean coast of western Turkey (Inan et al. 2007, Tan 2013). Since then, continuous monitoring of microseismicity was made, resulting in a wealth of data which, along with data provided from seismological stations of the permanent Hellenic Unified Seismological Network (HUSN), are capable to reveal the geometry and kinematic properties of the activated

structures. The earthquake catalog was integrated with the calculation of the local magnitudes of the events (Tan, 2013). The minimum magnitude recorded was $M_L=0.2$. For the purposes of the present scientific program an effort was attempted to determine the completeness magnitude, M_c , of the compiled catalogue. The calculation of M_c was accomplished by applying a modified from Wiemer and Wyss (2000) maximum likelihood goodness of fit test Leptokaropoulos et al. (2013).



Method	MAXC	GFT(90%)	GFT(95%)	MGFT
M_c	1.4	1.2	1.4	1.6

Fig. 3.19. Calculation of completeness magnitude, M_c , and b -value of Gutenberg-Richter power law for the study area. In the left frame squares indicate the incremental and circles the cumulative frequency magnitude distribution. The fitting curve was derived by application of maximum likelihood estimation method. In the right frame the goodness of fit test between the obtained power laws and the real data (triangles) or 1000 synthetic catalogues (squares), as a function of magnitude, M . The table shows M_c , as it was derived by the application of different methods: Maximum curvature (MAXC - Wiemer and Wyss, 2000), 90% and 95% goodness of fit (GFT90%, GFT95% - Wiemer and Wyss, 2000) and modified goodness of fit (MGFT - Leptokaropoulos et al., 2013).

By such way the M_c was found equal to 1.6. as shown in Figure 3.19. The application of this technique in sub-sets corresponding to 2-year data sets, shown that M_c remains stable and equal to 1.6, a fact that verifies the regular and efficient local network operation. Such a low completeness threshold implies that the specific dataset is the best catalogue ever compiled

for this area. The b-value, of the well known Gutenberg & Richter relation was found equal to 0.93, a value close to 1.00 which is considered that represents the normal seismic activity worldwide (Tan, 2013). The spatial variation of completeness magnitude and b-value is demonstrated in Figure 3.20.

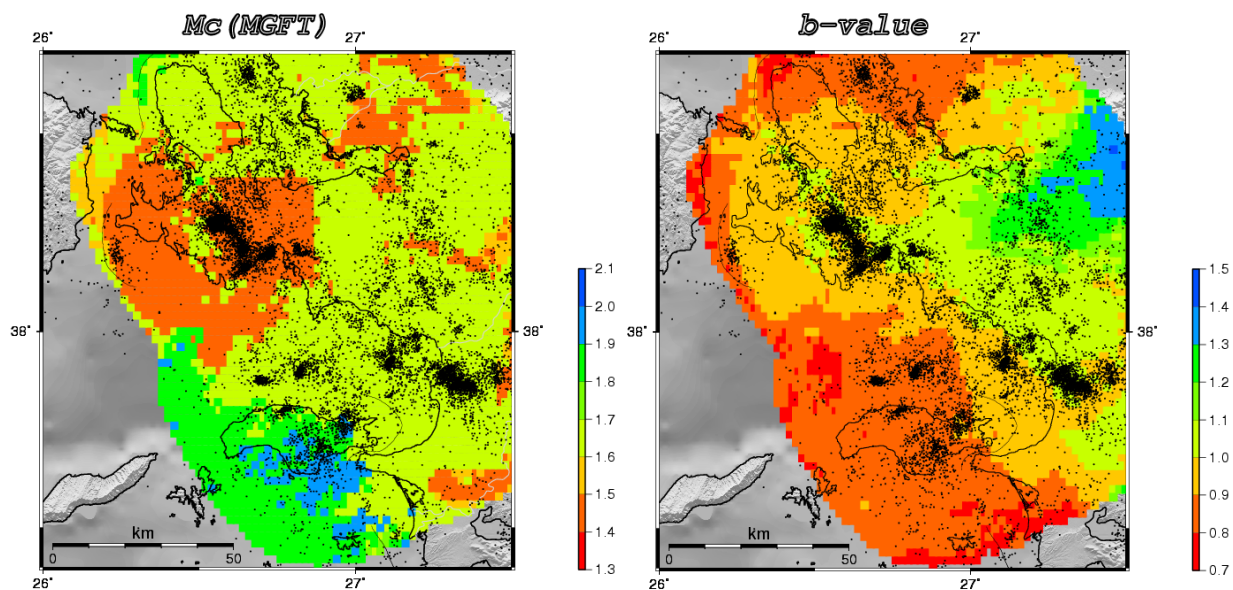


Fig. 3.20. Completeness magnitude, M_c , and b-value of Gutenberg-Richter power law for the study area calculated in a normal grid superimposed in the study area and sustained of 5016 rectangular cells with dimensions $0.02^\circ \times 0.02^\circ$. M_c and b-value were calculated from the data that are inside circular areas centered in the center of each cell with a radius of 30km. In order to avoid erroneous estimations caused by insufficient data samples a minimum of 300 events accommodated in each circular area and 1.5 magnitude unit range were set as constraints in order to perform the calculations. In such way M_c and b-value were calculated in 3691 cells which cover 73.6% of the study area.

3.3.2.3 Parameterization

The characteristic relaxation time was estimated from the Omori-Utsu law parameters (eq. 3.3) applied in the November 11th 2010 sequence (Fig. 3.21). The parameters were estimated as $K=20.4 \pm 5.1$, $p=0.92 \pm 0.08$, $c=-0.33 \pm 0.14$, which suggest a characteristic relaxation time equal to 215 days (106 – 520 days at 95% confidence level), assuming a background seismicity rate of 0.15 events/day as estimated from the declustered dataset. This value is found to be in good agreement with Figure 3.22, in which it is shown that the inter-

event time, averaged for 20-event sets returns to its background level after ~200 days.

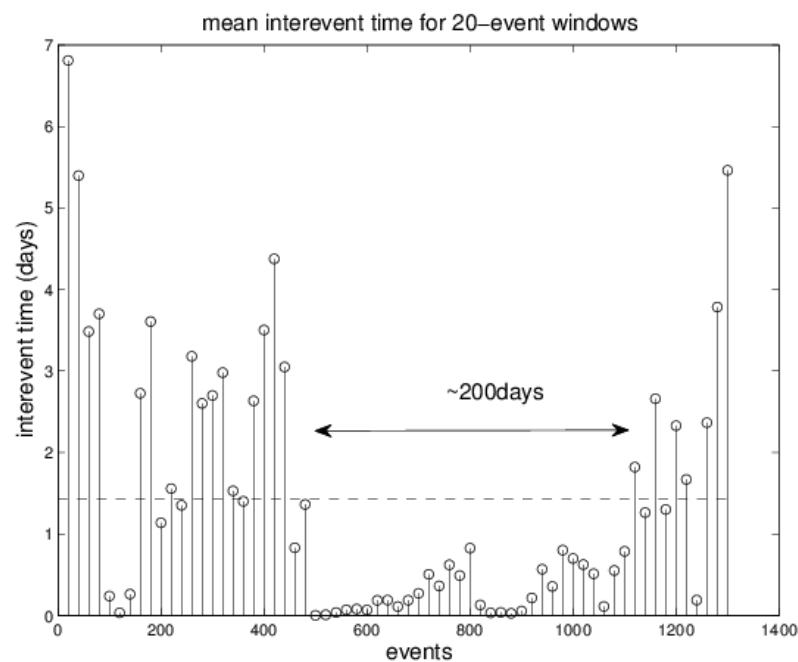


Fig. 3.21. The inter-event time plot shows that seismicity rate (the inverse of inter-event time) is returning to the background rate after approximately 200 days. These times yielded from averaging the times of overlapping 20-event windows. Dashed line shows the average inter-event time which is the inverse of the average background seismicity rate as it was estimated in the previous section.

For stressing rate we used the slip rates on fault segments calculated from GPS data analysis (Mc Clusky et al., 2000; Flerit et al., 2004; Reilinger et al., 2006) considering the 60% of the geodetic slip value to account for the seismic part of the secular tectonic motion (Ambraseys and Jackson, 1990). A stressing rate equal to ~0.04 bars/yr was estimated in such way, or equivalently $\sim 1.1 \cdot 10^{-4}$ bars/day, in agreement with Paradisopoulou et al. (2010). The aforementioned stressing rate value together with characteristic relaxation time $t_a=220$ days, were applied in equation 2.8 for obtaining the product $A\sigma=0.025$ bars.

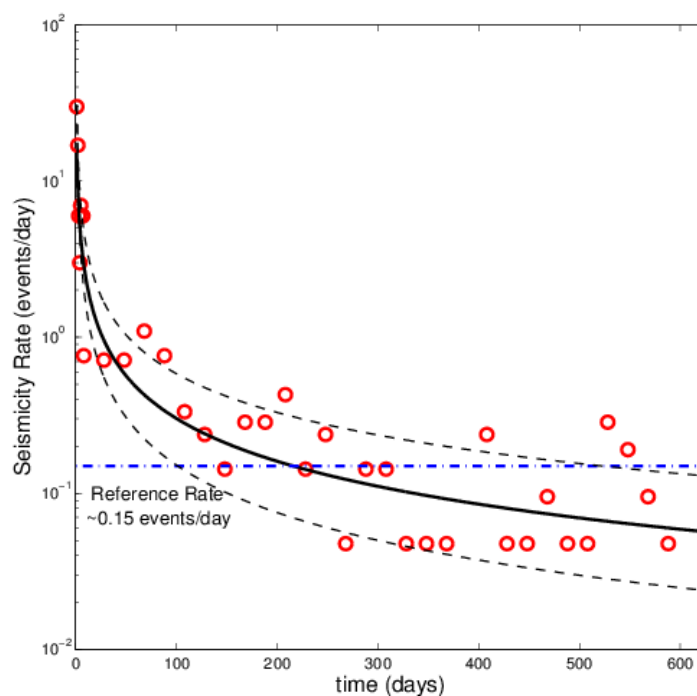


Fig. 3.22. Seismicity rate decay over time (circles) and MOF fitting (solid line) with its 95% confidence interval (dashed lines) after the November, 11th, 2010 sequence. The first five points (solid circles) show the daily seismicity rates for the first five days after the main shock. The rest of the circles represent the daily seismicity rates smoothed over 1-month non-overlapping periods. The horizontal dotted line demonstrates the background seismic activity as derived from the declustered, cutting the MOF curve at $t_a \sim 220$ days.

3.3.2.4 Results – Discussion

The temporal evolution of stress field as derived from seismicity rate differences in the entire study site is shown in Figure 3.23. The stress changes have been calculated for overlapping 150-days windows considering a characteristic relaxation time equal to 220 days. The two dominant stress peaks are directly associated with $M \geq 5.0$ earthquakes, whereas there is also an increasing trend connected with 2012 $M=5.0$ event which is yet not fully demonstrated because of the catalogue temporal limitation. Nevertheless, when the resolution is increased due to the time window tuning at a lower value (50 days), additional stress changes are revealed (Fig. 3.24). Besides the distinctive stress jumps associated with the 3 strongest events ($M \geq 5.0$) that took place in the study area, there are also significant stress peaks that do not exhibit a profound connection with any strong shocks although they correspond to a notable change on earthquake occurrence rates.

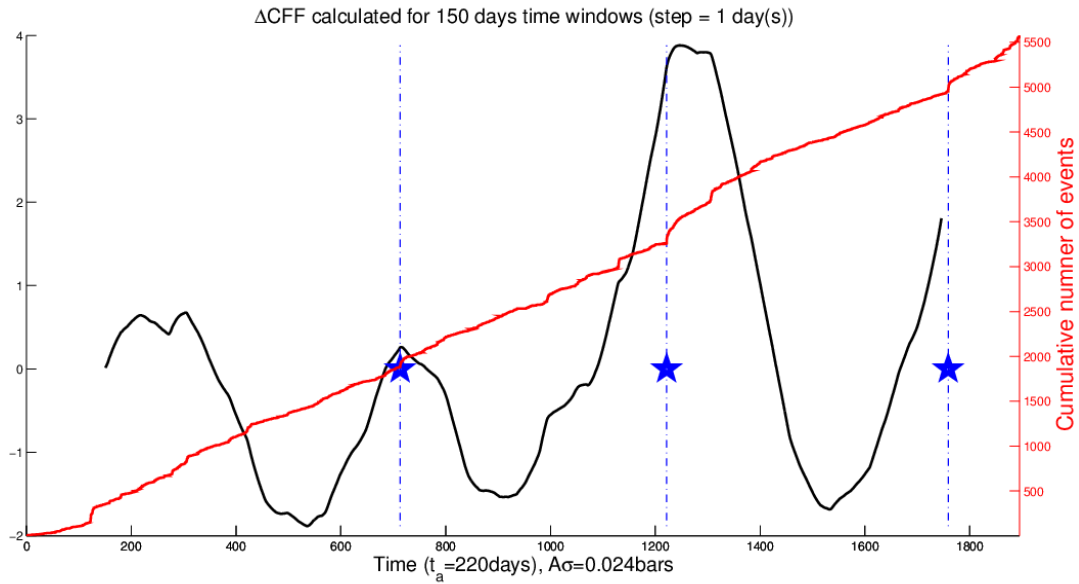


Fig. 3.23. Cumulative stress changes inverted from seismicity rate variation considering overlapping datasets corresponding to 150-days time windows for the entire study site shown in fig(). Blue asterisks denote the $M > 4.5$ events.

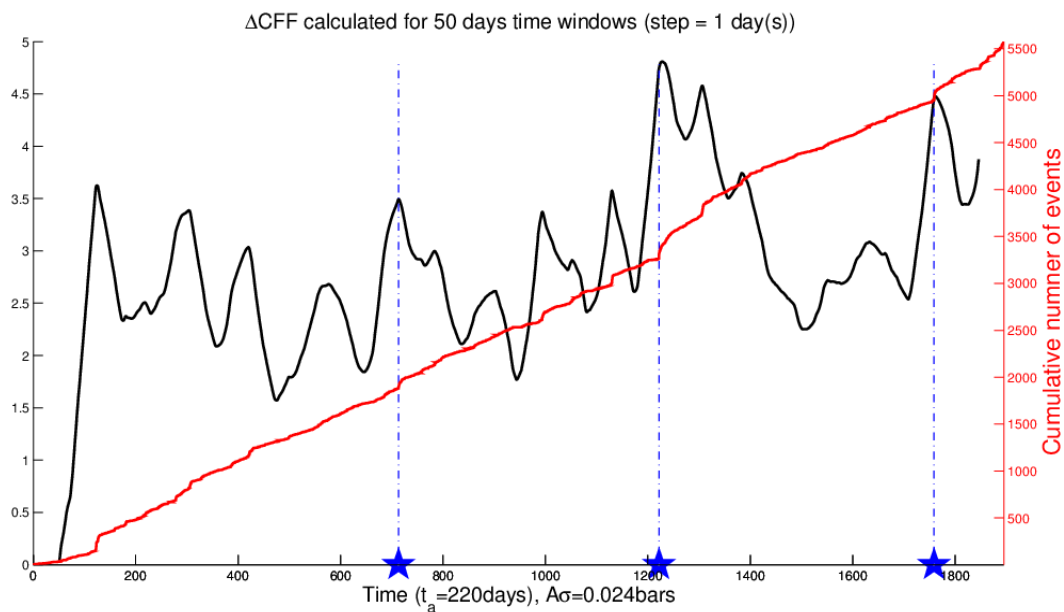


Fig. 3.24. Cumulative stress changes inverted from seismicity rate variation considering overlapping datasets corresponding to 50-days time windows for the entire study site shown in fig(). Blue asterisks denote the $M \geq 4.5$ events.

Figure 3.25 illustrates the spatial distribution of the derived stress changes arisen after the Samos $M=5.1$ earthquake, occurred on 20th June 2009. The epicenters of the earthquakes preceded and followed the mainshock are shown in Figure 3.26. For the calculation of these rates, we selected a time-

window corresponding to 500 days preceding and following the June 20th mainshock (Fig. 3.25), and then the stress changes derived from eq. (3.2) were mapped. This application was performed in a dense grid superimposed onto the study area with cells of 0.005° side. The stress values in each cell were smoothed by a Gaussian filter with radius 0.05°. The condition that each cell contains at least 2 events before or after the main shock was fulfilled. The parameter values applied were the same we used in the previous subsection and equal to $A\sigma=0.04\text{bars}$, $t_a=220\text{days}$ and $\dot{S}_r=0.04\text{bars/year}$. It is shown that both positive and negative stress changes are observed all over the study area but the highest values of stress increase and decrease are found close to the epicenter of the June 20th event. The stress decreases close to the epicenter, despite their lower values compared with the increases, may be a potential evidence for stress shadow induced by the main shock occurrence.

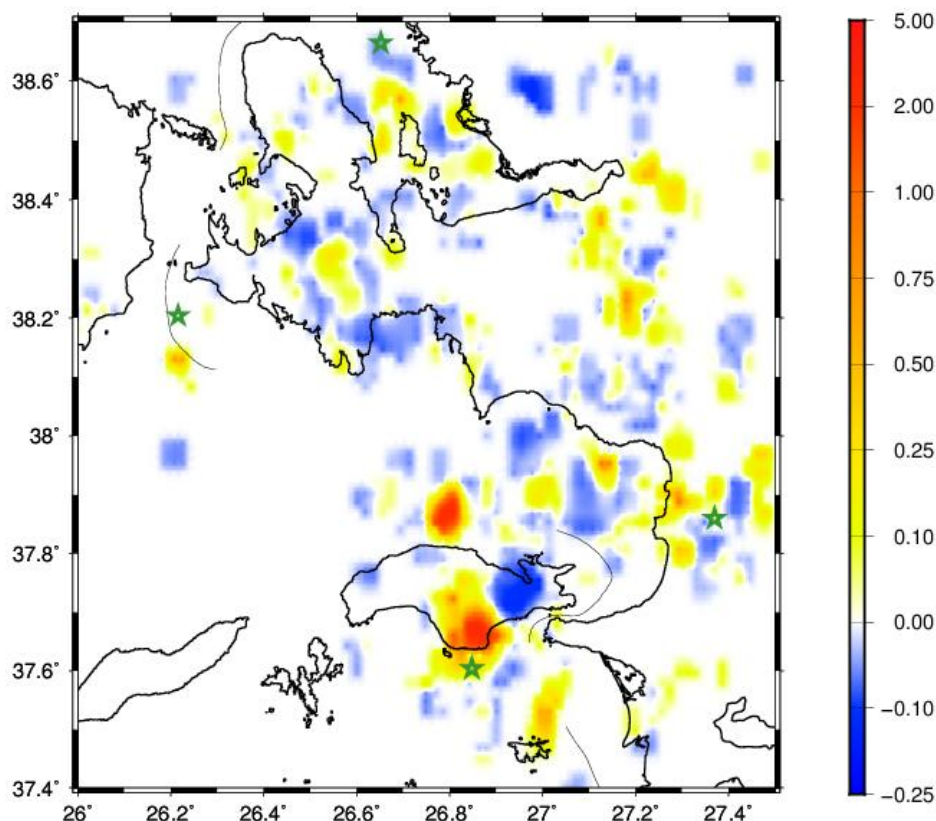


Fig. 3.25. Spatial variation of Coulomb stress derived from seismicity rate changes 500 days before and 500 days after the Samos 20th June 2009 event (just before the 11th November event). The smoothing parameter was set equal to 0.05° (eq. 2.17) and the spatial step was 0.005°. White cells represent areas with insufficient data either before or after the 20th June earthquake.

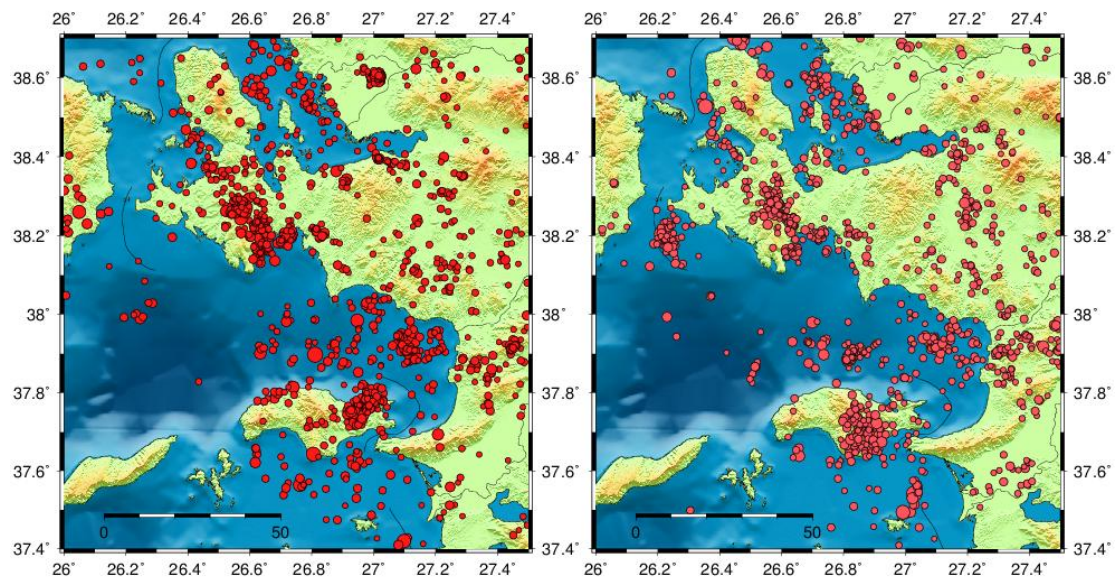


Fig. 3.26. Spatial distribution of the events occurred 500 days before and 500 days after the 20th June 2009 main shock from which the Coulomb stress changes of Figure (3.25) were derived.

Inverted stress changes from seismicity rates 500 days before and after the 11th November 2010 earthquake are shown in Figure 3.27. The epicenters of the earthquakes preceded and followed the mainshock are shown in Figure 3.28. The parameters applied were the same as described in the previous mentioned period (i.e. $\Delta\sigma=0.04\text{bars}$, $t_a=220\text{days}$ and $\dot{S}_r=0.04\text{bars/year}$). It is also shown in this case that despite the various stress changes detected during this almost 3-year period (1000 days), the largest amplitude stress increases are found close the epicenter of the November 11th 2010 event. These changes are more than one order of magnitude higher than the average stress changes derived for the rest of the study area. On the other hand stress decreases are definitely of lower amplitude and more widespread indicating that there is no evidence of induced stress shadows due the main shock occurrence.

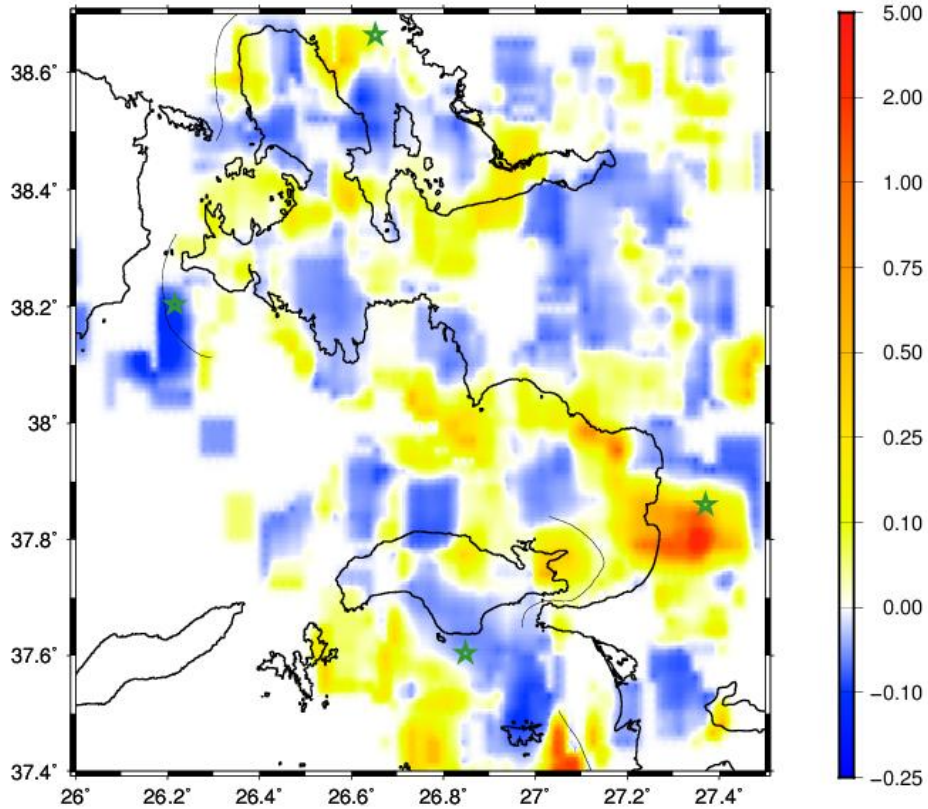


Fig. 3.27. Spatial variation of Coulomb stress derived from seismicity rate changes 500 days before and 500 days after. The smoothing parameter was set equal to 0.05° (eq. 2.17) and the spatial step was 0.005° . White cells represent areas with insufficient data either before or after the 11th November 2010 earthquake.

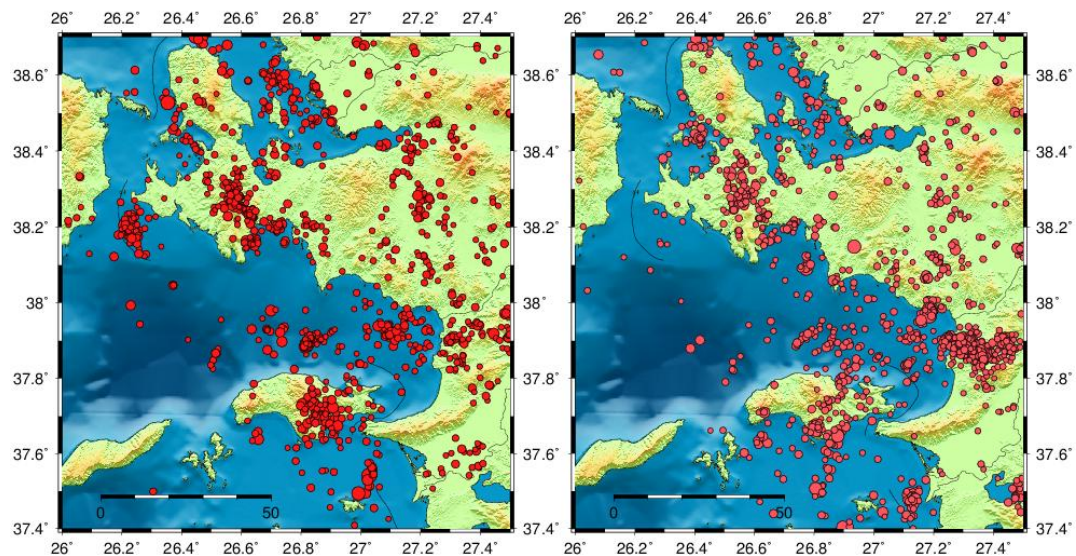


Fig. 3.28. Spatial distribution of the events occurred 500 days before and 500 days after the 11th November 2010 main shock from which the Coulomb stress changes of Figure (3.27) where derived.

For further investigation of these stress changes and associated seismicity rate variations, it was necessary that the study site should be

divided into two sub-areas which are easily distinguished from each other (Fig. 29) as far as the spatial distribution of epicenters is concerned: the Karaburun Peninsula to the north (sub-area 1) and Samos island with its adjacent areas (Kusadasi bay) to the south (sub-area 2). These two areas accommodate approximately 85% of the recorded seismicity above the common as individually calculated $M_c=1.6$. The analysis results derived for each sub-area are presented in the two following sections.

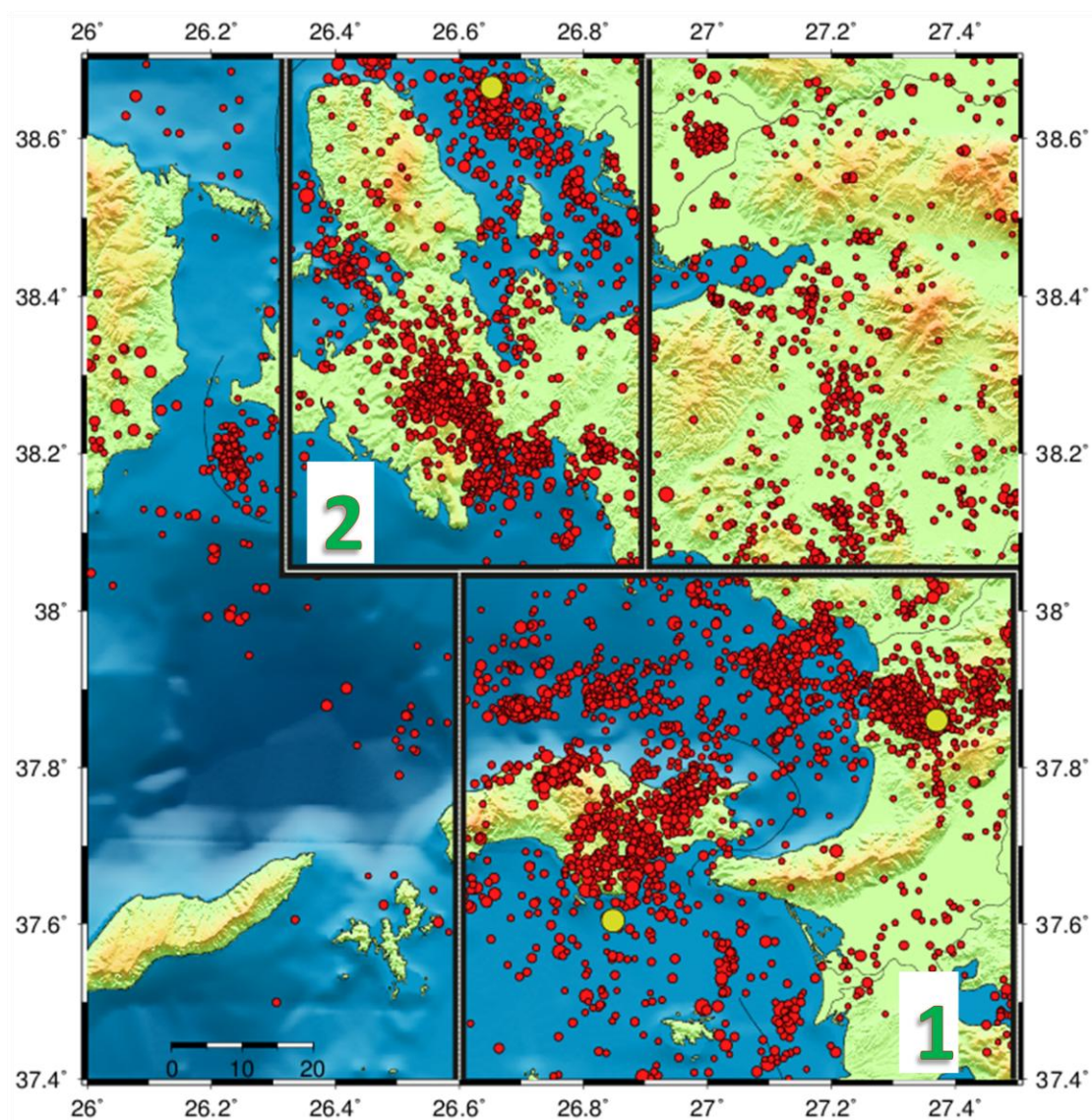


Fig. 3.29. Division of the study region in to sub-areas: Southern Area: Samos-Kusadasi (1). Northern Area: Karaburun Peninsula (2). Yellow circles indicated the strongest ($M \geq 5.0$) events epicenters whereas seismicity above $M_c=1.6$ for both sub-areas and the entire site is shown by red circles.

3.3.2.4.1. Samos-Kusadasi

The stress field evolution as a function of time for Samos-Kusadasi Area is displayed in Figure 3.30. Considering 50-days duration datasets it is shown that there are 6 distinctive stress peaks associated also with seismicity burst at significantly higher rates than the normally recorded activity. A space-time determination of this activity was accomplished by isolating clusters of events fulfilling the following criteria: The inter-event time between successive events should be less than 1 day and the inter-event distance should be less than 20km. After this clustering, the events which found in a distance from the cluster gravity centre larger than 3 standard deviations of the average distance were also removed. A minimum number of 25 events per cluster was finally set as an additional constraint. In such way 6 major clusters were identified (table 3.3) that correspond to the 6 largest peaks of Figure 3.30. Cluster number 5 could be divided into 3 sub-clusters (5a,b,c) according to internal differences in the inter-event times, which exhibit some fluctuations but these were much lower than the average unperturbed interevent time for the entire area (~2 days). The spatial distribution of these 6 clusters (with the 5th cluster divided into its 3 sub-clusters) are shown in Figure 3.31.

Three of the identified clusters (1, 3 and 5) correspond to mainshock-aftershock activity, with the strongest event ($M > 4$) occurring in the initial stages of the seismic burst and its difference with the strongest aftershock being more than 0.7 units. On the contrary the other 3 stress peaks, are more likely to be associated with swarm like activity (clusters 2, 4 and 6): In these clusters the maximum magnitude difference between the strongest shocks is roughly equal to 0.3 units. Moreover the strongest events (with $M < 4.0$) occurred when the activity was already in progress (except in cluster 4).

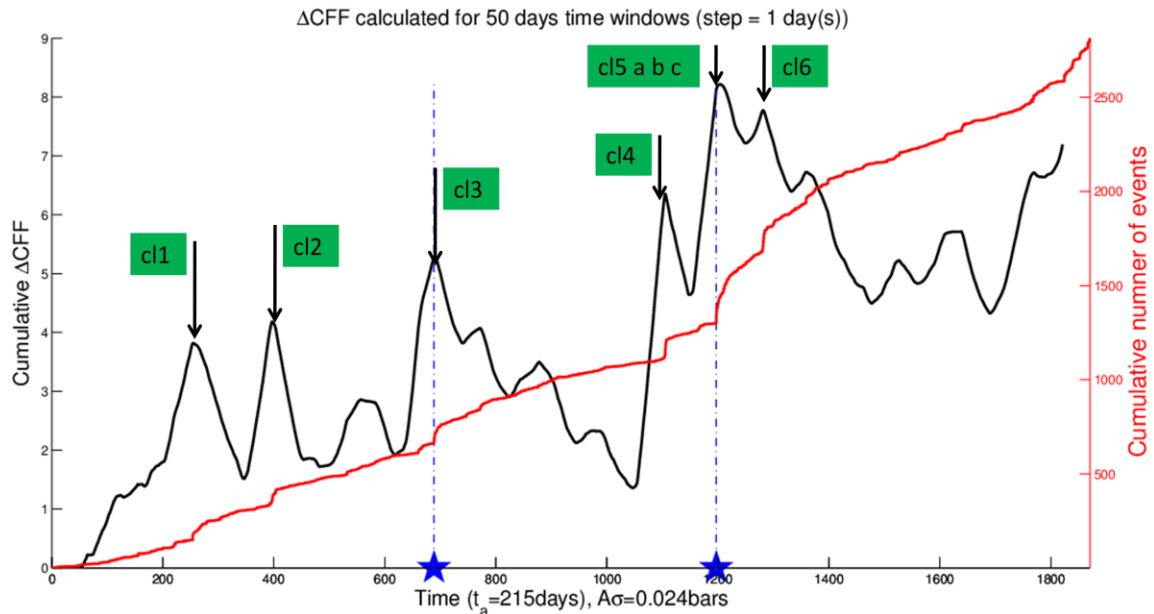


Fig. 3.30. Cluster identification by stress changes associated with their occurrence. Apart from the larger stress changes connected with $M \geq 5$ earthquakes (cl3 and cl5), 4 more clusters are shown to produce remarkable stress changes.

Table 3.3. Properties of the 6 clusters associated with stress changes in the study area SA1.

Cluster	Number of Events	Duration (days)	1 st Event's Magnitude	Largest Magnitude	ΔM between 2 strongest events	M_{max} Event
1	37	2	3.1	4.3	0.7	2 nd
2	39	2.8	1.7	3.3	0.1	24 th
3	77	7.1	5.1	5.1	1.7	1 st
4	83	2.5	2.7	3.8	0.3	4 th
5a-5b-5c	272	34.1	1.8	5.0	0.8	19 th
6	25	1.1	1.6	3.2	0.2	10 th

The next step was to compare the inverted from seismicity rate changes stress results with the ones obtained from the elastic dislocation model application. The elastic dislocation model is firstly applied to calculate Coulomb stress changes caused by the coseismic slip of the two moderate events occurrence. Then, reference rates and seismicity rates of the small magnitude events for different time increments after the main shock were spatially smoothed by the application of the selected PDF (eq. 2.15). The differences between the earthquake occurrence rates before and after the main shock were compared and used as input data in the stress inversion algorithm in order to provide an independent estimation of stress changes. Eventually

we investigated the quantitative correlation among the results derived from the two methods.

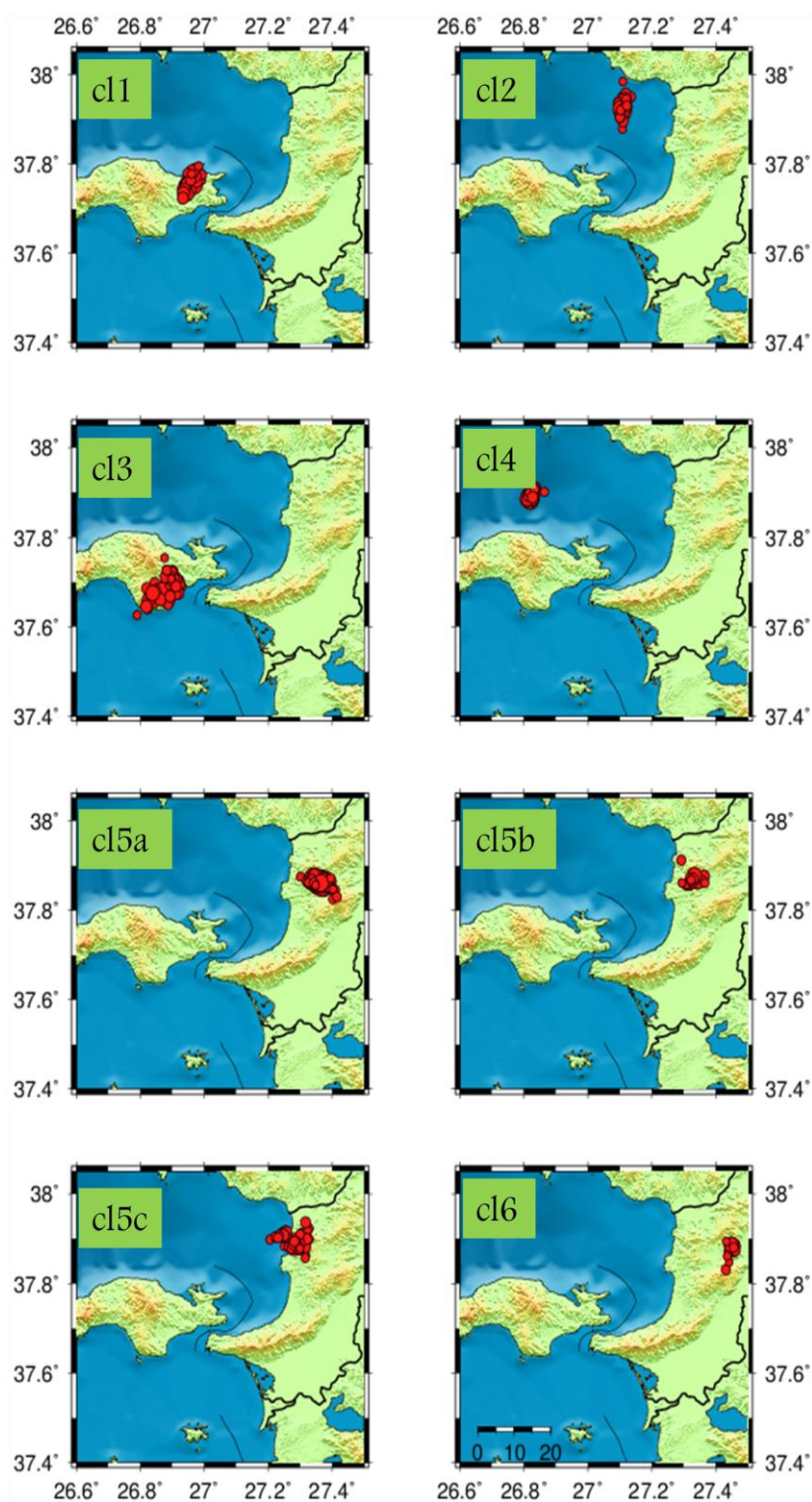


Fig. 3.31. Seismicity clusters associated with Δ CFF changes (Table 3.3. Clusters 5a, 5b and 5c are sub-clusters of the aftershock sequence followed the 11th November 2010 M=5.0 earthquake.

The analysis performed here is also based upon the observation that even small static stress changes result to considerable seismicity rate changes (e.g. [Harris, 2000](#); [Steady et al., 2005](#)). Thus we examine the proportion of the area where there is agreement in the sign of ΔCFF derived by the two methods. Following this aspect, the values of stressing rate and characteristic relaxation time do not affect the spatial distribution of the stress changes, but only their absolute value, such that the results we seek being insensitive to these parameter values fluctuation. We focused on the agreement of the ΔCFF sign instead and therefore the parameter values were set as mentioned in the previous sections: $\dot{S}_r = 0.04 \text{bar} / \text{yr}$, $A\sigma = 0.024 \text{bar}$ and $t_a = 220 \text{days}$. The only parameter that does affect the spatial pattern of the derived stress changes is the bandwidth, and thus the examination is carried out with respect to bandwidth fluctuation. For the calculation of Coulomb stress changes due to the 2 main shocks by the elastic dislocation approach, we adopted the focal mechanisms determined by ([Tan et al., 2014](#)).

Figure 3.32 shows the distribution of ΔCFF in the study area after the occurrence of 20th June 2009, Samos main shock. The epicenters of the events that followed these shocks are also depicted as grey and green circles. The stress tensor calculations were performed for a depth of 5km which is approximately the average depth of the majority of the aftershocks occurred during the following eight days. The spatial distribution of these events superimposed on ΔCFF suggests that most of these events were triggered by the coseismic stress changes of the June 20th main shock.

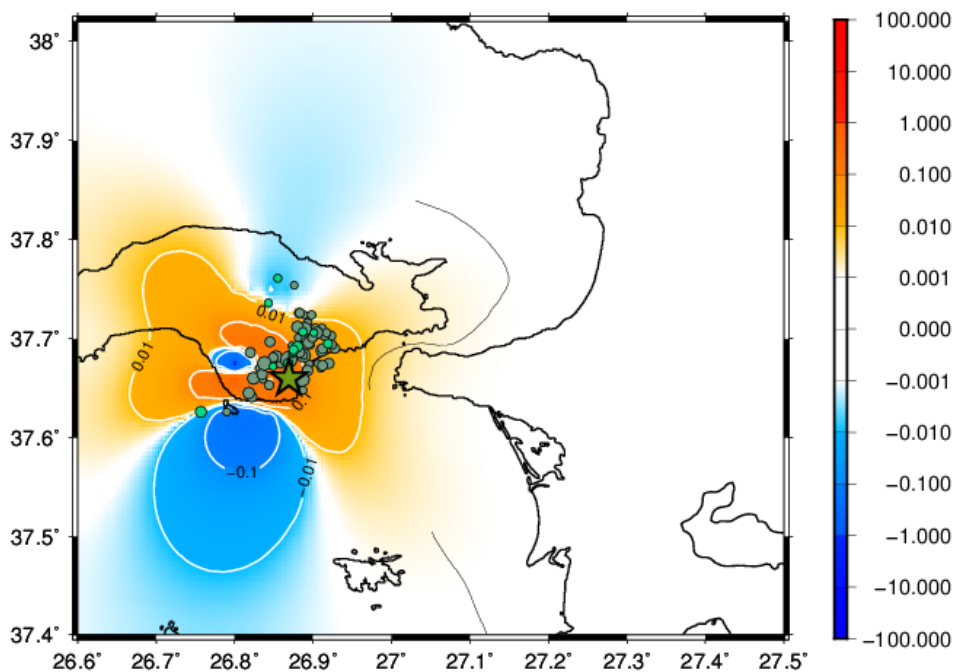


Fig. 3.32. Map with ΔCFF caused by the 20th June 2009 earthquake. Aftershocks followed since then are also plotted: Events occurred up to 5 days after the main shock (grey circles) and aftershocks occurred during the period from 6-8 days after the main shock (green circles). DCFE calculations are performed at 5km which corresponds to the average depth of these two clusters.

The coseismic stress changes associated with the 11th November 2010 event as they derived from the elastic dislocation approach are displayed in figures 3.33 and 3.34. These two figures correspond to different times elapsed from the main shock occurrence and also to different depth of the respective seismic clusters depicted. Figure 3.33 shows the coseismic stress changes calculated for a depth of 6km which corresponds to the average depth of the earthquakes recorded during the first 11 days followed the main shock of November 11th. The cluster that directly followed the main shock (indicated by grey circles) lasted for almost 1 week and consists of along fault aftershocks. Therefore it took place in areas where slip was too heterogeneous to be modeled by uniform displacement of a single rectangular fault segment. On the contrary significant part of the seismic cluster that occurred between the 8th and the 11th day after the main shock (green circles), is located on positive ΔCFF area, therefore it is very likely for this cluster to become triggered by the M=5.0 main shock.

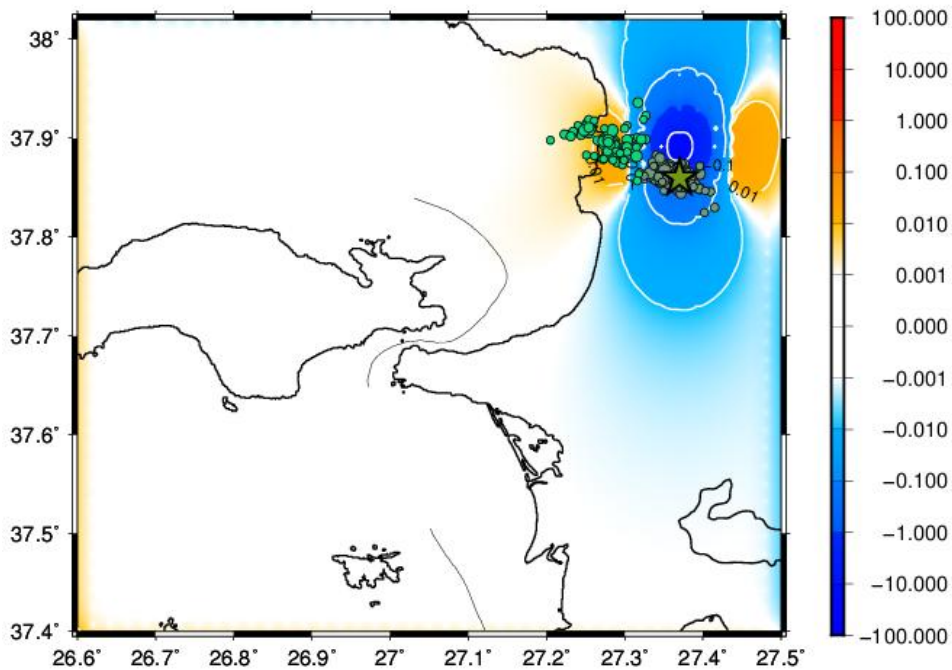


Fig. 3.33. Map with ΔCFF caused by the 11th June 2009 earthquake. Aftershocks followed since then are also plotted. Events occurred up to one week after the main shock (grey circles) and events occurred during the period from 8-11 days after the main shock (green circles). DCF calculations are performed at 6km which corresponds to the average depth of these two clusters.

Figure 3.34 shows the coseismic stress changes calculated at a depth of 10km which corresponds to the mean depth of the events occurred during the 70-73 days (grey cluster) and 149-151 days (green cluster) followed the main shock of November 11th. The first cluster is entirely located in positive stress change lobe, whereas the second one took place in an area where the stress remained almost unaltered due to the main shock occurred approximately 150 earlier. Therefore, unlike the first cluster, the second one might be either triggered by aftershocks followed the main event or associated with other phenomena, such as fluid flow and viscoelastic relaxation.

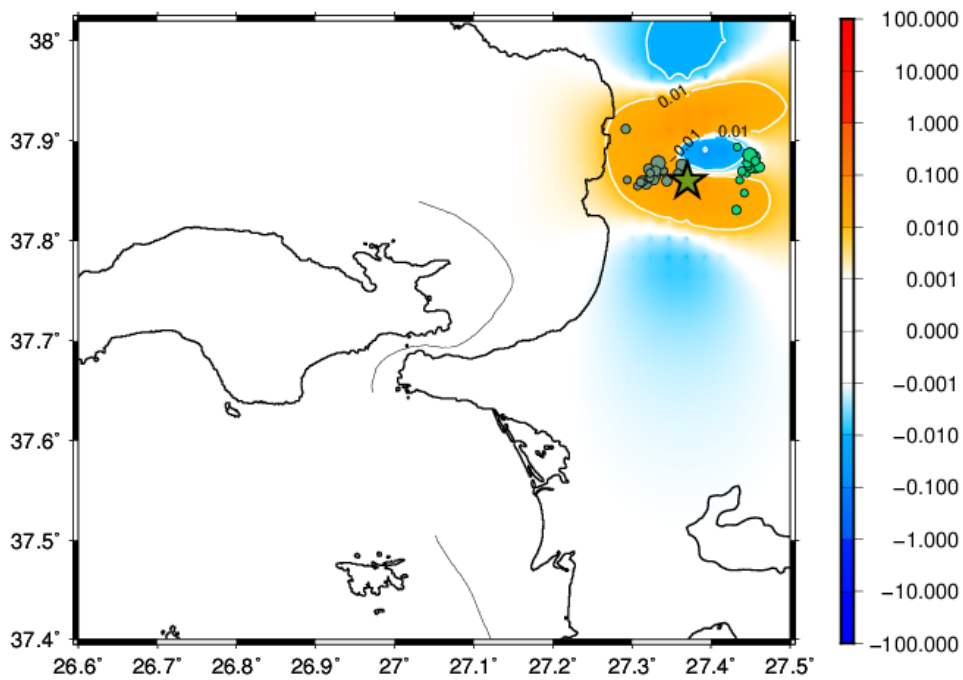


Fig. 3.34. Map with ΔCFF caused by the 11th November 2010 earthquake. Aftershocks followed since then are also plotted: Events occurred during the period from 70 to 73 days after the main shock (grey circles) and events occurred during the period from 149-151 days after the main shock (green circles). DCFE calculations are performed at 10km which corresponds to the average depth of these two clusters.

In Figure 3.35 the agreement percentage between the elastic dislocation and inversion from seismicity rates methods, as presented in this section, is plotted as a function of bandwidth, h . The average sign agreement is generally not sensitive in the bandwidth fluctuation between 0.03° - 0.06° , demonstrating an almost stable value of approximately 60% and 80% concerning the 2009 and 2010 earthquakes, respectively. This means that nearly $2/3$ and $4/5$ of the coseismic stress changes are compatible with the observed seismicity rate variations after the two main shocks, respectively. It is noteworthy that the high catalog accuracy has led to highly correlated aftershock epicenters with positive ΔCFF even in the near field. The accurate depth determination was also a very crucial precondition that ensured the robustness of the derived results.

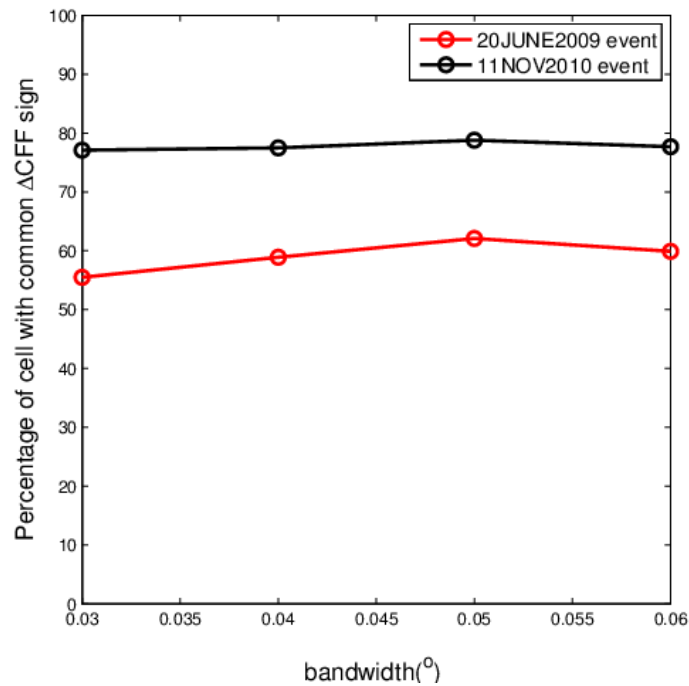


Fig. 3.35. Percentage of cells having common Δ CFF sign derived from both methods (Elastic dislocation model & Stress inverted from seismicity rate changes). The elastic dislocation models take into account the influence of 20th June 2009 (red line) and 11th November 2010 (black line) events, respectively. Reference seismicity rate is derived from 500 days before each main shock occurrence.

3.3.2.4.2. Karaburun Peninsula

The stress evolution through time was studied for this sub-area. No sufficient Δ CFF analysis could be performed in connection with the 1st May 2012 earthquake for 2 reasons: The first is that this event and the aftershocks that followed are located very close to the borders of the study area. More important is the fact that the catalog does not include the entire aftershock activity as it contains earthquakes occurred until the 18th of September, only ~150 days after the main shock, a period even smaller than the assumed characteristic relaxation time. Moreover, although the local magnitude of this event is assigned as 5.0, [Tan et al. \(2013\)](#) estimated the moment magnitude of this earthquake equal to 4.6. The temporal evolution of the stress field in the entire area and time span that the catalog covers were investigated instead, together with the stress changes connection with anomalies in earthquake production rates.

Figure 3.36 shows the stress field variations as a function of time for Karaburun Peninsula. Considering 50-days duration datasets it is shown that there are 6 distinctive stress peaks associated also with seismicity burst at significantly higher rates than the normally recorded activity. A space-time determination of this activity was accomplished by isolating clusters of events fulfilling the following criteria: The inter-event time between successive events should be less than 1 day and the inter-event distance should be less than 20km. After this clustering, the events which found in a distance from the cluster gravity centre larger than 3 standard deviations of the average distance were also removed. A minimum number of 25 events per cluster was set as a final constraint. In such way 5 major clusters were identified (table 3.4) that correspond to the 6 highest peaks of fig 3.36. The spatial distribution of the aforementioned 6 seismic clusters is shown in Figure 3.37.

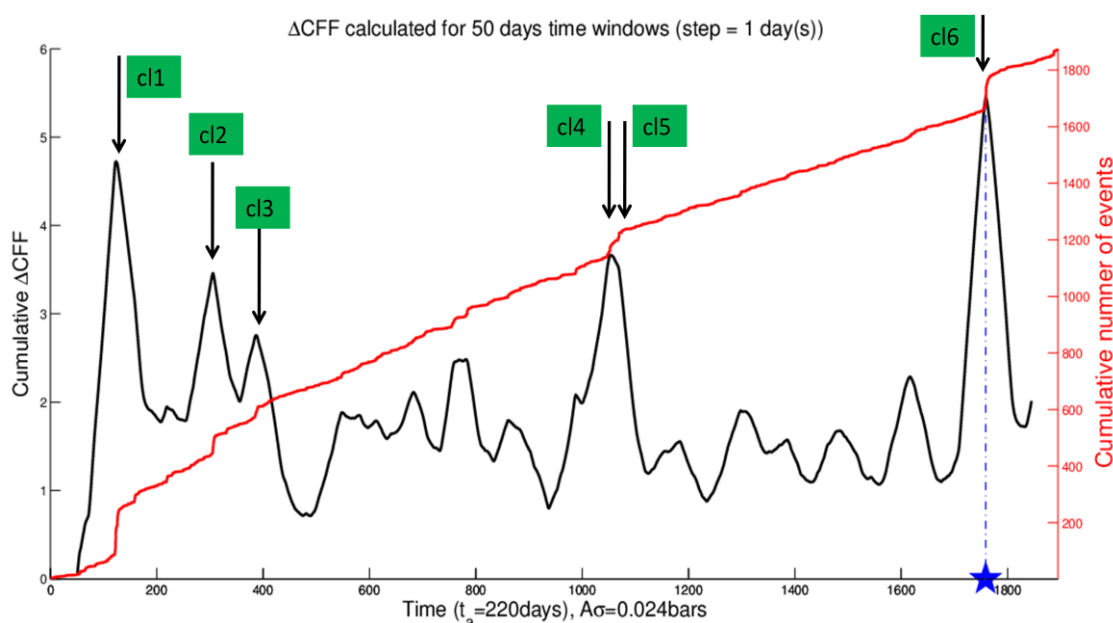


Fig. 3.36. Cluster identification by stress changes associated with their occurrence. Apart from the larger stress changes connected with $M \geq 5$ earthquakes (cl6), 5 more clusters are shown to produce remarkable stress changes.

Table 3.4. Properties of the 6 clusters associated with stress changes in the study area of Karaburun Peninsula.

Cluster	Number of Events	Duration (days)	1 st Event's Magnitude	Largest Magnitude	ΔM between 2 strongest events	M_{\max} Event
1	140	9.0	1.6	4.1	0.3	99 th
2	49	4.2	3.3	3.6	0.1	42 nd
3	23	3.8	2.1	3.2	0.2	4 th
4	20	3.9	2.1	2.9	0.7	5 th
5	21	5.2	1.8	2.2	0.0	3 rd
6	107	12	5.0	5.0	0.6	1 st

Three of the identified clusters (4 and 6) correspond to mainshock-aftershock activity, with the strongest event ($M=2.9$ and $M=5.0$) found in the initial stages of the seismic burst and its difference with the strongest aftershock being more than 0.6 magnitude units. On the contrary the remaining 4 clusters (clusters 1, 2, 3 and 5) represent swarm like activity. In these clusters the maximum magnitude difference between the strongest shocks is roughly equal to 0.3 units. Moreover the strongest events (with $M < 4.2$) occurred generally when the activity was already in progress.

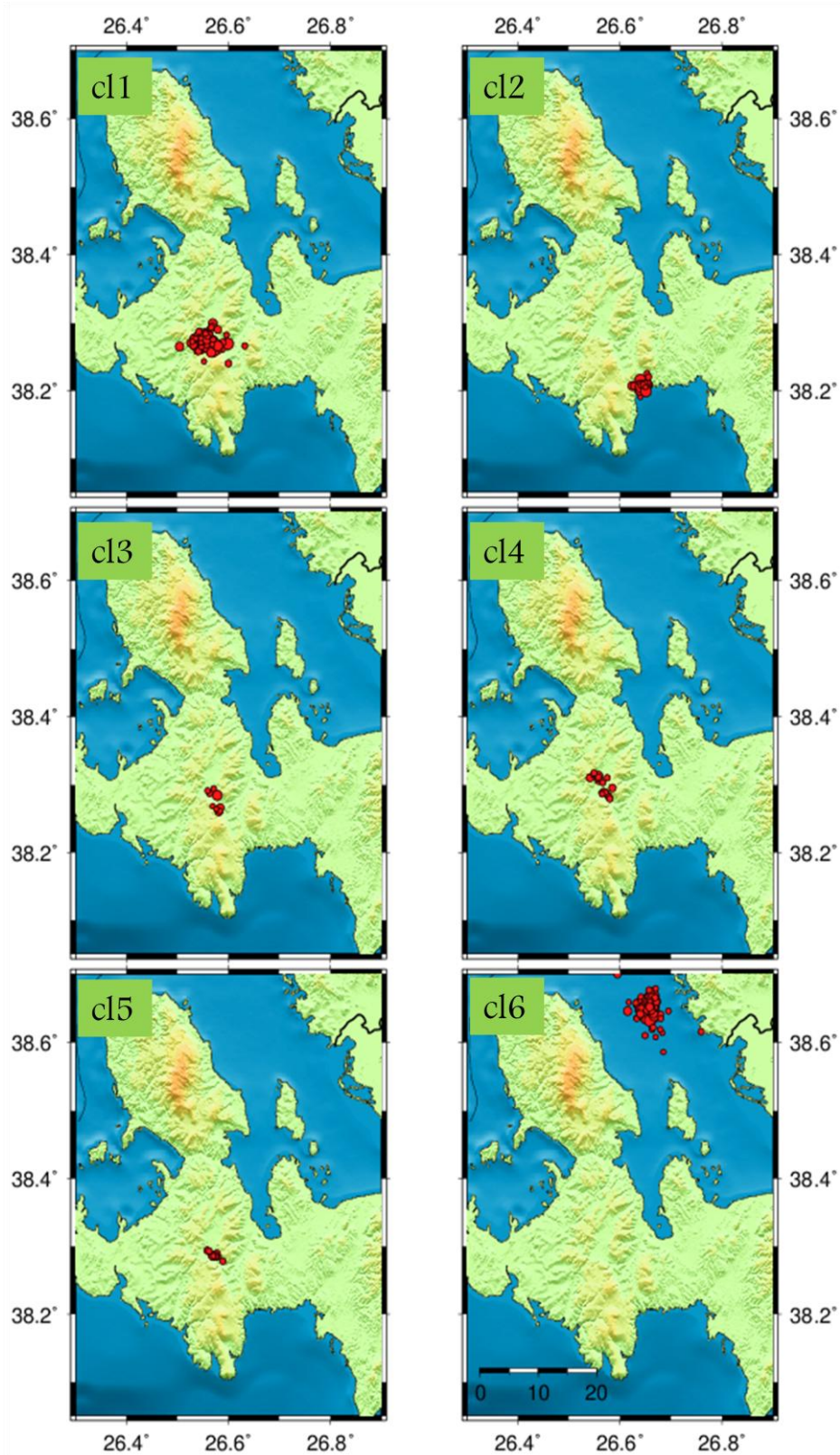


Fig. 3.37. Seismicity clusters associated with Δ CFF changes (Table 3.4).

3.3.3 Corinth Gulf (1975-2013)

A long term modeling of stress changes is carried out for Corinth Gulf by utilizing data since 1975 to seek for stress variation during a larger time scale, including bigger number of strong ($M \geq 5.5$) earthquakes. The temporal stress evolution since 1975 for different time windows corresponding to durations that are smaller than, equal to and larger than the calculated characteristic relaxation time are plotted in Figure 3.38. Patterns that could not be distinguished in the previous approaches because of insufficient resolution, are now revealed. When narrow time windows are tested, even small earthquake clusters appear to produce measurable stress increases which are usually followed by analogous decreases. These short-term stress changes may be artifacts arising from random seismicity fluctuations and ambiguous model performance when dealing with small data sets included in short time increments. As the time windows duration approaches t_a , these minor fluctuations are smoothed and the stress changes of all but the strongest earthquakes (followed by plenty of aftershocks) become insignificant. When the time window becomes approximately 1.5 times larger (1 year) than t_a , only 3 ΔCFF peaks are distinguished, associated with the 1984 $M=5.6$, 1995 $M=6.5$ and the 2010 doublet ($M5.5$, $M5.4$). The $M=5.9$ event (November, 18th, 1992) did not induced remarkable stress enhancement, on the basis of this seismicity rate change approach, because of its limited aftershock number. [Hatzfeld et al. \(1996\)](#) speculated that the reason of the depopulated aftershock sequence was the spatial change in the fault mechanical properties: A region of high strength is surrounded by regions of low strength, and the stress drop during the main shock does not increase significantly stresses in the surrounding region that could induce aftershocks. It is also notable that both 1995 and 2010 sequences occur after a relatively long term stress increase followed by subsequent stress drop just before the initiation of seismicity burst.

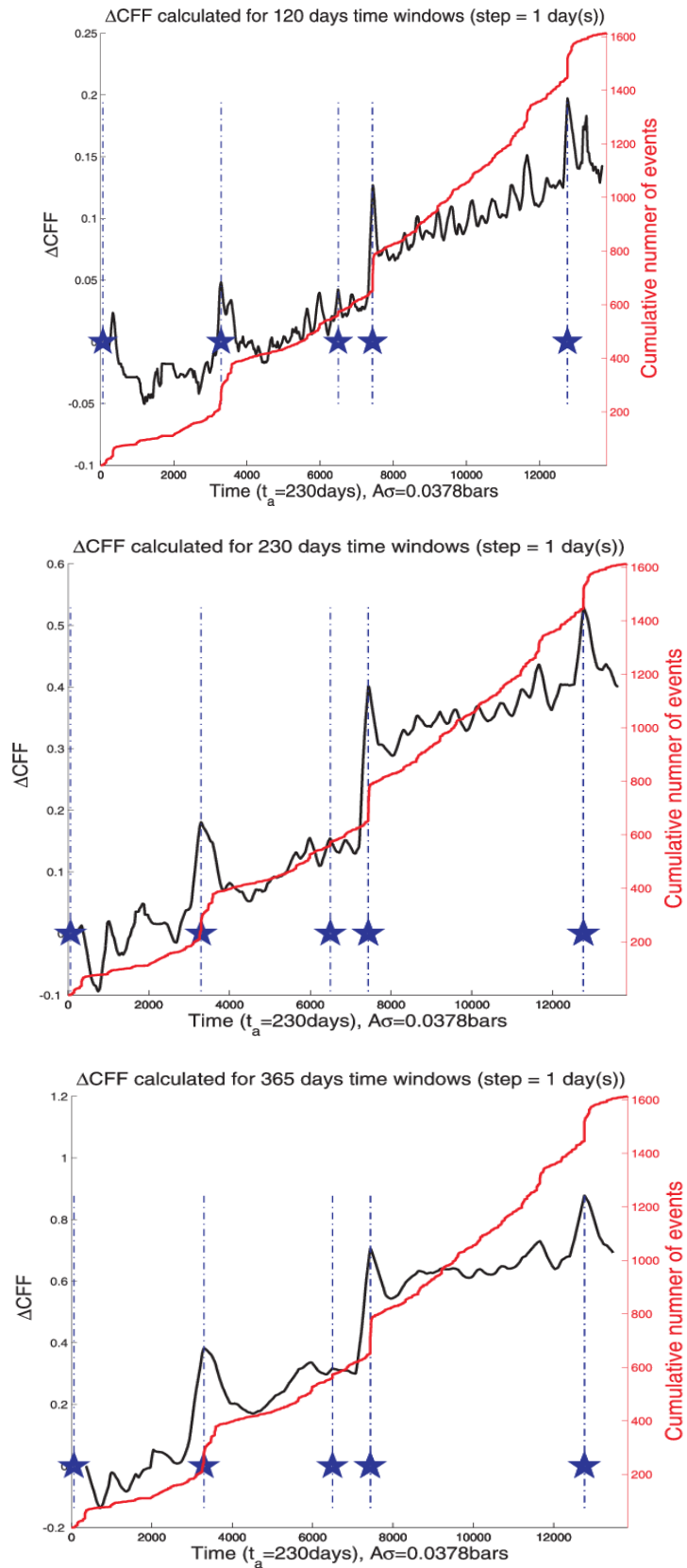
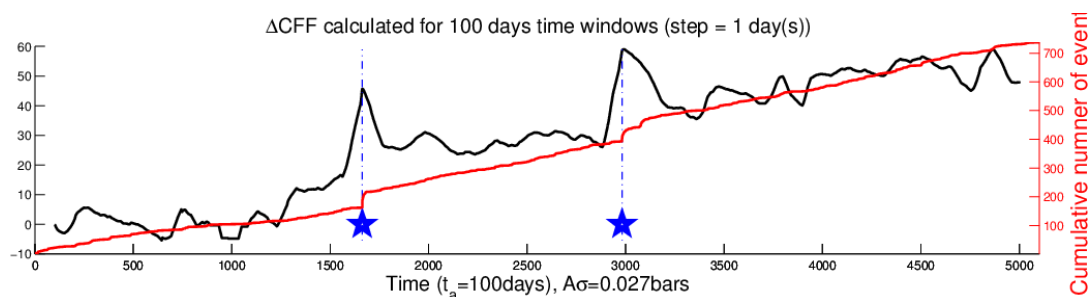


Fig. 3.38. Cumulative stress changes inverted from seismicity rate variation considering overlapping datasets of 120 days (upper frame), 230 days (middle frame) and 365 days (bottom frame) time windows. Blue stars indicate the $M \geq 5.5$ earthquakes.

3.3.4 Lefkada (1999-2013)

We utilized the dataset (1999-2013) corresponding to Lefkada-Cephalonia area in order to calculate stress changes by considering fixed time windows before and after successive calculation points (Fig. 3.39). The completeness magnitude for this time period was calculated equal to 3.2, such that 744 earthquakes are included in this dataset. Two strong earthquakes ($M \geq 5.5$) occurred in this area since 1999: The 2003, $M6.3$, Lefkada earthquake and the 2007, $M5.7$ earthquake, which was followed by a $M5.4$ event 3 months later. Figure 3.39 shows that these events induced the dominant stress changes in the area: In the upper frame the stress evolution through time by is demonstrated, considering 100-days overlapping temporal windows and a characteristic relaxation time equal to 100 days. This is a rather low value, but at this analysis the target is to provide a qualitative stress change pattern associated with earthquake production rates, rather than to calculate precise values of these changes. For this scope, t_a values identical to the time windows are preferred for demonstrating better the major stress changes, by amplifying the significant fluctuation of seismicity rates with respect to the background rate. It is clear that the only considerable stress changes are induced by $M \geq 5.5$ events whereas smaller magnitude events do not seem to be identified by seismicity rate changes related with them. This is also shown in the lower frame of Figure 3.39 where a largest window (and also t_a) are selected: All minor stress changes are smoothed and only the stress jumps associated with the strongest shocks are distinguished.



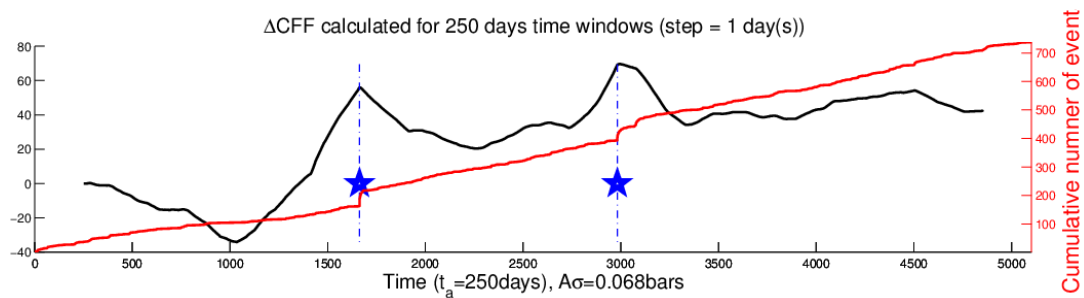


Fig. 3.39. Cumulative stress changes inverted from seismicity rate variation considering overlapping datasets of 100 days (upper frame) and 250 months (bottom frame) time windows. The characteristic relaxation time is fixed at values equal to the time windows (i. e. 100 and 250 days, respectively) and the stressing rate was set to 0.1bar/yr (see at section 2.3.2.3). Blue stars indicate the $M \geq 5.5$ earthquakes.

3.3.5 Western Crete (2009-2014)

The final case study presented in this chapter concerns the west Crete area (sub-area 3b, section 2.3.3). The dataset selected to be utilized for stress changes inversion correspond to the period between January 2009 – January 2014. Since then the Unified National Seismological Network provide a completeness magnitude as low as 2.8, such that 666 events with magnitude equal of higher than the aforementioned threshold have been recorded. On October 10th 2013, a $M=6.5$ earthquake struck close to the western coasts of Crete island. The stress jump associated with this event, as it was derived from seismicity rate changes is shown in Figure 3.40, derived for 50-days overlapping time windows. In the same figure several stress changes are also illustrated with none of them being directly associated with some strong earthquake.

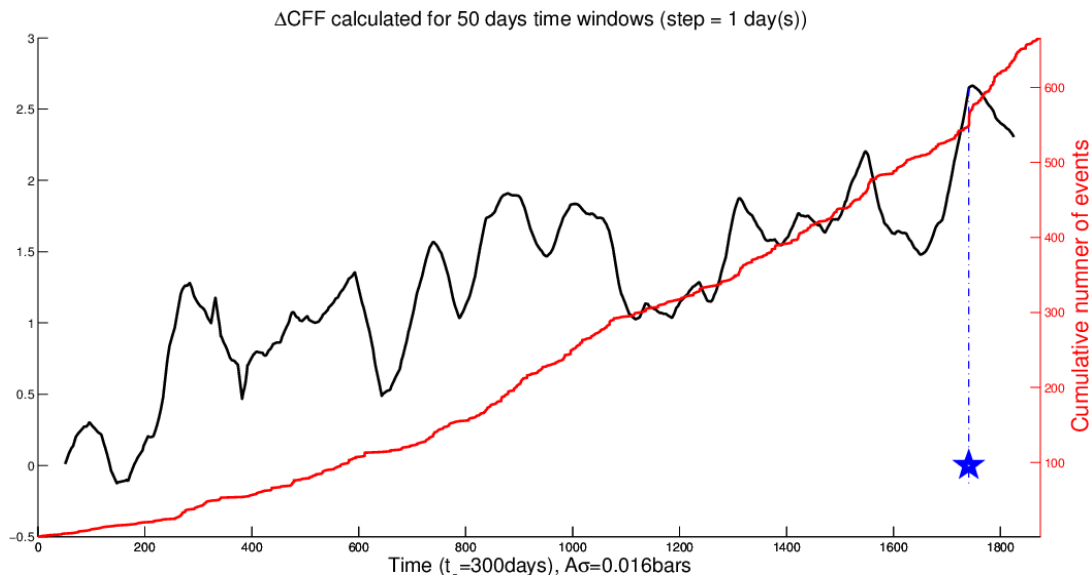


Fig. 3.40. Cumulative stress changes inverted from seismicity rate variation considering overlapping datasets covering 50-days time windows. The characteristic relaxation time is fixed at 300 days and the stressing rate was set to 0.02bar/yr (see at section 2.3.3.3). Blue stars indicate the $M \geq 5.5$ earthquakes.

More interesting is though the pattern derived by considering time windows of a broader range equal to 300 days (Fig. 3.41). Although stress changes in the edges of the figure were not computed due to the large time span it is shown that some long-term stress change might be evident. Short-term stress jumps are smoothed to reveal a period of ~ 250 days (approximately 800-1050 days in Figure 3.41) that demonstrates higher seismicity rates than the preceding and following periods. This also can be noticed by the change in the slope of the cumulative number of earthquakes (red line in figure 3.41), but it is more clear demonstrated by the inverted stress changes. The characteristic changes of the cumulative events curve's slope are also noted in figure 3.41. Except the first very low seismicity rate period there seems to be a switching between lower and higher seismicity rate periods. It is noteworthy that such long-term seismicity rate changes (or equivalently stress release) is not observed in none of the cases investigated in the previous sections. This fact constitutes an additional evidence of the complexity of the physical procedures underlying the seismogenesis process in the subduction zones.

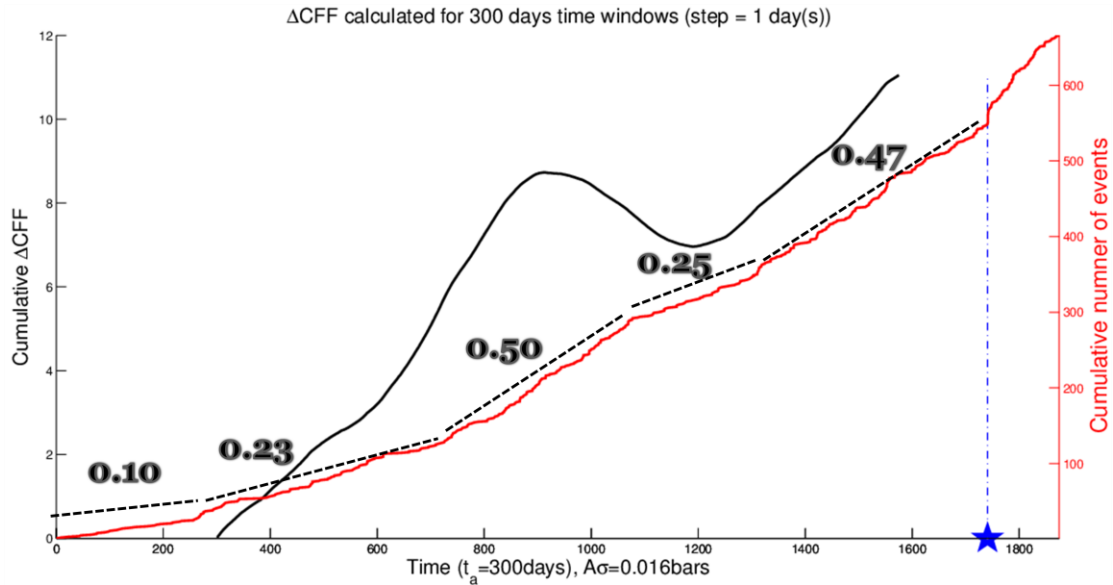


Fig. 3.41. Cumulative stress changes inverted from seismicity rate variation considering overlapping datasets covering 300-days time windows. The characteristic relaxation time is fixed at 300 days and the stressing rate was set to 0.02bar/yr (see at section 2.3.3.3). Blue stars indicate the $M \geq 5.5$ earthquakes. The dashed lines indicate the average trend of each cumulative seismicity segment and the number indicates its slope (events/day).

3.4 Discussion

In this study we attempted to derive static stress changes from the variation of earthquake production rates in selected areas of the Aegean region, by applying the [Dieterich et al. \(2000\)](#) Rate/State formulation. The aim was to investigate seismicity rate changes in both space and time domain and then obtain information concerning the associated stress field variations. This method is able to provide substantial results only in areas exhibit high seismicity rates and this activity is well monitored for a sufficient time period. For this purpose we utilized the data provided by the National and regional networks and sought for periods that ensure constantly high recording seismic rates. Nevertheless, even in such way we succeeded an $M_c=2.4$ and $M_c=1.6$ for a approximately 5 years periods, for Corinth Gulf and Samos-Karaburun, respectively, whereas, for example, [Toda and Matsumura \(2006\)](#) carried out their analysis with $M_c=1.5$ for a 24 year period. However, the purpose of this study was not to provide a forecast for a certain area, but to

take advantage of some of the best monitored areas in the Aegean region to obtain an independent estimation of Coulomb stress changes.

Although there are several not precisely determined and directly measured factors, (Rate/State model parameters, poroelastic effects, pre-existing fault orientations, random fluctuation of earthquake occurrence), the choice of the values applied here was done after thoroughly considering all the available information and data. The background rate (constant in space and time) was only considered in order to estimate the characteristic relaxation time and in turn, parameter $A\sigma$. The temporal analysis of stress variations was performed for subsequent datasets (exhibiting either equal event number or equal duration) whereas the spatial analysis was performed after spatially smoothing seismicity rates in certain areas. Therefore, background rate was estimated just to provide an alternative way to determine a representative value of characteristic relaxation time for aftershock decay. This later parameter, along with the stressing rate as it was derived by GPS data analysis, were applied in equation (2.8) for determining product $A\sigma$. This was done because we believe that t_a and \dot{S}_r can be more robustly determined by independent approaches, than $A\sigma$, the determination of which embodies several uncertainties and a wide range of plausible values.

The stresses were resolved onto receiver faults having identical geometrical features with the first mainshock. This approach seems to be a simplification, nevertheless, the study area is small and the available focal mechanisms indicate small deviations of the assumed faulting mechanism. This is verified by the results of [Karakostas et al. \(2012\)](#), suggesting an average fault geometry derived from 31 events in the area as: $258^\circ \pm 22^\circ$ strike and a $41^\circ \pm 11^\circ$ dip. Moreover, [Karakostas et al. \(2003\)](#) performed ΔCFF calculations for the Skyros, 2001 earthquake (North Aegean) applying strike, dip and rake angles covering a range of 40° . They showed that no remarkable

changes in the stress pattern were observed as far as the dip and rake concerned. In the case of Samos area, [Tan et al. \(2014\)](#) showed that normal faulting prevails (Fig. 3.42) with relative homogeneity in the observed type of faulting: pure normal or faulting with a slight strike slip component are observed close to the Turkish coast having an average dipping of 40°-45°. The T-Axis of maximum extension is also orientated in an almost north south direction in the entire area.

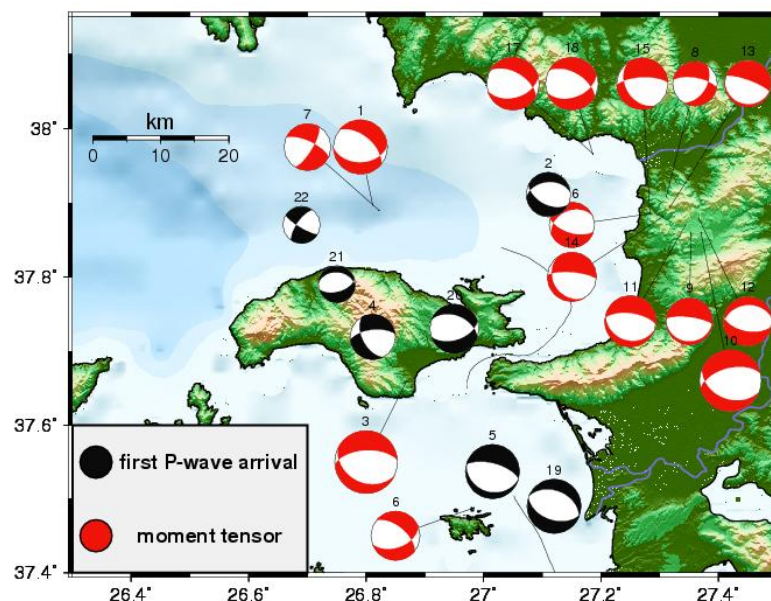


Fig. 3.42. Fault plane solutions of 19 events and 3 earthquake clusters occurred between 2008–2012 in the study area, as they were determined by either the first P-wave arrival method (black beach balls), or by Moment Tensor Inversion (red beach balls).

It is pointed out that the main target of this study was to test if the stress inversion formulation is appropriate to derive reliable results and therefore allow future works to handle seismicity rate changes as an alternative but reliable way to determine stress changes in the active deforming region of Aegean Sea and its adjacent areas. Under this point of view the Δ CFF results yielded by this approach were compared with the respective ones derived from the elastic dislocation model application. The accurate depth determination of the available earthquakes assisted in the resolution of the stress field at the respective depth layers. This led to sufficient correlation between the independent stress-estimating methods for both the best quality

datasets tested (Efpalio and Samos-Kusadasi). The agreement between the two approaches was sufficient even in the near field, which is inherently characterized by significant complexity and inhomogeneity at many scales. This agreement is better when off fault seismicity is considered, in order to eliminate the uncertainties of the forward modeled stress changes in the near field. Moreover, as stated in [Dieterich et al. \(2000\)](#) the inversion approach does not depend on previous models of specific structures and therefore it may also provide constraints on the models used to analyze observations of deformation.

The qualitative (stress pattern comparison) and quantitative (Δ CFF sign agreement of the two methods) correlation was proven to be sufficient enough, with 60-80% of the results being consistent with each other. Especially in the far field, more than 3/4 of the stress changes as they were calculated by the elastic dislocation model were successfully reproduced by the stress inversion methodology followed here. Nevertheless, although stress increases were adequately detected by the earthquake catalogs analysis, stress shadows could not be robustly indicated because of the relatively low levels of the reference seismicity rates.

Another important issue for discussion concerns the timescales that were considered in this analysis. The forward stress calculation modeling provides a snapshot of the stress field variation induced by the mainshocks. On the other hand, the inverse method intrinsically requires a considerable time window, accommodating sufficient data in order to estimate stress changes. However it is generally accepted that only the greatest events have major impact on Coulomb stress changes (e.g. [Ghimire et al., 2008](#)). In the Efpalio sequence studied in the present study, the strongest events (excluding the doublet) had magnitude smaller than 4.6, meaning that they are approximately 1 unit lower than the mainshocks (M=5.5 and M=5.4,

respectively). The respective magnitude difference for Samos-Kusadasi area is 0.6 magnitude units. According to that fact, we might expect that the evolution of the sequence only induced minor stress changes, such that the total stress pattern is negligibly modified. Following this assumption we compared the stress values derived by the two methods, considering the seismic data until the end of periods the catalogues cover. This was done in order to utilize the maximum number of available data, during timescales larger than the characteristic relaxation time, to obtain robust quantitative results. Nevertheless, shorter time windows were considered as well to reproduce the spatial stress pattern (figures 3.12, 3.25, 3.27) and compare it with the one derived by the forward modeling.

Also important is the fact that the model applied here was proved to constitute a very sensitive stress meter, able to detect even small stress changes associated with earthquake occurrence rate changes. In addition to the profound stress changes that follow a strong ($M \geq 5$) earthquake, the method adopted here was able to successfully detect both swarm-like activity and spatio-temporal seismic clusters. This cluster identification is very important and differs significantly from the simple inspection of the number of earthquakes occurred in positive and negative lobes: Space-time clusters clearly demonstrate considerable rate increases, interpreted as stress changes and are fully consistent with the ΔCFF pattern derived by the elastic dislocation approach (e.g. figures 3.17 and 3.32).

As a challenge for future research, relocated catalogues should be taken into consideration together with detailed slip models in order to model ΔCFF in the near field. The efficiency of the seismological networks is continuously improved and therefore the available datasets are enriched with more earthquakes at lower magnitudes, covering larger time periods. Consequently, catalog-based stress calculation method shall become a

promising tool for future studies. Accurate depth determination and focal plane solutions for more events may provide a very detailed 3-dimensional Coulomb stress model for along-fault aftershocks, which may help in the effort to comprehend the mechanisms of triggering and spatio-temporal evolution of aftershock sequences and swarms.

Chapter 4. Concluding Remarks

The conclusions obtained throughout the analysis carried out in the present study are highlighted as follows:

1. The method efficiency strongly depends on data adequacy and accuracy.
2. Longer testing periods with adequate number of remote aftershocks usually yield better correlation than shorter ones containing several onto fault aftershocks.
3. The correlation coefficient is mostly affected by the bandwidth selection (degree of spatial smoothing) rather than the Rate/State model parameter values.
4. Reference seismicity rates evaluated from longer periods generally lead to better correlation in comparison with the more recently selected ones. Exception is the cases when the completeness magnitude is high ($M > 4.0$) and therefore the data size limited.
5. Seismicity rate changes are forecasted better in positive ΔCFF areas than in stress shadows.
6. For the Subduction zone, the depths of 15km and 20km in the ΔCFF calculations along the subduction zone were found to lead to identical results. These results are also better than the ones derived from 10km depth calculations in 3 out of the 4 cases. Larger shear modulus value selection only slightly improves the correlation between observed and modeled seismicity rates.
7. The stress changes estimated from seismicity rate variations are in good agreement with the respective values calculated by the elastic dislocation model application, although the inversion procedure is more sensitive to data quality than the forward Rate/State modeling.

8. Most of the recent, (6 out of 8) $M_w > 6.0$ earthquakes, occurred after June 2012, are located in areas that the applied model predicts to be seismically enhanced.
9. High probabilities (>40%) for a strong event occurrence ($M \geq 6.5$) during the following decade are calculated for Corinth Gulf and most of the areas along the Hellenic Trench.

To summarize, it is shown that the evolution of seismicity is a function of many different parameters, with some of them being poorly constrained. Despite this fact, a simple model like the one applied in this Thesis is able to provide promising results, simulating well the time dependency of seismic activity in an actively deforming area such as the Aegean Sea and its surroundings. The crucial point is that adequate data are needed in order to obtain robust results for both forward and inverse model applications. Here is where the actual power of the Rate/State model lies: taking advantage of well-constrained natural quantities, together with high accuracy seismic data in order to determine the boundaries of parameters that cannot be directly measured and predict the impending activity. Time-dependent seismic hazard assessment becomes a feasible goal for this area, as a causative relationship between the modeled physical procedures and available data was established and verified. For this purpose, appropriate data selection and processing are vital as they significantly affect the forecasted seismicity rates. Finally, the parameter uncertainties should be also quantified in order to provide robust confidence bounds for future probabilistic seismic hazard assessment studies.

Appendix A - Earthquake Catalogue for Western Turkey

A catalogue for earthquakes that occurred in western Turkey during the period 1964–2010, was compiled for achieving homogeneity as far as the magnitudes are concerned (Leptokaropoulos et al., 2013). Seismicity data from the International Seismological Center (ISC) catalogue was utilized, which provides revised information on earthquakes that took place until 2010. The earthquakes that were recorded in the study area since 1964, with a focal depth shallower than 60km were selected. Data from approximately 80 Institutions were available for over 111,000 earthquakes occurred during the aforementioned period, with their magnitudes reaching 180,000 observations expressed in all diverse magnitude scales (i. e. moment magnitude, M_w , body wave magnitude, m_b , surface wave magnitude, M_s , local magnitude, M_L , and duration magnitude, M_d). There were many events, nevertheless, with no magnitude assigned and therefore they cannot be treated for the final catalogue. The first step was to secure magnitude scale homogeneity by converting as many magnitudes as possible to a common magnitude scale, chosen here to be the equivalent moment magnitude, M_w^* , taking as basis for this transformation the moment magnitude determined from the Global Centroid Moment Tensor (M_w GCMT). The technique applied for computing the parameters of the linear regressions between magnitude scales was the General Orthogonal Regression (see Appendix B for details and formulation). Figure A1 shows all the resulted relations whereas the corresponding statistical information is provided in Table A1.

We preferentially sought for relationships between M_w GCMT and moment magnitudes provided by other Institutions (Fig. A1a–c). Firstly the moment magnitude from the National Earthquake Information Center (M_w NEIC) which is considered identical (Scordilis, 2006), therefore taken commonly as one data sample with the notation M_w . Next the moment

magnitudes estimated by the Geodynamic Institute of the National Observatory of Athens (M_w NOA) (Fig.A1a), the Mediterranean Network (M_w MED) (Fig. A1b), and the Eidgenössische Technische Hochschule University of Zürich (M_w ZUR) (Fig. A1c) were selected and transformed, and thus 243 events with M_w^* were added in the catalogue by this procedure. Advantage is taken from the fact that the NOA is the only source that reports M_w 's as low as 3.4, which enables extrapolation of the relationships to lower magnitudes, considerably then increasing the size of the final catalogue. Given that moment magnitude is calculated with the same methodology (i.e. waveform inversion), an assumption was made that the relation between M_w GCMT and M_w NOA may be extrapolated for magnitudes lower than the range that the available data covers. Therefore, for each magnitude scale to be transformed, moment magnitude was taken either from GCMT or from M_w^* NOA (Fig A1d–n, with different notation).

Surface wave magnitudes, M_s , reported from the ISC, NEIC, European Mediterranean Seismological Center (EMSC) and the International Data Center (IDC) were then converted into M_w^* (Fig. A1d–g), along with body wave magnitudes, m_b , (Fig. A1h–k) reported from the same sources. Local magnitudes, M_L , from ISK and NOA (Fig. A1l–m) as well as duration magnitude, M_d , from NOA (Fig. A1n) were correlated with M_w , and more importantly the large number of the M_d estimated from ISK. The problem with this latter magnitude lies at the lack of commonly existing with M_w and therefore, M_d ISK was correlated with the equivalent moment magnitude as yielded from the conversion of body wave magnitude from ISC (M_w^{bISC} –Fig 2o). This conversion has as advantages the large number of observations (pairs of magnitudes for the same events) and the wide magnitude range covered. By this way we managed to treat events with magnitude down to M_d ISK=3.5. Fig. A1o evidences that linear regression cannot adequately

simulate this relation and therefore a second degree polynomial fitting was preferred.

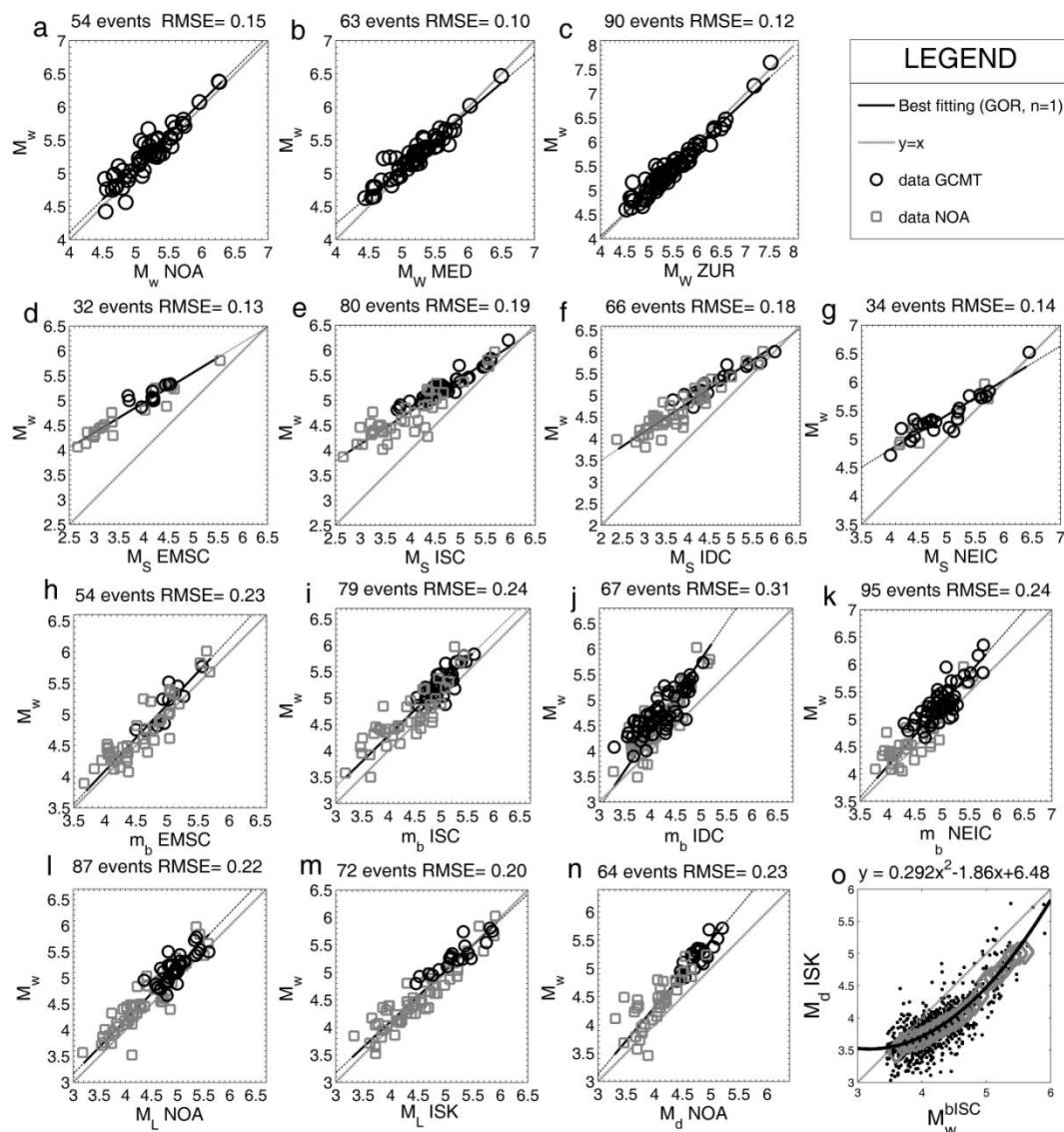


Fig. A1. Magnitude relations between various scales and Institutions and M_w GCMT (black circles) and M_w NOA (gray squares). The solid lines indicate the general orthogonal regression linear fitting, whereas the dashed lines indicate the bisector. For a better representation data were plotting after the addition of 3 random decimal digits to the x and y values. The number of pairs, the root mean square error (RMSE) and the linear correlation coefficient (R^2) is shown above each frame. Figure 2o shows the 2nd degree polynomial fitting between M_d ISK and the equivalent moment magnitude as it was calculated from the conversion of body wave magnitude reported from ISC (M_w^{blSC}). The diamonds correspond to the average values of M_d ISK per M_w^{blSC} unit.

Magnitude conversion into M_w^* was accomplished by giving priority to certain magnitude scales and estimates, and then following a rule for adopting the final M_w^* . When M_w GCMT or equivalently M_w NEIC were

available, these were directly adopted as M_w^* in our catalogue. If M_w was estimated from a different source, then the higher conversion priority was set where the RMS error was lower and thus $M_w^*_{MED}$, was firstly preferred, then $M_w^*_{ZUR}$ and finally $M_w^*_{NOA}$. For the earthquakes with reported magnitudes in other magnitude scales, the conversion was performed for all the assigned magnitudes (except M_d ISK) and the final M_w^* was estimated as a weighted average of all the available magnitudes, with a normalized weight inversely proportional to their RMS errors. Finally, if the only available magnitude was M_d ISK, then it was estimated from the 2nd degree polynomial. Thus an integrated catalogue, revised as to be homogeneous in the magnitude scale and comprising 9875 events with M_w^* ranging from 3.5 to 7.6, starting from 1964 until 2010 and from 35.00°N – 42.00°N latitude and 26.00°E – 32.00°E longitude is achieved (Fig. A2).

Table A1
Empirical relations for magnitude scales transformation

Relation	Source	b	a	RMS error	R ²	Number of events used and their magnitude range
$M_w^* = a + bM_w$	NOA	0.99±0.006	0.17±0.162	0.15	0.93	54 (4.5 - 6.3)
	MED	0.85±0.003	0.84±0.074	0.10	0.95	90 (4.4 - 6.5)
	ZUR	0.93±0.001	0.33±0.037	0.12	0.97	63 (4.5 - 6.5)
$M_w^* = a + bM_s$	EMSC	0.61±0.003	2.52±0.042	0.13	0.95	32 (2.6 - 4.6)
	ISC	0.65±0.002	2.15±0.033	0.19	0.93	80 (2.8 - 6.0)
	IDC	0.66±0.002	2.18±0.027	0.18	0.94	66 (2.4 - 6.0)
	NEIC	0.61±0.004	2.38±0.010	0.14	0.92	34 (4.0 - 5.9)
$M_w^* = a + bm_b$	EMSC	1.06±0.010	-0.15±0.219	0.23	0.90	54 (3.7 - 5.6)
	ISC	0.98±0.006	0.38±0.128	0.24	0.90	79 (3.2 - 5.6)
	IDC	1.46±0.021	-1.49±0.385	0.31	0.87	67 (3.5 - 5.0)
	NEIC	1.13±0.007	-0.39±0.169	0.24	0.89	95 (3.9 - 5.7)
$M_w^* = a + bM_l$	NOA	1.03±0.004	0.08±0.090	0.23	0.90	54 (3.5 - 5.5)
	ISK	0.93±0.003	0.39±0.070	0.20	0.94	72 (3.6 - 6.0)
$M_w^* = a + bM_d$	NOA	1.18±0.010	-0.43±0.182	0.23	0.91	64 (3.4 - 5.2)

The conversion form is shown in the first column. The second column gives the data source. The a and b values of the general orthogonal regression fitting, along with their standard errors are shown in the third and fourth column, respectively. The next three columns provide information on the RMS error, linear correlation coefficient (R²), number of observations and the respective magnitude range.

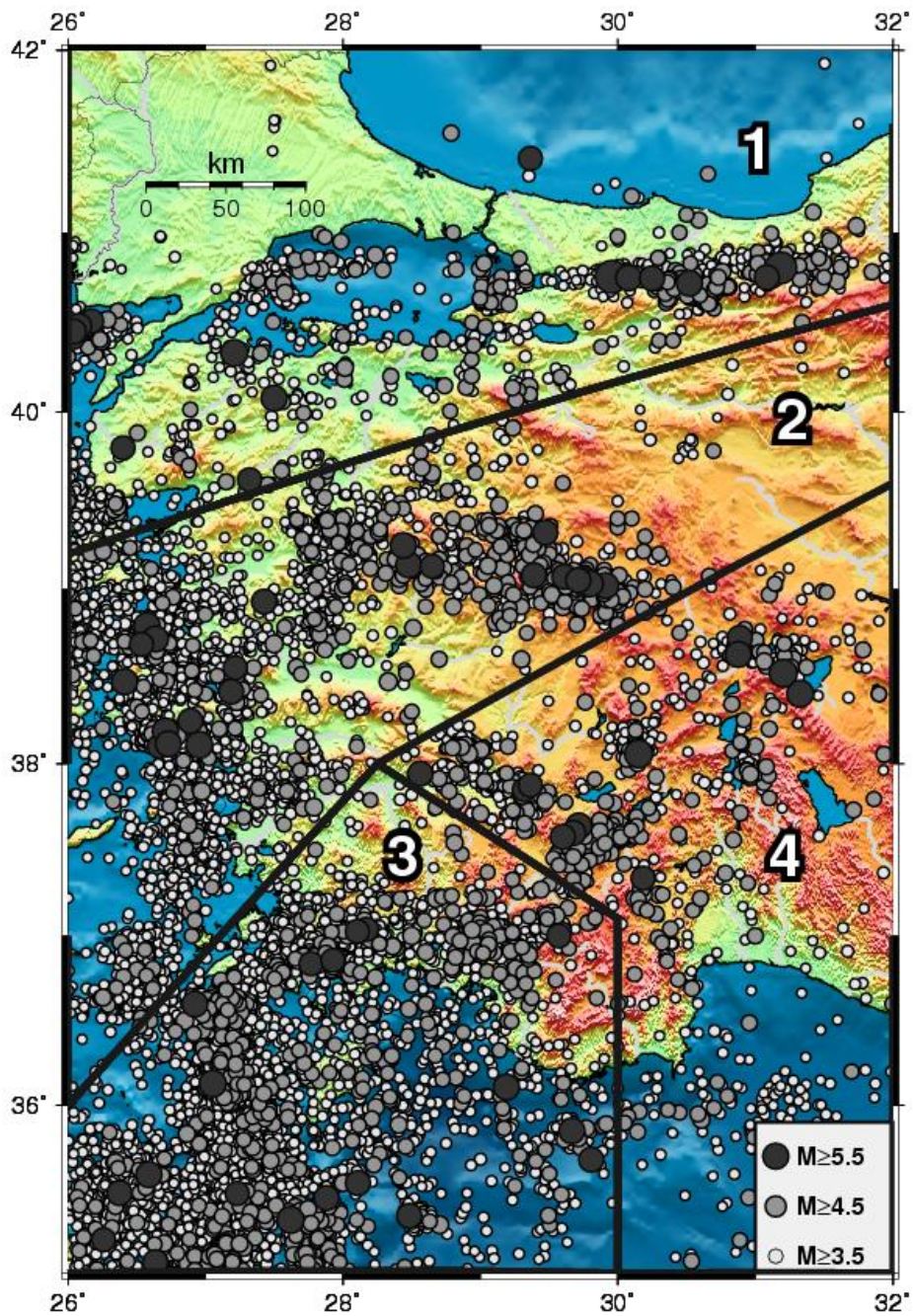


Fig. A2. Spatial distribution of earthquake epicenters during 1964-2010 in the study area (sub-areas selected for the Rate/State model applications are also here depicted) after the catalogue compilation, with magnitudes expressed as M^*w .

Appendix B - General Orthogonal Regression

After deriving relations between M_w and other magnitude scales published by different Institutions and, we applied the most reliable of them after taking into consideration the sample size, the RMS error, the linear correlation coefficient (R^2) and the uncertainties of the linear regression parameters, a and b (Leptokaropoulos et al., 2013). To obtain these relations we avoided using the ordinary least squares method which assumes that there are no uncertainties in the values of the independent variable. This may introduce systematic errors in magnitude conversion, apparent catalogue incompleteness and significant bias in the estimates of the b -value (Castellaro et al., 2006). Alternatively we applied the General Orthogonal Regression technique in order to avoid such artifacts (Castellaro and Gormann, 2007; Deniz and Yucemen, 2010; Wason et al., 2012, Lolli and Gasperini, 2012). According to this method the projection of the independent variable is done along a weighted orthogonal distance from the linear fitting curve. The values of the slope, b , and intercept, a , are estimated by Fuller (1987) formulae as

$$b = \frac{s_y^2 - ns_x^2 + \sqrt{(s_y^2 - ns_x^2)^2 + 4ns_{xy}^2}}{2s_{xy}}, \quad (B1)$$

$$a = \langle y \rangle - b\langle x \rangle, \quad (B2)$$

where s_x and s_y are the standard deviations of x and y variables respectively, s_{xy} is the sample covariance between x and y , $\langle y \rangle$ and $\langle x \rangle$ are the average values of y and x and $n=(\sigma(y)/\sigma(x))^2$, is the error variance ratio. Since the standard errors of the available data are unknown, we set $n=1$. Castellaro et al. (2006) showed that even if the applied values of the ratios of the errors is different from the real one, the orthogonal regression method still performs

better than the ordinary least squares. The errors of the slope and the intercept given the sample size, N, are expressed as follows

$$\hat{\sigma}_\beta^2 = \frac{(\hat{\sigma}_x + \hat{\sigma}_u) s_u - (-b \hat{\sigma}_u)^2}{(N-1) \hat{\sigma}_x^2} \quad , \quad (\text{B3})$$

$$\hat{\sigma}_a^2 = \frac{s_u}{N} + \langle x \rangle^2 \hat{\sigma}_\beta^2 \quad , \quad (\text{B4})$$

Where

$$\hat{\sigma}_x = \frac{\sqrt{(s_y^2 - n s_x^2)^2 + 4n s_{xy}^2} - (s_y^2 - n s_x^2)}{2n} \quad , \quad (\text{B5})$$

$$\hat{\sigma}_u = \frac{(s_y^2 + n s_x^2) - \sqrt{(s_y^2 - n s_x^2)^2 + 4n s_{xy}^2}}{2n} \quad , \quad (\text{B6})$$

$$s_u = \frac{(N-1)(n-b^2) \hat{\sigma}_u}{N-2} \quad . \quad (\text{B7})$$

Appendix C - Identification of Completeness Magnitude

The evaluation of M_c is usually accomplished by following two major approaches, the network-based (Schorlemmer and Woessner, 2008; Mignan et al., 2011) and the catalogue-based methods. The second approach is sustained of two different groups. The first one relies on the fact that the detection threshold due to the noise decreases during the night and therefore M_c is determined by considering the day-to-night ratio of earthquake frequency (Rydelek and Sacks, 1989; Taylor et al., 1990). The second group contains methods that follow the assumption of self-similarity of earthquake production, such that frequency-magnitude distribution of earthquakes can be simulated by a power law i.e. Gutenberg-Richter (G-R) law. The most frequently applied methods of this group are the Entire Magnitude Range (EMR) method (Ogata and Katsura, 1993; modified by Woessner and Wiemer, 2005), the Maximum Curvature (MAXC) method (Wiemer and Wyss, 2000), the Goodness-of-Fit Test (GFT) (Wiemer and Wyss, 2000), the M_c determination by b-value instability (Cao and Gao, 2002) and the Median Based Analysis of the Segment Slope (MBASS) (Amorèse, 2007). In an effort to determine M_c , Woessner and Wiemer (2005) and Mignan and Woessner (2012) overviewed and applied these methods and then compared their performance and stability.

The method here applied, the Modified Goodness-of-fit Test (MGFT, Leptokaropoulos et al., 2013) is based upon the Goodness-of-Fit Test (GFT), proposed by Wiemer and Wyss (2000). The procedure they followed is that a power law, as a function of minimum magnitude, M_i , is fitted for events with $M \geq M_i$, by application of maximum likelihood estimation. The synthetic data, i.e. the distribution of magnitudes which represent a perfect fit to the power law, is constructed in this way. Then the normalized, absolute difference, R ,

between the cumulative number of observed events (N_o) and the simulated ones (N_s) in each magnitude bin is computed and mapped according to the formula

$$R = \frac{\sum_{M_i}^{M_{\max}} |N_o - N_s|}{\sum_i N_o} \quad (C1)$$

If the data set above a specific magnitude M_i is incomplete, this difference, R , will be high. A model is found at an R -value at which a predefined percentage (usually 90% or 95%) of the observed data is modeled by a straight line, which means that 90% or 95% of the observed data can be simulated by the specific power law (Woessner and Wiemer, 2005).

A modified approach of this method (MGFT) is introduced and applied here: A synthetic dataset of N_i events is created by distributing random numbers according to the respective G–R law (Zechar, 2010), where N_i is the cumulative number of events with $M \geq M_i$ in the observed dataset. After k iterations of this process, k synthetic catalogues are created. Here, we are interested only in Frequency Magnitude Distributions (FMD) of the events and not in their spatial and temporal parameters (epicenter location, origin time). Therefore, the synthetic catalogues consist of events for which the only free parameter is the magnitude. We chose k to be equal to 1,000 and instead of comparing the offset between the real values and the theoretical distribution, 1,000 synthetic catalogues containing random events with the same data number and magnitude distribution are constructed for each magnitude bin. Thus, one more parameter, i.e. the occurrence frequency in each magnitude bin, is introduced. Starting from a minimum magnitude, M_i , parameters a and b of the G–R law are calculated following a maximum likelihood estimation for all events with $M_i \leq M \leq M_{\max}$. One of the mostly preferred techniques to estimate the b -value is the Maximum Likelihood

Estimate (Aki, 1965; Weichert, 1980; Utsu, 1999; Lombardi, 2003; Marzocchi and Sandri, 2003; Kagan, 2005; Kijko and Smit, 2012)

$$b = \frac{1}{\ln(10) [\langle M \rangle - (M_c - \Delta M / 2)]} , \quad (C2)$$

where $\langle M \rangle$ is the sample mean of the events considered and ΔM is the binning width of the catalogue, equal to 0.1 in the present study. Aki (1965) also estimated the b-value accuracy, σ_b , as

$$\sigma_b = \frac{b}{\sqrt{N}} , \quad (C3)$$

where N stands for the sample size. The difference between each one of these synthetic datasets and the observed ones is calculated following eq. (C1) and an average value of these differences is derived. Then, the whole procedure is repeated by considering M_{i+1} as minimum magnitude. A new G-R law is retrieved, by estimating the new a and b values, and given N_{i+1} , being the cumulative number of observed events with $M \geq M_{i+1}$. The mean values of the differences between the real FMD and the one derived from the synthetic catalogues for each magnitude bin are computed and mapped. The residuals are rather higher in this case, but there is an obvious minimum point and therefore, instead of considering an arbitrary selected level of fitting to power law, a more objective criterion is being applied.

Mc Results and Comparison with other Methods

The results derived from MGFT method were also compared with the ones yielded from the application of MAXC and the original GFT methods for the consistency of the three approaches to be tested. In general there is a good agreement among them especially when the catalogue of a study period contains sufficient number of data, while there is a significant deviation

among them for earlier periods with limited data. In these cases the technique introduced here provides a more conservative selection of M_c , about 0.1–0.4 units higher than MAXC and GFT(90%). GFT(95%) on the contrary, demonstrates inordinately higher M_c values for some of the cases in comparison with all the other methods. There are also some datasets where the 95% level cannot be achieved due to the relatively low sample size or the irregularities arise from the magnitude conversion procedure (in the case of the Western Turkey catalogue). The MGFT method is free from such behavior and therefore is more reliable when applied in datasets which demonstrate higher completeness level, or for short time intervals containing limited number of events. The proposed technique is proven to be more stable than the original GFT and independent of the R-value selection and also more conservative than the MAXC, which is already shown that tends to underestimate M_c (Woessner and Wiemer, 2005). We are confident that the technique introduced here can be easily applied to other regions with relatively low detection level but with high seismic hazard such as the eastern Anatolia, Aegean Sea and the surrounding areas.

Appendix D – Kernel Estimator of Magnitude Distribution and Exceedance Probability Estimation.

The kernel estimator approach proposed by [Kijko et al. \(2001\)](#) is a model-free alternative to estimating the magnitude distribution functions. This non-parametric approach, (also known as model free or data-driven), is based on the kernel density estimator that totals the symmetric probability densities (kernels), individually associated with data points as

$$\hat{f}(m|\{m_i\},h) = \frac{1}{nh} \sum_{i=1}^n K\left(\frac{m-m_i}{h}\right), \quad (D1.1)$$

where h , is a non negative smoothing parameter (bandwidth), m , is the magnitudes and $K(x)$ is a kernel function. The Kernel estimations chosen here for probability density (D1.2) and cumulative distribution (D1.3) have the forms of those adopted by [Lasocki and Orlecka-Sikora \(2008\)](#)

$$\hat{f}_m(m) = \frac{\sum_{i=1}^n \frac{1}{a_i h} \exp\left[-\frac{1}{2}\left(\frac{m-m_i}{a_i h}\right)^2\right]}{(\sqrt{2\pi}) \sum_{i=1}^n \left[\Phi\left(\frac{m_{\max}-m_i}{a_i h}\right) - \Phi\left(\frac{m_{\min}-m_i}{a_i h}\right)\right]}, \quad (D1.2)$$

$$\hat{F}_m(m) = \frac{\sum_{i=1}^n \left[\Phi\left(\frac{m-m_i}{a_i h}\right) - \Phi\left(\frac{m_{\min}-m_i}{a_i h}\right)\right]}{\sum_{i=1}^n \left[\Phi\left(\frac{m_{\max}-m_i}{a_i h}\right) - \Phi\left(\frac{m_{\min}-m_i}{a_i h}\right)\right]}, \quad (D1.3)$$

where n , is the sample size, $\Phi(x)$ is the standard Gaussian cumulative distribution, a_i ($i=1,2,\dots,n$) are the local bandwidth factors and m , is the magnitudes with $m_{\min} \leq m \leq m_{\max}$. Note that m_{\min} is equal to the completeness threshold of a given catalog. It is assumed that the magnitude distribution is unlimited from the right hand side (i.e. no fixed maximum magnitude). The shape of the kernel estimates depends primarily on the value of h . From the point of view of the use of estimators (D1.2), (D1.3) in the hazard analysis, a global, integrant agreement between the actual density and its estimates is of

the utmost importance. Therefore, we select the smoothing factor applying the least squares cross-validation technique that requires minimizing the integral of the squared difference between the actual density, $f(\xi)$, and the estimate (e.g. [Bowman et al., 1984](#))

$$\hat{f}(\xi) = \int_{-\infty}^{\infty} [\hat{f}(\xi) - f(\xi)]^2 d\xi . \quad (\text{D1.4})$$

It has been shown ([Kijko et al., 2001](#)) that in the case of the Gaussian kernel this criterion is fulfilled if h is the root of the equation

$$\sum_{i,j} \left\{ \left[\frac{(m_i - m_j)^2}{2h^2} - 1 \right] \exp \left[-\frac{(m_i - m_j)^2}{4h^2} \right] - 2 \left[\frac{(m_i - m_j)^2}{h^2} - 1 \right] \exp \left[-\frac{(m_i - m_j)^2}{2h^2} \right] \right\} = 2n . \quad (\text{D1.5})$$

The local bandwidth factors, $\{\alpha_i\}$ can modify the width of the kernels at certain data points. Due to the fact, that the most important for the hazard analysis range of magnitudes, is that of the larger values, where the data are very sparse, the present version of the estimators uses the bandwidth factors that widen the kernels associated with data points from this range ([Orlecka-Sikora and Lasocki, 2005](#))

$$a_1 = \frac{1}{\left[\frac{\hat{f}(m_i | \{m_i\}, h)}{g} \right]^{1/2}} , \quad (\text{D1.6})$$

where \hat{f} , is the constant kernel estimator in the unbounded magnitude range, and $g = \left[\prod_{i=1}^n \hat{f}(m_i | \{m_i\}, h) \right]^{1/n}$ is the geometric mean of all constant kernel estimates ([Silverman, 1986](#)). Finally, the exceedance probability, that is the probability of occurrence, in Δt time units, of events with sizes greater than or equal to m_p , occurring at an average rate, λ , is given by

$$R(m_p, \Delta t) = 1 - \exp \left(-\lambda \Delta t [1 - F_m(m_p)] \right) . \quad (\text{D1.7})$$

Appendix E – Forward Rate/State Modelling for the Efpalio 2010 Doublet

The forward Dieterich (1994) Rate/State model provides seismicity rate changes, as a function of time (eq. 2.9). By substituting in this equation ΔCFF values, $A\sigma$ (0.04 bars) and t_a (225days), along with the smoothed reference seismicity rates, r , (eq. 2.13) we obtained the forecasted rates, R , after the two main shocks. These rates were compared with the recorded seismicity rates and found to be in good agreement (Fig E1). A quantitative analysis (Fig E2) shows that especially after the second strong event the correlation coefficient between forecasted and observed seismicity rates is approximately 75% for a bandwidth equal to 0.03° . This is a significant result concerning the fact that after applying Silverman's formulation (eq. 2.17), $h=0.033^\circ$ is obtained a value almost identical with the one corresponds to the best correlation between real and synthetic seismicity rates. It is noteworthy that the best correlation between real and synthetic data is obtained for $h=0.03^\circ$ in both forward (Fig E2) and inverse (Fig 3.11 & 3.12) approaches. The inter-event time period (between the two mainshocks) exhibits lower correlation (50%-60%) but it is not representative of the standard model performance because of its short duration (~4 days) and the abundance of onto fault aftershocks.

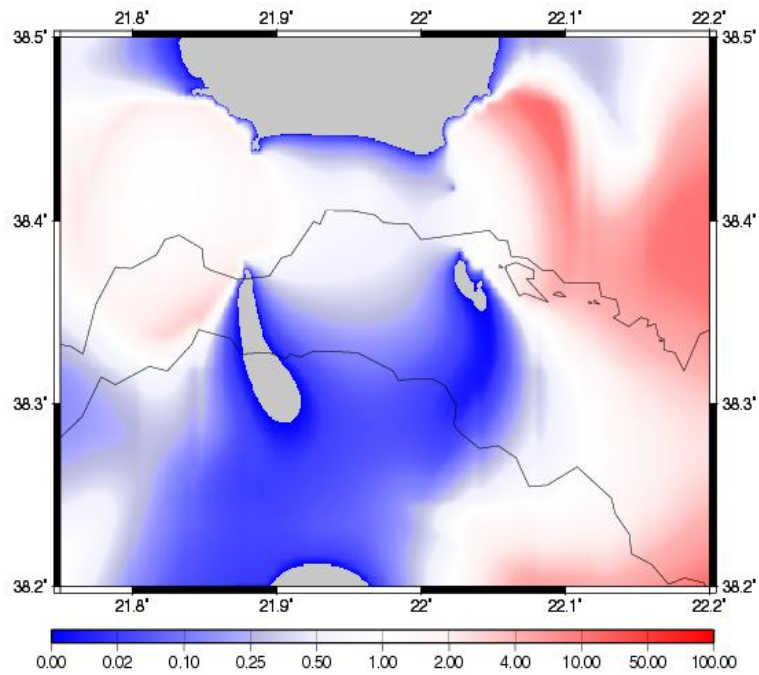


Fig. A1. Ratio of expected/observed seismicity rates given the reference seismicity rate calculated during 1 August 2008 to 18 January 2010 ($M > 2.4$). Red colors overestimate expected values in comparison with the real ones whereas blue colors show higher observed seismicity rates than the simulated ones. White areas correspond to ratio value between 0.5-2, suggesting sufficient model performance. Calculations are not performed in gray areas because of data insufficiency. Parameters values applied are: $h=0.03^\circ$, $t_a=225$ days, $\Delta\sigma=0.4$ bars.

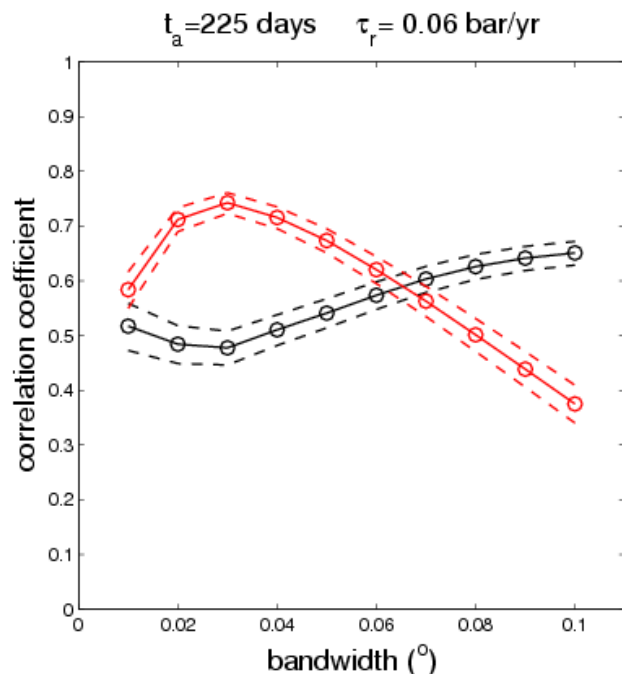


Fig. A2. Quantitative evaluation of the difference between observed-synthetic seismicity rates during the inter-event time period between the 2 strong events occurrence (18 January 2010 – 22 January 2010, black lines) and until the end of 2012 (red lines). Solid lines indicate the value of Pearson linear Correlation Coefficient whereas its 95% confidence intervals for each coefficient are also depicted by dashed lines.

References

1. Adamaki, A., E. Papadimitriou, G. Tsaklidis, and V. Karakostas (2011), Statistical properties of aftershock rate decay: Implications for the assessment of continuing activity, *Acta Geophys.*, 59, doi: 10.2478/ s11600-011-0016-2.
2. Adamopoulos, L. (1976), Cluster models for Earthquakes: Regional Comparisons, *Math. Geol.*, 8, 463-475.
3. Akaike, H. (1974), A new look at the statistical model identification, *IEEE Trans. Autom. Contr.*, AC-19, 716-723.
4. Aki, K. (1965), Maximum likelihood estimate of b in the formula $\log N = a - bM$ and its confidence limits, *Bull. Earthquake Res. Inst. Tokyo Univ.*, 43, 237-239.
5. Aktar, M., H. Karabulut, S. Özalaybey, and D. Childs (2007), A conjugate strike-slip fault system within the extensional tectonics of Western Turkey, *Geophys. J. Int.*, 171, 1363-1375.
6. Aktuğ, B., J. M. Nocquet, A. Cingoz, B. Parsons, Y. Erkan, P. England, O. Lenk, M. A. Gurdal, A. Kilicoglu, H. Akdeniz, and A. Tekgul (2009), Deformation of western Turkey from a combination of permanent and campaign GPS data: Limits to block-like behavior, *J. Geophys. Res.*, 114, doi:10.1029/2008JB006000.
7. Ambraseys, N. N. (2009), *Earthquakes in the eastern Mediterranean and the Middle East: a multidisciplinary study of 2000 years of seismicity*, Cambridge University Press, 947 pp, ISBN 978-0-521-87292-8.
8. Ambraseys, N. N., and J. A. Jackson (1990), Seismicity and associated strain of central Greece between 1890 and 1988, *Geophys. J. Int.*, 101, 663-708.
9. Ambraseys, N.N., and J. A. Jackson (1997), Seismicity and strain in the Gulf on Corinth since 1964, *J. Earthq. Eng.*, 1, 433-474.

10. Amorèse, D. (2007), Applying a change–point detection method on frequency–magnitude distributions, *Bull. Seismol. Soc. Am.*, 97, doi:10.1785/0120060181.
11. Armijo, R., B. Meyer, G. C. P. King, A. Rigo, and D. Papanastassiou (1996), Quaternary evolution of the Corinth Rift and its implication for the late Cenozoic evolution of the Aegean, *Geophys. J. Int.*, 126, 11–53.
12. Armijo, R., F. Flerit, G. King, and B. Meyer (2003), Linear elastic fracture mechanics explains the past and present evolution of the Aegean, *Earth Planet. Sci. Lett.*, 217, 85–95.
13. Aron, A., and J. Hardebeck (2009), Seismicity rate changes along the central California coast due to stress changes from the 2003 M 6.5 San Simeon and 2004 M 6.0 Parkfield earthquakes, *Bull. Seismol. Soc. Am.*, 99, 2280–2292.
14. Avallone A., P. Briole, A. M. Agatza-Balodimou, H. Billiris, O. Charade, C. Mitsakaki, A. Nercessian, K. Papazissi, D. Paradissis, and G. Veis (2004), Analysis of eleven years of deformation measured by GPS in the Corinth Rift Laboratory area, *C. R. Geosci.*, 336, 301–312.
15. Ayhan, M. E., R. Búrgmann, S. McCluskey, O. Lenk, B. Aktug, E. Herece, and R. E. Reilinger (2001), Kinematics of the $M_w=7.2$, 12 November 1999, Düzce, Turkey earthquake, *Geophys. Res. Lett.*, 28, 367–370.
16. Baker, C., D. Hatzfeld, H. Lyon-Caen, E. Papadimitriou, and A. Rigo (1997), Earthquake mechanisms of the Adriatic Sea and Western Greece: implications for the oceanic subduction-continental collision transition, *Geophys. J. Int.*, 131, 559–594.
17. Barka, A. A., H. S. Akyüz, E. Altunel, G. C. Sunal, Z. Çakir, A. Dikbas, B. Yeli, R. Armijo, B. Meyer, J. B. De Chabaliér, T. Rockwell, J. R. Dolan., R. Hartleb, T. Dawson, S. Christofferson, A. Tucker, T. Fumal, R. Langridge, H. Stenner, W. Lettis, J. Bachhuber, and W. Page (2002), The surface rupture and slip distribution of the 17 August, 1999 İzmit

- earthquake, $M = 7.4$, North Anatolian Fault, *Bull. Seismol. Soc. Am.*, 92, 43–60.
18. Bebbington, M. (2008), Estimating rate- and state- friction parameters using a two-node stochastic model for aftershocks, *Tectonophysics*, 457, 71-85.
 19. Beeler, N. M., R. W. Simpson, S. H. Hickman, and D. A. Lockner (2000), Pore fluid pressure, apparent friction and coulomb failure, *J. Geophys. Res.*, 105, 25,533-25,542.
 20. Beeler, N. M., E. Roeloffs, and W. McCausland (2014), Re-estimated of deep episodic slip on the occurrence and probability of great earthquakes in Cascadia, *Bull. Seismol. Soc. Am.*, 104, doi: 10.1785/0120120022.
 21. Belardinelli, M., M. Cocco, O. Coutant, and F. Cotton (1999), Redistribution of dynamic stress during coseismic ruptures: Evidence for fault interaction and earthquake triggering, *J. Geophys. Res.*, 104, 14,925–14,945, doi:10.1029 /1999JB900094.
 22. Belardinelli, M. E., A. Bizzarri, and M. Cocco (2003), Earthquake triggering by static and dynamic stress changes, *J. Geophys. Res.*, 108, doi:10.1029/ 2002JB001779.
 23. Belardinelli, M. E., A. Bizzarri, G. Berrino, and G. P. Ricciardi (2011), A model for seismicity rates observed during the 1982-1984 unrest at Caampi Flegrei caldera (Italy), *Earth Planet. Sci. Lett.*, 302, 287-298.
 24. Bell, R.E., L. C. McNeill, J. M. Bull, and T. J. Henstock (2008), Evolution of the offshore western Gulf of Corinth, *Bull. Geol. Soc. Amer.*, 120, 156 – 178.
 25. Bellier, O., S. Över, A. Poisson, and J. Andrieux (1997), Recent temporal change in the stress state and modern stress field along the North Anatolian Fault Zone (Turkey): *Geophys. J. Int.*, v. 131, p. 61-86.

26. Benetatos, C., A. Kiratzi, A. Ganas, M. Ziazia, A. Plessa, and G. Drakatos (2006), Strike slip motions in the Gulf of Siğaçık (western Turkey): Properties of the 17 October 2005 earthquake seismic sequence, *Tectonophysics*, 426, 263 – 279.
27. Bernard, B., P. Briole, B. Meyer, H. Lyon-Caen, J.-M. Gomez, C. Tiberi, C. Berge, R. Cattin, D. Hatzfeld, C. Lachet, B. Lebrun, A. Deschamps, F. Courboulex, C. Larroque, A. Rigo, D. Massonnet, P. Papadimitriou, J. Kassaras, D. Diagourtas, K. Makropoulos, G. Veis, E. Papazisi, C. Mitsakaki, V. Karakostas, E. Papadimitriou, D. Papanastassiou, M. Chouliaras, and G. Stavrakakis (1996), The Ms=6.2, June 15, 1995 Aigion earthquake (Greece): evidence for low angle normal faulting in the Corinth rift, *J. Seismol.*, 1, 131-150.
28. Bernard, P., H. Lyon-Caen, P. Briole., A. Deschamps, F. Boudin, K. Makropoulos, P. Papadimitriou, F. Lemeille, G. Patau, H. Billiris, D. Paradissis, K. Papazissi, H. Castarede, H. Charade, A. Nercessian, A. Avallone, F. Pacchiani, J. Zahradnik, S. Sacks, and A. Linde (2006), Seismicity, deformation and seismic hazard in the western rift of Corinth: New insights from the Corinth Rift Laboratory (CRL), *Tectonophysics*, 426, 7-30.
29. Bird, P., and Y. Kagan (2004), Plate-tectonic analysis of shallow seismicity: apparent boundary width, beta, corner magnitude, coupled lithosphere thickness and coupling in seven tectonic settings, *Bull. Seismol. Soc. Am.*, 94, 2380–2399.
30. Botev, Z. I., J. F. Grotowski, and D. P. Kroese (2010), Kernel density estimation via diffusion, *Ann. Stat.*, 38, 2916-2957.
31. Bowman, A. W., P. Hall, and D. M. Titterington (1984), Cross-validation in non-parametric estimation of probabilities and probability densities, *Biometrika*, 71, 341– 351.

32. Bowman, D. D., and G. C. P. King (2001), Stress transfer and seismicity changes before large earthquakes, *Earth Planet. Sci.*, 333, 591-599.
33. Bowman, D.D., G. Ouillon, C.G. Sammis, A. Sornette, and D. Sornette (1998), An observational test of the critical earthquake concept, *J. Geophys. Res.*, 103, B10, 24,359-24,372, doi: 10.1029/98JB00792.
34. Bozkurt, E. (2001), Neotectonics of Turkey - a synthesis, *Geodin. Acta*, 14, 3-30.
35. Bozkurt, E. (2003), Origin of NE-trending basins in western Turkey, *Geodin. Acta*, 16, 61-81.
36. Braunmiller, J., and J. Nabelek (1996), Geometry of continental normal faults: seismological constraints, *J. Geophys. Res.*, 10, 3045-3052.
37. Briole, P., A. Rigo, H. Lyon-Caen, J. C. Ruegg, K. Papazissi, C. Mitsakaki, A. Balodimou, G. Veis, D. Hatzfeld, and A. Deschamps (2000), Active deformation of the Corinth rift, Greece: Results from repeated Global Positioning System surveys between 1990 and 1995, *J. Geophys. Res.*, 105, 605-625.
38. Bufe, C.G., and D.J. Varnes (1993), Predictive modeling of the seismic cycle of the greater San Francisco Bay region, *J. Geophys. Res.*, 98, B6, 9871-9883, doi: 10.1029/93JB00357.
39. Cao, A. M., and S. S. Gao (2002), Temporal variation of seismic b-values beneath northeastern Japan island arc, *Geophys. Res. Lett.*, 29, doi:10.1029/2001GL013775.
40. Caputo, R., and S. Pavlides (1993), Late Cainozoic geodynamic evolution of Thessaly and surroundings (central-northern Greece), *Tectonophysics*, 223, 339-362.
41. Castellaro, S., F. Mulargia, and Y. Y. Kagan (2006), Regression problems for magnitudes, *Geophys. J. Int.*, 165, 913-930.

42. Castellaro, S., and P. Bormann (2007), Performance of different regression procedures on the magnitude conversion problem, *Bull. Seismol. Soc. Am.*, 97, 1,167-1,175.
43. Catalli, F., M. Cocco, R. Console, and L. Chiaraluce (2008), Modeling seismicity rate changes during the 1997 Umbria-Marche sequence (central Italy) through a rate-and-state dependent model, *J. Geophys. Res.*, 113, B11301, doi:10.1029/2007JB005356.
44. Chan, C. H., M. Sørensen, D. Stromeyer, G. Grünthal, O. Heidback, A. Hakimhashemi, and F. Catalli (2010), Forecasting Italian seismicity through a spatio-temporal physical model: importance of considering time-dependency and reliability of the forecast, *Ann. Geophys.*, 53, 3, doi: 10.4401/ag-4761.
45. Chan, C. -H., Y. -M. Wu, and J. -P. Wang (2012), Earthquake forecasting using the rate-and-state friction model and a smoothing Kernel: application to Taiwan, *Nat. Hazards Earth Syst. Sci.*, 12, 3045–3057.
46. Clarke, P. J., R. R. Davies, P. C. England, B. Parsons, H. Billiris, D. Paradissis, G. Veis, P. A. Cross, P. H. Denys, V. Ashkenazi, R. Bingley, H. G. Kahle, M. V. Muller and P. Briole (1998), Crustal strain in central Greece from repeated GPS measurements in the interval 1989–1997, *Geophys. J. Int.*, 135, 1, 195– 214.
47. Cloetingh, S. A. P. L., P. A. Ziegler, P. J. F. Bogaard, P. A. M. Andriessen,, I. M. Artemieva, G. Bada, R. T. van Balen, F. Beekman, Z. Ben-Avraham, J. -P. Brun, H. P. Bunge, E.B. Burov, R. Carbonell, C. Facenna, A. Friedrich, J. Gallart, A. G. Green, O. Heidbach, A. G. Jones, L. Matenco, J. Mosar, O. Oncken, C. Pascal, G. Peters, S. Sliampa, A. Soesoo, W. Spakman, R. A. Stephenson, H. Thybo, T. Torsvik, G. de Vicente, F. Wenzel, M. J. R Wortel, and TOPO-EUROPE Working Group (2007), TOPO-EUROPE: the geoscience of coupled deep Earth-surface

- processes., *Glob. Planet. Change*, 58, 1–118. doi:10.1016/j.gloplacha.2007.02.008.
48. Cocco, M., and J. R. Rice (2002), Pore pressure and poroelasticity effects in Coulomb stress analysis of earthquake interactions, *J. Geophys. Res.*, 107, B2, 10.1029/2000JB000138.
 49. Cocco, M., S. Hainzl, F. Catalli, B. Enescu, A. M. Lombardi, and J. Wossner (2010), Sensitivity study of forecasted aftershock seismicity based on coulomb stress calculation and rate- and state- dependent frictional response, *J. Geophys. Res.*, 115, B05307, doi:10.1029/2009JB006838.
 50. Comninakis, P. E., and B. C. Papazachos (1980), Space and time distribution of the intermediate focal depth earthquakes in the Hellenic Arc, *Tectonophysics*, 70, T35-T47.
 51. Console, R., and M. Murru (2001), A simple and testable model for earthquake clustering, *J. Geophys. Res.*, 106, 8699– 8711.
 52. Console, R., M. Murru, and A. M. Lombardi (2003), Refining earthquake clustering models, *J. Geophys. Res.*, 108, 2468, doi:10.1029/2002 JB002130.
 53. Console, R., M. Murru, and F. Catalli (2006), Physical and stochastic models of earthquake clustering, *Tectonophysics*, 417, 141-153.
 54. Console, R., D.A. Rhoades, M. Murru, F. F. Evison, E. E. Papadimitriou, and V. G. Karakostas (2006), Comparative performance of time-invariant, long-range and short-range forecasting models on the earthquake catalogue of Greece, *J. Geophys. Res.*, 111, B09304; doi: 10.1029/2005JB004113.
 55. Console, R., and F. Catalli (2006), A rate-state model for aftershock triggered by dislocation on a rectangular fault: a review and new insights, *Ann. Geophys.*, 49, 1259-1273.
 56. Console, R., M. Murru, F. Catalli, and G. Falcone (2007), Realtime forecasts through an earthquake clustering model constrained by the

- rate-and-state constitutive law: Comparison with a purely stochastic ETAS model, *Seismol. Res. Lett.*, 78, 49-56.
57. Console, R., M. Murru, and G. Falcone (2010), Probability gains of an epidemic-type aftershock sequence model in retrospective forecasting of $M \geq 5$ earthquakes in Italy, *J. Seismol.*, 14, 9-26; doi: 10.1007/s10950-009-9161-3.
 58. Console, R., M. Murru, and G. Falcone (2010), Perturbation of earthquake probability for interacting faults by static Coulomb stress changes, *J. Seismol.*, 14, 67-77, doi: 10.1007/s10950-008-9149-4.
 59. Console, R., M. Murru, and G. Falcone (2010), Retrospective forecasting of $M \geq 4.0$ earthquake in New Zealand, in Seismogenesis and Earthquake Forecasting: The Frank Evison Volume, *Pure Appl. Geophys.*, doi: 10.1007/s00024-010-0068-2.
 60. Console, R., D. D. Jackson, and Y. Y. Kagan (2010), Using the ETAS model for catalog declustering and seismic background assessment, *Pure Appl. Geophys.*, 167, 819-830.
 61. Console, R., G. Falcone, V. Karakostas, M. Murru, E. Papadimitriou, and D. Rhoades (2013), Renewal models and co-seismic stress transfer in the Corinth Gulf, Greece, fault system, *J. Geophys. Res.*, 118, 3655-3673.
 62. Corral, A. (2003), Local distributions and rate fluctuations in a unified scaling law for earthquakes, *Phys. Rev. Lett.*, 68, doi: 10.1103/PhysRevE.68.035102.
 63. Cornell, A. C. (1968), Engineering Seismic Risk Analysis, *Bull. Seismol. Soc. Am.*, 58, 1583-1606.
 64. Correig, A. M., M. Urquizú, J. Vila, and S. C. Manrubia (1997), Aftershock series of event February 18, 1996: An interpretation in terms of self-organized criticality, *J. Geophys. Res.*, 102, 27407-27420.

65. Çiftçi, N.B., and E. Bozkurt (2009), Pattern of normal faulting in the Gediz Graben, SW Turkey, *Tectonophysics* 473, 234-260, doi: 10.1016/j.tecto.2008.05.036.
66. Davis, S. D., and C. Frohlich (1991), Single-link cluster analysis, synthetic earthquake catalogs and aftershock identification, *Geophys. J. Int.*, 104, 289–306.
67. Davies, R., P. England, B. Parsons, H. Billiris, D. Paradissis, and G. Veis (1997), Geodetic strain of Greece in the interval 1892– 1992, *J. Geophys. Res.*, 102, 24,571– 24,588.
68. Deniz, A., and M. S. Yüçemen (2010), Magnitude conversion problem for the Turkish earthquake data, *Nat. Hazards*, 55, 333-352.
69. Dieterich, J. H. (1979), Modeling of rock friction, I, experimental results and constitutive equations, *J. Geophys. Res.*, 84, 2161-2168.
70. Dieterich, J. H. (1994), A constitutive law for rate of earthquake production and its application to earthquake clustering, *J. Geophys. Res.*, 99, 2601–2618.
71. Dieterich, J. H., and B. Kilgore (1996), Implications of fault constitutive properties for earthquake prediction, *Proc. Natl. Acad. Sci.*, 93, 3787-3794.
72. Dieterich, J. H., V. Cayol, and P. Okubo (2000), The use of earthquake rate changes as a stress meter at Kilauea volcano, *Nature*, 408, 457-460.
73. Dieterich, J. H., V. Cayol, and P. Okubo (2003), Stress changes before and during the Puo-Kupaianaha eruption, *U.S. Geol. Surv. Prof. Pap.*, 1676, 187-202.
74. Doutsos T., N. Kontopoulos, and G. Poulimenos (1988), The Corinth–Patras rift as the initial stage of continental fragmentation behind an active island arc (Greece), *Basin Res*, 1, 177–190.
75. Drakatos, G., J. Latoussakis, and J. Drakopoulos (1994), Some Features of Aftershock Pattern in Cephalonia Island (Greece) Region, *2nd workshop*

- statistical models and methods in seismology applications on prevention and forecasting of earthquakes*, Cephalonia 2-5 June, 1993.
76. Drakatos, G., and J. Latoussakis (1996), Some Features of Aftershock Patterns in Greece, *Geophys. J. Int.*, 126, 123-134.
 77. Drakatos, G. (2000), Relative Seismic Quiescence before Large Aftershocks, *Pure Appl. Geophys.*, 157, 1407-1421.
 78. Drakos, A. G., C. S. Stiros, and A. A. Kiratzi (2001), Fault Parameters of the 1980 ($M_w=6.5$) Volos, Central Greece, Earthquake from Inversion of Repeated Leveling Data, *Bull. Seismol. Soc. Am.*, 91, 1673-1684.
 79. Du, W. -X., and L. R., Sykes (2001), Changes in frequency of moderate-size earthquakes and coulomb Failure stress before and after the Landers, California, earthquake of 1992, *Bull. Seismol. Soc. Am.*, 91, 725-738.
 80. Efron, B., and R. J. Tibshirani (1993), *An Introduction to the Bootstrap*, CRC Press, Boca Raton, Fla.
 81. Elsworth, W. L., A. G. Lindth, W. H. Prescott, and D. G. Herd (1981), *The 1906 San Francisco earthquake and the seismic cycle*, in *Earthquake Prediction: An International Review* (eds. Simpson, D. W. and P. G., Richards), (AGU, Washington, D. C. 1981), 126-140 pp.
 82. Erickson, L. (1986), *User's manual for DIS3D: a three-dimensional dislocation program with applications to faulting in the Earth*. Master's thesis, Stanford University, Stanford, CA, 167 pp.
 83. Evison, F., and D. Rhoades (1998), Long-term seismogenic process for major earthquakes in subduction zones, *Phys. Earth. Planet. Inter.*, 108, 185-199.
 84. Evison, F., and D. Rhoades (2000), The precursory earthquake swarm in Greece, *Ann. Geofis.*, 43, 991-1009.

85. Evison, F. F., and D. A. Rhoades (2002), Precursory scale increase and long term seismogenesis in California and northern Mexico, *Ann. Geophys.*, 45, 479-495.
86. Evison, F. F., and D. A. Rhoades (2004), Long term seismogenesis and self-organized criticality, *Earth Planets Space*, 56, 749-760.
87. Falcone G., R. Console, and M. Murru (2010), Short-term and long term earthquake occurrence models for Italy: ETES, ERS and LTST, *Ann. Geophys.*, 53, doi:10.4401/ag-4760.
88. Fedotov, S. A. (1965), The seismic cycle, quantitative seismic zoning, and long-term seismic forecasting, in *Seismic Zoning of the USSR*, eds. Medvedev, S. A., Moscow: Izdatel'stvo "Nauka", 1968.
89. Felzer, K. R., T. W. Becker, R. E. Abercrombie, G. Ekström, and J. R. Rice (2002), Triggering of the 1999 M_w 7.1 Hector Mine earthquake by aftershocks of the 1992 M_w 7.3 Landers earthquake, *J. Geophys. Res.*, 107, 2190, doi:10.1029/2001JB000911.
90. Felzer, K. R., and E. E. Brodsky (2005), Testing the stress shadow hypothesis, *J. Geophys. Res.*, 110, B05S09, doi:10.1029/2004JB003277.
91. Felzer, K. R., and E. E. Brodsky (2006), Decay of aftershock density with distance indicates triggering by dynamic stress, *Nature*, 441, 735-738.
92. Felzer, K. R. (2008), Calculating California Seismicity Rates (Appendix I), USGS Open File Report 2007-1437I, CGS *Special Report 203I*, SCEC *Contribution #1138I*, Version 1.0.
93. Flerit F., R. Armijo, G. King, and M. Bertrand (2004), The mechanical interaction between the propagating North Anatolian Fault and the back-arc extension in the Aegean, *Earth Planet. Sci. Lett.*, 224, 347-362.
94. Frankel, A. F., C. Mueller, T. Barnhard, D. Perkins, E. V. Leyendecker, N. Dickman, S. Hanson, and M. Hopper (1996), *National seismic hazard maps* (USGS Open-File Report 1996), 96-532.

95. Frohlich, C., and S. D. Davis (1990), Single link cluster analysis as a method to evaluate spatial and temporal properties of earthquake catalogs, *Geophys. J. Int.*, 100, 19-32.
96. Fuller, W. A. (1987), *Measurement Error Models*, Wiley, New York, NY, 440 pp.
97. Ganas, A., G. Drakatos, S. B. Pavlides, G. N. Stavrakakis, M. Ziazia, E. Sokos, and V. K. Karastathis (2005), The 2001 Mw=6.4 Skyros earthquake, conjugate strike-slip faulting and spatial variation in stress within the central Aegean Sea, *J. Geodyn.*, 39, 61-77.
98. Ganas, A., K. Chousianitis, E. Batsi, M. Kolligri, A. Agalos, G. Chouliaras, and K. Makropoulos (2012), The January 2010 Efpalion earthquakes (Gulf of Corinth, Central Greece): earthquake interactions and blind normal faulting, *J. Seismol.*, doi: 10.1007/s10950-012-9331-6.
99. Gardner, J., and L. Knopoff (1974), Is the sequence of earthquakes in Southern California, with aftershock Removed, Poissonian?, *Bull. Seismol. Soc. Am.*, 64, 1363-1367.
100. Genç, C.Ş., Ş. Altunkaynak, Z. Karacık, M. Yazman, and Y. Yılmaz (2001), The Çubukludağ graben, south of İzmir: its tectonic significance in the Neogene geological evolution of the western Anatolia, *Geodin. Acta*, 14, doi: 10.1016/S0985-3111(00)01061-5.
101. Ghimire, S., K. Katsumata, and M. Kasahara (2008), Spatio-temporal evolution of Coulomb stress in the Pacific slab inverted from the seismicity rate change and its tectonic interpretation in Hokkaido, Northern Japan, *Tectonophysics*, 455, 25-42.
102. Gomberg, J., N. Beeler, and M. Blanpied (2000), On rate-state and Coulomb failure models, *J. Geophys. Res.*, 105, 7857-7871.
103. Gomberg, J. (2001), The failure of earthquake failure models, *J. Geophys. Res.*, 106, 16253-16263.

104. Gomberg, J., P. Bodin, and P. A. Reasenberg (2003), Observing earthquakes triggered in the near field by dynamic deformations, *Bull. Seismol. Soc. Am.*, 93, 118-138.
105. Gomberg, J., M. E. Belardinelli, M. Cocco, and P. Reasenberg (2005), Time-depended earthquake probabilities, *J. Geophys. Res.*, 110, B05S04, doi:10.1029/2004JB003405.
106. Gomberg, J., P. Reasenberg, M. Cocco, and M. E. Belardinelli (2005), A frictional population model of seismicity rate change, *J. Geophys. Res.*, 110, B05S03, doi:10.1029/2004JB003404.
107. Govers, R., and M. J. R. Wortel (2005), Lithosphere tearing at STEP faults: Response to edges of subduction zones, *Earth Planet. Sci. Lett.*, 236, 505-523.
108. Guatteri, M., P. Spudich, and G. Beroza (2001), Inferring rate and state friction parameters from a rupture model of the 1995 Hyogo-ken Nanbu (Kobe) Japan earthquake, *J. Geophys. Res.*, 106, 26,511–26,522, doi:10.1029/2001JB000294.
109. Habermann, R. E. (1981), *Precursory seismicity patterns: Stalking the mature seismic gap*, in *Earthquake prediction - An international review*, edited by D. W. Simpson and P. G. Richards, 29 - 42, American Geophysical Union, Washington, D. C.
110. Habermann, R. E. (1983), Teleseismic detection in the Aleutian island arc, *J. Geophys. Res.*, 88, 5056-5064.
111. Habermann, R. E., and M. Wyss (1984), Background seismicity rates and precursory seismic quiescence: Imperial Valley, California, *Bull. Seismol. Soc. Am.*, 74, 1743–1755.
112. Hagiwara, Y. (1974), Probability of earthquake occurrence as obtained from a Weibull distribution analysis of crustal strain, *Tectonophysics*, 23, 313-318.

113. Hainzl, S., and Y. Ogata (2005), Detecting fluid signals in seismicity data through statistical earthquake modeling, *J. Geophys. Res.*, 110, doi:10.1029/2004JB003247.
114. Hainzl, S., and T. Kraft (2006), Analysis of complex seismicity pattern generated by fluid diffusion and aftershock triggering, *paper presented at the 4th International Workshop on Statistical Seismology (STATSEI4), Inst. of Stat. Math.*, 9-13 January 2006, Kanagawa, Japan.
115. Hainzl, S., B. Enescu, M. Cocco, J. Woessner, F. Catalli, R. Wang, and F. Roth (2009), Aftershock modeling based on uncertain stress calculations, *J. Geophys. Res.*, 114, doi:10.1029/2008JB006011.
116. Hainzl, S., S. Steacy, and D. Marsan (2010), Seismicity models based on Coulomb stress calculations, *Community Online Resource for Statistical Seismicity Analysis*, doi:10.5078/corssa-32035809. Available at <http://www.corssa.org>.
117. Hainzl, S., G. B. Brietzke, and G. Zöller (2010), Quantitative earthquake forecasts resulting from static stress triggering, *J. Geophys. Res.*, 115, doi:10.1029/2010JB007473.
118. Hainzl, S., G. Zoller, and R. Wang (2010), Impact of the receiver fault distribution on aftershock activity, *J. Geophys. Res.*, 115, doi:10.1029/2008JB006224.
119. Hainzl, S., Y. Ben-Zion, C. Cattania, and J. Wassermann (2013), Testing atmospheric and tidal earthquake triggering at Mt. Hochstaufen, Germany, *J. Geophys. Res.*, 118, 1-11.
120. Hall, P., S. J. Sheather, M. C. Jones, and J. S. Marron (1991), On optimal data-based bandwidth selection in kernel density estimation, *Biometrika*, 78, 263-269.
121. Hardebeck, J. L., J. J. Nazareth, and E. Hauksson (1998), The static stress change triggering model: constraints from two southern California aftershock sequences, *J. Geophys. Res.*, 103, 24 427–24 437.

122. Hardebeck, J. L. (2004), Stress triggering and earthquake probability estimates, *J. Geophys. Res.*, 109, B04310, doi:10.1029/2003JB002437.
123. Harris, R. A. (2000), Earthquake stress triggers, stress shadows, and seismic hazard, *Curr. Science*, 79, 1215-1225.
124. Harris, R. A., and R. W. Simpson (1998), Suppression of large earthquakes by stress shadows: A comparison of Coulomb and Rate/State failure, *J. Geophys. Res.*, 103, 24,439–24,451.
125. Hatzidimitriou P. M., E. E. Papadimitriou, D. M. Mountrakis, and B. C. Papazachos (1985), The seismic parameter b of the frequency-magnitude relation and its association with the geological zones in the area of Greece, *Tectonophysics*, 120, 141-151.
126. Hatzfeld D., G. Pedotti, P. Hatzidimitriou, and K. Makropoulos (1990), The strain pattern in the western Hellenic arc deduced from a microearthquake survey. *Geophys. J. Int.*, 101, 181–202.
127. Hatzfeld, D., and C. Martin (1992), Intermediate depth seismicity in the Aegean defined by teleseismic data, *Earth Planet. Sci. Lett.*, 113, 267– 275.
128. Hatzfeld D., D. Kementzetzidou, V. Karakostas, M. Ziazia, S. Nothard, D. Diagourtas, A. Deshamps, G. Karakaisis, P. Papadimitriou, M. Scordilis, R. Smith, N. Voulgaris, A. Kiratzi, K. Makropoulos, M. Bouin, and P. Bernard (1996), The Galaxidi earthquake sequence of November 18, 1992: a possible geometrical barrier within the normal fault system of the Gulf of Corinth (Greece), *Bull. Seismol. Soc. Am.*, 86, 1987–1991.
129. Hatzfeld, D., M. Ziazia, D. Kementzetzidou, P. Hatzidimitriou, D. Panagiotopoulos, K. Makropoulos, P. Papadimitriou, and A. Deschamps (1999), Microseismicity and focal mechanisms at the western termination of the North Anatolian Fault and their implications for continental tectonics, *Geophys. J. Int.*, 137, 891–908.
130. Hatzfeld, D., V. Karakostas, M. Ziazia, I. Kassaras, E. Papadimitriou, K. Makropoulos, N. Voulgaris, and Ch. Papaioannou (2000),

- Microseismicity and faulting geometry in the Gulf of Corinth (Greece), *Geophys. J. Int.*, 141, 438-456.
131. Helmstetter, A., and D. Sornette (2003), Importance of direct and indirect triggered seismicity in the ETAS model of seismicity, *Geophys. Res. Lett.*, 30, 1576, doi:10.1029/2003GL017670.
 132. Helmstetter, A., and D. Sornette (2003), Foreshocks explained by cascades of triggered seismicity, *J. Geophys. Res.*, 108, 2457, doi:10.1029/2003JB002409.
 133. Helmstetter, A., and D. Sornette (2003), Predictability in the Epidemic-Type aftershock sequence model of interacting triggered seismicity, *J. Geophys. Res.*, 108, 2482, doi:10.1029/2003JB002485.
 134. Helmstetter, A., and B. E. Shaw (2005), Estimating stress heterogeneity from aftershock rate, *J. Geophys. Res.*, 110, B05S08, doi:10.1029/2004JB003286.
 135. Helmstetter, A., Y. Kagan, and D. Jackson (2006), Comparison of short-term and time-independent earthquake forecast models for southern California, *Bull. Seism. Soc. Am.*, 96, 90–106.
 136. Helmstetter, A., Y. Kagan, and D. Jackson (2006), Importance of small earthquakes for stress transfers and earthquake triggering, *J. Geophys. Res.*, 110, B05S08, doi:10.1029/2004JB003286.
 137. Helmstetter, A., and B. E. Shaw (2006), Relation between stress heterogeneity and aftershock rate in the rate-and-state model, *J. Geophys. Res.*, 111, doi:10.1029/2005JB004077.
 138. Helmstetter, A., and B. E. Shaw (2009), Afterslip and aftershocks in the rate-and-state friction law, *J. Geophys. Res.*, 114, B01308, doi:10.1029/2007JB005077.
 139. Herrero, A., and P. Bernard (1994), A kinematic self-similar rupture process for earthquakes, *Bull. Seismol. Soc. Am.*, 84, 1216-1228.

140. Hollenstein, C., A. Geiger, H. -G. Kahle, and G. Veis (2006), CGPS time series and trajectories of crustal motion along the West Hellenic arc, *Geophys. J. Int.*, 164, 182–191, doi:10.1111/j.1365-246X.2005.02804.
141. Hollenstein, Ch., M. D. Müller, A. Geiger, and H. –G. Kahle (2008), GPS-Derived coseismic displacements associated with the 2001 Skyros and 2003 Lefkada earthquakes in Greece, *Bull. Seismol. Soc. Am.*, 98, 149-161.
142. Imamura, A. (1937), *Theoretical and applied seismology*, (Maruzen, Tokyo).
143. Inan, S., S. Ergintav, R. Saatçılar, B. Tüzel, and Y. İravul (2007), Turkey makes major investment in earthquake research, *EOS Trans. Am. Geophys. Union*, 88, 333-334.
144. Jackson, J. A., and D. P. McKenzie (1988), The relationship between plate motions and seismic tensors and the rate of active deformation in the Mediterranean and Middle East., *Geophys. J. Int.*, 93, 45–73.
145. Jacobs, K. M., E. G. C. Smith, M. K. Savage, and J. Zhuang (2013), Cumulative rate analysis (CURATE): A clustering algorithm for swarms dominated catalogs, *J. Geophys. Res.*, 118, 553-569.
146. Jansky J., O. Novotny, V. Plicka, J. Zahradnik, and E. Sokos (2011), Earthquake location from P-arrival times only: problems and some solutions. *Stud. Geophys. Geod.*, 56, doi:10.1007/s11200-011-9036-2.
147. Jaumé, S. C., D. Weatherley, and P. Mora (2000), Accelerating seismic energy release and evolution of event time and size statistics: Results from two heterogeneous cellular automaton models, *Pure Appl. Geophys.*, 157, 2209-2226.
148. Jolivet, L., J. P. Brun, P. Gautier, S. Lallemand, and M. Patriat (1994), 3D-kinematics of extension in the Aegean region from the early Miocene to the present, insights from the ductile crust, *Bull. Soc. Geol. Fr.*, 165, 195-209.
149. Jones, L. M., and E. Hauksson (1997), The seismic cycle in southern California: Precursor or response?, *Geophys. Res. Lett.*, 24, 469-472.

150. Kagan, Y. Y. (1991), Likelihood analysis of earthquake catalogues, *Geophys. J. Int.*, 106, 135–148.
151. Kagan, Y. Y. (2005), Earthquake slip distribution: A statistical model, *J. Geophys. Res.*, 110, B05S11, doi:10.1029/2004JB003280, 1–15.
152. Kaneko, Y., and N. Lapusta (2008), Variability of earthquake nucleation in continuum models of rate-and state faults and implications for aftershock rates, *J. Geophys. Res.*, 113, doi:10.1029/2007JB005154.
153. Karagianni, E., P. Paradisopoulou, and V. Karakostas (2013), Spatio-temporal earthquake clustering in the Western Corinth Gulf, *Bull. Seismol. Soc. Greece*, XLVII, 2013.
154. Karakostas, V. G., E. E. Papadimitriou, G. F. Karakaisis, C. B. Papazachos, E. M. Skordilis, G. Vargemezis, and E. Aidona (2003), The 2001 Skyros, northern Aegean, Greece, earthquake sequence: off – fault aftershocks, tectonic implications, and seismicity triggering, *Geophys. Res. Lett.*, 30, doi:10.1029/2002gl015814.
155. Karakostas, V. G., E. E. Papadimitriou, and C. B. Papazachos (2004), Properties of the 2003 Lefkada, Ionian Islands, Greece, earthquake seismic sequence and seismicity triggering, *Bull. Seismol. Soc. Am.*, 95, 1976-1981.
156. Karakostas, V. (2008), Seismicity rate changes in association with the pre-stress field, *3rd National Conference of and seismic protection and engineering seismology*, 5-7 November, 2008.
157. Karakostas, V. (2009), Seismicity patterns before strong earthquakes in Greece, *Acta Geophys.*, 57, 367-386.
158. Karakostas, V. G., and E. E. Papadimitriou (2010), Fault complexity associated with the 14 August 2003 Mw6.2 Lefkada, Greece, aftershock sequence, *Acta Geophys.*, doi: 10.2478/s11600-010-0009-6.
159. Karakostas, V. G., E. E. Papadimitriou, M. D. Tranos, and B. C. Papazachos (2010), Active seismotectonic structures in the area of Chios

- island, north Aegean sea, revealed from microseismicity and fault plane solutions, *Bull. Geolog. Soc. Greece*, 4, 2064-2074.
160. Karakostas, V., E. Karagianni, and P. Paradisopoulou (2012), Space-time analysis, faulting and triggering of the 2010 earthquake doublet in western Corinth Gulf, *Nat. Hazards*, 63, 1181-1202.
 161. Karakostas, V., E. Papadimitriou and D. Gospodinov (2014), Modelling the 2013 North Aegean (Greece) seismic sequence: geometrical and frictional constraints, and aftershock probabilities, *Geophys. J. Int.*, doi: 10.1093/gji/ggt523.
 162. Kellis-Borok, V. I., and V. G. Kossobokov (1986), Time of increased probability for the great earthquakes of the world, *Computational Seismology*, 19, 45–58.
 163. Kijko, A., and G. Graham (1998), Parametric-historic procedure for probabilistic seismic hazard analysis, Part I. Estimation of maximum regional magnitude m_{max} , *Pure Appl. Geophys.*, 152, 413-442.
 164. Kijko, A., and G. Graham (1999), Parametric-historic procedure for probabilistic seismic hazard analysis, Part II. Assessment of seismic hazard at specified site, *Pure Appl. Geophys.*, 154, 1-22.
 165. Kijko, A., S. Lasocki, and G. Graham (2001), Nonparametric seismic hazard analysis in mines, *Pure Appl. Geophys.*, 158, 1655-1676.
 166. Kijko, A., and A. Smit (2012), Extension of the Aki-Utsu b-value estimator for incomplete catalogs, *Bull. Seismol. Soc. Am.*, 102, 1283-1287.
 167. Kilb, D., J. Gomberg, and P. Bodin (1998), Aftershock triggering by dynamic and static Coulomb stress changes, *EOS (suppl.)*, 79, F647.
 168. Kilb, D., J. Gomberg, and P. Bodin (2000), Triggereing of earthquake aftershocks by dynamic stresses, *Nature*, 408, 570-574.
 169. Kilb, D., J. Gomberg, and P. Bodin (2002), Aftershock triggering by complete dynamic and static Coulomb stress changes, *J. Geophys. Res.*, 107, B4, 2060, 10.1029/2001JB000202

170. King, G. C. P., A. Hubert–Ferrari, S. S. Nalbant, B. Meyer, R. Armijo, and D. Bowman (2001), Coulomb interactions and the 17 August, 1999 Izmit, Turkey earthquake, *Earth Planet. Sci. Lett.*, 333, 557–569.
171. Kiratzi, A. A., G. S. Wagner, and C. A. Langston (1991), Source parameters of some large earthquakes in Northern Aegean determined by body waveform Inversion, *Pure Appl. Geophys.*, 135, 515-527.
172. Kiratzi, A. A., and E. Louvari (2001), Source parameters of the Izmit–Bolu 1999 (Turkey) earthquake sequences from teleseismic data, *Ann. Geofis.*, 44, 33–47.
173. Kiratzi, A., and E. Louvari (2003), Focal mechanisms of shallow earthquakes in the Aegean Sea and the surrounding lands determined by waveform modelling: a new database, *J. Geodyn.*, 36, 251-274.
174. Kiratzi, A., and N. Svirgkas (2013), A study of the 8 January 2013 Mw5.8 earthquake sequence (Lemnos Island, East Aegean Sea), *Tectonophysics*, 608, 452-460.
175. Kossobokov, V. G., V. I. Keilis-Borok, D. L. Turcotte, and B. D. Malamud (2000), Implications of a statistical physics approach for earthquake hazard assessment and forecasting, *Pure Appl. Geophys.*, 157, 2323-2349.
176. Kosteletzky, J., and J. Dousa (2012), Results of geodetic measurements during the January 2010 Efpalio earthquakes at the western tip of the Gulf of Corinth, central Greece, *Acta Geodyn. Geomater.*, 9, 291-301.
177. Kostrov, V. V. (1974), Seismic moment and energy of earthquakes, and seismic flow of rock, *Earth Phys.*, 1, 23-40.
178. Kurt, H., E. Demirbağ, and İ. Kuşçu (1999), Investigation of the submarine active tectonism in the Gulf of Gökova, southwest Anatolia – southeast Aegean Sea, by multi-channel seismic reflection data, *Tectonophysics*, 305, 477-496.

179. Laigle, M., A. Hirn, M. Sachpazi, and N. Roussos (2000), North Aegean crustal deformation: An active fault imaged to 10 km depth by reflection data, *Geology*, 28, 71–74.
180. Lasocki, S., and E. E. Papadimitriou (2006), Magnitude distribution complexity revealed in seismicity from Greece, *J. Geophys. Res.*, 111, B11309, doi:10.1029/2005JB003794.
181. Lasocki, S., and B. Orlecka-Sikora (2008), Seismic hazard assessment under complex source size distribution of mining-induced seismicity, *Tectonophysics*, 456, 28-37.
182. Latoussakis, J., and G. Drakatos (1994), A Quantitative Study of Some Aftershock Sequences in Greece, *Pure Appl. Geophys.*, 143, 603-616.
183. Latoussakis, J., G. Stavrakakis, J. Drakopoulos, D. Papanastasiou, and G. Drakatos (1991), Temporal Characteristics of Some Earthquake Sequences in Greece, *Tectonophysics*, 193, 299-310.
184. LePichon, X., and J. Angelier (1979), The Hellenic arc and trench system: A key to the neotectonic evolution of the eastern Mediterranean area, *Tectonophysics*, 60, 1-42.
185. Leptokaropoulos, K. M., B. E. E. Papadimitriou, Orlecka-Sikora, and V. G. Karakostas (2012), Seismicity rate changes in association with the evolution of the stress field in northern Aegean Sea, Greece, *Geophys. J. Int.*, 188, 1322–1338.
186. Leptokaropoulos, K. M., V. G. Karakostas, E. E. Papadimitriou, A. K. Adamaki, O. Tan, and S. İnan (2013), A homogeneous earthquake catalogue compilation for western turkey and magnitude of completeness determination, *Bull. Seismol. Soc. Am.*, 103, 5, 2739-2751.
187. Leptokaropoulos, K. M., E. E. Papadimitriou, B. Orlecka-Sikora, and V. G. Karakostas (2014), Forecasting seismicity rates in western Turkey as inferred from earthquake catalog and stressing history, *Nat. Hazards*, doi: 10.1007/s11069-014-1181-9.

188. Leptokaropoulos, K. M., E. E. Papadimitriou, B. Orlecka-Sikora, V. G. Karakostas, and F. Vallianatos, (2014), Time dependent earthquake occurrence rates along the Hellenic arc, *Bull Seismol. Soc. Am.*, 104, doi: 10.1785/0120130298
189. Leptokaropoulos K. M., E. E. Papadimitriou, B. Orlecka-Sikora, and V. Karakostas (2014), Evaluation of Coulomb Stress Changes from Earthquake Productivity Variations in Western Corinth Gulf, Greece, (*Submitted in Pure Appl. Geophys., Under Revision*)
190. Lin, J., and R. S. Stein (2004), Stress triggering in thrust and subduction earthquakes and stress interaction between the southern San Andreas and nearby thrust and strike slip faults, *J. Geophys. Res.*, 109, B02303, doi:10.1029/2003JB002607.
191. Linker, J., and J. Dieterich (1992), Effects of variable normal stress on rock friction: Observations and constitutive equations, *J. Geophys. Res.*, 97, 4923–4940, doi:10.1029/92JB00017.
192. LLenos, A. L., J. J. McGuire, and Y. Ogata (2009), Modeling seismic swarms triggered by aseismic transients, *Earth Planet. Sci. Lett.*, 281, 59-69.
193. Lockner, D. A., and N. M. Beeler (1999), Premonitory slip and tidal triggering of earthquakes, *J. Geophys. Res.*, 104, 20,133-20,151.
194. Lolli, B., and P. Gasperini (2012), A comparison among general orthogonal regression methods applied to earthquake magnitude conversions, *Geophys. J. Int.*, 190, 1,135-1,151.
195. Lombardi, A. M. (2003), The maximum likelihood estimator of b-value for mainshocks, *Bull Seismol. Soc. Am.*, 93, 2082+2088.
196. Lombardi, A. M., M. Cocco, and W. Marzocchi (2010), On the increase of background seismicity rate during the 1997-1998 Umbria-Marche, central Italy, sequence: Apparent variation of fluid driven triggering?, *Bull. Seismol. Soc. Am.*, 100, 3, 1138-1152.

197. Louvari, E., A. A. Kiratzi, and B. C. Papazachos (1999), The Cephalonia Transform fault and its extension to western Lefkada Island (Greece), *Tectonophysics*, 308, 223–236.
198. Louvari, E. (2000), *A detailed seismotectonic study in the Aegean Sea and the surrounding area with emphasis on the information obtained from microearthquakes*. PhD Thesis, Aristotle Univ., Thessaloniki, Greece, 373 pp.
199. Lyon-Caen H, P. Papadimitriou, A. Deschamps, P. Bernard, K. Makropoulos, F. Pacchiani, and G. Patau (2004), First results of the CRLN seismic network in the western Corinth Rift: evidence for old-fault reactivation. *C. R. Geosci.*, 336,343–351.
200. Ma, K. F., C. H. Chan, and R. S. Stein (2005), Response to seismicity to Coulomb stress triggers and shadows of the 1999 $M_w=7.6$ Chi-Chi, Taiwan, earthquake, *J. Geophys. Res.*, 110, B05S19, doi:10.1029/2004JB003389.
201. Maccaferri, F., E. Rivalta, L. Passarelli, and S. Jónsson (2013), The stress shadow induced by the 1975-1984 Krafla rifting episode, *J. Geophys. Res.*, 118, 1109-1121.
202. Maeda, K., and S. Wiemer (1999), Significance test for seismicity rate changes before the 1987 Chiba-Toho-Okai earthquake ($M6.7$) Japan, *Ann. Geofis.*, 42, 833-850.
203. Mallman, E. P., and M. D. Zoback (2007), Assessing elastic Coulomb stress transfer models using seismicity rates in southern California and southern Japan, *J. Geophys. Res.*, 112, B03304, doi:10.1029/2005JB004076.
204. Mallman, E. P., and T. Parsons (2008), A global search for stress shadows, *J. Geophys. Res.*, 113, B12304, doi:10.1029/2007JB005336.
205. Margaris, V. N., N. P. Theodoulidis, Ch. A. Papaioannou, and B. C. Papazachos (1990), Strong motion duration of earthquakes in Greece, *in Proceedings of the XXII Gen. Assembly ESC*, vol. 2, 865-870.

206. Marsan, D. (2003), Triggering of seismicity at short time scales following Californian earthquakes, *J. Geophys. Res.*, 108, B52266, doi:10.1029/2002JB001946.
207. Marsan, D., and S. S. Nalbant (2005), Methods for measuring seismicity rate changes: A review and a study of how the m-w 7.3 Landers earthquake affected the aftershock sequence of the m-w 6.1 Joshua Tree earthquake, *Pure Appl. Geophys.*, 162, 1151-1185.
208. Marsan, D., and O. Lengliné (2008), Extending earthquake's reach through cascading, *Science*, 319, 1076-1079.
209. Marsan, D., and M. Wyss (2010), Models and techniques for analyzing seismicity, *Community Online Resource for Statistical Seismicity Analysis*, doi:10.5078/corssa-25837590., Available at <http://www.corssa.org>.
210. Marzocchi, W., and L. Sandri (2003), A review and new insights on the estimation of the b-value and its uncertainty, *Ann. Geophys.*, 46, 1271-1282.
211. Marzocchi, W., J. Selva, A. Piersanti, and E. Boschi (2003), On the long-term interaction among earthquakes: Some insight from a model simulation, *J. Geophys. Res.*, 108, 2538, doi:10.1029/2003JB002390.
212. Marzocchi, W., and A. M. Lombardi (2008), A double branching model for earthquake occurrence, *J. Geophys. Res.*, doi:10.1029/2007JB005472.
213. Matsu'ura, S. R. (1986), Precursory quiescence and recovery of aftershock activities before some large aftershocks, *Bull. Earth. Res. Inst.*, 61, 1-65.
214. Matthews, M. V., and P. A. Reasenber (1988), Statistical methods for investigating quiescence and other temporal seismicity patterns, *Pure Appl. Geophys.*, 126, 357-372.
215. McClusky, S., S. Balassanian, A. Barka, C. Demir, S. Ergintav, I. Georgiev, O. Gurkan, M. Hamburger, K. Hurst, H. Kahle, K. Kastens, G. Kekelidze, R. King, V. Kotzev, O. Lenk, S. Mahmoud, A. Mishin, M.

- Nadariya, A. Ouzounis, D. Paradissis, Y. Peter, M. Prilepin, R. Reilinger, I. Sanli, H. Seeger, A. Tealeb, M. N. Toksöz, and G. Veis (2000), Global Positioning System constraints on plate kinematics and dynamics in the eastern Mediterranean and Caucasus, *J. Geophys. Res.*, 105, 5695-5719.
216. McGuire, R. K. (2004), *Seismic hazard and risk analysis*, Earthquake Engineering research institute, Oakland, California, 240 pp.
217. McKenzie, D. P. (1970), The plate tectonics of the Mediterranean region, *Nature*, 226, 271–299.
218. McKenzie, D. P. (1972), Active tectonics of the Mediterranean region, *Geophys. J. R. astr. Soc.*, 30, 109-185.
219. McKenzie, D. P. (1978), Active tectonics of the Alpine-Himalayan belt: the Aegean Sea and surrounding regions, *Geophys. J. R. astr. Soc.*, 55, 217-254.
220. Mesimeri, M, E. Papadimitriou, V. Karakostas, and G. Tsaklidis (2013), Earthquake clusters in NW Peloponnese, *Bull. Seismol. Soc. Greece*, XLVII, 2013.
221. Messini, A. D., E. E. Papadimitriou, V. G. Karakostas, and I. Baskoutas (2007), Stress interaction between thrust faults along the SW Hellenic Arc (Greece), *Bull. Geolog. Soc. Greece*, 40, 386-398.
222. Mignan, A., D. D. Bowman, and G. P. C. King (2006), An observational test of the origin of accelerating moment release before large earthquakes, *J. Geophys. Res.*, 111, B11304, doi:10.1029/2006JB004374.
223. Mignan, A., M. J. Werner, S. Wiemer, C.-C. Chen, and Y.-M. Wu (2011), Bayesian estimation of the spatially varying completeness magnitude of earthquake catalogs, *Bull. Seismol. Soc. Am.*, 101, doi:10.1785/0120100223.
224. Mignan, A., and J. Woessner (2012), Estimating the magnitude of completeness for earthquake catalogs, *Community Online Resource for Statistical Seismicity Analysis*, doi:10.5078/corssa-00180805, Available at <http://www.corssa.org>.

225. Mogi, K. (1969), Some features of recent seismic activity in and near Japan, (2) Activity before and after great earthquakes, *Bull. Earthq. Res. Inst.*, 47, 395-417.
226. Mogi, K. (1977), Seismic activity and earthquake prediction, *In Proc. Earthquake Prediction Symp.*, Tokyo, 203-214.
227. Mogi, K. (1981), *Seismicity in western Japan and long term earthquake forecasting*, in *Earthquake Prediction: An International Review*, (eds. Simpson, D. W. and P. G., Richards), (AGU, Washington, D. C. 1981), 43-51.
228. Mogi, K. (1985), *Earthquake Prediction*. Tokyo: Academic Press.
229. Molchan, G. M., and O. E. Dmitrieva (1992), Aftershock identification: methods and new approaches, *Geophys. J. Int.*, 109, 501-516.
230. Molchan, G., and T. Kronrod (2005), On the spatial distribution of seismicity rate, *Geophys. J. Int.*, 162, 899-909.
231. Mountrakis, D., A. Kiliadis, S. Pavlides, N. Zouros, N. Spyropoulos, M. Tranos, and N. Soulakelis (1993), Field study of the southern Thessaly highly active fault zone, *Proceedings of the 2nd Congress of the Hellenic Geophysical Union, May 5–8, 1993, Florina, Greece*, 2, 603–614.
232. Mountrakis, D., A. Kiliadis, E. Vavliakis, A. Psilovikos, and E. Thomaidou (2003), Neotectonic map of Samos Island (Aegean Sea, Greece): Implication of Geographical Information Systems in the geological mapping. In: *4th European Congress on Regional Geoscientific Cartography and information Systems, Bologna, Italy*, 11-13.
233. Musmeci, F., and D. Vere-Jones (1992), A space-time clustering model for historical earthquakes, *Ann. Inst. Stat. Math.*, 44, 1–11.
234. Murru, M., R. Console, and G. Falcone (2009). Real-time earthquake forecasting in Italy, *Tectonophysics*, 470, 214-223.

235. Nalbant, S. S., A. Hubert, and G. C. P. King (1998), Stress coupling between earthquakes in northwest Turkey and the north Aegean Sea, *J. Geophys. Res.*, 103, 24,469–24,486.
236. Nocquet, J. M., (2012), Present–day kinematics of the Mediterranean: A comprehensive overview of GPS results. *Tectonophysics*, 579, 220–242.
237. Nostro, C., L. Chiaraluce, M. Cocco, D. Baumont, and O. Scotti (2005), Coulomb stress changes caused by repeated normal faulting earthquakes during the 1997 Umbria-Marche (central Italy) seismic sequence, *J. Geophys. Res.*, 110, B05S20, doi:10.1029/2004JB003386.
238. Novotny, O., E. Sokos, and V. Plicka (2012), Upper crustal structure of the western Corinth Gulf, Greece, inferred from arrival times of the January 2010 earthquake sequence, *Stud. Geophys. Geod.*, 56, 1007-1018, doi: 10.1007/ s11200-011-0482-7.
239. Ocañoğlu, N., E. Demirbag, and İ. Kuşçu (2004), Neotectonic structures in the area offshore of Alaçati, Doğanbey and Kuşadası (western Turkey): evidence of strike-slip faulting in the Aegean extensional province, *Tectonophysics*, 391, doi: 10.1016/j.tecto.2004.07.008.
240. Ogata, Y. (1988), Statistical models for earthquake occurrences and residual analysis for point processes, *J. Am. Stat. Assoc.*, 83, 9-27.
241. Ogata, Y. (1998), Space-time point-process models for earthquake occurrences, *Ann. Inst. Stat. Math.*, 50, 379– 402.
242. Ogata, Y. (2004), Space-time model for regional seismicity and detection of crustal stress changes, *J. Geophys. Res.*, 109, B03308, doi:10.1029/2003 JB002621.
243. Ogata, Y., and K. Katsura (1993), Analysis of the temporal and spatial heterogeneity of magnitude frequency distribution inferred from earthquake catalogs, *Geophys. J. Int.*, 113, 727-738.

244. Ogata, Y., K. Katsura, and M. Tanemura (2003), Modelling heterogeneous space-time occurrences of earthquake and its residual analysis, *Appl. Stat. (J. R. Stat. Soc, Ser. C)*, 52, 499–509.
245. Ogata, Y. (2005), Detection of anomalous seismicity as a stress change sensor, *J. Geophys. Res.*, 110, B05S06, doi:10.1029/2004JB003245.
246. Omori, F. (1894), On the aftershocks of earthquake, *J. Coll. Sci. Imp. Univ. Tokyo*, 7, 11-200.
247. Orlecka-Sikora, B., and S. Lasocki (2005), Nonparametric characterization of mining induced seismic sources, in Proceedings of the Sixth International Symposium on Rockburst and Seismicity in Mines 9 –11 March 2005, Australia, edited by Y. Potvin and M. Hudyma, 555 – 560, *Aust. Cent. for Geomech.*, Nedlands.
248. Pacchiani F, and H. Lyon-Caen (2010), Geometry and spatio-temporal evolution of the 2001 Agios Ioanis earthquake swarm (Corinth Rift, Greece), *Geophys. J. Int.*, 180, 59–72.
249. Palyvos, N., K. Pavlopoulos, E. Froussou, H. Kranis, K. Pustovoytov, S. L. Forman, and D. Minos-Minopoulos (2010), Paleoseismical investigation of the oblique-normal Ekkara ground rupture zone accompanying the M 6.7–7.0 earthquake on 30 April 1954 in Thessaly, Greece: Archaeological and geochronological constraints on ground rupture recurrence, *J. Geophys. Res.*, 115, B06301, doi:10.1029/2009JB006374.
250. Papadimitriou, E. E., and B. C. Papazachos (1985), Evidence for precursory seismicity patterns in the Ionian Islands (Greece), *Earthquake Pred. Res.*, 3, 95–103.
251. Papadimitriou, E.E. (1993), Focal mechanism along the convex side of the Hellenic Arc and its tectonic significance, *Boll. Geof. Teor. Appl.*, 35, 401–426.

252. Papadimitriou, E. E., and L. R. Sykes (2001), Evolution of the stress field in the northern Aegean Sea (Greece), *Geophys. J. Int.*, 146, 747–759.
253. Papadimitriou, E. E. (2002), Mode of strong earthquake recurrence in central Ionian Islands (Greece). Possible triggering due to Coulomb stress changes generated by the occurrence of previous strong shocks, *Bull. Seism. Soc. Am.*, 92, 3293–3308.
254. Papadimitriou, E. E., and V. G. Karakostas (2003), Episodic occurrence of strong (M_w 6.2) earthquakes in Thessalia area (central Greece), *Earth Planetary Science Letters*, 215, 395–409.
255. Papadimitriou, E. E., G. Sourlas, and V. G. Karakostas (2005), Seismicity variations in the southern Aegean, Greece, before and after the large (M7.7) 1956 Amorgos Earthquake due to evolving stress, *Pure Appl. Geophys.*, 162, 783-804.
256. Papadimitriou, E. E., F. F. Evison, D. A. Rhoades, V. G. Karakostas, R. Console, and M. R. Murru (2006), Long term seismogenesis in Greece: Comparison of the evolving stress field and precursory scale increase approaches, *J. Geophys. Res.*, 111, doi:10.1029/2005JB003805.
257. Papadimitriou, E. E., G. Kaviris and K. Makropoulos (2006), The $M_w=6.3$ 2003 Lefkada earthquake (Greece) and induced stress transfer changes, *Tectonophysics*, 423, 73-82.
258. Papadimitriou, E. E., and V. G. Karakostas (2008), Rupture model of the great AD 365 Crete earthquake in the southwestern part of the Hellenic Arc, *Acta Geophys.*, 56, 293-312.
259. Papaioannou, Ch. A., and B. C. Papazachos (2000), Time-Independent and Time-Dependent seismic hazard in Greece based on seismotectonic sources, *Bull. Seismol. Soc. Am.*, 90, 22-33.

260. Papastamatiou, D., and N. Mouyiaris (1986a), The Sofades earthquake of April 30, 1954—Field observations of Giannis Papastamatiou, *Geol. Geophys. Stud.*, sp. volume, 341–362.
261. Papastamatiou, D., and N. Mouyiaris (1986b), The earthquake of April 30, 1954, in Sophades (central Greece), *J. R. Astron. Soc. Can.*, 87, 885–895.
262. Papathanassiou, G., S. Valkaniotis, and S. Pavlides (2007), Applying the INQUA scale to the Sofades 1954, Central Greece, earthquake, *Bull. Geol. Soc. Greece*, 40, 1226–1233.
263. Papazachos, B. C. (1980), Seismicity rates and long-term earthquake prediction in the Aegean Area, *Quaterniones Geodaeisae*, 3, 171-190.
264. Papazachos, B. C., and P. E. Comninakis (1969), Geophysical features of the Greek Island Arc and Eastern Mediterranean Ridge, *Com. Ren. Séances Conf. Reunie Madrid*, 16, 74–75.
265. Papazachos, B. C., and P. E. Comninakis (1971), Geophysical and tectonic., features of the Aegean Arc, *J. Geophys. Res*, 76, 35, 8517-8533.
266. Papazachos, B. C., and P. E. Comninakis (1982), Long-term earthquake prediction in the Hellenic trench-arc system, *Tectonophysics*, 86, 3-16.
267. Papazachos, B. C., D. G. Panagiotopoulos, T. M. Tsapanos, D. M. Mountrakis, and G. Ch. Dimopoulos (1983), A study of the 1980 summer seismic sequence in the Magnesia region of Central Greece, *Geophys. J. R. astr. Soc.*, 75, 155-168.
268. Papazachos, B. C., and C. Papazachou (2003), *The Earthquakes of Greece*, Ziti Publ., Thessaloniki, 317 pp.
269. Papazachos, B. C., and A. Kiratzi (1996), A detailed study of the active crustal deformation in the Aegean and surrounding area. *Tectonophysics*, 253, 129–153.
270. Papazachos, C. B., and G. Nolet (1997), P and S deep velocity structure of the Hellenic Arc obtained by robust nonlinear inversion of travel times, *J. Geophys. Res.* 102, 8349-8367.

271. Papazachos, B. C., E. E. Papadimitriou, A. A. Kiratzi, C. B. Papazachos, and E. K. Louvari (1998), Fault plane solutions in the Aegean Sea and the surrounding area and their tectonic implication, *Bol. Geof. Teor. Applic.*, 39, 199-218.
272. Papazachos C. B. (1999), An alternative method for a reliable estimation of seismicity with an application in Greece and the Surrounding area, *Bull. Seismol. Soc. Am.*, 89, 111-119.
273. Papazachos, C. B., E. M. Scordilis, G. F. Karakaisis, and B. C. Papazachos (2005), Decelerating preshock seismic deformation in fault regions during critical periods, *Bull. Geol. Soc. Greece*, 36, 1490-1498.
274. Papazachos, B. C., D. M. Mountrakis, C. B. Papazachos, M. D. Tranos, G. F. Karakaisis and A. S. Savvaidis (2001), The faults that caused the known strong earthquakes in Greece and surrounding areas during 5th century B. C. up to present, *Proceedings of the 2nd Conference on Earthquake Engineering and Engineering Seismology, 28–30 September 2001, Thessaloniki*, 1, 17–26.
275. Papazachos, B. C., G. F. Karakaisis, C. B. Papazachos, and E. M. Scordilis, (2006), Perspectives for earthquake prediction in the Mediterranean and contribution of geological observations, *J. Geol. Soc. London*, 260, 689-707.
276. Papazachos, B. C., E. M. Scordilis, D. G. Panagiotopoulos, C. B. Papazachos, and G. F. Karakaisis (2004), Global relations between seismic fault parameters and moment magnitude of earthquakes, *Bull. Geol. Soc. Greece*, 36, 1482–1489.
277. Papazachos, B. C., B. G. Karakostas, C. B. Papazachos, and E. M. Scordilis (2000), The geometry of the Benioff zone and lithospheric kinematics in the Hellenic Arc, *Tectonophysics* 319, 275-300.

278. Papazachos, B. C., P. E. Comninakis, E. M. Scordilis, G. F. Karakaisis, and C. B. Papazachos (2009), A catalogue of earthquakes in the Mediterranean and surrounding area for the period 1901 – Sep. 2009, *Publ. Geophys. Laboratory, University of Thessaloniki*.
279. Paradisopoulou, P. (2009), *Contribution to seismicity study of Greek region in association with Coulomb stress changes (in Greek)*, Phd Thesis, doi: 10.12681/eadd/19313.
280. Paradisopoulou, P. M., E. E. Papanimitriou, V. G. Karakostas, T. Taymaz, A. Kiliyas, and S. Yolsal (2010), Seismic hazard evaluation in western Turkey as revealed by stress transfer and time-dependent probability calculations, *Pure Appl. Geophys.*, doi: 10.1007/s00024-010-0085-1.
281. Parsons, T. (2002), Global Omori law decay of triggered earthquakes: Large aftershocks outside the classical aftershock zone, *J. Geophys. Res.*, 107, doi:10.1029/2001JB000646.
282. Parsons, T. (2004), Recalculated probability of $M \geq 7$ earthquakes beneath the Sea of Marmara, Turkey, *J. Geophys. Res.*, 109, doi:10.1029/2003JB002667.
283. Parsons, T., R. S. Stein, R. W. Simpson, and P. A. Reasenbergs (1999), Stress sensitivity of fault seismicity: A comparison between limited-offset oblique and major strike slip faults, *J. Geophys. Res.*, 104, 20,183-20,202.
284. Parsons, T., S. Toda, R. S. Stein, A. Barka, and J. H. Dieterich (2000), Heightened odds of large earthquakes near Istanbul: An interaction-based probability calculation, *Science*, 288, 661–665.
285. Parsons, T. (2005), Significance of stress transfer in time-dependent earthquake probability calculations, *J. Geophys. Res.*, 110, doi:10.1029/2004JB003190.

286. Parsons, T., Y. Ogata, J. Zhuang, and E. L. Geist (2012), Evaluation of static stress change forecasting with prospective and blind tests, *Geophys. J. Int.*, 188, 1425–1440, doi: 10.1111/j.1365-246X.2011.05343.x.
287. Parsons, T., and M. Segou (2014), Stress, distance, magnitude and clustering influences on the success or failure of an aftershock forecast: The 2013 M6.6 Lushan earthquake and other examples, *Seismol. Res. Lett.*, 85, doi:10.1785/0220130100.
288. Pavlides, S. (1993), Active faulting in multi-fractured seismogenic areas: Examples from Greece, *Z. Geomorphol.*, 94, 57–72.
289. Pearce, F.D., S. Rondenay, M. Sachpazi, M. Charalampakis, and L. H. Royden (2012), Seismic investigation of the transition from continental to oceanic subduction along the western Hellenic Subduction Zone, *J. Geophys. Res.*, 117, doi.org/10.1029/2011JB009023.
290. Peng, Z., J. E. Vidale, M. Ishii, and A. Helmstetter (2007), Seismicity rate immediately before and after main shock rupture from high-frequency waveforms in Japan, *J. Geophys. Res.*, 112, doi:10.1029/2006JB004386.
291. Perfettini, H., J. Schmittbuhl, and A. Cochard (2003), Shear and normal load perturbations on a two-dimensional continuous fault: 2. Dynamic triggering, *J. Geophys. Res.*, 108, B9, 2409, doi:10.1029/2002JB001805.
292. Perfettini, H. and J. – P. Avouac (2004), Postseismic relaxation driven by brittle creep: A possible mechanism to reconcile geodetic measurement and the decay rate of rate of aftershocks, application to the Chi-Chi earthquake, Taiwan, *J. Geophys. Res.*, 109, doi:10.1029/2003JB002488.
293. Perfettini, H., and J. -P. Avouac (2007), Modeling afterslip and aftershocks following the 1992 Landers earthquake, *J. Geophys. Res.*, 112, B07409, doi:10.1029/2006JB004399.
294. Peter, Y., H. -G. Kahle, M. Cocard, G. Veis, S. Felekis, and D. Paradissis (1998), Establishment of a continuous GPS network across the

- Kephalonia Fault Zone, Ionian Islands, Greece, *Tectonophysics* 294, 253–260.
295. Petersen, M. D., C. S. Mueller, A. D. Frankel, and Y. Zeng (2008), Spatial seismicity rates and maximum magnitudes for background earthquakes (Appendix J), USGS Open File Report 2007-1437J, *CGS Special Report 203J, SCEC Contribution #1138J*, Version 1.0.
296. Piromallo, C., and A. Morelli (2003), P-wave tomography of the mantle under the Alpine–Mediterranean area, *J. Geophys. Res.*, 108, doi.org/10.1029/2002JB001757.
297. Pinar, A. (1998), Source inversion of the October 1, 1995, Dinar earthquake ($M_s=6.1$): a rupture model with implications for seismotectonics in SW Turkey, *Tectonophysics*, 292, 255-266.
298. Poliakov, A. N. B., R. Dmowska, and J. R. Rice (2002), Dynamic shear rupture interactions with fault bends and off-axis secondary faulting, *J. Geophys. Res.*, 107, B11, doi:10.1029/2001JB000572.
299. Pollitz, F. F., and I. S. Sacks (2002), Stress triggering of the 1999 Hector mine earthquake by transient deformation following the 1992 Landers earthquake, *Bull. Seismol. Soc. Am.*, 92, 1487-1496.
300. Pollitz, F. F., and M. J. S. Johnston (2006), Direct test of static stress versus dynamic stress triggering of aftershocks, *Geophys. Res. Lett.*, 33, doi:10.1029/2006GL026764.
301. Rathbun, S. L. (1993), Modelling marked spatio-temporal point patterns, *Bull. Int. Stat. Inst.*, 55, 379–396.
302. Reasenber, P. (1985), Second order moment of central California Seismicity, 1969-1982, *J. Geophys. Res.*, 90, 5479–5495.
303. Reasenber, P. A., and R. W. Simpson (1992), Response of regional Seismicity to the Static Stress Change Produced by the Loma Prieta Earthquake, *Science*, 255, 1687-1690.

304. Reilinger, R., S. McClusky, P. Vernant, S. Lawrence, S. Ergitav, R. Cakmak, H. Ozener, F. Kadirov, I. Guliev, R. Stepanyan, M. Nadariya, G. Hahubia, S. Mahmoud, K. Sakr, A. ArRajehi, D. Paradissis, A. Al-Aydrus, M. Prilepin, T. Guseva, E. Evren, A. Dmitrotsa, S. V. Filikov, F. Gomez, R. Al-Ghazzi, and G. Karam (2006), GPS constraints on continental deformation in the Africa-Arabia-Eurasia continental collision zone and implications for the dynamics of plate interactions, *J. Geophys. Res.*, 111, doi:10.1029/2005JB004051.
305. Richards-Dinger, K., R. S. Stein, and S. Toda (2010), Decay of aftershock density with distance does not indicate triggering by dynamic stress, *Nature*, doi:101038/nature09402.
306. Rigo, A., H. Lyon-Caen, H. R. Armijo, A. Deschamps, D. Hatzfeld, K. Makropoulos, P. Papadimitriou, and I. Kassaras (1996), A microseismic study in the western part of Gulf of Corinth (Greece): implications for large scale normal faulting mechanisms, *Geophys. J. Int.*, 126, 663-668.
307. Ritsema, A. (1974), The earthquake mechanics of the Balkan region, *R. Netherl. Meteorol. Inst., De Bilt, Sci. Rep.*, 74-4.
308. Roberts, S. and J. Jackson (1991), Active normal faulting in central Greece: An overview, in the *Geometry of Normal Faults*, ed. Roberts, A. M. et al., *Spec. Publ. Geol. Soc. London*, 56, 125-142.
309. Robinson, R., and P. J. McGinty (2000), The enigma of the Arthur's Pass, New Zealand, earthquake 2. The aftershock distribution and its' relation to regional and induced stress fields, *J. Geophys. Res.*, 105, 16,139 – 16,150.
310. Roumelioti, Z., C. Benetatos, and A. Kiratzi (2009), The 14 February 2008 earthquake (M6.7) sequence offshore south Peloponnese (Greece): Source models of the three strongest event, *Tectonophysics*, 471, 272-284.
311. Rousset, B., S. Barbot, J. -P. Avouac, and Y. -J. Hsu (2012), Postseismic deformation following the 1999 Chi-Chi earthquake, Taiwan: implication for lower-crust rheology, *J. Geophys. Res.*, 117, doi:10.1029/2012JB009571.

312. Rydelek, P. A., and I. S. Sacks (1989), Testing the completeness of earthquake catalogs and the hypothesis of self-similarity, *Nature*, 337, 251-253.
313. Sachs, M. K., M. R. Yoder, D. L. Turcotte, J. B. Rundle, and B. D. Malamud (2012), Black swarms, power laws and dragon kings: earthquakes, volcanic eruptions, landslides, wildfires, floods, and SOC models, *Eur. Phys. J. Special Topics*, 205, 167-182.
314. Saichev, A., and D. Sornette (2006), Powel law distribution of seismic rates: theory and data analysis, *Eur. Phys. J.*, 49, 377-401.
315. Sain, S. R., K. A. Baggerly, and D. W. Scott (1994), Cross-validation of multivariable densities, *J. Am. Stat. Assoc.*, 89, 807-817.
316. Scholz, C. H. (1998), Earthquakes and friction laws, *Nature*, 391, 37 - 42.
317. Scholz, C. H. (2002), *The Mechanics of Earthquakes and Faulting*, Cambridge University Press, Cambridge, 439 pp.
318. Schorlemmer, D., and J. Woessner (2008), Probability of detecting an earthquake, *Bull. Seismol. Soc. Am.*, 98, doi 10.1785/0120070105.
319. Scordilis, E. M. (2006), Empirical global relations converting M_s and m_b to moment magnitude, *J. Seismol.*, 10, 225-236.
320. Scordilis, E. M., G. F. Karakaisis, B. G. Karakostas, D. G. Panagiotopoulos, P. E. Comninakis, and B. C. Papazachos (1985), Evidence for transform faulting in the Ionian Sea: The Cephalonia Island earthquake sequence, *Pure Appl. Geophys.*, 123, 388-397.
321. Şengör, A. M. C., M. Satır, and R. Akkok (1984), Timing of tectonic events in the Menderes Massif, western Turkey: implications for tectonic evolution and evidence for Pan-African basement in Turkey, *Tectonics*, 3, 693-707.
322. Shaw, B. (2012), *Active tectonics of the Hellenic subduction zone*, Springer Theses, 169 pp.

323. Shan, B., X. Xiong, Y. Zheng, and F. Diao (2009), Stress changes on major faults caused by Mw7.9 Wenchuan earthquake, *Sci. China – Earth Sci.*, 52, 593-601.
324. Shimazaki, K. (1978), Correlation between intraplate seismicity and interplate earthquakes in Tohoku, northeastern Japan, *Bull. Seismol. Soc. Am.*, 68, 181-192.
325. Silverman, B. W. (1978), Choosing the window width when estimating a density, *Biometrika*, 65, 1–11.
326. Silverman, B. W. (1986), *Density Estimation for Statistic and Data Analysis*, Chapman and Hall, London, 175 pp.
327. Simpson, R. W., and P. A. Reasenberg (1994), Earthquake-induced static stress changes on central California faults, in the Loma Prieta, California earthquake of October 17, 1989 – Tectonic processes, and models, *ed. Simpson R. W., U. S. Geol. Surv. Prof. Pap.*, 1550–F, F55–F89.
328. Smith, D. E., and T. H. Heaton (2011), Models of stochastic, spatially varying stress in the crust compatible with focal-mechanism data, and how stress inversions can be biased toward the stress rate, *Bull. Seismol. Soc. Am.*, 101, 1396-1421.
329. Sokos E, J. Zahradnik, A. Kiratzi, J. Jansky, F. Gallovic, O. Novotny, J. Kostelecky, A. Serpetsidaki, and A. Tselentis (2012), The January 2010 Efpalio earthquake sequence in the western Corinth Gulf (Greece). *Tectonophysics*, 530–531, 299–309.
330. Sornette, D. (2009), Dragon kings, black swans and the prediction of crises, *Int. Terraspace Sci. Eng.*, 2,1
331. Spakman, W., M. J. R. Wortel, and N. S. Vlaar (1988), The Hellenic subduction zone: a tomographic image and its geodynamic implications, *Geophys. Res. Lett.* 15, 60-63.

332. Steacy, S., J. Gomberg, and M. Cocco (2005), Introduction to special section: Stress transfer, earthquake triggering, and time-dependent seismic hazard, *J. Geophys. Res.*, 110, doi:10.1029/2005JB003692.
333. Steacy, S., S. S. Nalbant, J. McCloskey, C. Nostro, O. Scotti, and D. Baumont (2005), Onto what planes should Coulomb stress perturbation be resolved?, *J. Geophys. Res.*, 110, doi:10.1029/2004JB003356.
334. Stein, R. S., A. A. Barka, and J. H. Dieterich (1997), Progressive failure on the North Anatolian fault since 1939 by earthquake stress triggering, *Geophys. J. Int.*, 128, 594–604.
335. Stein, R. S. (1999), The role of stress transfer in earthquake occurrence, *Nature*, 402, 594–604.
336. Stein, R. S. (2003), Earthquake conversations, *Sci. Am.*, 288, 72-79.
337. Straub, C., H. G. Kahle, and C. Schindler (1997), GPS and geologic estimates of the tectonic activity in the Marmara sea region, NW Anatolia, *J. Geophys. Res.*, 102, 27,587-27,601.
338. Suckale, J., S. Rondenay, M. Sachpazi, M. Charalampakis, A. Hosa, and L. H. Royden (2009), High resolution seismic imaging of the Western Hellenic subduction zone using teleseismic scattered waves, *Geophys. J. Int.*, doi.org/10.1111/j.1365-246X.2009.04170.x.
339. Sykes, L. R. (1996), Intermediate- and long – term earthquake prediction, Earthquake Prediction: The scientific challenge, *Proc. Natl. Acad. Sci., USA*, 3721-3725.
340. Tajima, F., and H. Kanamori (1985), Global Survey of aftershock area expansion patterns, *Phys. Earth Planet. Inter.*, 40, 77–134.
341. Tan, O. (2013), The dense micro-earthquake activity at the boundary between the Anatolian and South Aegean microplates, *J. Geodyn.*, 65, 199-217.
342. Tan, O., E. E. Papadimitriou, Z. Pabucçu, V. Karakostas, A. Yörük, and K. Leptokaropoulos (2014), A detailed analysis of microseismicity is

- Samos and Kusadasi (Eastern Aegean Sea) areas, *Acta Geophys.*, doi: 10.2478/s11600-013-0194-1.
343. Taylor, D. W. A., J. A. Snoke, I. S. Sacks, and T. Takanami (1990), Non-linear frequency- magnitude relationship for the Hokkaido corner, Japan, *Bull. Seismol. Soc. Am.*, 80, 605-609.
344. Taymaz, T., J. A. Jackson, and D. McKenzie (1991), Active tectonics of the north and central Aegean Sea. *Geophys. J. Int.*, 106, 433-490.
345. Taymaz, T., and S. Price (1992), The 1971 May 12 Burdur earthquake sequence, SW Turkey: A synthesis of seismological and geological observations, *Geophys. J. Int.* 108, 589-603.
346. Tiampo, K. F., J. B. Rundle, and W. Klein (2006), Premonitory seismicity changes prior to the Parkfield and Coalinga earthquakes in southern California, *Tectonophysics*, 413, 77-83.
347. Tibi, R., J. Blanco, and A. Fatehi (2011), An alternative and efficient cluster-link approach for declustering of earthquake catalogs, *Seismol. Res. Lett.*, 82, 509-518.
348. Toda, S., R. S. Stein, P. A. Reasenberg, and J. H. Dieterich (1998), Stress transferred by the 1995 Mw = 6.9 Kobe, Japan, shock: Effect on aftershocks and future earthquake probabilities, *J. Geophys. Res.*, 103, 24,543-24,565.
349. Toda, S., and R. S. Stein (2002), Response of the San Andreas fault to the 1983 Coalinga-Nuñez earthquakes: An application of interaction-based probabilities for Parkfield, *J. Geophys. Res.*, 107, 10.1029/2001 JB000172.
350. Toda, S., R. S. Stein, and T. Sagiya (2002), Evidence from the AD 2000 Izu islands earthquake swarm that stressing rate governs seismicity, *Nature*, 419, 58-61.
351. Toda, S., and R. S. Stein (2003), Toggling of seismicity by the 1997 Kagoshima earthquake couplet: A demonstration of time-dependent stress transfer, *J. Geophys. Res.*, 108, doi:10.1029/2003 JB002527.

352. Toda, S., R. S. Stein, K. Richards-Dinger, and S. Bozkurt (2005), Forecasting the evolution of seismicity in southern California: Animations built on earthquake stress transfer, *J. Geophys. Res.*, 110, doi:10.1029/2004JB003415.
353. Toda, S., and S. Matsumura (2006), Spatio-temporal stress states estimated from seismicity rate changes in the Tokai region, central Japan, *Tectonophysics*, 417, 53-68.
354. Toda, S., J. Lin, M. Meghraoui, and R. S. Stein (2008), 12 May 2008 M=7.9 Wenchuan, China, earthquake calculated to increase failure stress and seismicity rate on three major fault systems, *Geophys. Res. Lett.*, doi:10.1029/2008GL034903.
355. Toda, S., and Enescu, B., 2011. Rate/State Coulomb stress transfer model for the CSEP Japan seismicity forecast, *Earth Planets Space*, 63, 171-185.
356. Tsapanos, T. M., P. Mäntyniemi, and A. Kijko (2004), A probabilistic seismic hazard assessment for Greece and the surrounding region including site-specific considerations, *Ann Geophys-Italy*, 47, 1675-1688.
357. Tselentis, G- A., and L. Danciu (2010), Probabilistic seismic hazard assessment in Greece – Part 1: Engineering ground motion parameters, *Nat. Hazards Earth Syst. Sci.*, 10, 25-39.
358. Tselentis, G- A., L. Danciu, and E. Sokos (2010), Probabilistic seismic hazard assessment in Greece – Part 2: Acceleration response spectra and elastic input energy spectra, *Nat. Hazards Earth Syst. Sci.*, 10, 41-49.
359. Tsukakoshi, Y., and K. Shimazaki (2006), Temporal behavior of the background seismicity rate in central Japan, 1998 to mid-2003, *Tectonophysics*, 417, 155–168.
360. Utsu, T. (1969), Aftershock and Earthquake Statistics (I): Some Parameters Which Characterize an Aftershock Sequence and Their Interrelations, *J. Fac. Sci, Hokkaido Univ. Ser. VIII, Geophys.*, 3, 129-195.

361. Utsu, T. (1999), Representation and analysis of the earthquake size distribution: A historical review and some new approaches, *Pure Appl. Geophys.*, 155, 509–535.
362. Vidale, J. E., D. C. Agnew, M. S. Johnston, and D. H. Oppenheimer (1998) Absence of earthquake correlation with earth tides: An indication of high preseismic fault stress rate, *J. Geophys. Res.*, 103, 24567-24572.
363. Vidale, J., D. Agnew, D. Oppenheimer, C. Rodriguez, and H. Houston (1998), A weak correlation and extensional normal stress rate from lunar tides, *Eos (suppl.)*, 79, F641.
364. Voisin, C., M. Campillo, I. R. Ionescu, F. Cotton, and O. Scotti (2000), Dynamic versus static stress triggering and friction parameters: Inferences from the November 23, 1980, Irpinia earthquake, *J. Geophys. Res.*, 105, 21,647-21,659.
365. Wang F., and T. H. Jordan (2014), Comparison of probabilistic seismic-hazard models using averaging-based factorization, *Bull. Seismol. Soc. Am.*, 104, 1230-1257.
366. Wang, J. C., C. F. Shieh, and T. M. Chang (2003), Static changes as a triggering mechanism of a shallow earthquake: case study of the 1999 Chi-Chi (Taiwan) earthquake, *Phys. Earth Planet. Int.*, 135, 17-25.
367. Wang, L., R. Wang, F. Roth, B. Enescu, S. Hainzl, and S. Ergintav (2009), Afterslip and viscoelastic relaxation following the 1999 M7.4 Izmit earthquake from GPS measurements, *Geophys. J. Int.*, doi: 10.1111/j.1365-246X.2009.04228.x.
368. Wang, L., S. Hainzl, M. S. Özeren, and Y. Ben-Zion (2010), Postseismic deformation induced by brittle rock damage of aftershock, *J. Geophys. Res.*, 115, B10422, doi:10.1029/2010JB007532.
369. Wang, L., S. Hainzl, G. Zöller, and M. Holschneider (2012), Stress- and aftershock- constrained joint inversions for coseismic and postseismic

- slip applied to the 2004 M6.0 Parkfield earthquake, *J. Geophys. Res.*, 117, B07406, doi:10.1029/2011JB009017.
370. Wang, W. H., and C. H. Chen (2001), Static stress transferred by the 1999 Chi-Chi, Taiwan, earthquake: Effects on the stability of the surrounding fault systems and aftershock triggering with a 3D fault-slip model, *Bull. Seismol. Soc. Am.*, 91, 1041-1052.
371. Ward, S. N. (1998), On consistency of earthquake moment release and space geodetic strain rates: Europe, *Geophys. J. Int.*, 135, 1011–1018.
372. Wason, H. R., R. Das, and M. L. Sharma (2012), Magnitude conversion problem using general orthogonal regression, *Geophys. J. Int.*, 190, 1,091-1,096.
373. Weatherley, D., S. C. Jaumé, and P. Mora (2000), Evolution of stress deficit and changing rates of seismicity in cellular automaton models of earthquake faults, *Pure Appl. Geophys.*, 157, 2183-2207.
374. Weichert, D. (1980), Estimation of earthquake recurrence parameters for unequal observation periods for different magnitudes, *Bull. Seism. Soc. Am.*, 70, 1337–1356.
375. Wells, D. L., and K. J. Coppersmith (1994), New empirical relationships among magnitude, rupture length, rupture width, rupture area and surface displacement, *Bull. Seismol. Soc. Am.* 84, 974–1002.
376. Werner, M. J., A. Helmstetter, D. D. Jackson, Y. Y. Kagan, and S. Wiemer, (2010), Adaptively smoothed seismicity earthquake forecasts for Italy, *Ann. Geophys.*, 53, doi:10.4401/ag-4839.
377. Wessel, P., and W. H. F. Smith (1998), *New improved version of the Generic Mapping Tools Released*, EOS Trans. AGU, 79, 579.
378. Wesson, R. L. (1987), Modeling aftershock migration and afterslip of the San Juan Bautista, California, earthquake of October 3, 1972, *Tectonophysics*, 144, 214–229.

379. Westaway, R. (1993), Neogene evolution of the Denizli region of western Turkey, *J. Struct. Geol.*, 15, 37–53.
380. Wiemer, S., and M. Wyss (2000), Minimum magnitude of completeness in earthquake catalogs: Examples from Alaska, the Western United States, and Japan, *Bull. Seismol. Soc. Am.*, 90, 4, 859-869.
381. Woessner, J., E. Hauksson, S. Wiemer, and S. Neukomm (2004), The 1997 Kagoshima (Japan) earthquake doublet: A quantitative analysis of aftershock rate changes, *Geophys. Res. Lett.*, 31, doi:10.1029/2003GL018858.
382. Woessner, J., and S. Wiemer (2005), Assessing the quality of earthquake catalogs: Estimating the magnitude of completeness and its uncertainty, *Bull. Seismol. Soc. Am.*, 95, 684-698.
383. Wyss, M., and M. Baer (1981), Seismic quiescence in the western Hellenic arc may foreshadow large earthquakes, *Nature*, 289, 785-787.
384. Wyss, M., and R. E. Habermann (1979), Seismic quiescence precursory to a past and a future Kurile Island earthquake, *Pure Appl. Geophys.*, 117, 1195-1211.
385. Wyss, M., and S. Wiemer (2000), Change in the probability for earthquakes in southern California due to the Landers magnitude 7.3 earthquake, *Science*, 290, 1334-1338.
386. Xie, C., Y. Zhu, X. Lei, H. Yu, and X. Hu (2010), Pattern of stress change and its effect on seismicity rate caused by Ms8.0 Wenchuan earthquake, *Sci. China – Earth Sci.*, 53, 1260–1270 doi: 10.1007/s11430-010-4025-9.
387. Yolsal-Çevikbilen, S., and T. Taymaz (2012), Earthquake source parameters along the Hellenic subduction zone and numerical simulations of historical tsunamis in the Eastern Mediterranean, *Tectonophysics*, 536, 61-100.
388. Zechar, J. D. (2010), Evaluating earthquake predictions and earthquake forecasts: a guide for students and new researchers, *Community Online*

Resource for Statistical Seismicity Analysis, doi:10.5078/corssa-77337879,
Available at <http://www.corssa.org>.

389. Ziv, A. (2003), Foreshocks, aftershocks, and remote triggering in quasi-static fault models, *J. Geophys. Res.*, 108, doi:10.1029/2002JB002318.
390. Ziv, A., and A. M. Rubin (2000), Static stress transfer and earthquake triggering: No lower threshold in sight?, *J. Geophys. Res.*, 105, 13631-13642.
391. Ziv, A., and A. M. Rubin (2003), Implications of rate-and-state friction for properties of aftershock sequence: Quasi-static inherently discrete simulations, *J. Geophys. Res.*, 108, doi:10.1029/2001JB001219.
392. Zhuang, J., Y. Ogata, and D. Vere-Jones (2002), Stochastic declustering of space–time earthquake occurrences, *J. Am. Stat. Assoc.*, 97, 369–380.
393. Zhuang, J., Y. Ogata, and D. Vere-Jones (2004), Analyzing earthquake clustering features by using stochastic reconstruction, *J. Geophys. Res.*, 109, B05301, doi:10.1029/2003JB002879.
394. Zhuang, J., C.P. Chang, Y. Ogata, and Y.I. Chen (2005), A study on the background and clustering seismicity in the Taiwan region by using point process models, *J. Geophys. Res.*, 110, doi:10.1029/2004JB003157.
395. Zhuang, J., M.J. Werner, S. Hainzl, D. Harte, and S. Zhou (2011), Basic seismicity: spatiotemporal models, *Community Online Resource for Statistical Seismicity Analysis*, doi:10.5078/corssa-07487583. Available at <http://www.corssa.org>.